Modeling and characterization of non-ideal compressible flows in unconventional turbines

Tosto, F.

DOI
10.4233/uuid:1b163f58-5570-4915-8999-8f5dd644ed7b

Publication date
2023

Document Version
Final published version

Citation (APA)
Tosto, F. (2023). *Modeling and characterization of non-ideal compressible flows in unconventional turbines*. [Dissertation (TU Delft), Delft University of Technology]. https://doi.org/10.4233/uuid:1b163f58-5570-4915-8999-8f5dd644ed7b

Important note
To cite this publication, please use the final published version (if applicable).
Please check the document version above.

MODELING AND CHARACTERIZATION OF NON-IDEAL COMPRESSIBLE FLOWS IN UNCONVENTIONAL TURBINES

Dissertation

for the purpose of obtaining the degree of doctor
at Delft University of Technology,
by the authority of the Rector Magnificus prof. dr. ir. T.H.J.J. van der Hagen,
chair of the Board for Doctorates,
to be defended publicly on
Tuesday 17 October 2023 at 10:00 am

by

Francesco TOSTO, MsC

Master of Science in Aerospace Engineering, Politecnico di Torino, Italy
born in Torino, Italy

This dissertation has been approved by the promotors.

Composition of the doctoral committee:

Rector Magnificus	chairperson
Prof. dr. ir. P. Colonna	Delft University of Technology, *promotor*
Dr. M. Pini	Delft University of Technology, *copromotor*
Independent members:	
Prof. dr. R. Pecnik	Delft University of Technology
Prof. dr. S.J. Song	Seoul National University, South Korea
Prof. dr. A. Wheeler	University of Cambridge, United Kingdom
Prof. dr. C. Corre	École centrale de Lyon, France
Prof. dr. S. Hickel	Delft University of Technology, *reserve member*
Other members:	
Dr. C. Lettieri	Space Exploration Technologies Corporation, USA

Keywords: Dense vapor, Organic fluid, Turbine, Loss breakdown, Solidity, Direct Numerical Simulation (DNS)

Printed by: Gildeprint

Front & Back: Contour of the density gradient within an air boundary layer flow obtained from a direct numerical simulation (DNS).

ISBN 978-94-6419-941-3

An electronic version of this dissertation is available at
http://repository.tudelft.nl/.

Dedicato a mamma e papà

CONTENTS

SUMMARY

The vast majority of energy conversion systems currently makes use of fossil fuels, whose combustion generates harmful greenhouse gases. Transitioning to renewable energy sources is thus paramount to limiting the environmental impact of human activities on the climate. In this regard, the harvesting of wasted thermal energy constitutes a promising strategy to increase the efficiency of industrial processes and mobile engines. For instance, technologies such as organic Rankine cycle (ORC) systems enable the energy discarded during the conversion processes to the atmosphere to be repurposed and generate CO_2-neutral electricity or additional mechanical work.

The efficiency of such systems is subordinate to that of each of the components, among which, is the turbine. Designing more efficient ORC turbines inherently leads to a higher thermodynamic cycle efficiency. However, these turbines operate with complex organic compounds, and part of the expansion process often occurs in the dense vapor state, where the thermodynamic properties exhibit significant deviations from the variations predicted by the ideal gas law. As a consequence, available guidelines for the design of turbomachinery operating with air or steam cannot be used, as they would lead to incorrect sizing and wrong performance estimations. The development of generalized guidelines for turbine design is possible only through a thorough investigation of the internal non-ideal compressible flow inside the vane passage, and by accurately discerning all the possible loss sources.

The research outlined in this thesis aims at characterizing non-ideal compressible internal flows of dense vapors and developing new guidelines for the design of unconventional turbines operating with organic fluids, such as those operating in organic Rankine cycle power systems.

The influence of both the complexity of the fluid molecules and the thermodynamic state on the flow field is evaluated for some paradigmatic one-dimensional flow configurations. For these processes, loss mechanisms and relevant trends in flow variables are both qualitatively and quantitatively estimated. Moreover, a detailed analysis of the viscous dissipation in turbulent wall-bounded flows of dense vapor is performed by resorting to direct numerical simulations (DNS). Results are compared against those from an in-house reduced-order model (ROM) code solving the two-dimensional boundary layer equations. The combined effects of the working fluid, its thermodynamic state, and the flow compressibility on the flow deviation downstream of turbine cascades are then investigated by means of Reynolds Averaged Navier-Stokes (RANS) calculations on a representative geometry. The results obtained from the simulations are compared against those estimated with reduced-order physical models. Finally, an investigation of the influence of both compressibility and fluid molecular complexity on the optimal solidity of axial turbines is performed using RANS calculations. New design guidelines for the selection of optimal solidity in the preliminary design of non-conventional turbomachinery are proposed and discussed.

Results show that turbines operating with compounds characterized by a high complexity of the molecular structure are arguably subjected to higher losses in the mixing region, as well as exhibiting larger viscous dissipation at a given Reynolds number. Moreover, the fluid strongly affects the operational range of the turbine, as well as its design.

SAMENVATTING

Het overgrote deel van de energie centrales maakt gebruik van fossiele brandstoffen, waarbij schadelijke broeikasgassen vrijkomen. Om de impact van de mens op het milieu en klimaat te beperken is het daarom uitermate belanrijk om over te stappen naar duurzame energiebronnen. Een manier om de efficientie van industriele processen en motoren van voertuigen te verhogen is de terugwinning van de warmte die bij deze processen vrijkomt. Een voorbeeld van technologie die dit mogelijk maakt is het organische Rankine process (ORC). ORC systemen kunnen restwarmte die normaal gesproken niet wordt benut gebuiken om CO_2 neutrale energie op te wekken of extra vermogen kunnen leveren aan het betreffende proces.

De efficientie van een dergelijk system is afhankelijk van de bevattende componenten, onder andere de turbine. Het verhogen van de efficientie van de ORC turbine resulteert daarom in een verhoogde efficientie voor het gehele systeem. Het ontwerp van de betreffence turbines wordt echter gehinderd door de moeilijkheden omtrend het modeleren van de complexe, organische stoffen die als drijfstof in het systeem worden gebruikt. Aangezien dergelijke stoffen compleet andere eigenschappen hebben dan bijvoorbeeld lucht of stoom zijn er geen algemene richtlijnen omtrend het ontwerp van ORC turbines. Het gebruik van ontwerprichtlijnen voor stoom- of lucht turbines zou leiden tot een incorrect ontwerp en prestatie voorspellingen. De ontwikkeling van algemene richtlijnen voor turbine ontwerp kan worden bewerkstelligd door grondig onderzoek te doen naar de effecten van niet-ideale, compresible stroming door turbine schoepen, en door het onderscheiden van de mogelijke oorzaken van verliezen.

Het doel van het onderzoek beschreven in dit proefschrift is het bestuderen van niet-ideale, interne stromingen van organische stoffen en het ontwikkelen van nieuwe richtlijnen voor het ontwerp van onconventionele turbines met organische drijfstoffen, idem ORC systemen.

De invloed van zowel de moleculaire complexiteit en de thermodynamische toestand op het stromingsveld werd gevalueerd voor enkele paradigmatische, één-dimensionale test cases. Hierbij werden de verliesmechanismen en relevante stromingsvariablelen zowel kwalitatief en kwantitatief geanalyseerd. Daarnaast werd een gedetaileerde analyse uitgevoerd omtrend de viscose dissipatie in de turbulente grenslaag van dichte dampen doormiddel van directe numerieke simulaties (DNS). De resultaten werden vergeleken met die van een zelfontwikkeld, gesimplificeerd model (ROM), ontwikkeld voor het oplossen van de twee-dimensionale grenslaagvergelijkingen. Vervolgens werden de gecombineerde effecten van zowel de stofeigen moleculaire complexiteit en de thermodynamische toestand op het stromingsveld achter turbine bladen onderzocht doormiddel van Reynolds Averaged Navier-Stokes (RANS) berekeningen. De resultaten werden opnieuw vergeleken met data verkregen doormiddel van gesimplificeerde modellen. Tenslotte werd de invloed van moleculaire complexiteit en compressibiliteit onderzocht op de optimale soliditeit van turbines doormiddel van RANS berekeningen. Naar deze

resultaten worden nieuwe richtlijnen omtrend de selectie van de optimale soliditeit van turbines met complexe drijfstoffen opgemaakt.

Naar de resultaten wordt geconcludeerd dat turbines met een drijfstof van hoge moleculaire complexiteit hogere verliezen lijden waar stromingen mixen en een verhoogde visceuze dissipatie voor een bepaald Reynolds getal zich voortdoet in de stroom. Daarnaast heeft de drijfstof een grote invloed op zowel het operationele berijk van de turbine als het geoptimalizeerde ontwerp.

1

INTRODUCTION

1.1. CONTEXT

Humanity has been experiencing an ever-increasing demand for energy, whose growth rate sparked after the second world war (Fig. 1.1). The vast majority of the primary energy used by man currently comes from the combustion of fossil fuels, which, in turn, contributes to the emission of greenhouse gases such as carbon dioxide (CO_2) and other harmful substances (NOx). It is estimated that CO_2 emissions have increased by almost 64% since 1990 [1]. The dependency on fossil fuels must thus be drastically reduced to limit the effects on the climate. The global temperature has increased by 1 °C since the end of the 19^{th} century and it is forecast that it will increase between 1.1 and 5.4 °C by 2100 [2]. It is expected that sea levels, which have already increased by 10 cm since 1993, will increase by 30 to 240 cm by 2100 if the warming proceeds at this rate [3]. Transitioning to a climate-neutral society is of paramount importance, thus it is indisputable that the transition to renewable energy sources must be a priority for all countries.

Clean electric energy is nowadays obtained by converting natural energy resources such as wind, solar radiation, biomass fuels, and geothermal and water reservoirs. The renewable energy revolution will happen only if all countries will adapt to the local availability of natural energy sources, thus flexibly implementing suitable technologies for their conversion. Emancipation from fossil fuels is inherently the basis of a more peaceful world: most countries are still importing oil, coal, and natural gas from other parts of the world. As a consequence, reliable distribution of fossil fuel amongst the countries can only be guaranteed through international treaties, which can, in turn, be overcome in case of political instabilities in the supplying nations. Hence, conflicts and sanctions can affect the energy supply chain, damaging the economy of the importing countries. The recent Russian-Ukraininan conflict is a good example: sanctions against the Russian Federation have caused a spike in the energy prices in many countries [4]. As a remarkable side effect, switching to renewable energy sources would cause a drop in the costs related to the distribution infrastructure: indeed, the distance between the source of primary energy and the points of utilization would be drastically reduced.

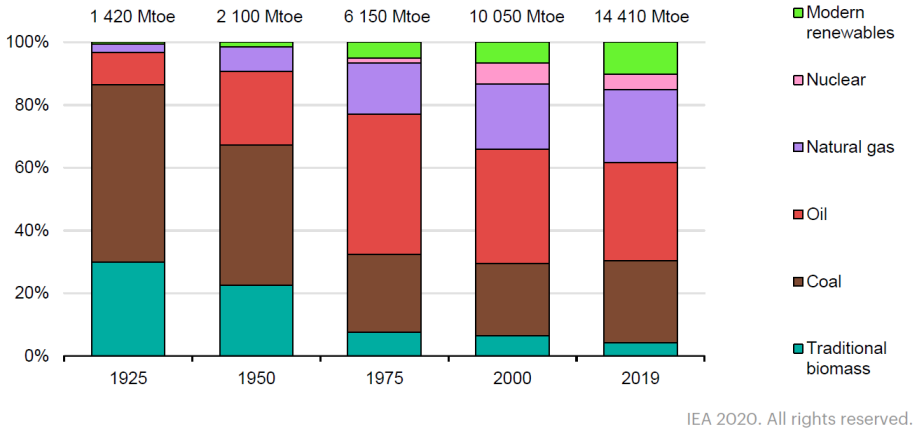

Figure 1.1: Global primary energy demand by fuel, 1925-2019. Courtesy of the International Energy Agency [1].

Up to some decades ago, the cost of technologies for the conversion of renewable energy sources was higher than that of fossil-fuel-based ones. One can argue that huge side-effects costs related to, e.g., health, local and global ecological climate impact due to fossil-fuel-based technology were not accounted for. However, the scenario is rapidly changing. According to the 2020 *Renewable Power Generation Cost* report by IRENA [5], the installation costs of concentrating solar-thermal power stations, onshore and offshore wind farms have decreased, respectively, by 16%, 13% and 9% with respect to the previous year. Moreover, according to the same report, during the last decade, the global weighted-average levelised cost of electricity of solar photovoltaic technology for newly commissioned projects fell from 0.381 to 0.057 USD/kWh, while that of onshore and offshore wind projects fell from 0.089 to 0.039 USD/kWh and from 0.162 to 0.084 USD/kWh, respectively. For comparison, the cost of fossil fuel-derived electric energy in G20 countries ranges today between 0.055 and 0.148 USD/kWh[1]. Energy generated from renewable sources is thus increasingly becoming the backbone of power generation systems. It must be noted, however, that this drastic change mostly concerns developed countries: developing and under-developed countries still rely on fossil fuel-based technology, and the transition to renewable sources is not prioritized or envisioned in the short term [8].

The harvesting of currently wasted thermal energy from industrial processes and all sorts of engines, stationary or mobile, is an enormous albeit still greatly under-used renewable-equivalent energy resource. The thermal energy discarded during these anthropic energy conversion processes to the atmosphere could be repurposed to generate CO_2-neutral electricity. It is conservatively estimated that at least 150 TWh of electricity per year could be generated by harvesting currently untapped thermal energy from industrial processes in the EU 27 countries [2]. This amount corresponds to the combined

[1] Importantly, the problem of the discontinuity of renewable energy generation is being tackled and the cost of electricity storage is also decreasing at an impressive pace [6], while other suitable technologies such as water electrolysis are also rapidly progressing [7].

[2] No engines/compressors for natural gas distribution are considered in the calculations, only wasted thermal energy from industrial plants is taken into account

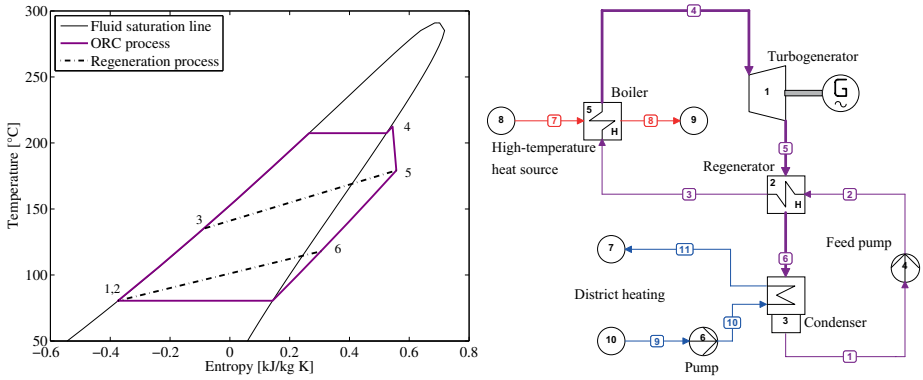

(a) (b)

Figure 1.2: (a) Thermodynamic process of an exemplary superheated/regenerated ORC power plant in the *Ts* diagram and (b) corresponding process flow diagram (b). Specifications: condensing temperature 80 °C, evaporating pressure 3.5 bar, pinch point temperature difference in the evaporator 30 K, superheating of 5 K, isentropic efficiency of the turbine and the pump 0.90 and 0.65, respectively, no pressure losses. Adapted from Colonna et al [10].

annual consumption of electricity in both the Netherlands and Denmark combined or about half of the electricity produced in Italy in 2021. Moreover, 75 Mton/yr of CO_2 emissions would be produced if the electricity were generated by burning natural gas. The interested reader is referred to Ref. [9] for complete and detailed information.

Waste-heat-to-power can be achieved through different technologies, among which the organic Rankine cycle (ORC) power system stands out. The organic Rankine cycle is a Rankine thermodynamic cycle whereby the working fluid is an organic compound and not water [9]. The selection of the optimal working fluid allows for overcoming the limitation of steam power plants, which are suitable only for the conversion of large capacity and high-temperature energy sources [10]. Figure 1.2a shows the thermodynamic processes forming a superheated/regenerated cycle in the *Ts* diagram of the working fluid, and Fig. 1.2b shows the corresponding process flow diagram. Often, the regenerated cycle configuration is chosen to further increase the conversion efficiency of the power plant. ORC power systems offer several advantages over other suitable conversion systems. First of all, the technology applies to thermal energy sources that can range in capacity from a few kW to hundreds of MW, and the temperature difference between the thermal source and sink can range from approximately 30 °C to 500 °C [10]. Therefore, ORC power systems can be employed to convert energy from geothermal reservoirs [11], [12], solar concentrators [13], biomass combustors [14], and, importantly, industrial waste heat [9], [15]. Moreover, the extreme flexibility of ORC technology is due to the possibility of selecting the optimal working fluid depending on both the capacity and the temperature of the primary energy source. The overall conversion efficiency and the feasibility and performance of the expander are inherently related to the working fluid thermodynamic properties and, in particular, to the density and specific enthalpy change over the heating process and the expansion process, see Refs. [10], [16] for

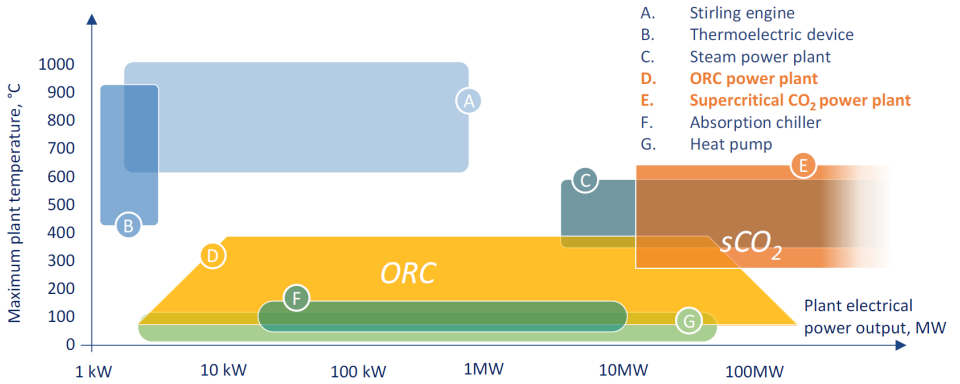

Figure 1.3: Range of applicability in terms of capacity and temperature of the source of various technologies for thermal energy harvesting. Courtesy of KCORC [9].

more details. Other advantages characterizing this technology include high efficiency at both nominal and off-design conditions, modularity, small footprint, reliability, and low operating and maintenance cost. Furthermore, cooling can also be achieved with air rather than water, thus overcoming the regulatory issues related to the utilization of rivers, lakes, or seawater for cooling purposes. The ORC system is also a suitable technology for mobile applications. For instance, several research studies have assessed the feasibility of waste heat recovery (WHR) from truck engines by means of mini-ORC systems [9]. The implementation of ORC-based WHR systems in fuel cells or hydrogen-fueled internal combustion engines has also been assessed in some other research works [17], [18], which highlighted a large potential for efficiency improvements. Moreover, the integration of ORC power systems onboard an aircraft is gaining increasing interest, see e.g. De Servi *et al* [19]. In particular, recent research is focusing on the potential impact of adding an organic Rankine cycle (ORC) waste heat recovery system to the gas turbine of the auxiliary power unit (APU) of an aircraft [20].

However, an ORC power system still remains inherently more expensive than a fossil-fuel-based power plant: to make this technology more accessible, the payback time has to be decreased. The reasons for the higher capital expenditure (CAPEX) and longer payback time of ORC systems, in contrast, for example, to that of a gas turbine power plant, are many. First, the thermal energy conversion efficiency of an ORC power plant is lower due to the inherently lower maximum cycle temperature: for an exemplary 5 MW gas turbine, the thermal efficiency is approximately 30% [21], while for an ORC system delivering the same output power thermal efficiency drops to ~ 25% [22]. Furthermore, a gas turbine achieves high cycle efficiency without heat exchangers, given that the transfer of primary energy happens in the combustor and heat rejection is direct to the atmosphere, being the cycle open [14]. This results in a comparatively small installation. The cost of power plants strongly depends on the material amount, which in turn is bound to its manufacturing cost. For example, a 5MW gas turbine operating at a maximum temperature of 1400^oC weighs approximately 27 ton for a cost of ~ 900 EUR/kW [21]. Con-

versely, an ORC power plant with similar specifics operates with a heat source at 300^{o}C and weighs 250 ton (including both the primary heat exchanger and the condenser) for a total cost of approximately 13M EUR (corresponding to a specific cost of 2600 EUR/kW), and a levelised cost of energy (LCOE) of 40-50 EUR/MWh[3]. It can be argued that such a difference in capital expenditure (CAPEX) is due to the required bulky heat exchangers for thermal energy input and rejection. Given that the majority of the power plant production costs comes from the purchase and manufacturing of its material, using large heat exchangers is economically detrimental. In addition, gas turbines are produced in batches of several units, thus inducing an economy of production, which is still absent for ORC power plants of this size. In summary, even if an ORC power plant may benefit from the availability of primary energy at no cost, the return on investment of the implementation of an ORC system is bound to be lower than that of the gas turbine because the efficiency is lower and the CAPEX is higher. This is true as long as societal costs like those caused by pollution and externalities due to the impact on the environment and climate change are not factored in.

With regard to waste heat recovery systems for propulsion engines, the miniaturization of the components still remains a challenge to overcome. This holds, for example, for WHR systems for long-haul truck engines, where, due to the need to reduce the volume and the weight of the expander, there is a large potential for efficiency improvements, as shown, e.g., in the work by Espinosa [23]. From a technical point of view, diesel engines for maritime applications are potentially suitable for the implementation of WHR systems. In such applications, up to 50% of the fuel energy content is dissipated as waste heat at various temperature levels. Recently, the International Maritime Organization (IMO) has issued stricter regulations to enforce the shipping industry to reduce emissions [24]. From a technical point of view, weight and volume requirements are less strict than those for land mobile applications. Recent studies have also shown that implementing organic Rankine cycle units recovering heat from the exhaust gases of diesel engines aboard ships could yield fuel savings between 10% and 15% [25]. Similar considerations also hold for diesel engine-powered trains, which still constitute a primary means of transportation in both Eastern Europe and developing countries [26].

To increase the return on investment and promote the use of ORC technology for waste heat recovery, research efforts must aim at improving the fluid dynamic performance of the expander. Bridging the gap between the gas cycle-based power plant and the ORC one is possible through research and development, without entailing a rise in the unit cost. On the contrary, improvement of the heat exchanging equipment can often be only achieved by increasing the amount of heat transfer surfaces, resulting thus in an increase in the cost of each unit.

1.2. MOTIVATION

As briefly addressed in Sec. 1.1, improving the fluid dynamic efficiency of turbines has a positive impact on the payback of ORC systems at the cost of research and development activities, but it does not imply additional costs for each unit, because the material and manufacturing costs would remain substantially unvaried. The research documented

[3]The author expresses his gratitude to dr. Aldo Serafino (Enertime) for sharing this information.

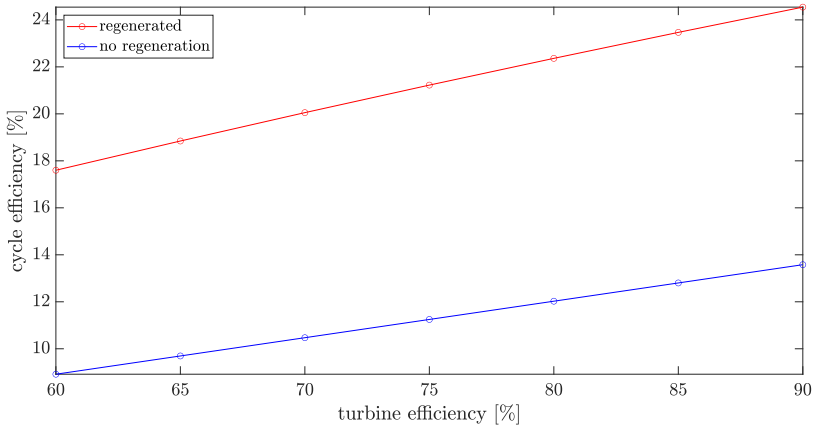

Figure 1.4: Influence of turbine efficiency on system efficiency for a regenerated and non-regenerated organic Rankine cycle power plant. Exemplary calculations have been performed using siloxane MM as the working fluid. The system operates between T_{min} = 30°C and T_{max} = 300°C, with a maximum subcritical pressure of p_{max} = 18.4 bar.

in this dissertation aims at developing knowledge for increasing the fluid dynamic efficiency of ORC turbomachinery. Designing more efficient ORC turbines inherently leads to a higher thermodynamic cycle efficiency. Figure 1.4 shows how the efficiency of the expander affects that of the thermodynamic cycle. Calculations have been performed for a simple Rankine cycle and for a regenerated one, using an in-house code [16]. The graph shows that a 5% improvement in the turbine total-to-static isentropic efficiency with respect to the baseline might lead to an overall increase of ≈ 1.1 - 1.2% of the thermodynamic cycle efficiency. For a baseline plant of 8 MW with a thermodynamic efficiency of the regenerated cycle of 23% and a total-to-static isentropic efficiency of the expander of 85%, such an improvement on the expander efficiency leads to an increase in the cycle output power of ~ 95 kW. Assuming that the plant operates for 8000 hours/year, this increase in net output power would lead to a yearly electricity production increase of ~ 760 MWh which, assuming an average cost of the electricity of 280 EUR/MWh [4], corresponds to ~ 213k EUR of additional profit over the whole year. For comparison, the same calculation for the year 2019, i.e., before the beginning of the Covid-19 pandemic, would result in a saving of 28k EUR.

The design of turbines operating with steam or combustion gases as working fluids is based on well-established guidelines, and these machines have achieved very high efficiency. These guidelines cannot be used for ORC turbines, as they would lead to incorrect sizing and wrong performance estimation because they are specifically tailored for applications using air or steam as working fluids. Furthermore, the expansion process in ORC turbines usually starts in the dense vapor state, where the variation of the thermodynamic properties significantly departs from that predicted by the ideal gas law.

[4] Cost of energy in the Netherlands over the year 2022. Reference: European Power Price Tracker, url: https://ember-climate.org/data/data-tools/europe-power-prices/

In addition, due to the high complexity of the molecular structure, ORC working fluids are inherently characterized by low values of the speed of sound. As a consequence, the flow field is often in the transonic or supersonic regime, leading to the appearance of shock waves whose strength strongly depends on the fluid state and on the flow Mach number.

To better understand how the fluid influences the flow field of a turbine, one can first analyze simpler paradigmatic one- and two-dimensional flow configurations, see, e.g., Fig. 1.5. The change of the flow properties in a turbine stator vane can be qualitatively modelled using the relations describing the flow expansion in a one-dimensional nozzle. If the perfect gas equation of state does not hold, both the fluid state and the molecular complexity influence the nozzle shape, i.e., the needed area distribution A/A^*, being A the local nozzle area and A^* the throat area, to reach a determined expansion at the nozzle outlet (Fig. 1.5a). Similarly, the thermodynamic nonideality of the fluid determines the amount of flow turning in a Prandtl-Meyer expansion fan (Fig. 1.5). Expansion fans can be encountered in the proximity of the blade trailing edge and strongly influence the performance and operation of a turbine. The entity of gas dynamic effects due to the thermodynamic non-ideality of the fluid can be determined by inspecting the value of the so-called fundamental derivative of gas dynamics [27]

$$\Gamma = 1 + \frac{c}{\rho}\left(\frac{\partial \rho}{\partial c}\right)_s, \tag{1.1}$$

where c and ρ denote the sound speed and the density, respectively. It can be proved that values of Γ lower than unity, i.e., highly non-ideal flows, lead to a larger flow turning in expansion fans and larger values of the required area ratio in the divergent section of a nozzle to reach a given supersonic Mach number [28]. The blade design is usually performed to match the flow angle at the outlet in accordance with the specified velocity triangles: therefore, changes in the flow field due to the thermodynamic non-ideal state of the fluid directly affect the blade shape, the flow deviation, and the overall loss within the vane [29].

Currently, ORC turbines are often designed using experimental correlations: most of these are directly derived from those used for the design of gas and steam turbines. The initial mean-line design, therefore, might not correspond to the optimal one, and several steps of design optimization through time-consuming computational fluid dynamics (CFD) simulations or expensive experimental campaigns are required to improve it. To improve current design practices, research and development (R&D) efforts are needed to create reliable reduced-order models which can accurately predict the performance trends of the machine. Such models are primarily needed to improve and speed up the mean-line design phase, limiting thus the use of time-consuming numerical optimizations and/or expensive experimental campaigns. To develop such models, preliminary investigations on the influence of the fluid and its thermodynamic operating state on paradigmatic compressible flow configurations are needed to better discern the complex flow field developing inside turbomachinery for ORC systems.

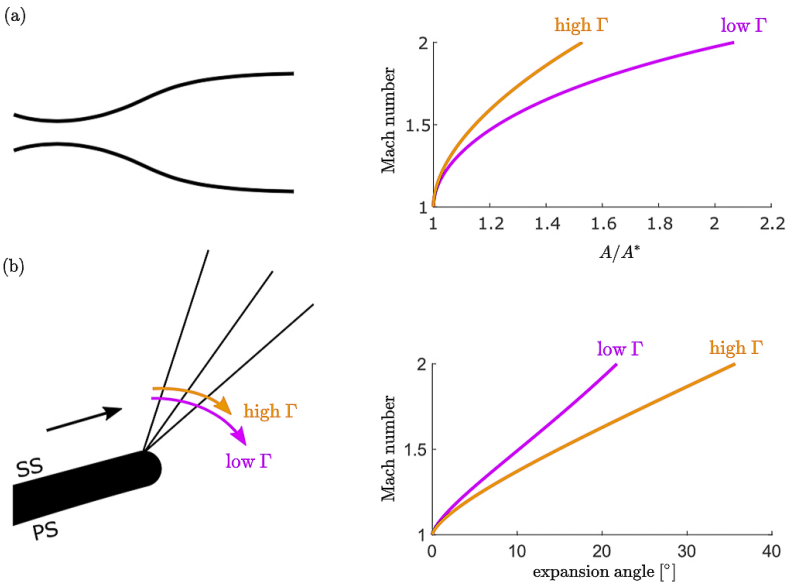

Figure 1.5: Influence of the fundamental derivative of gas dynamics Γ on (a) the area ratio of a converging-diverging nozzle and (b) the flow turning in Prandtl-Meyer expansion fans (bottom). Adapted from Baumgartner [30].

1.3. RESEARCH QUESTIONS

The motivations outlined in the previous section have led to the formulation of the following research questions.

1. **What is the influence of the working fluid and the thermodynamic conditions on the loss mechanisms in internal non-ideal flows?**

2. **What is the influence of the working fluid and the thermodynamic fluid state on the flow deviation and the operating range of axial turbines?**

3. **What is the influence of the fluid and its thermodynamic state on guidelines for the selection of the optimal solidity in axial turbines?**

To answer these questions, fundamental investigations on paradigmatic one-dimensional flow configurations, two-dimensional boundary layer flows, losses, and the design of unconventional turbine cascades have been conducted.

1.4. ORIGINAL CONTRIBUTIONS

The research contributions documented in this dissertation can be summarized as follows.

1. Theoretical frameworks for the analysis of one-dimensional and swirling compressible dense vapor flows have been derived. The influence of variation in cross-section area, external shaft work, flow injection, energy transfer as heat, friction, and flow mixing on dense vapor flows are studied as a function of characteristic fluid parameters.

2. The Grüneisen parameter G has been used for the first time to evaluate the molecular complexity of a fluid in relation to flow characteristics.

3. First-of-their-kind direct numerical simulations (DNS) of dense vapor boundary layer flows have been conducted. The results of these simulations have enabled the quantification, for the first time, of the contribution of each loss source to the overall dissipation of the boundary layer flow of an organic compound (hexamethyldisiloxane).

4. A reduced-order model solving the boundary layer equations for an arbitrary fluid and implementing the Cebeci-Smith eddy-viscosity turbulence model has been developed. The model provides the variation of each flow parameter across the boundary layer, as well as the value of the dissipation coefficient.

5. Physics-based models for the estimation of the flow deviation, the assessment of the losses, and the estimation of the optimal solidity value in turbine cascades operating with an arbitrary fluid have been developed and validated against the results of CFD simulations performed on a representative transonic turbine stator.

1.5. OUTLINE

All the material presented in this thesis has been presented at international conferences or published in established peer-reviewed journals. The content of this thesis is divided into six chapters, whose content is briefly outlined in the following.

Chapter 2 presents an evaluation of the influence of both fluid molecular complexity and thermodynamic non-ideality on some paradigmatic compressible non-ideal flow processes, using state-of-the-art fluid thermophysical models. Several definitions of molecular complexity are presented, as well as the Grüneisen parameter. Processes such as flow expansion in a convergent-divergent nozzle, channel flow with either heat addition or no-slip walls, mixing of co-flowing streams, and flow injection in a mainstream are investigated for fluids at different levels of molecular complexity and for different thermodynamic states. Loss mechanisms and relevant trends in flow variables are both qualitatively and quantitatively estimated.

Chapter 3 treats the various sources of dissipation in adiabatic boundary layers in zero-pressure gradient non-ideal compressible fluid flows. Direct numerical simulations of transitional, zero-pressure gradient boundary layers are performed with an in-house solver for two fluids with different levels of complexity of the fluid molecules. Different sets of thermodynamic free stream boundary conditions are selected to evaluate the influence of the fluid state on the frictional loss and dissipation mechanisms. Results

are compared with those obtained with an in-house reduced-order model (ROM) code solving the boundary layer equations in transformed coordinates for dense vapors. The same ROM is used to investigate the influence of compressibility on the dissipation coefficient for a larger number of fluids and free-stream flow conditions.

Chapter 4 reports a study on the effects of fluid molecular complexity and thermodynamic non-ideality on both flow deviation and critical choking in transonic turbine cascades operating with non-ideal compressible flows. Reynolds Averaged Navier-Stokes (RANS) calculations are used to qualitatively and quantitatively assess the variation of the flow deviation in a representative transonic turbine vane. Results are compared against values of flow deviation obtained with reduced-order physical models that can be used for design purposes. A loss breakdown analysis is also performed.

Chapter 5 describes the results of an investigation on the influence of both compressibility and fluid molecular complexity on the optimal solidity of linear turbine cascades. New reduced-order models for the selection of the optimal solidity in the preliminary design of non-conventional turbomachinery are introduced and discussed. Numerical simulations of the flow over exemplary stator blades are performed to assess the influence of both flow compressibility and axial solidity on the loss breakdown.

Chapter 6 summarizes the key takeaways and the limitations of this research. Indications for future work are also provided.

BIBLIOGRAPHY

[1] I. E. Agency, "Energy Technology Perspectives", en, Flagship Technical Report, 2021.

[2] Intergovernmental Panel on Climate Change, "Climate Change 2021: The Physical Science Basis", IPCC Sixth Assessment Report, 2022, p. 112.

[3] NASA, *Climate Change: Vital Signs of the Planet*, 2022.

[4] European Central Bank, "Economic Bulletin Issue 1, 2022", en, 2022.

[5] I. R. E. Agency, "Renewable Power Generation Costs 2020", en, Technical Report, 2021, p. 180.

[6] I. R. E. Agency, "Innovation landscape brief: Utility-scale batteries", en, Technical Report, 2019, p. 180.

[7] K. Zeng and D. Zhang, "Recent progress in alkaline water electrolysis for hydrogen production and applications", *Progress in Energy and Combustion Science*, vol. 36, no. 3, pp. 307–326, 2010, ISSN: 0360-1285. DOI: https://doi.org/10.1016/j.pecs.2009.11.002.

[8] T. Spencer and A. Mathur, "Energy Transition in Emerging and Developing Countries: Promoting the New Paradigm", en, G20 Insigths, Governing Climate Target, Energy Transition and Environmental Protection Policy Brief, 2019, p. 12.

[9] Knowledge Center on Organic Rankine Cycle (KCORC), "Thermal Energy Harvesting - the Path to Tapping into a Large CO2-free European Power Source", en, Thermal Energy Harvesting Advocacy Group White Paper, 2022, p. 57.

[10] P. Colonna, E. Casati, C. Trapp, *et al.*, "Organic Rankine Cycle Power Systems: From the Concept to Current Technology, Applications, and an Outlook to the Future", en, *Journal of Engineering for Gas Turbines and Power*, vol. 137, no. 10, p. 100 801, Oct. 2015, ISSN: 0742-4795. DOI: 10.1115/1.4029884.

[11] M. Astolfi, "Binary ORC (organic Rankine cycles) power plants for the exploitation of medium-low temperature geothermal sources - Part A: Thermodynamic optimization", en, p. 12, 2014.

[12] M. Astolfi, M. C. Romano, P. Bombarda, and E. Macchi, "Binary ORC (Organic Rankine Cycles) power plants for the exploitation of medium–low temperature geothermal sources – Part B: Techno-economic optimization", en, *Energy*, vol. 66, pp. 435–446, Mar. 2014, ISSN: 03605442. DOI: 10.1016/j.energy.2013.11.057.

[13] M. Astolfi, L. Xodo, M. C. Romano, and E. Macchi, "Technical and economical analysis of a solar–geothermal hybrid plant based on an Organic Rankine Cycle", *Geothermics*, vol. 40, no. 1, pp. 58–68, 2011, ISSN: 0375-6505. DOI: https://doi.org/10.1016/j.geothermics.2010.09.009.

[14] E. Macchi and M. Astolfi, *Organic Rankine Cycle (ORC) Power Systems: Technologies and Applications* (Energy 107), en. Elsevier, 2017, ISBN: 978-0-08-100510-1.

[15] T. Tartière and M. Astolfi, "A World Overview of the Organic Rankine Cycle Market", en, *Energy Procedia*, vol. 129, pp. 2–9, Sep. 2017, ISSN: 18766102. DOI: 10.1016/j.egypro.2017.09.159.

[16] S. Bahamonde, M. Pini, C. De Servi, A. Rubino, and P. Colonna, "Method for the preliminary fluid dynamic design of high-temperature mini-organic rankine cycle turbines", *J. Eng. Gas Turbines Power*, vol. 139, no. 8, pp. 082606/1–082606/14, Mar. 2017, ISSN: 0742-4795. DOI: 10.1115/1.4035841.

[17] G. Angelino and P. di Paliano, "Organic rankine cycles (orcs) for energy recovery from molten carbonate fuel cells", in *Collection of Technical Papers. 35th Intersociety Energy Conversion Engineering Conference and Exhibit (IECEC) (Cat. No.00CH37022)*, vol. 2, 2000, 1400–1409 vol.2. DOI: 10.1109/IECEC.2000.870957.

[18] C. De Servi, S. Campanari, A. Tizzanini, and C. Pietra, "Enhancement of the Electrical Efficiency of Commercial Fuel Cell Units by Means of an Organic Rankine Cycle: A Case Study", en, *Journal of Engineering for Gas Turbines and Power*, vol. 135, no. 4, p. 042 309, Apr. 2013, ISSN: 0742-4795, 1528-8919. DOI: 10.1115/1.4023119.

[19] C. D. Servi, L. Azzini, M. Pini, and P. Colonna, "Exploratory assessment of a combined-cycle engine concept for aircraft propulsion", en, in *Proceedings of the 1st Global Power and Propulsion Forum - GPPF2017*, 2017, GPPF-2017-78/1–11.

[20] D. Krempus, F. Beltrame, M. Majer, *et al.*, *Organic Rankine Cycle Waste Heat Recovery for Aircraft Auxiliary Power Units*, en, Toulouse, France, 2022.

[21] Siemens Energy AG, *Gas Turbine Portfolio Brochure*, 2022.

[22] Turboden S.p.A., *Waste Heat Recovery Brochure*, 2022.

[23] N. Espinosa, "Contribution to the study of waste heat recovery systems on commercial truck diesel engines.", 2011.

[24] I.-M. E. P. Committee *et al.*, "Reduction of ghg emissions from ships. fourth imo ghg study 2020", *Int. Marit. Organ.*, vol. 53, pp. 1689–1699, 2020.

[25] M. Mondejar, J. Andreasen, L. Pierobon, U. Larsen, M. Thern, and F. Haglind, "A review of the use of organic Rankine cycle power systems for maritime applications", en, *Renewable and Sustainable Energy Reviews*, vol. 91, pp. 126–151, Aug. 2018, ISSN: 13640321. DOI: 10.1016/j.rser.2018.03.074.

[26] I. E. nouvelles, *Trenergy - train energy efficiency via rankine-cycle exhaust gas heat recovery*, Delft, Netherlands, Accessed 13 December 2022.

[27] P. A. Thompson, "A Fundamental Derivative in Gasdynamics", en, *Physics of Fluids*, vol. 14, no. 9, p. 1843, 1971, ISSN: 00319171. DOI: 10.1063/1.1693693.

[28] A. Kluwick, "Non-Ideal Compressible Fluid Dynamics: A Challenge for Theory", en, *Journal of Physics: Conference Series*, vol. 821, p. 012 001, Mar. 2017, ISSN: 1742-6588, 1742-6596. DOI: 10.1088/1742-6596/821/1/012001.

[29] A. Giuffre' and M. Pini, "Design Guidelines for Axial Turbines Operating With Non-Ideal Compressible Flows", en, *Journal of Engineering for Gas Turbines and Power*, vol. 143, no. 1, p. 011 004, Jan. 2021, ISSN: 0742-4795, 1528-8919. DOI: 10.1115/1.4049137.

[30] D. Baumgartner, "Real gas effects in orc turbines", 2021. DOI: 10.17863/CAM.69867.

2

DENSE VAPOR EFFECTS IN COMPRESSIBLE INTERNAL FLOWS

Part of the content of this chapter appeared in:
F. Tosto, C. Lettieri, M. Pini and P. Colonna, *Dense-vapor effects in compressible internal flows*, Physics of Fluids, 33(8), doi: 086110/1-22, 2021.

Paradigmatic compressible one-dimensional flows provide insights regarding the loss mechanisms of fluid machinery components typical of power and propulsion systems, like turbomachines and heat exchangers. Their performance also depends on the working fluid, thus on both molecular complexity and thermodynamic state. Four typical flow configurations have been investigated, namely, Rayleigh and Fanno flow, mixing of two co-flowing streams, and flow injection into a mainstream. It was found that the Grüneisen parameter allows the quantitative characterization of the influence of molecular complexity on losses. Moreover, the influence of dense vapor effects has been evaluated and assessed in terms of other fluid parameters. The analysis allowed the quantification of how, in Rayleigh flows, the energy transferred as heat is converted into kinetic and internal energy of the fluid, and, in Fanno flows, entropy is generated due to friction. In Rayleigh flow, the fluid at the inlet of the channel must have more energy for the flow to choke, depending on the molecular complexity. Similarly, in Fanno flows and for a given value of the compressibility factor, molecular complexity determines the choking point in the channel, and the higher its value, the further downstream the location. Moreover, for both Fanno and Rayleigh flows, if the flow is subsonic and dense vapor effects are relevant, the Mach number varies non-monotonically along the channel. Finally, it was proven that the amount of entropy generated in mixing flows increases with both the fluid molecular complexity and with the thermodynamic non-ideality of the fluid states.

2.1. INTRODUCTION

Many chemical and energy conversion processes make use of working fluids that, in certain operating conditions, are operating in the dense vapor state. Thermodynamic and transport properties, collectively called *thermophysical properties*, of dense vapors, differ from those of the so-called ideal gas, see Fig. 2.1. A fluid is a dense vapor if it is operated in thermodynamic states occurring in the proximity of the dew line or near the vapor-liquid critical point. Flows in which the fluid is in these states are affected by large gradients of thermophysical properties [1]. Examples of energy conversion processes in which the working fluid can be affected by so-called non-ideal compressible fluid dynamic (NICFD) effects are the expansion occurring in the turbine stator of organic Rankine cycle (ORC) power systems [2], [3], the compression occurring in the compressor of supercritical carbon dioxide (sCO_2) power systems [4], and in the compressor of heat pumps [5].

Any process affected by non-ideal dense vapor effects makes the design of internal flow components more challenging because standard guidelines for the design of components operated with air or steam as working fluids cannot be employed, as they would lead to incorrect sizing and wrong performance estimations. For example, the design of compressors and turbines generally relies on well-established semi-empirical correlations developed for conventional machines using air, combustion gases, or steam as working fluids. These semi-empirical models do not provide sufficiently accurate results for turbomachinery operating with dense vapors, see, e.g., Giuffré and Pini [6]. Although methodologies for preliminary fluid dynamic design and optimization of, for example, turbines for ORC power systems [7]–[9], compressors for sCO_2 power systems [10], [11], and compressors for heat pumps [12] have been developed, no validated design guidelines for turbomachinery operating partially or completely with the working fluid in the dense vapor thermodynamic region are available yet.

Guidelines specifically developed for the meanline design of these machines would thus provide more accurate predictions of both efficiency and loss breakdown in turbines and compressors operating with dense vapors. Denton [13] first proposed a physics-based loss model for conventional turbomachinery. The model exploits the first principles applied to simplified one-dimensional flow configurations to estimate the entropy losses generated by different sources. He identified four loss mechanisms: viscous effects in boundary layers, viscous effects in mixing processes, shock waves, and heat transfer across temperature differences. However, the model is only valid under the ideal gas and incompressible flow assumptions. As proven by Giuffré and Pini [6], the generalization of the model to non-ideal compressible flows allows the development of a design framework that provides more accurate guidelines for unconventional turbomachinery.

Gaining a better physical understanding of how both the working fluid and the non-ideal gas dynamics features affect the flow field is paramount to designing efficient fluid machinery components. Following the seminal work of Thompson [14], the non-ideal fluid dynamics of dense vapor flows are governed by the fundamental derivative of gas dynamics, a fluid thermodynamic property defined as

$$\Gamma \equiv 1 + \frac{\rho}{c}\left(\frac{\partial c}{\partial \rho}\right)_s = \frac{c^4}{2v^3}\left(\frac{\partial^2 v}{\partial p^2}\right)_s, \tag{2.1}$$

where ρ is the density, c the speed of sound, and s the entropy. The fundamental derivative is related to the variation of the speed of sound with density along isentropic processes: for this reason, the propagation of the waves in dense fluids strongly depends on its value [15]. Equation 2.1 shows that the sign and the value of Γ can be inferred from the concavity of isentropic lines if displayed on the pressure-volume thermodynamic diagram of the fluid. If $\Gamma > 1$, the sound speed decreases along isentropic compression processes and increases along expansions: this situation is representative of fluid flows occurring during air compression and exhaust gas expansion in turbochargers or gas turbines. However, fluid flows for which $\Gamma < 1$ are also possible: in this case the speed of sound increases over compressions and decreases over expansions. Γ is greater than one if the fluid is in the dilute gas state, that is

$$\Gamma = (\gamma + 1)/2 \tag{2.2}$$

for the ideal gas, while the line $\Gamma = 1$ delimits vapor states closer to the dew line and to the vapor-liquid critical point of the fluid, for which $Z \equiv pv/(RT) < 1$, where Z is the so-called compressibility factor, see Fig. 2.1. Furthermore, it is theoretically predicted that the so-called Bethe–Zel'dovich–Thompson (BZT) fluids [14], [16], [17], whose molecules are rather complex, exhibit a thermodynamic region in the vapor phase where the fundamental derivative is negative. This is a necessary condition for the possibility of attaining non-classical gas dynamic phenomena such as rarefaction shock waves and compression fans [18] in flows. Works by Cramer [19], Zamfirescu [20], and Kluwick [21] provide an extensive review of the theory of non-classical gas dynamics. Experimental investigations aimed at proving the existence of rarefaction shock waves in BZT fluids were conducted in the past [22], and are still being performed [23], [24], using siloxanes as working fluids [17]. Moreover, experimental campaigns on dense vapor nozzle flows are currently being conducted with the aim of characterizing non-ideal compressible flows in presence of shock waves [25], [26]. Efforts are also made to enhance the theoretical understanding of compression and expansion phenomena in transonic [27] and supersonic [28]–[31] dense vapor flows.

Several studies investigating non-ideal compressible effects in characteristic one-dimensional flow processes have already been conducted. Kluwick [32] and Cramer [33] showed that, due to the non-monotonic variation of density with the Mach number, three sonic points rather than a single one may occur during isentropic supersonic expansions of BZT fluids. Therefore, a conventional converging-diverging nozzle is not sufficient to obtain a shock-free expansion from the subsonic to the supersonic regime, but unconventional nozzle shapes consisting of two throats are required. More recently, Guardone and Vimercati [34] outlined a set of exact solutions corresponding to ten different operating regimes in a converging-diverging nozzle using the rather inaccurate van der Waals thermodynamic model for the fluid. Baltadjiev [11] derived approximated relations between stagnation and static variables as a function of the flow Mach number and the isentropic exponents, i.e., $\phi_t/\phi = f(M, \gamma_{pv}, \gamma_{pT})$, where ϕ is a thermodynamic property (enthalpy, pressure, temperature or density), and the subscript t denotes stagnation quantities. These relations are formally similar to their ideal gas counterparts, the only difference being the use of the generalized isentropic exponents γ_{pv} and γ_{pT} (see Tab. 2.1) in place of γ. To derive these relations, Baltadjiev [11] assumed the same value

of the isentropic exponents for the stagnation and static variables. In addition, they extended the definition of corrected mass flow per unit area $\dot{m}_{\text{corr}}$ to the case of isentropic compressible flows of dense vapors. They found that its value depends only on the flow Mach number and the average value of the exponent γ_{pv} over the process. In particular, the maximum value of corrected mass flow per unit area at choking conditions decreases with increasing values of γ_{pv}.

Other studies investigated dense vapor effects in physical processes using one-dimensional theory with either constant energy transfer as heat or wall friction. These are often labeled as *Rayleigh* and *Fanno* flows, respectively; Anderson [35], Chap. 3, provides the complete analysis of both processes under the perfect gas assumption. Following the approach of Schnerr and Leidner [36], Cramer provided a qualitative analysis of Fanno [37] and Rayleigh [38] flows in dense vapors, with a focus on BZT fluids. For his analysis, he adopted the van der Waals fluid thermodynamic model. He proved that as many as three sonic points may occur in Rayleigh processes, while in Fanno flows as many as three sonic points corresponding to two maxima and one minimum in entropy may occur. However, the use of a thermodynamic model based on the van der Waals equation of state leads one to substantially overestimate the extent of the $\Gamma < 0$ region. Furthermore, non-classical gas dynamic studies are still purely theoretical in nature, and applications have not been devised yet. On the contrary, non-ideal flows occurring with the fluid in states characterized by $0 < \Gamma < 1$ are of relevant industrial interest. Characterizing the influence of non-ideal fluid dynamics on relevant turbulent viscous and diabatic processes becomes thus of prime importance to correctly predict the performance of internal flow devices. However, a quantitative understanding of the impact of the fluid state on both viscous turbulent and diabatic processes is scarcely documented in the literature.

The aim of this study is to evaluate the impact of both fluid molecular complexity and thermodynamic non-ideality on some paradigmatic compressible non-ideal flow processes, using state-of-the-art fluid thermophysical models. Loss mechanisms and relevant trends in flow variables are both qualitatively and quantitatively estimated.

The article is structured as follows. Section 2.2 lists the characteristic non-dimensional fluid parameters used in this study and discusses the importance of the Grüneisen parameter which is used here for the first time in relation to molecular complexity. In section 3.2, a general theoretical framework for one-dimensional compressible flows is derived from first-principle equations; here, the parameters introduced in section 2.2 are used to characterize these flows. The obtained framework can be used for preliminary investigations of loss mechanisms affecting the performance and operation of turbomachinery, heat exchangers, and in other engineering applications. Section 2.4 treats the impact of the fluid, namely of its molecules, on choking and the trend of flow variables in channel flows with constant thermal energy addition (Rayleigh flow) and wall friction (Fanno flow). In addition, the friction coefficient in turbulent channel flows of dense vapors is estimated with three-dimensional Reynolds Averaged Navier-Stokes simulations (RANS) of pipe flows and compared with values resulting from the friction coefficient formulation valid for incompressible flows. Section 2.5 describes the impact of the fluid and its properties on two paradigmatic one-dimensional mixing flow configurations, namely the mixing of two streams and flow injection. Section 5.5 outlines the

Definition	Ideal gas
$\beta_p = \frac{1}{v}\left(\frac{\partial v}{\partial T}\right)_p = \frac{1}{T} + \frac{1}{Z}\left(\frac{\partial Z}{\partial T}\right)_p$	$\frac{1}{T}$
$\beta_T = -\frac{1}{v}\left(\frac{\partial v}{\partial p}\right)_T = \frac{1}{p} + \frac{1}{Z}\left(\frac{\partial Z}{\partial p}\right)_T$	$\frac{1}{p}$
$\gamma_{pv} = \frac{\gamma}{\beta_T p}$	γ
$\gamma_{pT} = \frac{\gamma - 1}{\gamma}\frac{\beta_T p}{\beta_p T}$	$\frac{\gamma-1}{\gamma}$
$\Gamma = 1 + \frac{\rho}{c}\left(\frac{\partial c}{\partial \rho}\right)_s$	$\frac{\gamma+1}{2}$
$G = \frac{1}{\rho c_v}\left(\frac{\partial p}{\partial T}\right)_\rho = \gamma_{pv}\gamma_{Tp}$	$\gamma - 1$
$\Psi = \rho\left(\frac{\partial c^2}{\partial p}\right)_\rho = \gamma_{pv} + \left(\frac{\partial \gamma_{pv}}{\partial p}\right)_\rho p$	γ

Table 2.1: Secondary thermodynamic properties relevant for the study of one-dimensional flows.

main conclusions drawn from this study.

2.2. NON-DIMENSIONAL FLUID PROPERTIES CHARACTERIZING DENSE VAPORS

The ideal gas equation of state reads

$$p = \rho R T. \tag{2.3}$$

If equation 2.3 holds, then $Z = 1$. Fluid states close to the critical point or close to the dew line do not obey the ideal gas law, see Fig. 2.1. The isobaric and isochoric heat capacity, their ratio $\gamma = c_p/c_v$, and Z vary depending on the fluid state, see Reynolds and Colonna [39], Chap. 6. The principle of corresponding states is based on the observation that, at fixed reduced temperature and pressure, different fluids have, to a certain degree of approximation, the same value of Z, see Reynolds and Colonna [39], Fig. 6.6. Therefore, Z is a thermodynamic similarity parameter that is useful also for fluid dynamic analyses.

However, fluid-dynamic processes can be better examined by using other dimensionless state properties. Isentropic flows of dense vapors are described by the thermodynamic relation

$$p/\rho^{\gamma_{pv}} = \text{const.}, \tag{2.4}$$

in analogy with isentropic flows of fluids in the ideal gas state [40]. Figure 2.1 shows the variation of γ_{pv} in the temperature-entropy diagram for fluids made with molecules of different degrees of complexity.

Differentiation of equation 2.4 yields [41]

$$\gamma_{pv} = -\frac{v}{p}\left(\frac{\partial p}{\partial v}\right)_s = -\gamma\frac{v}{p}\left(\frac{\partial p}{\partial v}\right)_T = \frac{\gamma}{\beta_T p}, \tag{2.5}$$

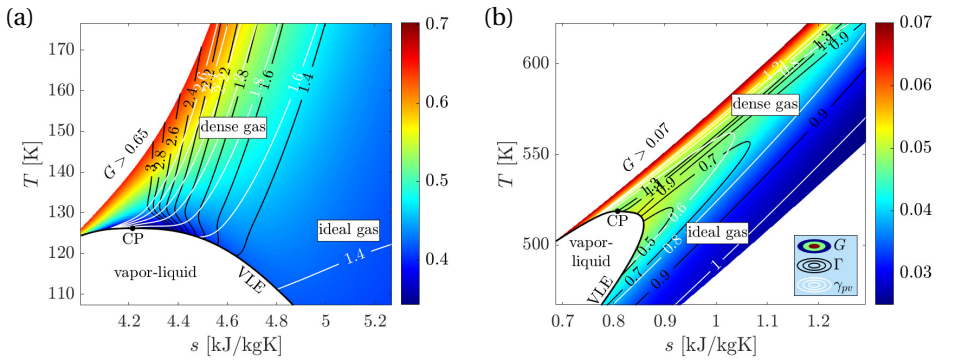

Figure 2.1: Temperature-entropy diagram for two fluids with different molecular complexity: (*a*) CO_2 and (*b*) siloxane MM. Colored contours report the variation of the Grüneisen parameter. Contours of fundamental derivative Γ (black) and generalized polytropic exponent γ_{pv} (white) are also displayed.

where β_T is the isothermal compressibility of the fluid, whose definition is reported in Tab. 2.1. Both β_T and γ are positive for all fluids in the vapor state; as a consequence, $\gamma_{pv} > 0$ for all fluid thermodynamic states. Differentiating Eq. 2.5 with respect to the specific volume leads to

$$\Gamma = \frac{1}{2}\left[\gamma_{pv} + 1 - \frac{v}{\gamma_{pv}}\left(\frac{\partial \gamma_{pv}}{\partial v}\right)_s\right]. \tag{2.6}$$

For flows with moderate variations of thermodynamic properties, the approximation $\Gamma \simeq (\gamma_{pv}+1)/2$ holds, therefore $\gamma_{pv} \approx$ const.. This relation is similar to the relation valid for the ideal gas, see Eq. 2.2.

If an isentropic process is considered and temperature and pressure are taken as primary variables, the governing law becomes

$$T p^{\gamma_{pT}} = \text{const.} \tag{2.7}$$

Its differentiation [41] yields

$$\gamma_{pT} = \frac{p}{T}\left(\frac{\partial T}{\partial p}\right)_s = \frac{\gamma - 1}{\gamma}\frac{\beta_T p}{\beta_p T}, \tag{2.8}$$

where γ_{pT} is the so-called isentropic pressure-temperature exponent, and β_p the isobaric compressibility of the fluid. The derivation is provided in App. 2.9.

Besides the fundamental derivative Γ, an additional non-dimensional parameter is required to evaluate the variation of the speed of sound in non-isentropic processes, see appendix 2.10. This parameter is defined as

$$\Psi \equiv \rho\left(\frac{\partial c^2}{\partial p}\right)_\rho = \gamma_{pv} + \left(\frac{\partial \gamma_{pv}}{\partial p}\right)_\rho p. \tag{2.9}$$

The second expression in Eq. 2.9 (see App. 2.9) highlights that Ψ is directly linked to the variation of γ_{pv} with pressure over an isochoric process. The term $\left(\partial \gamma_{pv}/\partial p\right)_\rho p$ is negative for fluids characterized by low complexity of the molecular structure in thermodynamic regions where $\rho > \rho_{cr}$ and $T \simeq T_{cr}$. However, in these cases, the absolute value of

this term never exceeds the one of γ_{pv}; as a consequence $\Psi > 0$ in the vapor region for all fluids. As discussed in Sec. 2.4, Ψ affects the variation of the Mach number in both Rayleigh and Fanno flows.

Finally, the Grüneisen parameter for fluids is defined as [42]

$$G \equiv \frac{1}{\rho c_v}\left(\frac{\partial p}{\partial T}\right)_v. \tag{2.10}$$

The Grüneisen parameter is commonly used in equations of state for solids to relate thermodynamic variables with the lattice vibrational spectra. In particular, Eq. 2.10 provides the average over the values of Grüneisen parameter calculated for each individual mode of the lattice vibrational spectrum of the solid [43]. This parameter is often assumed to be constant with temperature in solids. Arp *et al* [42] generalized the definition provided by Eq. 2.10 to fluid phases. Using the Maxwell thermodynamic relations [39] and Eqs. 2.5, 2.45 and 2.46, the Grüneisen parameter can also be be written as

$$\begin{aligned} G &= -\frac{v}{c_v}\left(\frac{\partial s}{\partial v}\right)_T = \frac{v}{c_v}\frac{\left(\partial s/\partial p\right)_T}{\left(\partial v/\partial p\right)_T} = -\frac{v}{c_v}\frac{\left(\partial v/\partial T\right)_p}{\left(\partial v/\partial p\right)_T} = \\ &= \frac{v}{c_v}\frac{\beta_p}{\beta_T} = \frac{\gamma-1}{\beta_p T} = \gamma_{pv}\gamma_{Tp}. \end{aligned} \tag{2.11}$$

The use of the Grüneisen parameter in fluid dynamics theory is quite limited [44], [45] and systematic studies involving G are limited to liquid flows [46], [47]. Recently, Mausbach *et al* [43] examined the variation of the Grüneisen parameter over the temperature-entropy diagram for 28 pure fluids. Estimations of the value of G based on molecular simulations are compared against values obtained with state-of-the-art multi-parameters equations of state models. Results showed that the Grüneisen parameter for vapor states increases with density and decreases with temperature for all the examined pure fluids, with the exception of water.

In general, fluids can be classified depending on the level of complexity of their molecules. A parameter for the evaluation of molecular complexity has been defined differently by different authors. Bethe [16] first proposed

$$\delta_\infty^c = \frac{c_{v\infty}(T_c)}{R}. \tag{2.12}$$

$c_{v\infty}$ is defined as the isochoric specific heat evaluated at the critical temperature T_c in the limit $v \to \infty$. Guardone and Argrow [48] concluded, based on an analysis conducted on selected BZT fluorocarbons, that dense-vapor effects are strongly influenced by δ_∞^c and by the acentric factor of the molecule. The authors also proved that, if the van der Waals and the Redlich-Kwong equations of state models are employed, the minimum values of the fundamental derivative of gas dynamics evaluated along both the critical isotherm and the saturation curve are monotonically increasing functions of δ_∞^c for the selected fluorocarbons. The minimum value of the fundamental derivative $\Gamma_{\min}$ along the vapor–liquid equilibrium curve is thus adopted in subsequent studies by the same group to classify the molecular complexity of fluids [28]. Using a thermodynamic approach based on the simple van der Waals model, Colonna and Guardone [49] and Harinck *et al* [50] explained the link between the value of δ_∞^c and molecular complexity from

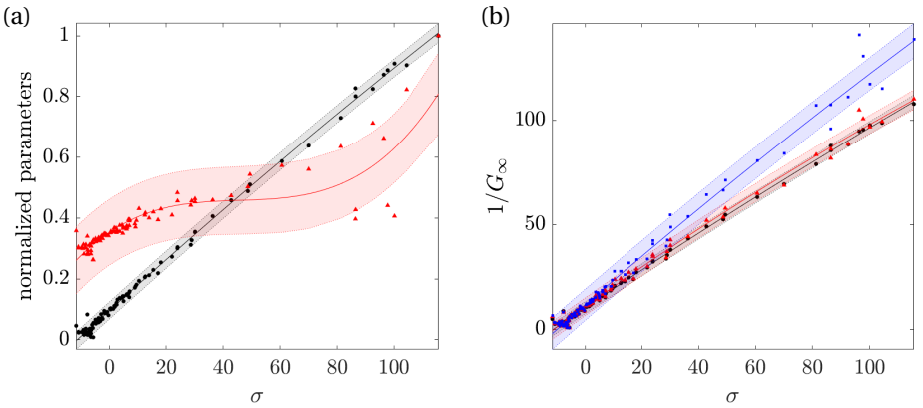

Figure 2.2: Fluid thermodynamic parameters that were defined to evaluate molecular complexity in previous studies ($\Gamma_{\min}$ and σ) and their relation with the Grüneisen parameter. All values are calculated with the multiparameter equation of state models implemented in a well-known property estimation program [51]. (a) Variation of ● $1/G_\infty = \delta^c_\infty$ and ▲ $1/(\Gamma_{\min}+1)$ with σ. $1/G_\infty$ is normalized with $1/G_{\infty,\min} = 107.92$, while $1/(\Gamma_{\min}+1)$ is normalized with $1/(\Gamma_{\min}+1)_{\min} = 1.29$ (b) Grüneisen parameter *vs* σ as a function of several values of reduced temperature and pressure. ● $T_r = 0.9$; $p_r = 0.05$, ▲ $T_r = 1$; $p_r = 0.65$, ■ $T_r = 1$; $p_r = 0.85$. Linear regression fitting curves are also reported as solid lines with their respective 95 % confidence bounds (shaded areas).

a physical point of view. According to the energy equipartition principle, the number of active degrees of freedom of the molecule evaluated at the critical temperature $N(T_c)$ is given by

$$N(T_c) = 2\frac{c_{v\infty}(T_c)}{R} = 2\delta^c_\infty. \tag{2.13}$$

As a result, molecular complexity does not depend on molecular weight. Furthermore, the trend of δ^c_∞ with the molar mass is strictly monotone if the considered fluids belong to the same class (e.g., hydrocarbons, siloxanes or fluorocarbons), therefore have similar molecular structures.

In the ideal gas limit, δ^c_∞ tends to the value of the inverse of the Grüneisen parameter evaluated at the critical temperature: combining Eq. 2.10 with $p = \rho ZRT$ yields

$$G = \frac{1}{\delta^c_\infty}\frac{c_{v\infty}}{c_v}\left[Z + T\left(\frac{\partial Z}{\partial T}\right)_\rho\right]. \tag{2.14}$$

In this equation, δ^c_∞ accounts for the molecular complexity of the fluid, while the remaining terms account for its departure from the ideal gas value. In the dilute gas region, $Z \to 1$, $c_v \to c_{v\infty}$ and the derivative of Z vanishes, therefore $G_\infty \to 1/\delta^c_\infty$, where G_∞ denotes the Grüneisen parameter evaluated according to the ideal gas assumption and along the critical isotherm.

In process and energy engineering, given that also processes entailing phase change are of interest, the molecular complexity of the working fluid is often evaluated by means

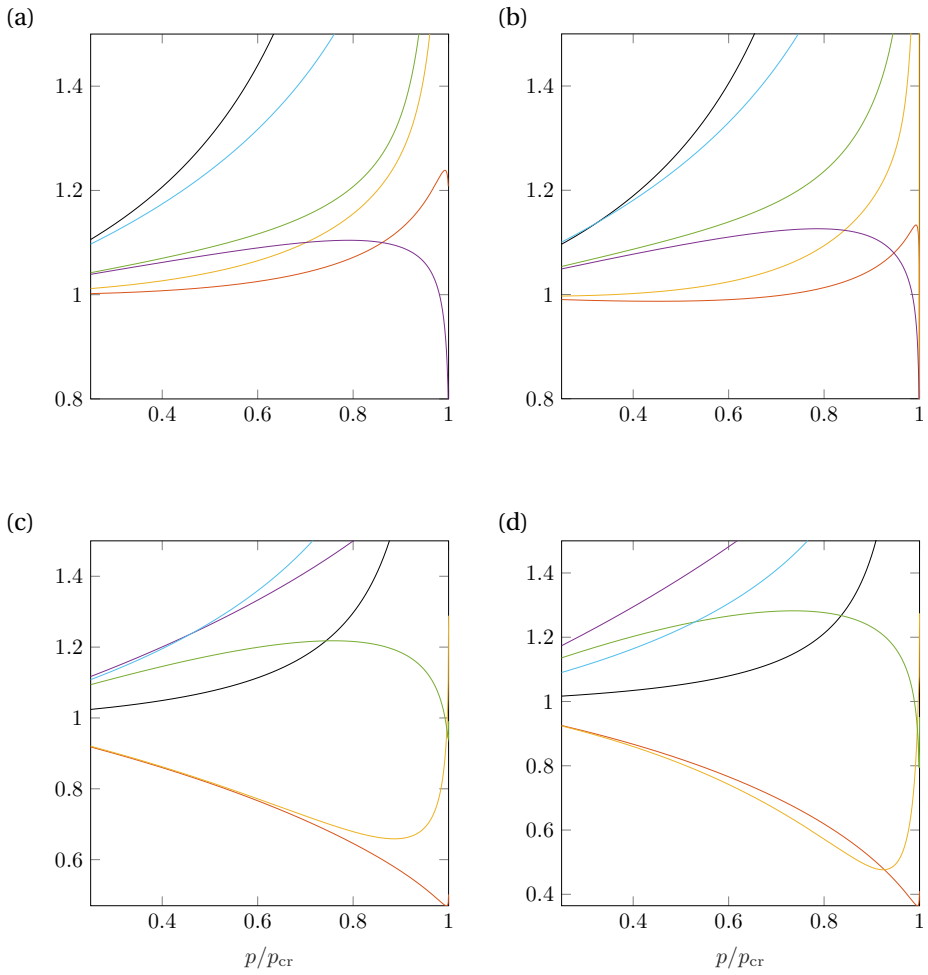

Figure 2.3: Variation of fluid properties along the critical isotherm for several fluids, where ∞ denotes properties estimated at $v \to \infty$. (a) nitrogen, (b) CO_2, (c) toluene and (d) siloxane MM. Fluid parameters: —— γ/γ_∞, —— $\gamma_{pv}/\gamma_{pv,\infty}$, —— Γ/Γ_∞, —— G/G_∞, —— Ψ/Ψ_∞, —— $1/Z$.

of the coefficient σ, defined as [52]

$$\sigma = \frac{T_{cr}}{R}\left(\frac{ds}{dT}\right)_{sat,T_r=0.7} = \\ = \frac{1}{0.7R}\left[\frac{(\gamma-1)}{G^2}\gamma_{pv}ZR - \frac{\gamma-1}{G}\frac{1}{\rho}\frac{dp_{sat}}{dT}\right]_{sat,T_r=0.7}, \tag{2.15}$$

where the subscript sat denotes dew point variables, and $T_r = 0.7$ means that the saturated property is evaluated for a temperature that is 0.7 times the critical value. Equation 2.15 highlights the link between σ and some fluid parameters. The σ coefficient is proportional to the slope of the dew line of the fluid in the Ts diagram, which is primarily a function of the heat capacity of the saturated vapor. Charts in Invernizzi [52] show that σ increases with the molecular complexity of the fluid. In particular, the slope of the dew line in the temperature entropy diagram, and thus σ, is positive for fluids with high molecular complexity. Conversely, σ is negative for fluids characterized by a simple molecular structure.

The graph in Fig. 2.2a can be used to compare the various definitions of molecular complexity with the aim of evaluating which parameter best fits results for a large number of fluids representative of a wide range of molecular complexities. All values are evaluated using multiparameter equations of state models for a number of fluids for which input data are available and that are implemented in a well-known commercial program [51]. Data of σ and the inverse of G_∞ (and thus δ^c_∞) are fitted with linear regression. A third-order polynomial function is instead used to fit $1/(\Gamma_{min}+1)$ with σ. Unity is added to the denominator to attain a smooth and monotone fit of the data also in case some BZT fluids characterized by $\Gamma_{min} < 0$ are included in the analysis. Maximum deviations between calculated $1/G_\infty$ and linearly interpolated values occur for $\sigma < 0$ and $\sigma > 80$. Deviations between calculated $1/(\Gamma_{min}+1)$ values from their polynomial fit are considerably larger (> 500%) for large values of molecular complexity, while they are smaller for low values.

Figure 2.2b shows the relation σ *vs* $(1/G)$ for three different sets of reduced temperatures and pressures and for the same fluids considered in Fig. 2.2a. The results prove that the linear relation between σ and $1/G$ is maintained, albeit less rigorously, also in the dense vapor region: substantial deviations from the linear relation between σ and $1/G$ can be observed only in the case $T_r = 1, p_r = 0.85$. G can therefore be used to quantify the complexity of pure fluid molecules and as non-dimensional property for the comparison of flow processes featuring different working fluids.

Graphs in Fig. 2.3 show the variation of each fluid parameter along the critical isotherm at $p < p_c$. Four different fluids of different molecular complexity are reported. Regardless of their molecular complexity, the specific heat ratio γ and the inverse of the compressibility factor Z increase monotonically with the reduced pressure p/p_{cr}. For values of pressure approaching that of the critical point, the value of γ increases more sharply, more so for simple molecules. For low molecular complexity fluids, the Grüneisen parameter peaks in the proximity of the critical point and converges to the ideal gas value as the pressure decreases. However, for fluids made of increasingly complex molecules (Figs. 2.3c-d), the ratio G/G_∞ is a monotonic function of the pressure, thus no maximum value exists. The trend of the function Ψ/Ψ_∞ is opposite to that of

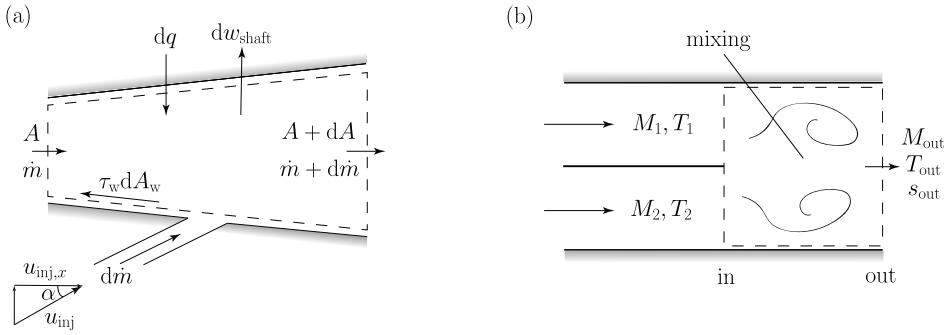

Figure 2.4: (a) Control volume for the analysis of one-dimensional compressible flows with variable cross-section area, energy transfer as heat or shaft work, wall friction and fluid injection. (b) Mixing of two co-flowing streams in a constant area channel. The dashed lines identify the control volume used for the mixing loss calculation.

G/G_∞. The parameter which is mostly affected by molecular complexity is the generalized isentropic exponent γ_{pv}. For low values of molecular complexity (Fig. 2.3a), γ_{pv} monotonically increases with pressure and tends to a finite value at the critical point. For moderate molecular complexity values (Fig. 2.3b), the $\gamma_{pv}/\gamma_{pv,\infty}$ function exhibits a minimum value, while for fluids made of complex molecules (Fig. 2.3c-d) the trend is monotone. Notably, $\gamma_{pv} < 1$ for states in the superheated vapor region of molecularly complex substances (see Fig. 2.1b). Finally, the fundamental derivative of gas dynamics monotonically increases with pressure in fluids with low molecular complexity. For fluids made of increasingly complex molecules (Figs. 2.3c-d), the function Γ/Γ_∞ exhibits a minimum in the proximity of the critical point.

Summarizing, all non-dimensional fluid properties carry information about the relevance of thermodynamic non-ideality of fluids. Nevertheless, depending on the type of analysis or application, one parameter can be more suited than the others. For example, the compressibility factor Z can be effectively used to ensure thermodynamic similarity between physical processes occurring in different fluids. The exponent γ_{pv}, instead, has recently been utilized to assess the impact of fluid non-ideality on the design of turbomachinery components. The design of turbine nozzles for ORC systems operating with dense vapors strongly depends on the value of γ_{pv} [53]. The value of the fundamental derivative of gas dynamics Γ is paramount for assessing dense vapor effects in relation to the propagation of waves in fluids. It can therefore be argued that the Grüneisen parameter is particularly suitable for the study of the role of fluid molecular complexity if paradigmatic non-reactive flows of pure fluids and mixtures are considered.

2.3. THEORETICAL FRAMEWORK

The derivation of the one-dimensional theoretical framework for the analysis of paradigmatic flows of dense vapors is based on the work of Shapiro [54], which is limited to ideal gas flows. This analysis was later further elaborated by Greitzer *et al* [55]. Arp *et al* [42] and, more recently, Baltadjiev *et al* [11] extended part of Shapiro's framework to the case of dense vapor flows, in which the fluid thermodynamic properties are obtained with an

arbitrary equation of state model. This framework is extended here to the case of non-isentropic processes and the fluid parameters introduced in Sec. 2.2 are used to quantify the influence of both the molecular complexity of the working fluid and the thermodynamic operating conditions.

The differential conservation equations for an infinitesimal control volume (see Fig. 2.4a) with variable cross-section area A, the frictional wall stresses τ_w, infinitesimal energy transfer as shaft work to the fluid $đw_{shaft}$, and as heat to the fluid $đq$, and mass flow injection $d\dot{m}$ read [55]

$$\frac{d\rho}{\rho} + \frac{du}{u} + \frac{dA}{A} = 0, \tag{2.16}$$

$$\rho u A du + A dp = -\rho A đw_{shaft} - \tau_w dA_w + d\dot{m}\left(u_{inj}\cos\alpha - u\right), \tag{2.17}$$

$$dh_t = dh + u du + \left[h_{inj} - h_{inj,in} + \frac{u^2}{2} - \frac{u_{inj}^2}{2}\right]\frac{d\dot{m}}{\dot{m}} = đq - đw_{shaft}, \tag{2.18}$$

where u is the absolute flow velocity, ρ the density, A the cross-section area, p the pressure, A_w the wetted surface area around the control volume, u_{inj} the velocity of the injected mass flow, α the mass flow injection angle, $h_{inj,in} = h_{inj}(T_{inj}, p_{inj})$ and $h_{inj} = h_{inj}(T, p)$ the specific static enthalpy of the injected fluid at the inlet and the outlet of the control volume, respectively.

The arbitrary equation of state in the volumetric form $p = \rho Z R T$ together with the calorimetric equation of state $h = h(T, p)$, forming the thermodynamic model, close the set of equations. The thermodynamic relations $s = s(T, p)$ and $c = c(\rho, s)$ allow one to derive the equations in the desired form.

The system of equations can be manipulated to obtain analytical relations between the infinitesimal variation of each flow quantity, for instance, pressure or temperature, and the variation of cross-sectional area, the energy transfer as heat, the shaft work, and the wall friction. The contribution due to the injected mass flow is neglected, and it is separately analyzed in Sec. 2.5. With this approach, one can analyze the influence of the non-ideality of the fluid properties on the variation of each flow quantity for a given change of cross-sectional area, energy transfer as heat and shaft work, and wall friction. Table 2.2 lists all these relations, whose derivation is reported in App. 2.10. All the relations can be formalized in the synthetic form

$$\left.\begin{aligned} \Phi = f_1\left(\frac{dA}{A}\right) + f_2\left(\frac{đq}{c_p T}\right) + \\ + f_3\left(\frac{đw_{shaft}}{c_p T}\right) + f_4\left(4C_f\frac{dx}{d_H}\right), \\ f_i = f_i(\gamma, \gamma_{pv}, \Gamma, G, \Psi, M), \qquad i = 1, ..., 4, \end{aligned}\right\} \tag{2.19}$$

where Φ is the normalized differential variation of a thermodynamic or fluid dynamic variable, e.g., temperature or flow velocity, C_f is the Fanning friction factor, and d_H is the hydraulic diameter. The f_i factors are termed *influence coefficients* [54] and solely depend on the Mach number and on some of the non-dimensional fluid properties introduced in Sec. 2.2. As a result, each of the flow quantities in the first column listed in

Tab. 2.2 is given by the summation of the product between each independent variable in the first row and the corresponding influence coefficient.

2.3.1. VALIDATION: FLOW EXPANSION IN A CONVERGENT-DIVERGENT NOZZLE

This case has already been treated extensively in the literature; here is only reported a comparison with recent experimental data obtained with a blow-down wind tunnel realizing the supersonic expansion of siloxane MDM. The accuracy of the one-dimensional framework has been quantitatively verified by comparing the values of Mach number and static pressure along the channel calculated with the equations of Tab. 2.2 against the experimental values documented in Spinelli *et al* [56]. Figure 2.5 shows the comparison between these experimental data and values obtained with the one-dimensional model valid for dense vapors and that valid for the ideal gas, see Anderson [35], Chap. 3. The governing flow equations were discretized with a first-order Euler scheme in space and solved numerically. Boundary conditions in terms of inlet total pressure, total temperature and Mach number were prescribed so that they matched the corresponding experimental values. Table 2.3 reports the main data identifying the four test cases considered in this analysis. Two different convergent-divergent nozzle geometries are considered for the cases termed M1.5H, M1.5L, and M2.0L, M2.0H by Spinelli *et al* [56]. Fluid properties of MDM are evaluated using the state-of-the-art multiparameter equation of state model by Thol *et al* [57]. The experimental data are those acquired at $t = 0$ s, i.e., immediately after the opening of the main control valve.

With reference to Fig. 2.5, the pressures calculated with the dense-vapor flow model match the experimental data with acceptable accuracy considering the limitations of the model: the relative difference between values obtained with the numerical model and values obtained from measurements never exceeds 6.5% for all cases. Mach numbers calculated with the one-dimensional model feature values that are within the uncertainty band associated with the experimental data. Values of pressure and Mach number computed with the ideal gas model are rather accurate if the inlet pressure is low, i.e., for the M1.5L and M2.0L test cases. The ideal gas model predictions are increasingly inaccurate with higher inlet pressures, as far as the values related to the divergent part of the nozzle are concerned ($Z_t \sim 0.65$ at the nozzle inlet). The discrepancy between the outlet static pressure calculated with the dense-vapor model and the ideal gas model is ~ 12% for both cases M1.5H and M2.0H and ~ 6% for the remaining cases.

2.4. PARADIGMATIC ONE-DIMENSIONAL COMPRESSIBLE FLOWS OF DENSE VAPORS

The influence coefficients $đq/(c_p T)$ and $4C_f \mathrm{d}x/d_H$ reported in Tab. 2.2 are instrumental to the analysis of Rayleigh and Fanno processes in dense vapors. These configurations are representative of actual flow processes in engineering applications. On the one hand, non-adiabatic flows can be encountered, for example, in small-scale turbines for ORC systems and heat exchangers. Moreover, the Rayleigh flow simplification can be adopted for the preliminary assessment of supercritical injection processes in combustors. On the other hand, profile losses due to the presence of a laminar or turbulent

	$\frac{\mathrm{d}A}{A}$	$\frac{\mathrm{d}q}{c_p T}$	$\frac{\mathrm{d}w_{shaft}}{c_p T}$	$4C_f\frac{\mathrm{d}x}{d_H}$
$\frac{\mathrm{d}\rho}{\rho}$	$\frac{M^2}{1-M^2}$	$-\frac{(\gamma-1)}{G}\frac{1}{1-M^2}$	$-\frac{(\gamma-1)}{G^2}\frac{1}{1-M^2}$	$-\frac{G+1}{2}\frac{M^2}{1-M^2}$
$\frac{\mathrm{d}p}{p}$	$\frac{\gamma_{pv}M^2}{(1-M^2)}$	$-\frac{\gamma_{pv}(\gamma-1)M^2}{G(1-M^2)}$	$-\frac{\gamma_{pv}(\gamma-1)}{G^2(1-M^2)}$	$-\frac{\gamma_{pv}M^2}{2}\frac{1+GM^2}{1-M^2}$
$\frac{\mathrm{d}T}{T}$	$\frac{GM^2}{1-M^2}$	$-\frac{\gamma M^2-1}{1-M^2}$	$-\frac{(\gamma-1)}{G(1-M^2)}$	$-\frac{G\left[(\gamma M^2-1)G+(\gamma-1)\right]}{(\gamma-1)(1-M^2)}\frac{M^2}{2}$
$\frac{\mathrm{d}M}{M}$	$-\frac{1+(\Gamma-1)M^2}{1-M^2}$	$\frac{(\gamma-1)}{G}\left[\frac{\Gamma}{1-M^2}-\frac{\Psi}{2}\right]$	$\frac{(\gamma-1)}{G^2}\frac{\Gamma}{1-M^2}$	$\left[\frac{(G+1)\Gamma}{(1-M^2)}-G\frac{\Psi}{2}\right]\frac{M^2}{2}$
$\frac{\mathrm{d}u}{u}$	$-\frac{1}{1-M^2}$	$\frac{(\gamma-1)}{G}\frac{1}{1-M^2}$	$\frac{(\gamma-1)}{G^2}\frac{1}{1-M^2}$	$\frac{G+1}{2}\frac{M^2}{1-M^2}$
$\frac{\mathrm{d}c}{c}$	$\frac{(\Gamma-1)M^2}{1-M^2}$	$-\frac{(\gamma-1)}{G}\left[\frac{(\Gamma-1)}{1-M^2}-\frac{\Psi}{2}\right]$	$-\frac{(\gamma-1)}{G^2}\frac{\Gamma-1}{1-M^2}$	$-\left[\frac{(G+1)(\Gamma-1)}{(1-M^2)}-G\frac{\Psi}{2}\right]\frac{M^2}{2}$
$\frac{\mathrm{d}s}{c_p}$	0	1	0	$\frac{G^2}{\gamma-1}\frac{M^2}{2}$
$\frac{\mathrm{d}h}{c_p T}$	$\frac{G^2}{\gamma-1}\frac{M^2}{1-M^2}$	$-\frac{M^2(G+1)-1}{\left(1-M^2\right)}$	$-\frac{1}{1-M^2}$	$-\frac{G^2(G+1)}{\left(\gamma-1\right)\left(1-M^2\right)}\frac{M^4}{2}$

Table 2.2: Influence coefficients for compressible channel flow and real gas in terms of γ, Γ, G, γ_{pv} and Ψ.

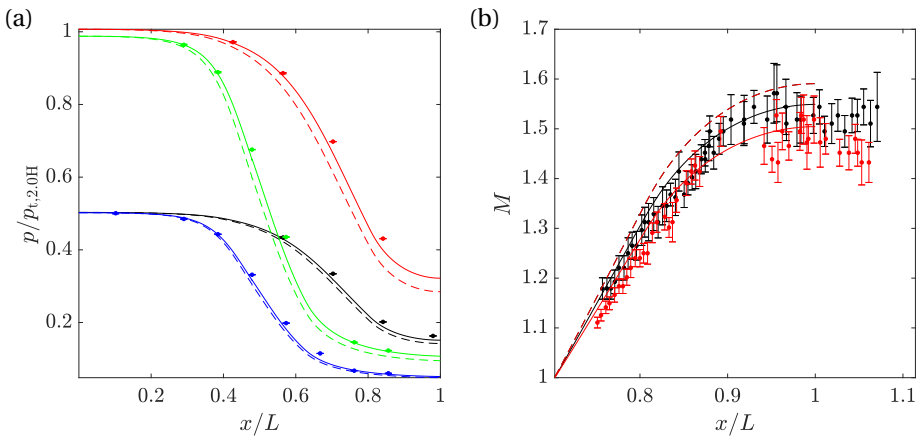

Figure 2.5: Validation of the one-dimensional equations for an isentropic vapor flow through a supersonic nozzle by comparison with measurements (Spinelli *et al* [56]). The working fluid is siloxane MDM. Results of calculations performed by assuming that the fluid obeys the ideal gas law are also reported. (*a*) pressure *vs* axial coordinate. (*b*) Mach number *vs* axial coordinate. For both graphs: —— fluid properties calculated with a multiparameter equation of state model [57], - - - fluid properties calculated with the ideal gas model, • measured values (pressure) or values derived from measured information (Mach) with corresponding error bars showing the 95% confidence interval of the mean; cases, as termed by Spinelli *et al* [56]: —— M1.5L, —— M1.5H, —— M2.0L, —— M2.0H.

Test	p_t [bar]	T_t [K]	$p_{r,t}$	$T_{r,t}$	Z_t
M1.5L	4.59	512.15	0.32	0.91	0.81
M1.5H	9.20	541.15	0.64	0.96	0.63
M2.0L	4.58	520.15	0.32	0.92	0.82
M2.0H	9.02	542.15	0.63	0.96	0.65

Table 2.3: Several flow properties identifying the inlet conditions of the selected test cases treated in Spinelli *et al* [56]. The total compressibility factor Z_t is calculated starting from the inlet total quantities.

Fluid	M_{mol} [g mol^{-1}]	T_{cr} [K]	p_{cr} [bar]	γ_∞	Γ_{min}	G_∞	marker
N_2	28.01	126.19	33.96	1.40	1.3390	0.40	——
O_2	32.00	154.58	50.43	1.40	1.3314	0.40	- - -
CO_2	44.01	304.13	73.77	1.30	1.1944	0.3004	——
isobutane	58.12	407.81	36.29	1.08	0.7105	0.0775	- - -
toluene	92.14	591.75	41.26	1.05	0.5849	0.0486	——
MM	162.38	518.70	19.39	1.03	0.3395	0.0272	- - -

Table 2.4: Fluids adopted for the analysis of Rayleigh and Fanno flows and characteristic properties. The markers in the last column are used in Figs. 2.6, 2.7, 2.11, 2.12.

boundary layer on blade surfaces and contributing to the total loss in turbomachinery can be modeled by means of the Fanno flow [13]. To the authors' knowledge, no study on the influence of the fluid on each of these paradigmatic flows in the non-ideal, albeit classical, regime is available in the literature. Only some studies about non-classical flows were carried out in the past [36]–[38], [42], [58], but they are based on the estimation of fluid thermodynamic properties by means of largely inaccurate thermodynamic models, such as the van der Waals equation of state.

For this analysis, equations in Tab. 2.2 are discretized with a first-order forward scheme for an infinitesimal control volume of length dx and numerically integrated over a given length. Non-dimensional fluid parameters are estimated within each infinitesimal control volume as the average of the value calculated at the edge of each control volume. Calculations are performed for nine different fluids (see Tab. 2.4) and different inlet conditions. State-of-the-art multiparameter equations of state models implemented in an in-house software for the calculation of thermophysical properties [51], [59] are adopted. To ensure thermodynamic similarity among all the fluids, two sets of inlet conditions in terms of reduced temperature and pressure are considered, namely those characterized by $T_\mathrm{r} = 1.05$, $p_\mathrm{r} = 1.15$ and by $T_\mathrm{r} = 0.9$, $p_\mathrm{r} = 0.05$. The compressibility factor associated with the high-pressure and high-temperature inlet condition is $Z \simeq 0.5$, while that associated with the dilute-gas inlet condition is $Z \simeq 1$. Calculations are stopped either when pressure and temperature equal the corresponding saturated values or the outlet Mach number M_out is equal to 1.4. For the majority of the considered fluids, the limit assures that, in the supersonic regime, the thermodynamic model is within its range of validity. The discretization is locally refined in the proximity of the sonic point to avoid numerical divergence.

2.4.1. RAYLEIGH FLOW OF DENSE VAPORS

Figures 2.6a and 2.6b show the Rayleigh curves evaluated for $Z \simeq 0.5$ and $Z \simeq 1$, respectively. Results are reported for the fluids of Tab. 2.4. The inlet Mach number M_in is set to 0.7. For each curve, the point at maximum $\Delta s/c_{p,\mathrm{in}}$, with $c_{p,\mathrm{in}}$ denoting the isobaric specific heat evaluated at the inlet, corresponds to the thermodynamic state where choking occurs. The channel flow is discretized in such a way that the energy transferred to each infinitesimal control volume of length dx is equal to dq = 100 J: this value has been chosen after sensitivity analysis. To assure a smooth solution at $M \simeq 1$, the value of both dx and dq are divided by a factor 1.75 every time the value of the first non-decimal unit of the parameter $10 \cdot M$, where M is the flow Mach number, increases of 1.

The use of the appropriate influence coefficients in Tab. 2.2 yields the relation

$$\frac{\mathrm{d}h}{\mathrm{d}q} = \frac{1}{T}\frac{\mathrm{d}h}{\mathrm{d}s} = -\frac{M^2(G+1)-1}{(1-M^2)}. \tag{2.20}$$

Equation 2.20 shows that at fixed reduced inlet temperature and pressure, both the Mach number and the Grüneisen parameter directly affect the variation of the specific enthalpy of the fluid along the duct. In particular, the Grüneisen parameter is related to the slope of the Rayleigh curves: fluids with higher molecular complexity exhibit a larger enthalpy increase if compared to fluids made of simpler molecules. This shows that, as expected, substances characterized by a low value of G convert into internal en-

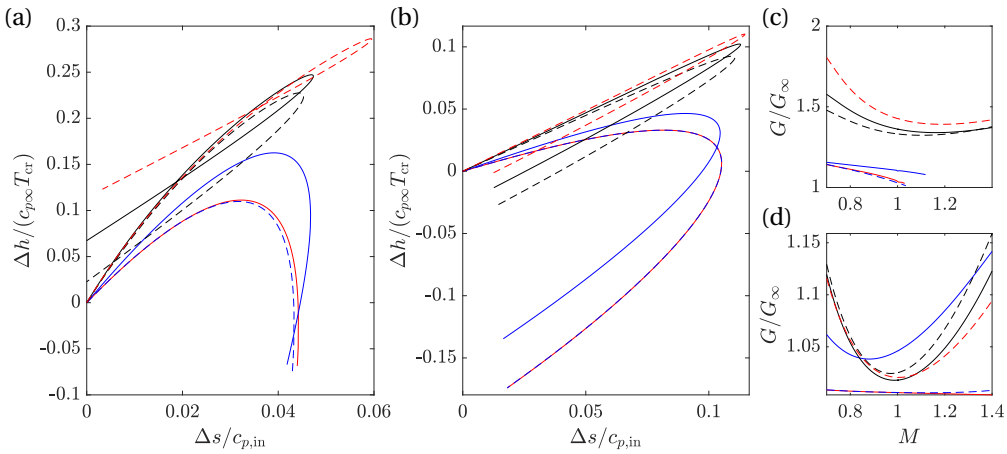

Figure 2.6: Rayleigh curves for different fluids at $M_{in} = 0.7$. Markers and colors identifying the curve in relation to each fluid are reported in Tab. 2.4. Considered cases: (a) $T_r = 1.05$, $p_r = 1.15$, $Z \simeq 0.5$; (b) $T_r = 0.9$, $p_r = 0.05$, $Z \simeq 1$. (c) and (d) report the variation of G/G_∞ for the processes displayed in (a) and (b), respectively.

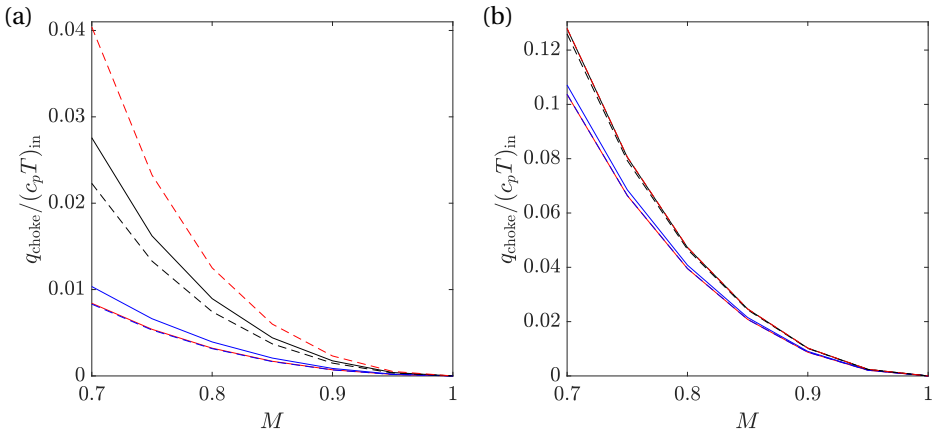

Figure 2.7: Non-dimensional energy transfer as heat required to attain choked conditions as a function of the inlet Mach number. Markers and colors identifying the curve in relation to each fluid are reported in Tab. 2.4. Considered cases: (a) $T_r = 1.05$, $p_r = 1.15$; (b) $T_r = 0.9$, $p_r = 0.05$.

ergy a larger amount of thermal energy transferred to the flow. Combining the relation $\mathrm{d}u/u = f(\gamma, G, M) \cdot \mathrm{d}q/(c_p T)$, which can be obtained with the influence coefficients of Tab. 2.2 with Eq. 2.48, leads to

$$\frac{\mathrm{d}E_\mathrm{k}}{\mathrm{d}q} = G\frac{M^2}{1-M^2}, \tag{2.21}$$

where $E_\mathrm{k} = u^2/2$ is the kinetic energy of the fluid. Conversely, substances characterized by high values of G, for instance, nitrogen or oxygen, convert a proportionally larger amount of thermal energy transferred to the flow into kinetic energy. Equation 2.21 shows that changes in kinetic energy scale linearly with the Grüneisen parameter of the fluid, or, equivalently, are inversely proportional to its molecular complexity. The distribution of the thermal energy input between the kinetic and internal energy of the fluid depends on the value of the isobaric specific heat capacity c_p at fixed thermodynamic conditions. From Eqs. 2.11, 2.47 and the relation $pv = ZRT$, it follows

$$\frac{c_p}{R} = \frac{(\gamma-1)}{G^2}\gamma_{pv}Z. \tag{2.22}$$

The factor $1/G^2$ is several orders of magnitude larger than the numerator. As a consequence, the specific heat at constant pressure times the molar mass is inversely proportional to the square of the Grüneisen parameter or, equivalently, directly proportional to the square of the molecular complexity of the fluid. Figures 2.6a-c show that G becomes larger than G_∞ for all the fluids if the fluid state approaches the critical point of the substance. This results in a steeper enthalpy increase at constant thermal energy input if compared to the case for which $Z \simeq 1$ (Figs. 2.6b-d). However, this effect is more pronounced for complex molecules, which exhibit a larger deviation of G from the baseline G_∞ value (Fig. 2.6c and Fig. 2.3). For substances characterized by low values of G_∞, the maximum value of enthalpy along a Rayleigh curve moves closer to the sonic point. Equating to zero Eq. 2.20 results in

$$M_{\max(h)} = \frac{1}{\sqrt{G+1}}. \tag{2.23}$$

For complex fluids, $M_{\max(h)} \sim 1$ as $G \to 0$, while $M_{\max(h)} = 1/\sqrt{\gamma}$ for a perfect gas. In other words, adding thermal energy to a subsonic flow of a dense vapor increases the static enthalpy until choking conditions are reached.

Figures 2.7a-b show the dimensionless thermal energy flux that is required to choke the flow at different subsonic inlet Mach numbers for both the $Z \simeq 0.5$ (Fig. 2.7a) and the $Z \simeq 1$ (Fig. 2.7b). Both graphs show that the larger the fluid molecular complexity, the larger the amount of energy that needs to be transferred as heat to the fluid to choke the flow. The influence of the fluid molecular complexity is less visible in the $Z \simeq 1$ case, i.e., if the fluid is in the dilute gas state.

The physical explanation of these results is that fluids made of complex molecules (low values of G_∞), thus with a large number of active molecular degrees of freedom, can store a larger quantity of thermal energy. Therefore, only a small share of the energy transferred as heat contributes to the increase of the kinetic energy of the flow (Eq. 2.21). Note also that the relative amount of thermal energy required to choke the flow starting

from subsonic inlet conditions is lower if $Z \simeq 0.5$ compared to the $Z \simeq 1$ case. The difference is larger for simple molecules ($\simeq 10$ times less than the amount evaluated for $Z \simeq 1$). This is due to the higher value of the isobaric specific heat capacity in the proximity of the critical point, whose increase is steeper for simple molecules, as it can be inferred from the trend of γ reported in Fig. 2.3. Similar conclusions for the supersonic Rayleigh flow of van der Waals fluids can be found in Schnerr and Leidner [36].

Figures 2.8a-b show the variation of Mach number with the normalized entropy increase at different inlet Mach numbers. The results are reported for nitrogen (Fig. 2.8a) and siloxane D_6 (Fig. 2.8b), a BZT fluid. Two sets of inlet temperature and pressure at a different level of thermodynamic non-ideality, namely $T_r = 1$, $p_r = 0.9$, and $T_r = 0.9$, $p_r = 0.05$ are considered. These cases correspond to a value of the compressibility factor at the inlet of $Z \simeq 0.5$ and $Z \simeq 1$, respectively. If the fluid is in the ideal gas state, the Mach number increases monotonically with the entropy, and, consequently, with the energy input as heat. Due to the higher number of molecular degrees of freedom, in Rayleigh flows of fluids made of more complex molecules, like, for instance, siloxane D_6, the Mach number increases less with the input of energy as heat if compared to Rayleigh flows of simpler molecules.

Figure 2.8b highlights that the trend of Mach number as a function of energy input as heat is non-monotone for subsonic Rayleigh flows of D_6: after an initial decrease, the Mach reaches a minimum and then increases. Solving $\mathrm{d}M/M = f(\mathrm{d}q) = 0$ yields an analytical relation for the inversion of the Mach number, namely

$$M_{\min} = \sqrt{1 - 2\frac{\Gamma}{\Psi}}, \tag{2.24}$$

which is defined for

$$\Gamma \geq \frac{\Psi}{2}. \tag{2.25}$$

If the fluid is in the dilute gas state, $Z \to 1$, $2\Gamma/\Psi \to (\gamma+1)/\gamma$, and $M_{\min}$ does not admit real solutions. The red line in Fig. 2.8b identifies the locus of $M_{\min}$ for different values of the inlet Mach number. Given that Ψ is greater than zero for all vapor thermodynamic states and for all fluids, also several non-BZT fluids exhibit thermodynamic states for which Eq. 2.25 is satisfied. This non-classical behavior is due to the steep increase of the speed of sound that dense vapors of complex molecules fluids exhibit in the proximity of the critical point, which prevails over the flow acceleration for $M_{in} < 1$.

Figure 2.9 depicts the boundaries of the thermodynamic region in which Eq. 2.25 holds in the temperature-entropy diagram of different fluids. The BZT region, i.e., the region satisfying the $\Gamma < 0$ condition, is also reported for comparison. Calculations based on state-of-the-art thermophysical models highlighted that fluids with $G_\infty < 0.059$ admit a thermodynamic region where the Eq. 2.25 is satisfied. Given the small extent of the BZT thermodynamic region of D_6 predicted by current thermodynamic models, effects on choking as the ones discussed by Cramer [38] and dependent on the van der Waals thermodynamic model are confined to a very restricted range of thermodynamic conditions close to the critical point. Therefore, they are almost impossible to visualize.

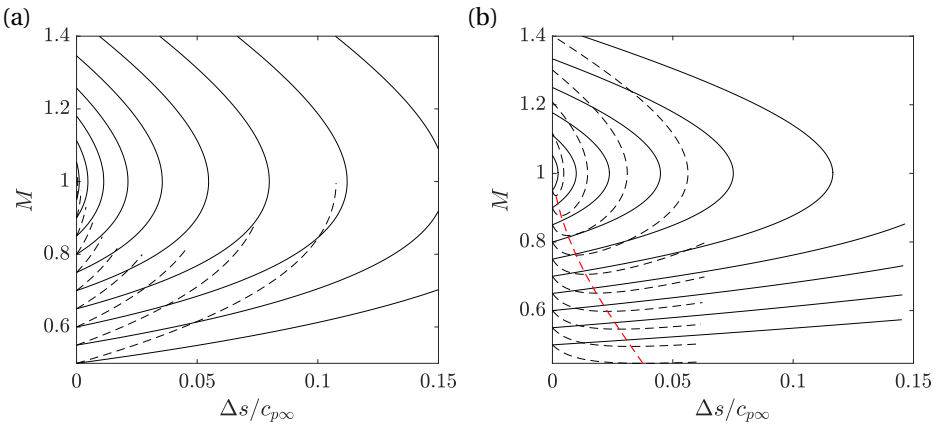

Figure 2.8: Mach number *vs* entropy in Rayleigh processes in (a) nitrogen and (b) siloxane D_6 for different inlet Mach numbers. Two sets of inlet reduced temperature and pressures are considered: - - - $T_r = 1$, $p_r = 0.9$; —— $T_r = 0.9$, $p_r = 0.05$. The red line in identifies the locus of M_{min}

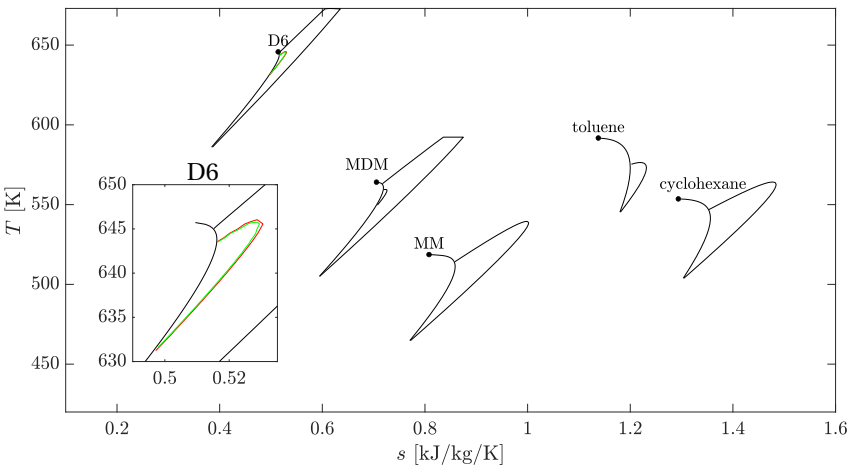

Figure 2.9: Boundaries of the thermodynamic regions encompassing states for which $\Gamma < \Psi/2$ in the temperature-entropy diagram for fluids with different molecular complexity. For siloxane D_6, a close-up of the regions in which $\Gamma < \Psi G/[2(G+1)]$ (red) and the $\Gamma < 0$ (green) is also displayed.

2.4.2. FANNO FLOW OF DENSE VAPORS

Fanno processes have been numerically assessed for all the fluids in Tab. 2.4. As shown in Tab. 2.2, the solution of the one-dimensional equations requires the specification of the friction factor coefficient C_f, which is directly proportional to the entropy generation due to viscous dissipation. Simple algebraic manipulation allows us to write

$$\zeta_s = \int_{s_{in}}^{s_{out}} \frac{T\mathrm{d}s}{\frac{1}{2}u^2} = \int_0^L \frac{4C_f \mathrm{d}x}{d_H}. \tag{2.26}$$

Equation 2.26 shows that the entropy generation due to friction in fully-developed channel flows depends on the Fanning friction coefficient and on the pipe aspect ratio L/d_H. Sciacovelli *et al* [60] recently determined the trend of C_f as a function of the Reynolds number for dense vapors in supersonic fully developed channel flows with isothermal walls by means of direct numerical simulations (DNS). The authors simulated flows of air and fluorocarbon PP11 ($C_{14}F_{24}$). They estimated the fluid properties using the perfect gas model for air and the Martin-Hou equation state for PP11. Results show that, for dense vapor flows, dynamic and thermal effects are decoupled to a large extent, and compressibility has a minor effect on the skin friction coefficient if compared to what happens for air flows. Therefore, the skin friction coefficient in dense organic vapor flows tends to the incompressible flow value given by Deans' equation for rectangular duct channels [61]. Numerical simulations of two-dimensional boundary layers with zero pressure gradient conducted by Pini and De Servi [62] further corroborate this finding. However, the study by Sciacovelli [60] has been conducted assuming isothermal channel walls and supersonic flow.

To assess the influence of both flow compressibility and thermodynamic fluid state also for the case of subsonic adiabatic channel flows of dense vapors, three-dimensional axial-symmetric steady-state numerical flow simulations were performed. This study also enabled the assessment of the accuracy of the well-established Colebrook–White empirical model for the computation of the friction factor coefficient in pipe flows [63]. Differently from the approach adopted by Sciacovelli [60], in this case, the Reynolds Averaged Navier Stokes (RANS) equations model was employed, together with Spalart-Allmaras (SA) turbulence closure model [64]. Despite the accuracy of existing turbulence models for dense vapor flows is not fully ascertained, the work documented in Otero *et al* [65] proved that eddy viscosity models such as SA can provide reasonably accurate values of boundary layer quantities for wall-bounded turbulent flows even in case of strong variations of fluid thermophysical properties. Therefore, the RANS model complemented by the SA eddy viscosity closure is deemed sufficient for the purpose of this analysis. The study described in Sciacovelli *et al* [66] further corroborates the validity of the approach: numerical analyses of turbulent channel flows simulated with four variants of the $k-\epsilon$ turbulence model demonstrate that all of the eddy viscosity models provide results that are in qualitative agreement with those obtained with DNS. The considered geometry is a straight 12 m-long pipe, limited to a circular sector of 36°. The pipe length was chosen such that fully developed flow is attained for all the case studies. The mesh consists of 1.2 million elements to ensure grid independence. Appendix 2.11 reports the results of the grid independence study. The grid is refined in the proximity of the wall to ensure accurate resolution of the boundary layer. The first

	T_r	p_r	M range (air)	M range (MM)
Z05	1.05	1.15	0.45-0.69	0.45–0.85
Z07sub	1	0.65	0.43-0.82	0.34–0.79
Z07super	1.1	1.05	0.34-0.72	0.32–0.80
Z1	0.9	0.05	0.6–0.8	0.51–0.83

Table 2.5: Values of the outlet reduced temperature and pressure and resulting Mach number range for each of the fluids under investigation.

cell height is set to $2 \cdot 10^{-8}$ m to guarantee $y^+ < 1$ for all the considered simulations. Rotational periodicity is attained by prescribing symmetry boundary conditions on the remaining interfaces. Flows of two fluids with different levels of molecular complexity are investigated, namely air in ideal gas conditions and siloxane MM. The viscosity value for air is set to $1.831 \cdot 10^{-5}$ Pa·s over the whole computational domain. Thermophysical properties of siloxane MM are estimated with state-of-the-art models implemented in a well-known commercial software [51]. Numerical simulations have been performed with commercial CFD software [67]. No-slip and adiabatic conditions are imposed at the smooth wall. Total inlet temperature and pressure are chosen such that prescribed values of T_r and p_r at the outlet, where the flow is fully developed, are obtained. Table 2.5 lists the four considered sets of T_r and p_r at the pipe outlet. These values were set such that the thermodynamic states of the simulated flows are 1) close to vapor-liquid critical state (case Z05 with $Z \simeq 0.5$), 2) in the subcritical and supercritical dense vapor region (cases Z07sub and Z07super, respectively, with $Z \simeq 0.7$) and 3) in the dilute gas state (case Z1 with $Z \simeq 1$). To study the effect of the Mach number on the friction coefficient at the pipe outlet, six values of normalized pressure difference $(p_{t,in} - p_{out})/L$ are prescribed for each set of T_r and p_r. Table 2.5 lists the values of the outlet reduced temperature and pressure for the four different cases, together with the resulting exit Mach number range. In all cases, the value of the Reynolds number calculated with the pipe diameter as reference dimension is sufficiently large to assume fully turbulent flow, i.e., $Re_D = \rho_m u_m D/\mu_{in} > 10^7$, where m stands for *meridional*. In accordance with the observations of Otero *et al* [65] and Sciacovelli *et al* [66], the turbulent Prandtl number is set to 0.9 in all simulations.

Figures 2.10a and 2.10b show the results for air (ideal gas) and siloxane MM. Overall, the values of C_f calculated with the Colebrook-White correlation valid for incompressible flows are larger than the ones obtained from numerical simulations. However, for channel flows with $M < 0.4$ at the outlet, the maximum relative difference between C_f values obtained from CFD simulations and those calculated with the empirical correlation is $\sim 3\%$. If $M > 0.4$, for channel flows of air modeled as an ideal gas, C_f values decrease with both M and Re_D, thus deviating from values calculated with the Colebrook-White correlation. Still in the case of air flows, if $M \simeq 0.7$, the calculated maximum relative difference between C_f values is $\simeq 9\%$ for the Z05, Z07sub, and Z07super cases, and $\simeq 16\%$ for the Z1 case. Conversely, in the case of siloxane MM flows, the C_f vs Re_D curves obtained from CFD simulations follow the same trend given by the Colebrook-White correlation, regardless of the value of M. Therefore, the value of the friction coefficient depends solely

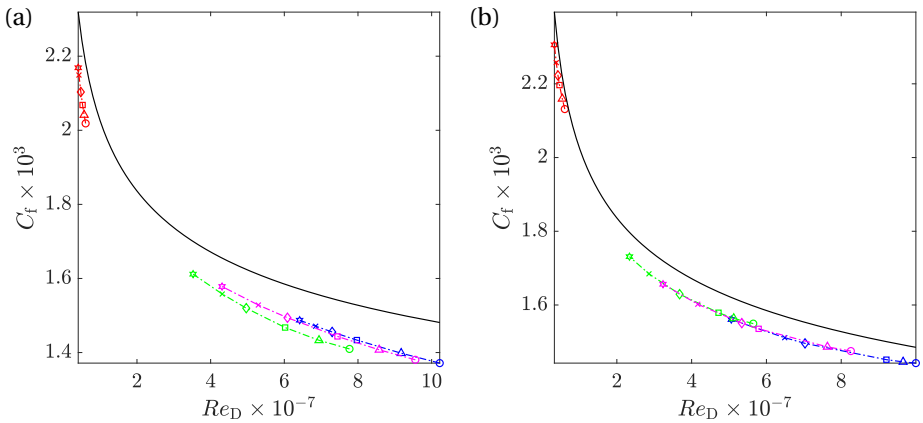

Figure 2.10: Friction coefficient C_f vs Reynolds number Re_D for compressible pipe flows. (a) air (ideal gas) and (b) siloxane MM. Values of C_f obtained from CFD simulations are compared with values calculated with the empirical Colebrook-White correlation. - - - case Z05; - - - case Z07sub; - - - case Z07super; - - - case Z1; ——Colebrook-White correlation.

on the Reynolds number in the case of flows of low-G fluids and is not influenced by the compressibility of the flow. A low value of the fluid Grüneisen parameter, indeed, implies a low value of the Eckert number of the flow. Simple algebraic manipulation gives

$$Ec = \frac{u^2}{c_p T} = \frac{G^2}{\gamma - 1} M^2, \tag{2.27}$$

which shows that Ec decreases with the fluid molecular complexity. The lower the Eckert number, the higher the heat capacity of the fluid and the lower the influence of the temperature both on viscous dissipation and on the value of the skin friction. This is in line with results described by Pini and De Servi [62], who studied dense-vapor effects on the dissipation coefficient C_d in compressible laminar boundary layers. Moreover, these results are also consistent with the outcome of the study of Chen *et al* [68], who performed DNS of fully-turbulent channel flows and observed that the averaged center-to-wall temperature ratio is lower in flows of organic fluids with large molecular complexity and decreases if the fluid state approaches that of the vapor-liquid critical point. Moreover, the Eckert number decreases if the thermodynamic state of the fluid approaches that of the critical point. This is due to the increase of the value of γ, which prevails over that of G, see Fig. 2.3.

Stemming from these considerations, the Colebrook-White relation is deemed sufficiently accurate for the estimation of the skin friction coefficient in compressible dense vapor flows. Given the lack of correlations for the friction factor coefficient in the case of compressible channel flows of arbitrary fluids, the Colebrook-White equation is also used to estimate C_f for channel flows of high G fluids. In addition, according to Eq. 2.26, the Colebrook-White equation provides a conservative estimation of the C_f value and, consequently, of the entropy loss coefficient in pipe flows. Furthermore, for subsonic flows, changes of the flow Re_D are more relevant than changes in M. To the authors' best

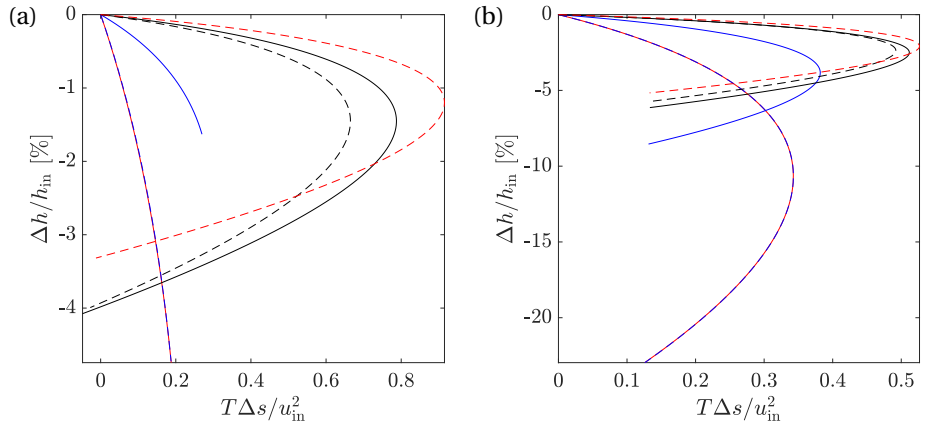

Figure 2.11: Fanno curves in the non-dimensionalized $h-s$ thermodynamic plane for different fluids at fixed inlet Mach number, $M_{\rm in} = 0.7$. The considered fluids can be identified with the colors and markers reported in Tab. 2.4. Two sets of inlet reduced temperatures and pressures are reported: (a) $T_{\rm r} = 1.05$, $p_{\rm r} = 1.15$; (b) $T_{\rm r} = 0.9$, $p_{\rm r} = 0.05$.

knowledge, the only available correlation for compressible pipe flow is that of Panhandle [69]. However, the validity of the relation is limited to Reynolds numbers between 5×10^6 and 1.4×10^7.

The viscous equations governing adiabatic flows that can be obtained in terms of the coefficients listed in Tab. 2.2 were solved to evaluate the influence of both fluid molecular complexity and dense vapor effects. The hydraulic diameter of the pipe is constant and equal to 0.1 m.

Figures 2.11a-b show the Fanno curves evaluated for $Z \simeq 0.5$ and $Z \simeq 1$. The entropy production is plotted in terms of the local entropy loss coefficient $T\Delta s/u_{\rm in}^2$. Results are displayed for the fluids of Tab. 2.4. The inlet Mach number is set to $M_{\rm in} = 0.7$. The molecular complexity of the fluid affects the value of Δh required to choke the flow for both the $Z \simeq 0.5$ and $Z \simeq 1$ cases. The combination of the enthalpy and entropy equations, see Tab. 2.2, yields

$$\frac{1}{T}\frac{\mathrm{d}h}{\mathrm{d}s} = -(G+1)\frac{M^2}{1-M^2}. \tag{2.28}$$

This relation shows that the slope of the Fanno curve depends on the value of G. As a consequence, the enthalpy drop that causes the flow to be choked decreases with increasing fluid molecular complexity and normalized entropy generation. If the fluid states are in proximity of the critical point at the inlet (case $Z \simeq 0.5$), the enthalpy drop at choking conditions is lower than the enthalpy drop leading to choking in case the fluid is in the dilute gas state. This finding is valid for all the investigated fluids and is related to the larger value of the dense-vapor isobaric heat capacity if compared to the ideal gas value.

Figures 2.12a-b show that the pipe length L^* required for the flow to be choked is significantly longer for flows of fluids made of complex molecules, regardless of the thermodynamic state and the inlet Mach number. This is a consequence of the higher entropy

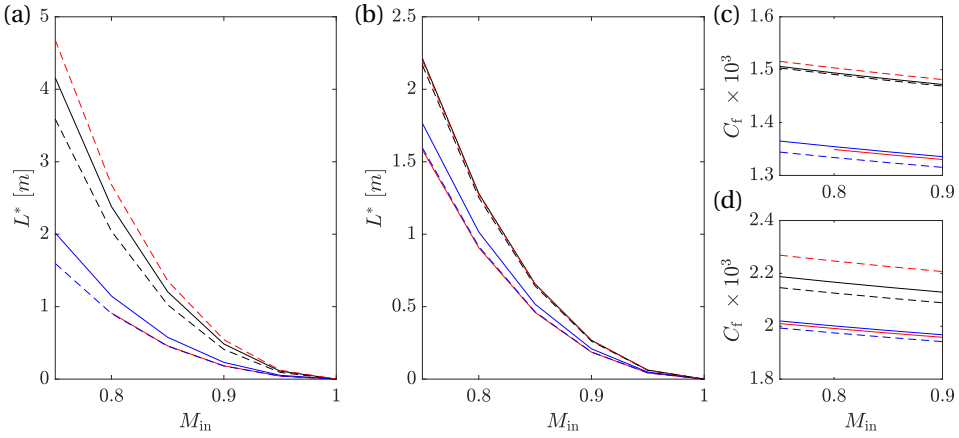

Figure 2.12: Pipe length required to choke the flow *vs* inlet Mach number. Two sets of inlet reduced temperature and pressure are considered: (a) $T_r = 1.05$, $p_r = 1.15$; (b) $T_r = 0.9$, $p_r = 0.05$. (c) and (d) depicts the variation of the friction coefficient with the inlet Mach number corresponding to the cases of Figs. a-b, respectively. Fluids are labeled with the colors and the markers reported in Tab. 2.4.

generation in choked Fanno flows of low-G fluids, see Fig. 2.11: viscous dissipation at the walls induces viscous heating of the flow, thus complex molecules of organic dense vapors allow a larger amount of the energy to be stored as internal energy of the fluid with a negligible or minor increase of the fluid temperature. Moreover, a smaller amount of internal energy is converted into kinetic energy; from Tab. 2.2, it follows that

$$\frac{\mathrm{d}E_k}{E_k} = (G+1)\,\frac{M^2}{1-M^2}\,\frac{4C_f \mathrm{d}x}{d_H}. \tag{2.29}$$

This equation shows that, if different fluids are compared at fixed reduced temperature and pressure at the inlet, the variation of the kinetic energy of the fluid is affected more by the decrease of the value of G than by the increase of the value of C_f, see Figs. 2.12c-d. Therefore, the increase of kinetic energy is low in flows of fluids made of complex molecules. As a consequence, in these flows, the fluid acceleration is smaller, and choking occurs further downstream. Furthermore, L^* increases if the fluid state approaches the critical point of the substance, regardless of its molecular complexity, due to the large value of the heat capacity in the dense vapor thermodynamic region, see Eq. 2.22.

Figures 2.13a-b show the variation of Mach number with the normalized pipe axial coordinate at different inlet Mach numbers. Results are reported for nitrogen (Fig. 2.13a) and siloxane D_6 (Fig. 2.13b). The same sets of inlet reduced temperature, reduced pressure, and Mach number introduced in Sec. 2.4.1 are also used here to fix the conditions of the flow. If the fluid is in the dilute gas state, the Mach number increases monotonically with the axial coordinate. At a fixed normalized axial coordinate, the Mach number increases less in the case of flows of fluids made of complex molecules such as siloxane D_6. However, if the fluid is in a thermodynamic state close to that of the critical point, the trend of the Mach number as a function of the axial coordinate be-

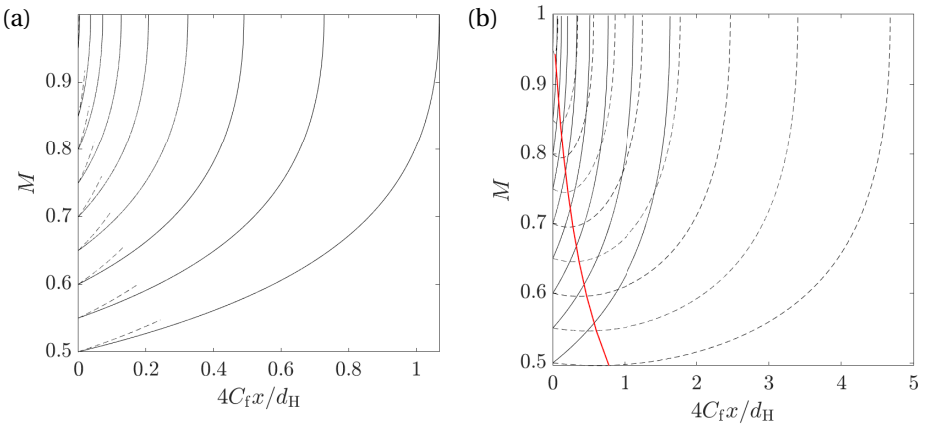

Figure 2.13: Mach number *vs* non-dimensional axial pipe coordinate for Fanno flows of (a) nitrogen and (b) siloxane D_6 for different inlet Mach numbers. Two sets of inlet reduced temperature and pressures are considered: ····· $T_r = 1.05$, $p_r = 1.15$; —— $T_r = 0.9$, $p_r = 0.05$.

comes non-monotone for Fanno flows of D_6: after an initial decrease, it reaches a minimum and then increases. Solving $\mathrm{d}M/M = f(4C_f \mathrm{d}x/d_H) = 0$ yields an analytical relation for the minimum value of the Mach number, namely

$$M_{\min} = \sqrt{1 - \frac{2\Gamma}{\Psi}\frac{G+1}{G}}. \tag{2.30}$$

which is defined for

$$\Gamma \geq \frac{\Psi}{2}\frac{G}{G+1}. \tag{2.31}$$

If the fluid is in the dilute gas state, $Z \to 1$, $2\Gamma/\Psi(G+1)/G \to (\gamma+1)/(\gamma-1)$, and $M_{\min}$ does not admit real solutions. The red line in Fig. 2.13b identifies the locus of $M_{\min}$ for different values of the inlet Mach number. Figure 2.9 shows the thermodynamic region formed by states for which Eq. 2.31 holds in the temperature-entropy diagram of D_6. Calculations based on state-of-the-art thermophysical models highlighted that fluids with $G_\infty < 0.0128$ admit a thermodynamic region where Eq. 2.31 is satisfied. The term $G/(G+1)$ is always greater than one. As a consequence, compared to Rayleigh flows, only a few fluids, mainly BZT fluids, exhibit a thermodynamic region where Eq. 2.30 admits a real solution.

2.5. MIXING OF DENSE VAPOURS STREAMS

Two configurations of mixing flows are considered, namely the co-flowing of two streams in either thermal or kinematic non-equilibrium and the injection of a flow into the main stream. Co-flowing mixing is representative, for example, of flow phenomena occurring in turbomachines and heat exchangers, like wake mixing downstream of a blade or a blunt body, while flow injection resembles, for example, tip leakage flow. For the case of

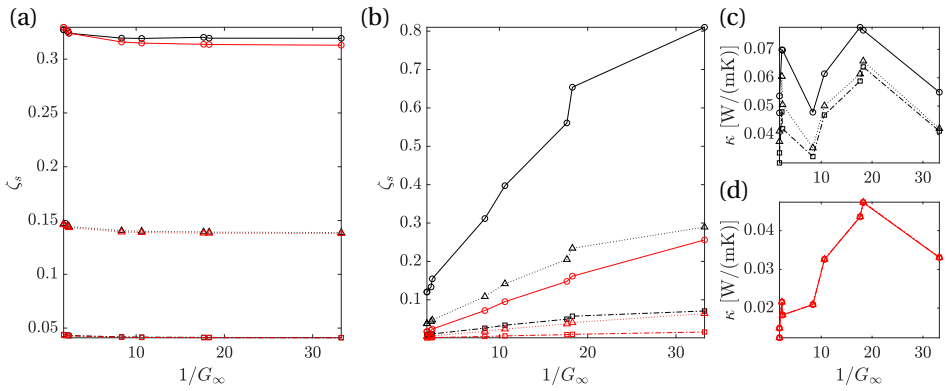

Figure 2.14: Irreversible entropy loss coefficient *vs* molecular complexity for mixing streams in (a) kinematic or (b) thermal non-equilibrium. Inlet thermodynamic conditions: $\overline{T}_{r,in} = 0.85$, $\overline{p}_{r,in} = 0.01$, $Z \simeq 1$ (red) and $\overline{T}_{r,in} = 1.05$, $\overline{p}_{r,in} = 1.15$ $Z \simeq 0.5$ (black). In Fig. a, – – –□– – –: $\Delta M = 0.2$, ·····△·····: $\Delta M = 0.6$, ——○——: $\Delta M = 1$. In Fig. b, – – –□– – –: $\Delta T/T_{crit} = 2\%$, ·····△·····: $\Delta T/T_{crit} = 6\%$, ——○——: $\Delta T/T_{crit} = 10\%$. For the case of thermal non-equilibrium, values of thermal conductivity *vs* molecular complexity evaluated for each fluid at $Z \simeq 0.5$ (c) and $Z \simeq 1$ (d) are reported. The same legend of Fig. b applies to both charts.

co-flowing mixing, entropy generation is calculated by applying the conservation laws and models for thermodynamic and transport properties of the fluid to the control volume sketched in Fig. 2.4b and assuming a mixed-out state at the outlet. The wall shear and the heat flux from the wall are neglected. The irreversible entropy generation is expressed in terms of the loss coefficient as

$$\zeta_{s,irr} = \frac{\overline{T}_{in,t}(s_{out} - s_{in})}{\frac{1}{2}\overline{u}_{in}^2}, \tag{2.32}$$

where $\overline{T}_{in,t}$ is the stagnation inlet temperature averaged over the mass flow, $\overline{u}_{in}$ is the mass-flow-averaged velocity at the inlet, and s_{out} is the mixed-out entropy at the outlet boundary. Two sets of inlet thermodynamic conditions are considered, namely $\overline{T}_{r,in} = 0.85$, $\overline{p}_{r,in} = 0.01$ and $\overline{T}_{r,in} = 1.05$, $\overline{p}_{r,in} = 1.15$, where $\overline{T}_{r,in}$ and $\overline{p}_{r,in}$ denote the mass-flow-averaged static temperature and pressure at the inlet. The first set of conditions is representative of a dilute gas case ($Z \simeq 1$), while the second of a flow occurring with the fluid states in proximity of the vapor-liquid critical point of the fluid ($Z \simeq 0.5$).

To study the effect of kinematic non-equilibrium, the reduced temperature of both streams is set to $\overline{T}_{r,in}$, while M_1 and M_2 are both set to $\overline{M}_{in} \pm \Delta M/2$, where $\overline{M}_{in} = 0.6$. Similarly, the effect of thermal non-equilibrium is evaluated by imposing $M_1 = M_2 = \overline{M}_{in}$ and T_1 and T_2 both equal to $\overline{T}_{r,in} \pm \Delta T_r/2$.

Figure 2.14a shows the results of the calculation of the entropy loss coefficient for flows in kinematic non-equilibrium and for the two considered sets of inlet conditions. It can be observed that the trend of the loss coefficient is barely dependent on both molecular complexity and dense vapor effects. Furthermore, the entropy generation solely depends on ΔM: the higher ΔM between the two streams, the higher the resulting $\zeta_{s,irr}$. Conversely, the fluid non-ideality and its molecular complexity affect the entropy loss in

the case of thermal non-equilibrium. If the inlet conditions are close to the critical point (Fig. 2.14b), the irreversible entropy loss coefficient increases regardless of the fluid. According to Greitzer *et al* [55], Chap. 1, the entropy production in a process in which heat transfer across a finite temperature difference occurs is proportional to the thermal conductivity of the fluid. Figures 2.14c-d illustrate the trends of the thermal conductivity of the fluid evaluated in the $Z \simeq 0.5$ and $Z \simeq 1$ cases, respectively. On a qualitative basis, it can be inferred that the thermal conductivity of the fluid increases as the state of the fluid departs from the dilute gas state. Furthermore, molecular complexity has a significant impact on the value of ζ_s. This trend is in accordance with what can be deduced from the equations governing the case of flow injection into the main stream (Eq. 2.34), which refer to a different flow configuration but the flow is subjected to the same underlying physics. A strictly physical explanation of the trend could not be fully clarified. However, the larger the specific heat capacity of the fluid, the lower the related temperature change for a fixed amount of exchanged thermal energy between the different streams. Therefore, low G fluids in the proximity of the critical point tend to remain in thermal non-equilibrium, thus increasing the irreversible entropy generation.

Contrary to the case of co-flow mixing, the entropy loss coefficient for the flow injection configuration is an analytical expression if the mass flow rate of the injected flow is small compared to that of the main stream. The control volume for the analysis of this mixing configuration is shown in Fig. 2.4a; here, the contributions due to changes in cross-sectional area, wall friction, energy transfer as heat, and shaft work are neglected. The fluid of the two streams is the same and the two streams are in mechanical equilibrium with each other, i.e., the mixing occurs at a fixed pressure value. This implies that the specific enthalpy of the injected flow after the mixing process is the same as that of the main flow, i.e., $h_{\text{inj}} = h$.

The conservation equations in the differential form are reported in Sec. 3.2, namely Eqs. 2.16,2.17, and 2.18. The wall viscous effects term is neglected, while the terms related to energy transfer as heat to the flow, to shaft work, and to variations in the cross-sectional area do not apply. Hence, following the same approach reported in Sec. 3.2 and App. 2.10, one can obtain a relation for the entropy variation of the main stream, namely

$$\frac{\mathrm{d}s}{c_p} = \frac{\mathrm{d}\dot{m}}{\dot{m}} \left\{ \frac{h_{\text{inj}}(T_{\text{inj}}) - h_{\text{inj}}(T)}{c_p T} + \frac{1}{2} \frac{G^2 M^2}{\gamma - 1} \left[\left(\frac{u_{\text{inj}}}{u} \right)^2 + -2 \left(\frac{u_{\text{inj}}}{u} \right) \cos\alpha + 1 \right] \right\}. \tag{2.33}$$

The irreversible entropy loss due to mixing is $\mathrm{d}s_{\text{irr}} = \mathrm{d}s - (s_{\text{inj}} - s)\mathrm{d}\dot{m}/\dot{m}$, where s and s_{inj} are the inlet entropy of the main and the injected streams, respectively [70]. By multiplying this relation by $2T/u^2$ and combining it with Eq. 2.48, the entropy loss coefficient can be expressed as

$$\zeta_{s,\text{irr}} = \zeta_s - \frac{2(\gamma - 1)}{G^2 M^2} \frac{\left(s_{\text{inj}} - s\right)}{c_p} \frac{\mathrm{d}\dot{m}}{\dot{m}}, \tag{2.34}$$

where

$$\zeta_s = \frac{T\mathrm{d}s}{u^2/2} = \frac{\mathrm{d}\dot{m}}{\dot{m}} \left\{ \frac{2(\gamma-1)}{G^2 M^2} \frac{h_{\mathrm{inj}}(T_{\mathrm{inj}}) - h_{\mathrm{inj}}(T)}{c_p T} + \right. \\ \left. + \left[\left(\frac{u_{\mathrm{inj}}}{u} \right)^2 - 2 \left(\frac{u_{\mathrm{inj}}}{u} \right) \cos\alpha + 1 \right] \right\}. \tag{2.35}$$

Equation 2.34 points out the contributions of kinematic and thermal non-equilibrium to the irreversible entropy generation. The second term of Eq. 2.35 depends solely on the velocity difference between the two streams and on the injection angle, hence, in the case of thermal equilibrium of the two streams, entropy generation is not affected by the state of the fluid and its molecular complexity. The charts in Fig. 2.14 related to the mixing of co-flowing streams show that in both configurations, molecular complexity and thermodynamic fluid state do not play a role. Conversely, in case of thermal non-equilibrium, they affect irreversible entropy generation.

More insights could be obtained by numerically solving Eq. 2.34 for two sets of inlet thermodynamic conditions, namely $T_r = 1.05$, $p_r = 1.15$ (ideal gas) and $T_r = 1.05$, $p_r = 0.01$ (dense vapor, $Z \simeq 0.5$). For both cases, three different inlet Mach numbers, namely $M = 0.3$, $M = 0.8$, and $M = 1.2$, and two sets of the injected flow temperature ratios were considered, i.e., $T_{\mathrm{inj}}/T = 0.95$ and $T_{\mathrm{inj}}/T = 1.05$. For all cases, the ratio between injected and main stream mass flows $\mathrm{d}\dot{m}/\dot{m}$ was set to 0.01. Figure 2.15a-b displays the results for the cases $Z \simeq 0.5$ and $Z \simeq 1$, respectively. If the inlet thermodynamic conditions depart significantly from those of the critical point, the dissipation linearly increases with molecular complexity. As $Z \to 1$, Eq. 2.34 resembles the ideal gas formulation reported in Greitzer *et al* [55]. As a consequence, $\zeta_{s,\mathrm{irr}}$ only depends on the ratio T_{inj}/T and on G_∞, given that $(\gamma-1) \to G_\infty$. For fixed values of T_{inj}/T and M, $\zeta_{s,\mathrm{irr}}$ decreases with G_∞. From Eqs. 2.34 and 2.35, it can be also inferred that the injection of a cooler stream leads to higher entropy generation. Furthermore, the dissipation decreases with the Mach number of the main flow.

The same observations apply to the $Z \simeq 0.5$ case. However, $\zeta_{s,\mathrm{irr}}$ increases of up to one order of magnitude for flows of complex molecules in thermodynamic states in the vicinity of the vapor-liquid critical point state (Fig. 2.15a). In accordance with Eq. 2.34, the charts show that reversible entropy generation increases in case the injected flow is cooler. In addition, as $\gamma \to \infty$, for thermodynamic states in the proximity of that of the critical point, regardless of the fluid, the effect of γ prevails on the effect of G.

2.6. CONCLUSION

This study is related to the investigation of the impact of fluid molecular complexity and dense vapor effects on paradigmatic one-dimensional flows, namely Rayleigh and Fanno flows, together with the mixing of two streams in kinematic and thermal non-equilibrium. The theoretical framework for the analysis of one-dimensional flows of perfect gases has been extended to the case of non-ideal compressible flows. Flows of several fluids at different reduced thermodynamic inlet conditions have been considered. State-of-the-art thermophysical models have been used to accurately estimate thermodynamic and transport properties of the fluids.

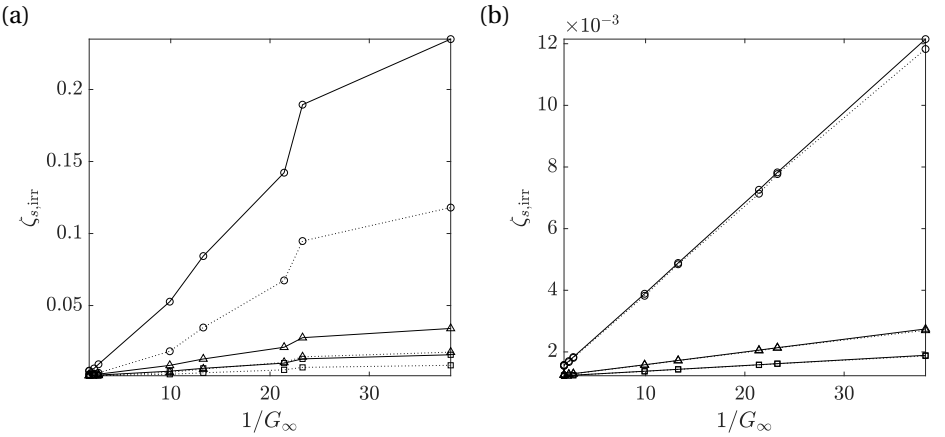

Figure 2.15: Irreversible entropy loss coefficient *vs* molecular complexity in flows with fluid states featuring (a) $Z \simeq 0.5$ and (b) $Z \simeq 1$. For both figures, ——: $T_{\mathrm{inj}}/T = 0.95$, ·····: $T_{\mathrm{inj}}/T = 1.05$, ○: $M = 0.3$, △: $M = 0.8$, □: $M = 12$.

Based on the results of the numerical analysis, the following conclusive remarks can be drawn.

1. The molecular complexity of a fluid scales with the inverse of the Grüneisen parameter G for a given thermodynamic state. In particular, the Grüneisen parameter evaluated for $v \to \infty$ is inversely proportional to the number of molecular degrees of freedom of the fluid molecule. This relation is qualitatively valid also for fluid states close to the vapor-liquid critical point. The Grüneisen parameter G is therefore arguably the best parameter to characterize molecular complexity given that it appears explicitly in paradigmatic flow equations.

2. In Rayleigh flows, the ratio between kinetic and internal energy of the fluid is determined by the complexity of the fluid molecules, as expected. The Grüneisen parameter determines the value of this ratio and affects the amount of energy transfer as heat causing flow choking.

3. RANS CFD simulations of subsonic channel flows showed that the Fanning friction coefficient C_{f} is arguably independent of the flow Mach number if the fluid is made of complex molecules. As a consequence, the Colebrook-White empirical correlation valid for incompressible flows provides accurate trends of C_{f} as a function of the Reynolds number Re_D even if the flow is compressible.

4. In a Fanno flow the molecular complexity of the fluid determines the location at which the flow is choked, which increases with increasing molecular complexity.

5. The relation between the Mach number and the production of entropy in Rayleigh and Fanno flows of complex-molecule fluids is non-monotonic if the inlet fluid state is at conditions close to those of the vapor-liquid critical point. The mini-

mum value of the Mach number is dependent on the fluid thermodynamic variables Γ, Ψ, and G.

6. In flows in which two streams at different inlet velocity and temperature mix, thermal non-equilibrium between the streams induces larger dissipation in fluids characterized by the high complexity of the molecular structure. Furthermore, the dissipation increases if the fluid state at the inlet of the channels approaches the vapor-liquid critical state.

7. The value of the Eckert number decreases with the complexity of the fluid molecular structure. As a consequence, thermal and dynamic effects can be decoupled, to a large extent, in fluids characterized by high molecular complexity.

Future research will aim at validating the obtained trends with high-fidelity numerical simulations and experiments in boundary layers and mixing processes in dense vapor flows. Additional research will also involve the estimation of the influence of both two-phase flows and mixtures of fluids on the one-dimensional processes considered here.

2.7. ACKNOWLEDGMENT

This research has been supported by the Applied and Engineering Sciences Domain (TTW) of the Dutch Organization for Scientific Research (NWO), Technology Program of the Ministry of Economic Affairs, grant # 15837.

2.8. DATA AVAILABILITY

The data that support the findings of this study are available from the corresponding author upon reasonable request.

2.9. APPENDIX A: USEFUL RELATIONS BETWEEN FLUID PARAMETERS

The derivation of analytical relations between some of the non-dimensional fluid parameters introduced in Sec. 2.2 is reported here for convenience. In a dense vapor, the specific enthalpy depends on both temperature and pressure, i.e., $h = h(T, p)$. The differential of the specific enthalpy reads

$$\mathrm{d}h = \left(\frac{\partial h}{\partial T}\right)_p \mathrm{d}T + \left(\frac{\partial h}{\partial p}\right)_T \mathrm{d}p = c_p \mathrm{d}T + \left(\frac{\partial h}{\partial p}\right)_T \mathrm{d}p. \tag{2.36}$$

Differentiating the Gibbs equation $\mathrm{d}h = T\mathrm{d}s + v\mathrm{d}p$ with respect to pressure at constant density yields

$$\left(\frac{\partial h}{\partial p}\right)_T = v + T\left(\frac{\partial s}{\partial p}\right)_T. \tag{2.37}$$

Using the Maxwell relation $(\partial s/\partial p)_T = (\partial v/\partial T)_p$ [71] and substituting Eq. 2.37 into Eq. 2.36 gives

$$\begin{aligned} \mathrm{d}h &= c_p \mathrm{d}T + \left[v - T\left(\frac{\partial v}{\partial T}\right)_p \right] \mathrm{d}p = \\ &= c_p \mathrm{d}T + \frac{(1-\beta_p T)}{\rho} \mathrm{d}p, \end{aligned} \tag{2.38}$$

where β_p is the isobaric compressibility, as reported in Tab. 2.1. Equation 2.38 can be substituted into the Gibbs equation to obtain

$$\mathrm{d}s = c_p \frac{\mathrm{d}T}{T} - \beta_p \frac{p}{\rho} \frac{\mathrm{d}p}{p}. \tag{2.39}$$

The total differential of the entropy $s = s(p,T)$ is given by

$$\mathrm{d}s = \left(\frac{\partial s}{\partial T}\right)_p \mathrm{d}T + \left(\frac{\partial s}{\partial p}\right)_T \mathrm{d}p. \tag{2.40}$$

Combining this equation with Eq. 2.39 gives

$$\frac{c_p}{T} = \left(\frac{\partial s}{\partial T}\right)_p = \left(\frac{\partial p}{\partial T}\right)_s \left(\frac{\partial v}{\partial T}\right)_p = \left(\frac{\partial p}{\partial T}\right)_s \frac{\beta_p}{\rho}, \tag{2.41}$$

which is obtained with the help of the so-called chain rule and the Maxwell relation $(\partial s/\partial p)_T = (\partial v/\partial T)_p$.

Similarly, by using the relations $e = e(T,v)$, $s = s(T,v)$, the Gibbs equation and the relations between thermodynamic derivatives listed in Bridgman [71], one can also obtain

$$\frac{c_v}{T} = \left(\frac{\partial s}{\partial T}\right)_v = -\left(\frac{\partial p}{\partial T}\right)_v \left(\frac{\partial v}{\partial T}\right)_s. \tag{2.42}$$

Here again the chain rule and the Maxwell relation $(\partial s/\partial p)_v = -(\partial v/\partial T)_s$ have been used. Simple algebraic manipulation of Eqs. 2.41 and 2.42 leads to

$$\frac{c_p - c_v}{c_v} = \frac{\gamma - 1}{\gamma} = \left(\frac{\partial p}{\partial T}\right)_v \left(\frac{\partial T}{\partial p}\right)_s = \frac{\beta_p}{\beta_T} \left(\frac{\partial T}{\partial p}\right)_s. \tag{2.43}$$

Differentiating the equation $T p^{-\gamma_{pT}} = \text{const.}$ gives

$$\left(\frac{\partial T}{\partial p}\right)_s = \gamma_{pT} \frac{T}{p}. \tag{2.44}$$

The combination of Eqs. 2.41 and 2.44 provides

$$\gamma_{pT} = \frac{\beta_p}{c_p} \frac{p}{\rho}; \tag{2.45}$$

similarly, Eq. 2.43 can be combined with Eq. 2.44 to obtain

$$\gamma_{pT} = \frac{\gamma - 1}{\gamma} \frac{\beta_T p}{\beta_p T}. \tag{2.46}$$

By manipulating Eqs. 2.5, 2.11, 2.45, and 2.44, a relation between γ_{pv}, G, β_p and β_T can be found and is

$$\frac{\beta_p}{c_p}\frac{p}{\rho} = \frac{\gamma-1}{\gamma}\frac{\beta_T p}{\beta_p T} = \frac{G}{\gamma_{pv}}. \tag{2.47}$$

The sound speed in a dense vapor can be expressed in terms of γ_{pv} and G using Eqs. 2.5, 2.11 and 2.47 as

$$c^2 = \left(\frac{\partial p}{\partial \rho}\right)_s = \gamma_{pv}\frac{p}{\rho} = \frac{G^2}{\gamma-1}c_p T. \tag{2.48}$$

Finally, The combination of Eq. 2.48 with Eq. 2.47 allows us to write

$$\frac{p}{\rho u^2} = \frac{1}{\gamma_{pv} M^2}. \tag{2.49}$$

2.10. APPENDIX B: DERIVATION OF THE INFLUENCE COEFFICIENTS

The general volumetric equation of state valid for dense vapors $p = \rho Z R T$ is adopted to derive some relations among fluid properties that are used to obtain expressions for the influence coefficients. Differentiation of the volumetric equation of state gives

$$\frac{\mathrm{d}p}{p} = \frac{\mathrm{d}\rho}{\rho} + \frac{\mathrm{d}T}{T} + \frac{\mathrm{d}Z}{Z}. \tag{2.50}$$

Given that $Z = Z(p, T)$, the first-order expansion of the differential dZ yields

$$\frac{\mathrm{d}Z}{Z} = \frac{T}{Z}\left(\frac{\partial Z}{\partial T}\right)_p \frac{\mathrm{d}T}{T} + \frac{p}{Z}\left(\frac{\partial Z}{\partial p}\right)_T \frac{\mathrm{d}p}{p}. \tag{2.51}$$

Using the relations reported in Tab. 2.1, this expression can be substituted into Eq. 2.50 to obtain

$$\beta_T p\frac{\mathrm{d}p}{p} - \beta_p T\frac{\mathrm{d}T}{T} = \frac{\mathrm{d}\rho}{\rho}, \tag{2.52}$$

or, alternatively, making use of the definitions of γ_{pv} and G, one obtains

$$\frac{\gamma}{\gamma_{pv}}\frac{\mathrm{d}p}{p} - \frac{\gamma-1}{G}\frac{\mathrm{d}T}{T} = \frac{\mathrm{d}\rho}{\rho}. \tag{2.53}$$

The combination of Eq. 2.38 reported in App. 2.9 with Eqs. 2.47 and 2.11 gives

$$\frac{\mathrm{d}h}{c_p T} = \frac{\mathrm{d}T}{T} + \frac{G-(\gamma-1)}{\gamma_{pv}}\frac{G}{\gamma-1}\frac{\mathrm{d}p}{p}. \tag{2.54}$$

Manipulating the Gibbs equation, together with Eqs. 2.54 and 2.47, provides a relation for the specific entropy variation, i.e.,

$$\frac{\mathrm{d}s}{c_p} = \frac{\mathrm{d}T}{T} - \frac{G}{\gamma_{pv}}\frac{\mathrm{d}p}{p}. \tag{2.55}$$

Consider now the momentum Eq.2.17. The friction term can be rewritten as a function of the non-dimensional friction coefficient C_f and of the so-called hydraulic diameter, defined as $d_H = 4A/p_w$, where p_w is the wet perimeter. Dividing all the terms of the equation by $\rho u^2 A$ yields

$$\frac{du}{u} + \frac{p}{\rho u^2}\frac{dp}{p} = -\frac{\cancel{d}w_{shaft}}{u^2} - \frac{1}{2}4C_f\frac{dx}{d_H} + \frac{d\dot{m}}{\dot{m}}\left(\frac{u_{inj}}{u}\cos\alpha - 1\right), \tag{2.56}$$

Equations 2.48 and 2.49 can be substituted into the momentum Eq.2.56 to obtain

$$\frac{du}{u} + \frac{1}{\gamma_{pv}M^2}\frac{dp}{p} = -\frac{(\gamma-1)}{G^2M^2}\frac{\cancel{d}w_{shaft}}{c_pT} - \frac{1}{2}4C_f\frac{dx}{d_H} + \\ + \frac{d\dot{m}}{\dot{m}}\left(\frac{u_{inj}}{u}\cos\alpha - 1\right), \tag{2.57}$$

where the Mach number is used in place of the speed of sound. The energy equation (Eq. 2.18) can be manipulated to find a relation between pressure and temperature. Dividing all terms by c_pT and inserting Eqs. 2.48, 2.49 and 2.54 yields

$$\frac{dT}{T} + \frac{G-(\gamma-1)}{\gamma_{pv}}\frac{G}{\gamma-1}\frac{dp}{p} + \frac{G^2M^2}{\gamma-1}\frac{du}{u} = \\ = \frac{\cancel{d}q}{c_pT} - \frac{\cancel{d}w_{shaft}}{c_pT} + \left\{\frac{h_{inj,in}-h_{inj}}{c_pT} + \right. \\ \left. + \frac{1}{2}\frac{G^2M^2}{\gamma-1}\left[\left(\frac{u_{inj}}{u}\right)^2 - 1\right]\right\}\frac{d\dot{m}}{\dot{m}}. \tag{2.58}$$

Consider $c = c(\rho, s)$; the total differential of the speed of sound can therefore be written as

$$dc = \left(\frac{\partial c}{\partial \rho}\right)_s d\rho + \left(\frac{\partial c}{\partial s}\right)_\rho d\rho. \tag{2.59}$$

Using the definition of the fundamental derivative of gas dynamics (Eq. 2.1), the first derivative in Eq. 2.59 can be rewritten as

$$\left(\frac{\partial c}{\partial \rho}\right)_s = (\Gamma - 1)\frac{c}{\rho}. \tag{2.60}$$

The Maxwell thermodynamic relations and Eq. 2.10 can be combined to obtain a formulation for the derivative appearing as the second term of Eq. 2.59, i.e.,

$$\left(\frac{\partial c}{\partial s}\right)_\rho = \frac{1}{2c}\left(\frac{\partial c^2}{\partial s}\right)_\rho = \frac{1}{2c}\frac{\left(\partial c^2/\partial p\right)_\rho\left(\partial p/\partial T\right)_\rho}{(\partial s/\partial e)_\rho(\partial e/\partial T)_\rho} = \\ = G\frac{T}{2c}\Psi = \frac{\gamma-1}{\beta_p T}\frac{T}{2c}\Psi, \tag{2.61}$$

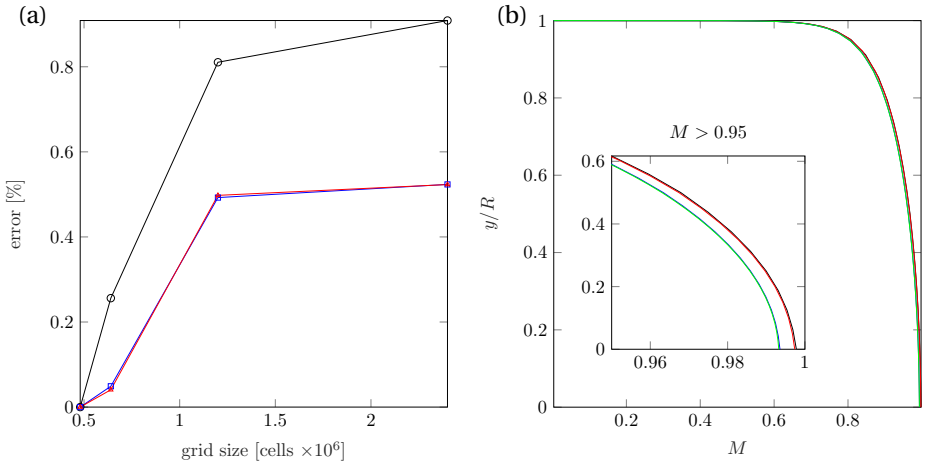

Figure 2.16: Grid independence study. (a) Relative deviation, as a function of the computational mesh size, of the values of —○— C_f, —□— M, and —△— Re_D from the ones computed using the coarsest mesh of $480k$ cells. Each variable is calculated with a mass flow average over the outlet section of the pipe. (b) Mach number at the outlet pipe section *vs* normalized radial coordinate for four different computational grids. Grid size: — 480k, — 640k — 1.2m, — 2.4m. A close-up of the Mach profile in the proximity of the pipe center line is also displayed.

where $(\partial s/\partial e)_\rho = 1/T$ according to Bridgman [71] and $(\partial e/\partial T)_\rho = c_v$. The combination of the last two relations with Eq. 2.59 yields

$$\frac{\mathrm{d}c}{c} = (\Gamma-1)\frac{\mathrm{d}\rho}{\rho} + \frac{\gamma-1}{\beta_p T}\frac{T}{2c}\Psi = (\Gamma-1)\frac{\mathrm{d}\rho}{\rho} + \beta_p T\frac{\Psi}{2}\frac{\mathrm{d}s}{c_p} = \\ = (\Gamma-1)\frac{\mathrm{d}\rho}{\rho} + \frac{\gamma-1}{G}\frac{\Psi}{2}\frac{\mathrm{d}s}{c_p}. \tag{2.62}$$

Note that the second term cancels out if the process is isentropic. Given that $M \equiv u/c$, it is also possible to relate the change of speed of sound to the change of Mach number via

$$\frac{\mathrm{d}M}{M} = \frac{\mathrm{d}u}{u} - \frac{\mathrm{d}c}{c} \tag{2.63}$$

The combination of Eqs. 2.16, 2.53, 2.54, 2.55, 2.57, 2.58, 2.62 and 2.63 provides analytical relations between each flow quantity and changes of cross-sectional area, energy transfer as heat, shaft work, wall friction, and mass flow injection. These relations are summarized in Tab. 2.2 and can be formally expressed through the synthetic formulation reported in Eq. 4.9. Neglecting the contributions due to shaft work, energy transfer as heat, wall friction, and changes of cross-section, the entropy increase of the main flow due to fluid injection in the control volume can also be retrieved. In particular, the combination of Eqs. 2.16, 2.55, 2.57 and 2.58 results in Eq. 2.33.

2.11. MESH SENSITIVITY ANALYSIS

A study of the sensitivity to the grid resolution for the CFD simulations treated in Sec. 2.4.2 was performed. Simulations of flows of siloxane MM with $T_{r,out} = 1.05$, $p_{r,out} = 1.15$ at the pipe outlet and $p_{t,r} = 1.7$ at the inlet were run for several grids with different levels of refinement. A total of four grids with 480k, 640k, 1.2 million, and 2.4 million cells were considered. Figure 2.16 shows the results of the mesh sensitivity analysis. The relative deviation of the values of both C_f, M and Re_D between the finest and the coarsest grid is < 1% for all variables, see Fig. 2.16a. Minimal differences depending on the grid density were also observed in terms of the Mach number profile at the pipe outlet (Fig. 2.16b): the largest difference is of 0.4% at the channel mid-line.

BIBLIOGRAPHY

[1] H. Nemati, A. Patel, B. J. Boersma, and R. Pecnik, "Mean statistics of a heated turbulent pipe flow at supercritical pressure", *Int. J. Heat Mass Transfer*, vol. 83, pp. 741–752, Apr. 2015, ISSN: 00179310. DOI: 10.1016/j.ijheatmasstransfer.2014.12.039.

[2] P. Colonna, E. Casati, C. Trapp, *et al.*, "Organic Rankine Cycle Power Systems: From the Concept to Current Technology, Applications, and an Outlook to the Future", en, *Journal of Engineering for Gas Turbines and Power*, vol. 137, no. 10, p. 100 801, Oct. 2015, ISSN: 0742-4795. DOI: 10.1115/1.4029884.

[3] E. Macchi and M. Astolfi, *Organic Rankine Cycle (ORC) Power Systems: Technologies and Applications* (Energy 107), en. Elsevier, 2017, ISBN: 978-0-08-100510-1.

[4] K. Brun, P. Friedman, and R. Dennis, *Fundamentals and Applications of Supercritical Carbon Dioxide (SCO2) Based Power Cycles*. Elsevier, 2017, pp. xv–xvii, ISBN: 978-0-08-100804-1. DOI: 10.1016/B978-0-08-100804-1.06001-1.

[5] C. Arpagaus, F. Bless, M. Uhlmann, J. Schiffmann, and S. S. Bertsch, "High temperature heat pumps: Market overview, state of the art, research status, refrigerants, and application potentials", *Energy*, vol. 152, pp. 985–1010, Jun. 2018, ISSN: 03605442. DOI: 10.1016/j.energy.2018.03.166.

[6] A. Giuffre' and M. Pini, "Design Guidelines for Axial Turbines Operating With Non-Ideal Compressible Flows", en, *Journal of Engineering for Gas Turbines and Power*, vol. 143, no. 1, p. 011 004, Jan. 2021, ISSN: 0742-4795, 1528-8919. DOI: 10.1115/1.4049137.

[7] S. Bahamonde, M. Pini, C. De Servi, A. Rubino, and P. Colonna, "Method for the preliminary fluid dynamic design of high-temperature mini-organic rankine cycle turbines", *J. Eng. Gas Turbines Power*, vol. 139, no. 8, pp. 082606/1–082606/14, Mar. 2017, ISSN: 0742-4795. DOI: 10.1115/1.4035841.

[8] K. Rosset, V. Mounier, E. Guenat, and J. Schiffmann, "Multi-objective optimization of turbo-ORC systems for waste heat recovery on passenger car engines", *Energy*, vol. 159, pp. 751–765, Sep. 2018, ISSN: 03605442. DOI: 10.1016/j.energy.2018.06.193.

[9] C. M. De Servi, M. Burigana, M. Pini, and P. Colonna, "Design method and performance prediction for radial-inflow turbines of high-temperature mini-organic Rankine cycle power systems", *J. Eng. Gas Turbines Power*, vol. 141, no. 9, pp. 091021/1–091021/12, Aug. 2019, ISSN: 0742-4795. DOI: 10.1115/1.4043973.

[10] A. Romei, P. Gaetani, A. Giostri, and G. Persico, "The role of turbomachinery performance in the optimization of supercritical carbon dioxide power systems", *Journal of Turbomachinery*, vol. 142, no. 7, pp. 071001/1–071001/11, Jun. 2020, ISSN: 0889-504X. DOI: 10.1115/1.4046182.

[11] N. D. Baltadjiev, C. Lettieri, and Z. S. Spakovszky, "An investigation of real gas effects in supercritical CO2 centrifugal compressors", *Journal of Turbomachinery*, vol. 137, no. 9, Sep. 2015, 091003/1–091003/13, ISSN: 0889-504X. DOI: 10.1115/1.4029616.

[12] J. Schiffmann and D. Favrat, "Design, experimental investigation and multi-objective optimization of a small-scale radial compressor for heat pump applications", *Energy*, vol. 35, no. 1, pp. 436–450, 2010, ISSN: 0360-5442. DOI: https://doi.org/10.1016/j.energy.2009.10.010.

[13] J. D. Denton, "The 1993 IGTI scholar lecture: Loss mechanisms in turbomachines", *Journal of Turbomachinery*, vol. 115, no. 4, pp. 621–656, Oct. 1993, ISSN: 0889-504X. DOI: 10.1115/1.2929299.

[14] P. A. Thompson, "A Fundamental Derivative in Gasdynamics", en, *Physics of Fluids*, vol. 14, no. 9, p. 1843, 1971, ISSN: 00319171. DOI: 10.1063/1.1693693.

[15] P. A. Thompson and K. C. Lambrakis, "Negative shock waves", *J. Fluid Mech.*, vol. 60, no. 1, pp. 187–208, Aug. 1973, ISSN: 0022-1120, 1469-7645. DOI: 10.1017/S002211207300011X.

[16] H. A. Bethe, "On the theory of shock waves for an arbitrary equation of state", in *Classic papers in shock compression science*, J. N. Johnson and R. Chéret, Eds., New York, NY: Springer New York, 1942, pp. 421–495, ISBN: 978-1-4612-2218-7. DOI: 10.1007/978-1-4612-2218-7_11.

[17] P. Colonna, A. Guardone, and N. R. Nannan, "Siloxanes: A new class of candidate Bethe-Zel'dovich-Thompson fluids", *Phys. Fluids*, vol. 19, no. 8, pp. 086102/1–086102/12, Aug. 2007, ISSN: 1070-6631, 1089-7666. DOI: 10.1063/1.2759533.

[18] A. Kluwick, Ed., *Nonlinear waves in real fluids* (Courses and lectures / International Centre for Mechanical Sciences 315). Springer, 1991, ISBN: 978-3-211-82277-7.

[19] M. S. Cramer and A. Kluwick, "On the propagation of waves exhibiting both positive and negative nonlinearity", *J. Fluid Mech.*, vol. 142, pp. 9–37, May 1984, ISSN: 0022-1120, 1469-7645. DOI: 10.1017/S0022112084000975.

[20] C. Zamfirescu, A. Guardone, and P. Colonna, "Admissibility region for rarefaction shock waves in dense gases", *J. Fluid Mech.*, vol. 599, pp. 363–381, Mar. 2008, ISSN: 0022-1120, 1469-7645. DOI: 10.1017/S0022112008000207.

[21] A. Kluwick, "Non-Ideal Compressible Fluid Dynamics: A Challenge for Theory", en, *Journal of Physics: Conference Series*, vol. 821, p. 012 001, Mar. 2017, ISSN: 1742-6588, 1742-6596. DOI: 10.1088/1742-6596/821/1/012001.

[22] A. A. Borisov, A. A. Borisov, S. S. Kutateladze, and V. E. Nakoryakov, "Rarefaction shock wave near the critical liquid–vapour point", *J. Fluid Mech.*, vol. 126, pp. 59–73, Jan. 1983, ISSN: 0022-1120, 1469-7645. DOI: 10.1017/S002211208300004X.

[23] T. Mathijssen, M. Gallo, E. Casati, *et al.*, "The flexible asymmetric shock tube (FAST): A Ludwieg tube facility for wave propagation measurements in high-temperature vapours of organic fluids", *Exp. Fluids*, vol. 56, no. 10, p. 195, Oct. 2015, ISSN: 0723-4864, 1432-1114. DOI: 10.1007/s00348-015-2060-1.

[24] T. Mathijssen, "Experimental observation of non-ideal compressible fluid dynamics: With application in organic Rankine cycle power systems", Ph.D. dissertation, Delft University of Technology, 2017.

[25] G. Cammi, A. Spinelli, F. Cozzi, and A. Guardone, "Automatic detection of oblique shocks and simple waves in Schlieren images of two-dimensional supersonic steady flows", *Measurement*, vol. 168, p. 108 260, 2021, ISSN: 0263-2241. DOI: https://doi.org/10.1016/j.measurement.2020.108260.

[26] G. Cammi, C. C. Conti, A. Spinelli, and A. Guardone, "Experimental characterization of nozzle flow expansions of siloxane mm for orc turbines applications", *Energy*, vol. 218, p. 119 249, 2021, ISSN: 0360-5442. DOI: https://doi.org/10.1016/j.energy.2020.119249.

[27] A. Kluwick and E. A. Cox, "Steady small-disturbance transonic dense gas flow past two-dimensional compression/expansion ramps", *J. Fluid Mech.*, vol. 848, pp. 756–787, Aug. 2018, ISSN: 0022-1120, 1469-7645. DOI: 10.1017/jfm.2018.368.

[28] D. Vimercati, G. Gori, and A. Guardone, "Non-ideal oblique shock waves", en, *Journal of Fluid Mechanics*, vol. 847, pp. 266–285, Jul. 2018, ISSN: 0022-1120, 1469-7645. DOI: 10.1017/jfm.2018.328.

[29] D. Vimercati, A. Kluwick, and A. Guardone, "Oblique waves in steady supersonic flows of Bethe–Zel'dovich–Thompson fluids", *J. Fluid Mech.*, vol. 855, pp. 445–468, Nov. 2018, ISSN: 0022-1120, 1469-7645. DOI: 10.1017/jfm.2018.633.

[30] A. Kluwick and E. A. Cox, "Weak shock reflection in channel flows for dense gases", *J. Fluid Mech.*, vol. 874, pp. 131–157, Sep. 2019, ISSN: 0022-1120, 1469-7645. DOI: 10.1017/jfm.2019.415.

[31] D. Vimercati, A. Kluwick, and A. Guardone, "Shock interactions in two-dimensional steady flows of Bethe–Zel'dovich–Thompson fluids", *J. Fluid Mech.*, vol. 887, Mar. 2020, ISSN: 0022-1120, 1469-7645. DOI: 10.1017/jfm.2019.1053.

[32] A. Kluwick, "Transonic nozzle flow of dense gases", *J. Fluid Mech.*, vol. 247, pp. 661–688, Feb. 1993, ISSN: 0022-1120, 1469-7645. DOI: 10.1017/S0022112093000618.

[33] M. S. Cramer and R. N. Fry, "Nozzle flows of dense gases", *Phys. Fluids A*, vol. 5, no. 5, pp. 1246–1259, May 1993, ISSN: 0899-8213. DOI: 10.1063/1.858610.

[34] A. Guardone and D. Vimercati, "Exact solutions to non-classical steady nozzle flows of Bethe–Zel'dovich–Thompson fluids", *J. Fluid Mech.*, vol. 800, pp. 278–306, Aug. 2016, ISSN: 0022-1120, 1469-7645. DOI: 10.1017/jfm.2016.392.

[35] J. D. Anderson, *Modern Compressible Flow: With Historical Perspective*, 2nd ed. McGraw-Hill, 1990, ISBN: 978-0-07-001673-6.

[36] G. H. Schnerr and P. Leidner, "Diabatic supersonic flows of dense gases", *Phys. Fluids A*, vol. 3, no. 10, pp. 2445–2458, Oct. 1991, ISSN: 0899-8213. DOI: 10.1063/1.858183.

[37] M. S. Cramer, J. F. Monaco, and B. M. Fabeny, "Fanno processes in dense gases", *Phys. Fluids*, vol. 6, no. 2, pp. 674–683, Feb. 1994, ISSN: 1070-6631, 1089-7666. DOI: 10.1063/1.868307.

[38] M. S. Cramer, "Rayleigh processes in single-phase fluids", *Phys. Fluids*, vol. 18, no. 1, pp. 016101/1–016101/15, Jan. 2006, ISSN: 1070-6631, 1089-7666. DOI: 10.1063/1.2166627.

[39] W. C. Reynolds and P. Colonna, *Thermodynamics: fundamentals and engineering applications*. Cambridge University Press, Sep. 2018, ISBN: 9780521862738. DOI: https://doi.org/10.1017/9781139050616.

[40] D. A. Kouremenos and K. A. Antonopoulos, "Isentropic exponents of real gases and application for the air at temperatures from 150 K to 450 K", *Acta Mech.*, vol. 65, no. 1-4, pp. 81–99, Jan. 1987, ISSN: 0001-5970, 1619-6937. DOI: 10.1007/BF01176874.

[41] N. Baltadjiev, "An investigation of real gas effects in supercritical CO2 compressors", Ph.D. dissertation, Massachussets Institute of Technology, Sep. 2012.

[42] V. Arp, J. M. Persichetti, and G.-B. Chen, "The Grüneisen parameter in fluids", *J. Fluids Eng.*, vol. 106, no. 2, pp. 193–200, 1984, ISSN: 00982202. DOI: 10.1115/1.3243100.

[43] P. Mausbach, A. Köster, G. Rutkai, M. Thol, and J. Vrabec, "Comparative study of the Grüneisen parameter for 28 pure fluids", *J. Chem. Phys.*, vol. 144, no. 24, pp. 244505/1–244505/11, Jun. 2016, ISSN: 0021-9606, 1089-7690. DOI: 10.1063/1.4954282.

[44] V. Arp, "Thermodynamics of single-phase one-dimensional fluid flow", *Cryogenics*, vol. 15, no. 5, pp. 285–289, May 1975, ISSN: 00112275. DOI: 10.1016/0011-2275(75)90120-4.

[45] L. R. F. Henderson, "General laws for propagation of shock waves through matter", in *Handbook of Shock Waves*, Elsevier, 2001, pp. 143–183, ISBN: 978-0-12-086430-0. DOI: 10.1016/B978-012086430-0/50004-X.

[46] P. Mausbach and H. O. May, "Direct molecular simulation of the Grüneisen parameter and density scaling exponent in fluid systems", *Fluid Phase Equilib.*, vol. 366, pp. 108–116, Mar. 2014, ISSN: 03783812. DOI: 10.1016/j.fluid.2014.01.015.

[47] R. Casalini, U. Mohanty, and C. M. Roland, "Thermodynamic interpretation of the scaling of the dynamics of supercooled liquids", *J. Chem. Phys.*, vol. 125, no. 1, pp. 014505/1–014505/9, Jul. 2006, ISSN: 0021-9606, 1089-7690. DOI: 10.1063/1.2206582.

[48] A. Guardone and B. M. Argrow, "Nonclassical gasdynamic region of selected fluorocarbons", *Phys. Fluids*, vol. 17, no. 11, pp. 116102/1–116102/17, Nov. 2005, ISSN: 1070-6631, 1089-7666. DOI: 10.1063/1.2131922.

[49] P. Colonna and A. Guardone, "Molecular interpretation of nonclassical gas dynamics of dense vapors under the van der Waals model", *Phys. Fluids*, vol. 18, no. 5, pp. 056101/1–056101/14, May 2006, ISSN: 1070-6631, 1089-7666. DOI: 10.1063/1.2196095.

[50] J. Harinck, A. Guardone, and P. Colonna, "The influence of molecular complexity on expanding flows of ideal and dense gases", *Phys. Fluids*, vol. 21, no. 8, pp. 086101/1–086101/13, Aug. 2009, ISSN: 1070-6631, 1089-7666. DOI: 10.1063/1.3194308.

[51] E. W. Lemmon, I. H. Bell, M. L. Huber, and M. O. McLinden, *NIST standard reference database 23: Reference fluid thermodynamic and transport properties-REFPROP, version 10.0, National Institute of Standards and Technology*, 2018. DOI: 10.18434/T4JS3C.

[52] C. M. Invernizzi, *Closed Power Cycles* (Lecture Notes in Energy). London: Springer London, 2013, vol. 11, ISBN: 978-1-4471-5139-5. DOI: 10.1007/978-1-4471-5140-1.

[53] A. P. S. Wheeler and J. Ong, "The Role of Dense Gas Dynamics on Organic Rankine Cycle Turbine Performance", en, *Journal of Engineering for Gas Turbines and Power*, vol. 135, no. 10, p. 102 603, Oct. 2013, ISSN: 0742-4795, 1528-8919. DOI: 10.1115/1.4024963.

[54] A. H. Shapiro, *The Dynamics and Thermodynamics of Compressible Fluid Flow*. The Ronald Press Company, 1953, vol. 1.

[55] E. M. Greitzer, C. S. Tan, and M. B. Graf, *Internal Flow: Concepts and Applications*. Cambridge University Press, 2004, ISBN: 978-0-511-61670-9. DOI: 10.1017/CBO9780511616709.

[56] A. Spinelli, G. Cammi, S. Gallarini, *et al.*, "Experimental evidence of non-ideal compressible effects in expanding flow of a high molecular complexity vapor", *Exp. Fluids*, vol. 59:126, pp. 2–16, 2018. DOI: 10.1007/s00348-018-2578-0.

[57] M. Thol, F. H. Dubberke, E. Baumhögger, J. Vrabec, and R. Span, "Speed of sound measurements and fundamental equations of state for octamethyltrisiloxane and decamethyltetrasiloxane", *Journal of Chemical & Engineering Data*, vol. 62, no. 9, pp. 2633–2648, Sep. 2017, ISSN: 0021-9568, 1520-5134. DOI: 10.1021/acs.jced.7b00092.

[58] W. M. Kirkland, "A polytropic approximation of compressible flow in pipes with friction", *J. Fluids Eng.*, vol. 141, no. 12, pp. 21404/1–21404/7, Dec. 2019, ISSN: 0098-2202, 1528-901X. DOI: 10.1115/1.4043717.

[59] P. Colonna, T. P. van der Stelt, and A. Guardone, *FluidProp (Version 3.1): A program for the estimation of thermophysical properties of fluids*, A computer program since 2004, 2019.

[60] L. Sciacovelli, P. Cinnella, and X. Gloerfelt, "Direct numerical simulations of supersonic turbulent channel flows of dense gases", *J. Fluid Mech.*, vol. 821, pp. 153–199, Jun. 2017, ISSN: 0022-1120, 1469-7645. DOI: 10.1017/jfm.2017.237.

[61] R. Dean, "Reynolds number dependence of skin friction and other flow variables in two-dimensional rectangular duct flow", *J. Fluids Eng.*, vol. 100 (2), pp. 215–223, Jun. 1978. DOI: 10.1115/1.3448633.

[62] M. Pini and C. De Servi, "Entropy generation in laminar boundary layers of non-ideal fluid flows", *Non-Ideal Compressible Fluid Dynamics for Propulsion and Power: Lecture Notes in Mechanical Engineering*, F. di Mare, A. Spinelli, and M. Pini, Eds., pp. 104–117, 2020. DOI: 10.1007/978-3-030-49626-5_8.

[63] C. F. Colebrook and C. M. White, "Experiments with fluid friction in roughened pipes", *Proceedings of the Royal Society*, pp. 1–15, Aug. 1937. DOI: https://doi.org/10.1098/rspa.1937.0150.

[64] P. Spalart and S. Allmaras, "A one-equation turbulence model for aerodynamic flows", in *30th Aerospace Sciences Meeting and Exhibit*, Reno, NV, U.S.A.: American Institute of Aeronautics and Astronautics, Jan. 1992. DOI: 10.2514/6.1992-439.

[65] G. J. Otero R., A. Patel, R. Diez S., and R. Pecnik, "Turbulence modelling for flows with strong variations in thermo-physical properties", *Int. J. Heat Fluid Flow*, vol. 73, pp. 114–123, Oct. 2018, ISSN: 0142727X. DOI: 10.1016/j.ijheatfluidflow.2018.07.005.

[66] L. Sciacovelli, P. Cinnella, and X. Gloerfelt, "A priori tests of RANS models for turbulent channel flows of a dense gas", *Flow Turbul. Combust.*, vol. 101, no. 2, pp. 295–315, Sep. 2018, ISSN: 1386-6184, 1573-1987. DOI: 10.1007/s10494-018-9938-y.

[67] I. Ansys, *Ansys CFX release 19.1*, Canonsburg, PA, 2019.

[68] T. Chen, B. Yang, M. Robertson, and R. Martinez-Botas, "Direct numerical simulation of real-gas effects within turbulent boundary layers for fully-developed channel flows", in *Proceedings of Global Power and Propulsion Society GPPS - Chania20*, 2020, pp. 0068/1–0068/12.

[69] C. Crane, "Flow of fluids through valves, fittings and pipe", New York, Tech. Rep. 410, 1982.

[70] J. B. Young and R. C. Wilcock, "Modeling the air-cooled gas turbine: Part 1—General thermodynamics", *Journal of Turbomachinery*, vol. 124, no. 2, pp. 207–213, 2002, ISSN: 0889504X. DOI: 10.1115/1.1415037.

[71] P. W. Bridgman, "A complete collection of thermodynamic formulas", *Phys. Rev.*, vol. 3, no. 4, pp. 273–281, Apr. 1914, ISSN: 0031-899X. DOI: 10.1103/PhysRev.3.273.

3

INVESTIGATION OF NON-IDEAL EFFECTS IN COMPRESSIBLE BOUNDARY LAYERS OF DENSE VAPORS

Part of the content of this chapter appeared in:
F. Tosto, A. Wheeler and M. Pini, *Investigation of Non-Ideal Effects in Compressible Boundary Layers of Dense Vapors*, Physics of Fluids, 2023 (TO BE SUBMITTED).

In this work, we present an investigation about the sources of dissipation in adiabatic boundary layers of non-ideal compressible fluid flows. Direct numerical simulations (DNS) of transitional, zero-pressure gradient boundary layer flows are performed for two fluids characterized by different complexity of the fluid molecules, namely air and siloxane MM. Different sets of thermodynamic free stream boundary conditions are selected to evaluate the influence of the fluid state on both the frictional loss and the dissipation mechanisms. The thermophysical properties of siloxane MM are calculated with a state-of-the-art equation of state. Results show that the dissipation due to both time-mean strain field, irreversible heat transfer, and turbulent dissipation differ significantly depending on both the molecular complexity of the fluid and its thermodynamic state. The dissipation coefficient calculated from the DNS results is then compared against the one obtained using a reduced-order model (ROM) which solves the two-dimensional boundary layer flow equations for an arbitrary fluid [1]. Results from both the DNS and the ROM show that low values of the overall dissipation are observed in the case of fluids made of simple molecules, e.g., air, and if the fluid is at a thermodynamic state in the proximity of that of the vapor-liquid critical point.

3.1. INTRODUCTION

The irreversible entropy generation due to viscous processes in boundary layers is one of the loss mechanisms mainly affecting the performance of internal flow devices such as turbomachines or heat exchangers. With regards to turbomachinery, viscous dissipation in boundary layers may account for up to one-sixth of the total loss in a turbine [2]. The share increases in compressors, where the flow becomes more prone to separation due to adverse pressure gradients. Fluid flow characteristics strongly affect the viscous dissipation, which depends on the Reynolds and Mach number of the free stream, the regime of the boundary layer, i.e., laminar or turbulent, and the fluid thermo-physical properties.

The overall dissipation within a boundary layer flow can be estimated with the rate of entropy change in the streamwise direction, which is proportional to the cube of the free-stream velocity and to the dissipation coefficient, C_d. C_d is particularly convenient as a parameter for the characterization of dissipation in boundary layer flows. Unlike the skin friction coefficient C_f, C_d shows a weak dependence on the boundary layer shape factor, which defines the ratio between displacement and momentum thicknesses, i.e., $H = \delta^*/\theta$. Therefore, it better characterizes the amount of dissipation occurring across the shear layer. Moreover, as pointed out by Denton [2] and Schlichting [3], the dissipation coefficient is almost insensitive to the streamwise pressure gradient in turbulent boundary layers. As a consequence, the zero pressure gradient boundary layer flow represents a meaningful test case for studying dissipation mechanisms. Furthermore, its value strongly depends on the boundary layer regime, i.e., laminar or turbulent. In the turbulent regime, turbulence dissipation also contributes to the overall rate of entropy generation, while in laminar flows the dissipation is solely due to the strain field of the mean flow and the irreversible entropy generation due to heat transfer between the fluid particles. Analytical solutions and correlations for the skin friction coefficient and the dissipation coefficient in zero-pressure gradient incompressible boundary layer flows are well established in literature [3]. Both coefficients solely depend on the local Reynolds number, defined as a function of either the x-coordinate or the momentum thickness θ, respectively. Corrections based on the value of the Chapman-Rubesin parameter $CR = \rho\mu/(\rho_e\mu_e)$ [4] or the shape factor [5] are also available for the compressible flow case.

Despite the many research studies on dissipation in boundary layer flows, little knowledge has been developed on how both the complexity of the molecular structure of the fluid and the fluid thermodynamic state influence the viscous dissipation and the loss breakdown across the shear layer. Such knowledge is paramount to properly quantifying losses in internal flow devices operating with organic compounds in the supercritical or dense vapor state, like turbomachinery and heat exchangers of organic Rankine cycle turbogenerators [6], supercritical carbon dioxide (sCO_2) power systems [7], absorption chillers [8], and heat pumps [9], [10]. Gaining physical insights into the dissipation mechanisms occurring in nonideal compressible flows is instrumental, for instance, to developing physical models that can be used for the optimal preliminary design of turbines and compressors.

In flow processes occurring in thermodynamic states in which the fluid is a dense vapor, a supercritical fluid, or a compressible liquid, the fluid thermo-physical proper-

ties can exhibit large variations that, in turn, affect the flow evolution, the turbulence dynamics, and, consequently, the viscous dissipation. The gas dynamics of dense vapor flows is governed by the so-called fundamental derivative of gas dynamics [11], defined as

$$\Gamma \equiv 1 + \frac{\rho}{c}\left(\frac{\partial c}{\partial \rho}\right)_s, \tag{3.1}$$

where ρ is the density, c the speed of sound, and s the entropy. Kluwick [12] firstly investigated the physics of the unperturbed zero-pressure gradient laminar boundary layer flow of dense vapors. His analysis showed that, for a fluid characterized by a high complexity of the molecular structure, the Eckert number is much lower than unity, i.e., $Ec << 1$. For such fluids, no large gradients in temperature can thus be observed across the boundary layer. As a consequence, the thermodynamic and the kinematic fields are decoupled and compressible flow effects become less relevant than in wall-bounded flows of perfect gases. Similar findings were obtained by Cramer *et al* [13], who examined the validity of classical scaling laws for the skin friction coefficient in zero-pressure gradient laminar boundary layers for a range of fluids and thermodynamic states, and by de Servi and Pini [14], who investigated the dissipation coefficient C_d in zero-pressure gradient laminar boundary layer flows of various fluids. According to their results, for fluids made of large molecules, the values of both the skin friction and the dissipation coefficients approach those characterizing incompressible air flows. Sciacovelli *et al* conducted direct numerical simulations of channel [15] and flat plate [16] flows of perfluoro-perhydrophenanthrene PP11 at $M_\mathrm{e} > 2$. They found that quantities such as the skin friction coefficient and the Nusselt number are weakly affected by compressibility effects, as the state of the dense vapor boundary layer is almost insensitive to friction heating. However, simulations were performed in thermodynamic and fluid dynamic conditions which depart from those pertaining to paradigmatic flow processes in process and energy applications (for instance, those characterizing compression or expansion processes in gas turbines or ORC power systems).

The objective of this work is an investigation on the sources of dissipation in the adiabatic, zero-pressure gradient boundary layer flow of fluids in the dense vapor state. Direct numerical simulations of transitional, zero-pressure gradient boundary layer flows are performed using an in-house solver. Two fluids characterized by different levels of molecular complexity are considered, namely air and hexamethyldisiloxane (MM). Different sets of free-stream thermodynamic conditions are chosen to evaluate the influence of the fluid state on both the frictional loss and the dissipation mechanisms. State-of-the-art equations of state models [17] implemented in a well-known program [18] are used to estimate the thermo-physical properties of siloxane MM. Results are compared against those obtained with a reduced-order model (ROM) [14] which solves the boundary layer equations in transformed coordinates for arbitrary fluids. The ROM is then used to perform a comprehensive study on the influence of the fluid, the thermodynamic state, and the compressibility on the dissipation of several compounds of engineering interest.

This paper is structured as follows. In Sec. 3.2, the approach to evaluating the dissipation in a fully-resolved turbulent boundary layer is discussed. The Falkner-Skan transformed boundary layer equations used to develop the reduced-order model are also

documented, as well as the analytical relation for the estimation of the dissipation coefficient. Section 3.3 describes the methodology used to set up and run both the DNS and the ROM calculations. In this section, the test cases investigated in this study are also listed and discussed. In Sec 3.4, the results of the study are treated. Finally, Sec. 4.4 lists the main conclusions of the work.

3.2. THEORETICAL BACKGROUND

3.2.1. DISSIPATION IN TURBULENT BOUNDARY LAYER FLOWS

One way of gaining physical insights into the dissipation occurring within a turbulent boundary layer flow is to i) numerically resolve the small scales of the turbulent structures by performing direct numerical simulations (DNS), ii) average the pertinent flow variables over a time span long enough to ensure that the flow is statistically stationary, and iii) evaluate the contribution of each loss source. According to Hughes and Brighton [19], losses can be estimated by accounting for the rise of entropy due to irreversible processes. Considering a control volume embedding the whole turbulent boundary layer within two given streamwise locations, the rate of entropy change is calculated as

$$\frac{\partial}{\partial t}\int_V \rho s \mathrm{d}V = \int_V \frac{(\tau\cdot\nabla)\mathbf{V}}{T}\mathrm{d}V - \int_S \rho s \mathbf{V}\cdot\mathrm{d}\mathbf{S} - \int_S \frac{\mathbf{q}}{T}\mathrm{d}\mathbf{S} + \int_V \frac{\mathbf{q}\cdot\mathbf{q}}{kT^2}\mathrm{d}V, \tag{3.2}$$

where V and S denote the control volume and the surfaces at its boundaries, respectively, ρ the density, s the entropy per unit mass, $\mathbf{V}$ the velocity, T the temperature, $\mathbf{q}$ the energy transfer as heat, and k the thermal conductivity of the fluid. By integrating Eq. 3.2 over a time span large enough to obtain statistically stationary flow, one obtains [20]

$$\int_V \overline{\theta}\mathrm{d}V = \int_S \overline{\rho s\mathbf{V}}\cdot\mathrm{d}\mathbf{S} + \int_S \overline{\left(\frac{\mathbf{q}}{T}\right)}\cdot\mathrm{d}\mathbf{S}, \tag{3.3}$$

where the overline denotes time-averaged quantities. The two terms on the right-hand side describe the time-averaged fluxes of entropy and the reversible entropy generation due to heat transfer across the control volume surfaces, respectively. The overall dissipation is $\overline{\theta}$, which can be rewritten as

$$\overline{\theta} = \overline{\frac{\Phi}{T} + \frac{\epsilon}{T} + \frac{\zeta}{T}}. \tag{3.4}$$

The first two terms on the right-hand side, i.e., $\overline{\Phi/T + \epsilon/T}$, account for the viscous dissipation, which can be further split into contributions due to the time-mean strain field, $\overline{\Phi/T}$, and the unsteady effects, i.e., the turbulent kinetic energy dissipation, $\overline{\epsilon/T}$. The third term on the right-hand side, $\overline{\zeta/T}$, is the contribution to the irreversible entropy generation due to heat transfer between the fluid molecules.

3.2.2. LOSS BREAKDOWN AND DISSIPATION COEFFICIENT VIA NUMERICAL COMPUTATIONS

DIRECT NUMERICAL SIMULATIONS

The procedure to calculate the three loss contributions to the overall dissipation using the results obtained from a DNS is exemplified in the following. The time-dependent

dissipation term, i.e., the sum $\Phi/T+\epsilon/T$, and the irreversible heat transfer term, ζ/T, are calculated at each simulation time step. During the post-process, the time average of these terms, i.e., $\overline{\Phi/T+\epsilon/T}$ and $\overline{\zeta/T}$, can be computed knowing the time span of the simulation. From the Favre-averaged flow field, it is also possible to calculate the contribution due to the time-mean strain, $\overline{\Phi/T}$, which can then be subtracted from $\overline{\Phi/T+\epsilon/T}$ to obtain the contribution due to turbulent dissipation, $\overline{\epsilon/T}$. Alternatively, for a boundary layer in equilibrium, the integral of $\overline{\Phi/T}$ across the boundary layer thickness at a given streamwise location can be obtained by subtracting the integral of $\overline{\zeta/T}$ across the boundary layer thickness and the time-averaged turbulence production $\overline{P}$, defined as

$$\overline{P}=-\frac{1}{\rho_e u_e^3}\int_0^\delta \overline{\rho u_i u_j}\frac{\partial u_i}{\partial x_j}\mathrm{d}y, \tag{3.5}$$

from the entropy flux, calculated using the first term on the right-hand side of Eq. 3.3. In Eq. , the subscript e denotes the free stream quantities. For an equilibrium boundary layer, the production term $\overline{P}$ is equal to the turbulence dissipation, $\overline{\epsilon}$. The approach just described is used in this study because the integration of the turbulence production is less sensitive to mesh size than that of $\overline{\epsilon/T}$.

The turbulence production is also used to compute the dissipation coefficient that, for a compressible flow case, can be written as

$$C_d=\overline{P}+\frac{1}{\rho_e u_e^3}\int_0^\delta \mu\left(\frac{\partial u_i}{\partial x_j}\right)^2\mathrm{d}y, \tag{3.6}$$

where the first term is the contribution to the dissipation due to the turbulent production, which is equal to the turbulent dissipation in equilibrium boundary layers, while the second one is the contribution due to the time-mean strain field. The dissipation coefficient here defined takes into account the dissipation of mechanical energy of the mean flow rather than that of the total mechanical energy, in agreement with the approach used to compute dissipation coefficients with conventional Reynolds-averaged Navier–Stokes solvers.

3.2.3. REDUCED-ORDER MODELLING

Assuming a two-dimensional and stationary, turbulent flow, the resulting set of boundary layer flow equations can be solved numerically via reduced-order modelling.

Using Cebeci's approach [21], [22], the boundary layer equations can be transformed in a third-order partial-differential system of equations by using the so-called *compressible Falkner-Skan transformation.* To obtain the transformed equations, the coordinate transformation $(x,y)\rightarrow(x,\eta)$ is introduced, as well as the stream function ψ. Such scaling quantities are defined as

$$\eta=\sqrt{\frac{V_e}{\mu_e\rho_e x}}\int\rho\mathrm{d}y, \tag{3.7}$$

$$\psi(x,y)=\sqrt{\rho_e\mu_e V_e x}\,f(x,\eta), \tag{3.8}$$

where V denotes the magnitude of the velocity vector of the Cartesian components u and v and the subscript e the free stream conditions. Identifying with the superscript

$'$ the derivative with respect to η, the resulting momentum and energy equations for a two-dimensional steady-state boundary layer flow read, respectively,

$$(bf'')' + m_1 f f'' + m_2 \left[c - (f')^2\right] = x\left(f'\frac{\partial f'}{\partial x} - f''\frac{\partial f}{\partial x}\right), \tag{3.9}$$

$$(eg' + df'f'')' + m_1 f g' = x\left(f'\frac{\partial g}{\partial x} - g'\frac{\partial f}{\partial x}\right), \tag{3.10}$$

with

$$f'' = \tilde{v}, \tag{3.11}$$

$$f' = \tilde{u}, \tag{3.12}$$

$$g' = \tilde{p}. \tag{3.13}$$

where $\tilde{u} = u/u_e$, $g = h_t/h_{t,e}$. $\tilde{v}$ and $\tilde{p}$ denote the derivatives of f' and g, respectively. Appendix 3.7 reports the definition of all the coefficients in Eqs. 3.9-3.10. The system of equations is valid for both laminar and turbulent regimes, but in the case of turbulent flow, it requires the definition of an eddy viscosity model. For laminar boundary layer flows, the solution $f(x,\eta)$ is self-similar; therefore, the terms on the right-hand side of Eqs. 3.9-3.10 are equal to zero. This is not the case for turbulent flows, because both the eddy viscosity ν_T and the turbulent Prandtl number Pr_T vary with the Reynolds number. For an adiabatic zero-pressure gradient boundary layer, i.e., $m_1 = m_2 = 0$, the boundary conditions in transformed variables read

$$f = 0, \qquad f' = 0 \qquad g' = 0 \qquad \text{at } \eta = 0, \tag{3.14}$$

$$f' = 1, \qquad g = 1 \qquad \text{at } \eta = \eta_e, \tag{3.15}$$

which implies that, at the wall, there is no mass transfer across the surface, the no slip-condition is ensured, i.e., $u(y=0) = 0$, and no energy is transferred from the wall to the fluid. At the boundary layer edge, instead, the speed and the total enthalpy values are equal to those of the free stream. The main advantage of using the Falkner-Skan coordinate transformation is that the velocity profiles weakly depend on the value of the free-stream Mach number. Therefore, the growth of the boundary-layer thickness along the x coordinate is limited, and, from a computational perspective, a numerical solver would only require small adaptations of the mesh across the wall-normal direction. Moreover, the dependence of the solution on the x coordinate vanishes for the laminar regime, although it still affects the solution for the turbulent regime.

It is also possible to compute the overall dissipation in the boundary layer using transformed coordinates. The rate of entropy generation is computed by integrating the local entropy generation across the boundary layer thickness [2], and reads

$$\dot{S} = \int_0^\delta \frac{\tau_{xy}}{T}\frac{\partial u_x}{\partial y}\mathrm{d}y = \frac{1}{\sqrt{Re_x}}\int_0^{\eta_e} CR\frac{T_e}{T}\tilde{v}^2\mathrm{d}\eta, \tag{3.16}$$

where τ_{xy} denotes the local shear stress. For turbulent flows, both τ_{xy} and CR include the contribution of the eddy viscosity, whose value has to be estimated by means of a turbulence model. $\dot{S}$ can then be normalized to obtain the dissipation coefficient, defined

Table 3.1: Characteristic fluid properties of air, carbon dioxide, and siloxane MM. γ_∞ is the specific heat ratio calculated in the dilute gas state. The lower and upper bound of γ_{pv} are those occurring in the thermodynamic region defined by $s > 1.01 s_{cr}$ and by the thermal stability limits of each molecule.

	M_{mol} [kg/kmol]	T_{cr} [K]	p_{cr} [bar]	γ_∞	Γ_∞
air	28.96	132.82	38.50	1.40	1.20
CO_2	44.01	304.13	73.77	1.29	1.13
isobutane	58.12	407.81	36.29	1.08	1.04
toluene	92.14	591.75	41.26	1.05	1.02
MM	162.3	518.70	19.31	1.03	1.01

Table 3.2: Test cases evaluated in this study. Free-stream conditions and grid resolution parameters are reported. For all cases, the free stream Mach number is set to 0.95.

	fluid	$p_{r,e}$	$T_{r,e}$	Z_e	Ec_e	L_x [m]	H
air	air ideal gas	0.0264	2.182	1	$1.1 \cdot 10^{-3}$	0.023	1.84
iMM	siloxane MM	0.1	1	0.96	$1.5 \cdot 10^{-4}$	$5 \cdot 10^{-3}$	1.45
niMM	siloxane MM	1.15	1.05	0.54	$6.8 \cdot 10^{-5}$	$4.42 \cdot 10^{-4}$	1.49
	fluid	x^+	$y^+_{1^{st}}$	$y^+_{10^{th}}$	z^+	$n_i \times n_j \times n_k$	
air	air ideal gas	9.06	0.88	9.85	9.06	$2500 \times 800 \times 250$	
iMM	siloxane MM	9.13	0.88	9.85	9.13	$2500 \times 800 \times 250$	
niMM	siloxane MM	8.82	0.88	9.85	8.82	$2500 \times 800 \times 250$	

as

$$C_d = \frac{T_e \dot{S}}{\frac{1}{2}\rho_e V_e^3}. \tag{3.17}$$

C_d depends on several boundary layer quantities, in accordance to the relation

$$C_d = f(Re_\theta, M_e, H, Z_e, \gamma_{pv,e}, G_\infty) \tag{3.18}$$

where H is the shape factor, Re_θ is the Reynolds number based on the momentum thickness θ, and G_∞ the Grüneisen parameter at $v \to \infty$, which measures the molecular complexity of the fluid: the lower the value of G_∞, the higher the fluid molecular complexity [23]. The value of the compressibility factor $Z_e = p_e v_e/(RT_e)$ and that of the generalized isentropic exponent $\gamma_{pv,e}$ [24], [25] in the free stream set the thermodynamic state of the fluid. Alternatively, reduced state variables $p_{r,e}$ and $T_{r,e}$ can be used for the same purpose.

3.3. METHODOLOGY

3.3.1. DNS SETUP

To accurately evaluate the loss breakdown of a boundary layer flow, direct numerical simulations of zero-pressure gradient boundary layer flows of air and siloxane MM were performed. Table 3.1 lists the main properties of both fluids, together with those of other fluids whose related investigation is reported in Sec. 3.4.2. The simulations were performed using *3DNS* [20], a multiblock structured compressible Navier–Stokes solver for

Table 3.3: Grid resolution normalized with the Kolmogorov length scale for the cases listed in Tab. 3.2. The resolution is evaluated at the wall (subscript w) and at the boundary layer edge (subscript e).

	$(\Delta x/\eta)_w$	$(\Delta y/\eta)_w$	$(\Delta z/\eta)_w$	$(\Delta x/\eta)_\delta$	$(\Delta y/\eta)_\delta$	$(\Delta z/\eta)_\delta$
air	7.5	0.7	0.7	1.1	0.4	0.1
iMM	25.3	1.5	1.7	2.4	0.4	0.2
niMM	37.7	3	3.3	3.2	0.7	0.3

high-performance computations. The code can handle multi-block computations, with parallelization of the computational resources within each block. Spatial discretization is achieved with a fourth-order dispersion relation preserving (DRP) finite difference central scheme [26] coupled with an eighth-order standard filter. Explicit time stepping is implemented with a four-stage fractional step Runge–Kutta method. Additionally, skew-symmetric splitting is used to stabilize the convective terms. Characteristic boundary conditions as described in Poinsot and Lele [27] are used to minimize the effect of reflecting pressure waves. The accuracy of the numerical model with respect to loss prediction has been assessed and is documented in previous works [20], [28], [29].

Three different high-fidelity numerical simulations have been run. Table 3.2 lists the free stream conditions and the values of grid quality parameters for each test case. The values of the Eckert number in the free stream, defined as

$$Ec_e = \frac{V_e}{c_{p,e} T_e} \tag{3.19}$$

where c_p is the specific heat at constant pressure, are also reported. All simulations have been performed by imposing a free-stream Mach number of 0.95. The first case is a simulation of the boundary layer flow of air modeled as an ideal gas at standard conditions, i.e., $T_e = 288$ K and $p_e = 1$ bar. The *iMM* and *niMM* cases, instead, refer to simulations of siloxane MM flows whereby the free stream state is in dilute gas conditions and in dense vapor conditions, respectively. The thermodynamic and transport properties of siloxane MM are calculated using entropy-based functional forms, which are explicit in density and internal energy, for both the equation of state and the constitutive law. This equation has been developed by fitting the values of compressibility factor, viscosity and thermal conductivity obtained from accurate thermo-physical models [17] onto polynomial surfaces, according to the methodology described by Wheeler in Ref. [30].

Figure 3.1 shows the computational grid used for the air case. The number of grid points in each direction, as well as the corresponding values of x^+, y^+ at the first cell in the wall proximity, and z^+ are reported in Tab. 3.2. According to the guidelines reported by Poggie *et al.* [31], i.e., $10 \leq x^+ \leq 20$ and $5 \leq z^+ \leq 10$, the simulations performed in this study can be classified as DNS. Table 3.3 lists the characteristic cell lengths along x, y, and z in relation to the Kolmogorov length scale, defined as $\eta = [\bar{\mu}/(\bar{\rho}^3 \bar{\epsilon})]^{0.25}$. Both the values calculated in the wall proximity and of the boundary layer edge are listed in the table. As already pointed out by Sciacovelli *et al* [15], [16], due to the inherently large density and Reynolds number characterizing the flows of organic compounds, mesh resolution requirements are stricter than those needed to accurately simulate turbulent air flows. The characteristic cell length is much larger than the Kolmogorov length scale for

the *iMM* and *niMM* cases. The largest values are those related to the *niMM* case, due to the larger density of the fluid. The plate length is defined to ensure $Re_L = 5 \cdot 10^5$ at the outlet for all cases, where L is the plate length. To limit the amount of blockage and to ensure spanwise de-correlation, i.e., to allow all the turbulent structures to develop within the domain, the corresponding channel height and width are defined as 20% and 10% of the plate length, respectively. The prescribed height of the domain ensures that the influence of the blockage caused by the upper free-slip surface on the flow is negligible: the measured values of Clauser's beta parameter [32], defined as

$$\beta_{\mathrm{Cl}} = \frac{\delta^*}{\tau_{\mathrm{w}}} \frac{\mathrm{d}p}{\mathrm{d}x}, \tag{3.20}$$

are within the $-0.1 < \beta_{\mathrm{Cl}} < 0$ range for all the investigated cases. Therefore, the mildly favourable pressure gradient induced by the presence of an upper wall has a negligible effect on the boundary layer flow. Stagnation temperature and pressure boundary conditions are prescribed at the inlet, static pressure is instead prescribed at the outlet. No-slip adiabatic wall conditions are imposed at the wall. The upper surface is modelled as a free-slip wall, while periodic boundary conditions are imposed on the two side surfaces along the spanwise direction. To avoid numerical instability at the leading edge, a laminar self-similar profile of velocity and static enthalpy computed using the Blasius solution at $Re_x = 10^5$ is imposed at the inlet. The CFL number is one. No sub-scale modelling for the turbulence is applied.

To initialize the turbulent simulations, laminar two-dimensional computations using the boundary conditions listed in Tab. 3.2 were first performed. Then, three-dimensional laminar simulations were performed for the first 10,000 time steps, the two-dimensional solution being used to initialize the computation. After 10,000 time steps, transition to turbulence is promoted by introducing a body-force trip at a location x such that $Re_x = 2 \cdot 10^5$. A forcing term consisting of a square wave across the plate width, i.e., along the z-direction, is introduced in the momentum equation, i.e.,

$$\rho u_i = \rho u_i \left[1 - f_k(z) f(x,y)\right], \tag{3.21}$$

where k is the node index along the z direction. The forcing terms $f_k(z)$ and $f(x,y)$ are defined as

$$f(x,y) = e^{-S\left[(x-x_{\mathrm{trip}})^2 + (y-y_{\mathrm{trip}})^2\right]}, \tag{3.22}$$

$$f_k(z) = \begin{cases} 1 & \text{if } \mathrm{mod}(k,12) < 6 \\ 0 & \text{if } \mathrm{mod}(k,12) \geq 6. \end{cases} \tag{3.23}$$

The forcing scale S is set equal to the local boundary layer thickness at the trip streamwise location. To enhance computational robustness, the trip is set to linearly grow from an amplitude of 0 to its maximum amplitude within 1000 iterations.

Statistical averages are performed over the span-wise direction and over at least two convective time units based on the free-stream velocity and the axial chord. During the simulations, time-mean flow field and turbulence quantities are calculated using a Favre (density-weighted) time-averaging technique. The DNS simulations have been run on the Dutch national supercomputer Snellius [33]. Each simulation, consisting of 500 million grid points, has been run on 30 nodes, each of them consisting of 128 AMD Rome

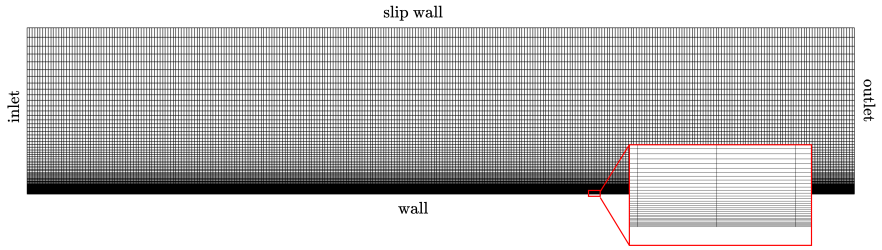

Figure 3.1: Computational domain used to simulate the air case. To better visualize the mesh structure, only one every 8 grid line is shown along both the x and y coordinates is shown. A detail of the near-wall grid is also displayed.

7H12 processors with a CPU speed of 2.6 GHz and 256 GiB memory per node. On average, each simulation has consumed 250 million core hours to run ~ 400k time steps.

3.3.2. REDUCED-ORDER MODEL SETUP

The in-house boundary-layer Matlab code *BLnI*, in which the system of PDE described in Sec. 3.2.3 is discretized and numerically solved, is used to estimate the viscous dissipation in boundary layer flows of several compounds. The system of equations is solved numerically with the Keller-Box method [21]. First, the differential equations are converted into an equivalent first-order system of equations. The derivatives are then approximated using a centred finite difference scheme over a rectangular and nonuniform grid discretized in the $x-\eta$ plane. Newton's method is used to solve the resulting algebraic system of equations. The numerical scheme is unconditionally stable and is second-order accurate. Thermo-physical fluid properties are estimated using a well-known program [18]. Turbulent calculations are performed using the Cebeci-Smith turbulence model, where the eddy viscosity is modelled as a function of the velocity field, the density ratio $c = \rho_e/\rho$, the Chapman-Rubesin parameter $CR = (\rho V)/(\rho_e V_e)$ and the local Reynolds-number Re_x. Appendix 3.8 lists all the equations defining the Cebeci-Smith eddy viscosity and eddy conductivity models.

The same cases reported in Tab.3.2 were computed with *BLnI* to verify the results by comparison with those obtained with DNS. Likewise, for the DNS, the transition is triggered at a streamwise location such that $Re_x = 2 \cdot 10^5$. The plate length over which the flow is in the turbulent regime also matches that of the high-fidelity numerical simulations.

In addition, to gain further insight into the influence of the fluid and nonideal thermodynamic effects on viscous dissipation, a systematic study was carried out. A second set of calculations was run for the fluids listed in Tab. 3.1. For each fluid, several simulations using the boundary conditions listed in Tab. 3.4 were run. Each pair of reduced temperature and pressure values fixes the free stream thermodynamic state and, in turn, the values of the compressibility factor Z_e and of the isentropic exponent $\gamma_{pv,e}$. For each pair of $T_{r,e}$ and $p_{r,e}$, 10 simulations at increasing values of the free stream Mach number ranging between 0 and 1.8 were performed. The plate length was adapted to achieve $Re_L = 10^6$ for all simulations. The domain was discretized with a grid consisting of 150

Table 3.4: Boundary conditions for the second set of simulations conducted with *BLnI*

	$T_{r,e}$	$p_{r,e}$	M_e	$\gamma_{pv,e}$
$Z_e \sim 1$	1	0.1	0.01-1.8	0.99
$Z_e \sim 0.5$	1.05	1.15	0.01-1.8	0.60
$Z_e \sim 0.25$	1.01	1.1	0.01-1.8	1.40

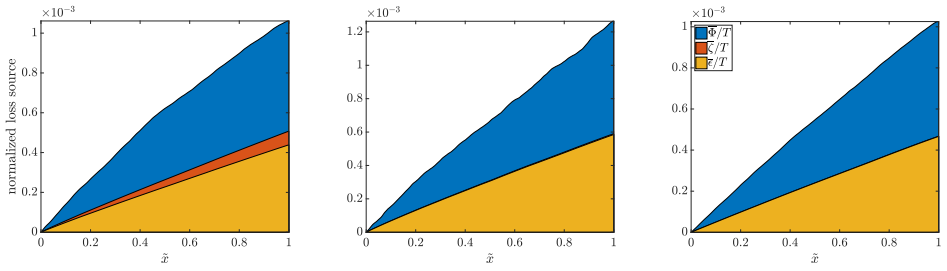

(a) (b) (c)

Figure 3.2: Dissipation breakdown along the flat plate for the cases (a) *air*, (b) *iMM* and (c) *niMM*. The integration of each contribution is performed from $\tilde{x} = 0$ to $\tilde{x} = 1$, where $\tilde{x} = (x - x_{tr})/(L - x_{tr})$. Each loss is normalized by $\rho_e V_e^3 L/T_e$.

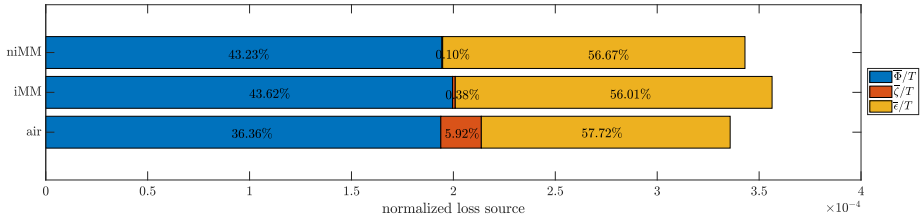

Figure 3.3: Dissipation breakdown evaluated at a streamwise location corresponding to $Re_\theta \simeq 800$ for the cases listed in Tab. 3.2. Percentages for each dissipation source are also reported.

points in the streamwise direction and 100 in the wall-normal direction. The first grid spacing in the normal-to-wall direction was set to 0.00001 m, with a grid expansion factor of 1.02. These values were proven to ensure grid-independent results. The solver calculates the boundary layer flow variables at each streamwise location, from inlet to outlet. If needed, the mesh size along the wall-normal η direction is automatically adapted to account for the growth of the boundary layer. Adiabatic conditions are imposed on the wall.

3.4. RESULTS

3.4.1. DISSIPATION ANALYSIS BY MEANS OF DNS

Figure 3.2 shows the results of the loss breakdown analysis based on the approach described in Sec. 3.2.1 for the cases listed in Tab. 3.2. To avoid non-physical results due

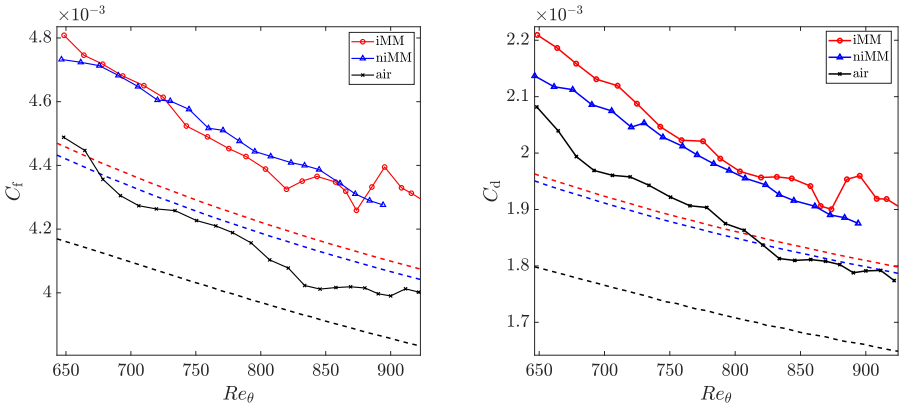

Figure 3.4: (a) Skin friction coefficient *vs* Re_θ and (b) dissipation coefficient *vs* Re_θ for all the cases of Tab. 3.2. Results from DNS and turbulent simulations conducted with *BLnI* are plotted in solid and dashed lines, respectively.

to the presence of the transition trip, the entropy fluxes (Eq. 3.3), the overall turbulence production $\overline{P}$ (Eq. 3.2.2), and the values of both the dissipation due to time-mean strain field $\overline{\Phi/T}$ and irreversible heat transfer $\overline{\zeta/T}$ (Eq. 3.4) have been computed by integrating over a control volume encompassing the equilibrium region up to the streamwise location x which is considered for the loss breakdown evaluation. For all the cases, the inlet boundary of the control volume is located after the transition point at $x/L \sim 0.35$ ($Re_\theta \sim 500$ at this location). The values of the shape factor H in the equilibrium region are nearly constant for all the cases under investigation,i.e., the flow is in equilibrium: Table 3.2 lists their values. Fig. 3.3 shows the loss breakdown at a streamwise location corresponding to $Re_\theta \simeq 850$ to better appreciate the quantitative differences among the three cases. The percentage of the contribution of each loss source in relation to the total dissipation is also reported.

Overall, the *iMM* and *niMM* cases are characterized by a larger total dissipation at fixed Re_θ than the *air* case. Moreover, the boundary layer flow of siloxane MM at $Z_e \sim 1$ is more dissipative than that of the same fluid in thermodynamic conditions for which $Z_e \sim 0.5$. Concerning the breakdown of each loss source, the contribution of the turbulence dissipation is quantitatively similar for all three cases, the *iMM* case featuring the lowest share ($\sim 56\%$). The contribution due to irreversible heat transfer is negligible in the *iMM* and *niMM* cases. In the *air* case, such a contribution becomes relevant ($\sim 6\%$) and the one due to the time-mean strain field reduces by $\sim 7\%$ in comparison to the values obtained for the two MM cases. This result can be explained as follows: in perfect gases of fluids made of simple molecules, the heat generated by the dissipation of the turbulent kinetic energy at small scales induces variations of temperature larger than those occurring in fluids characterized by high molecular complexity, such as siloxane MM. In particular, the boundary layer flows of compounds characterized by high molecular complexity exhibit small temperature variations across the shear layer, thus limiting the diffusion of energy as heat among contiguous flow streams.

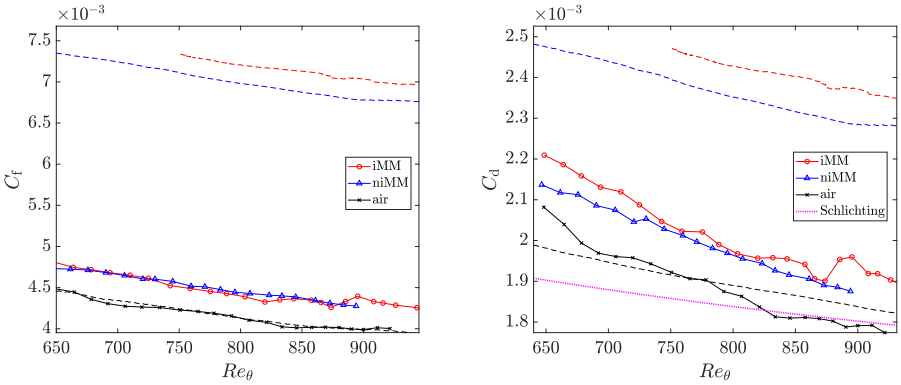

Figure 3.5: (a) Skin friction coefficient *vs* Re_θ and (b) dissipation coefficient *vs* Re_θ for all the cases of Tab. 3.2. Relations obtained with empirical correlations are also plotted for comparison. The dashed lines report the C_f *vs* Re_θ and the C_d *vs* Re_θ functions computed with the correlation by Drela and Giles [5]. The magenta line in figure (b) denotes the $C_d - Re_\theta$ function obtained using Schlichting's correlation.

Figure 3.4 shows the variation of both the friction (Fig. 3.4a) and the dissipation coefficients (Fig. 3.4b) as a function of Re_θ for the cases of Tab. 3.2. The results of the calculations conducted with *BLnI* are also displayed. Trends obtained from the DNS in the proximity of the tripping point are not reported due to non-physical phenomena resulting from the simulation. The graphs show that the variations of both coefficients calculated from the DNS results qualitatively match those predicted by the reduced-order model. However, at fixed Re_θ, both C_f and C_d values estimated with *BLnI* do not match those obtained from the DNS results: for the *air* case, the maximum deviation is $\sim 5\%$ on C_f and $\sim 10\%$ on C_d.

Among the three cases under scrutiny, the lowest C_d value is found for the *air* case. This finding suggests that flows of fluids made of simple molecules are characterized by lower values of dissipation at fixed M_e and Re_θ. This trend can be explained by inspecting the value of the freestream Eckert number (see Tab. 3.2), which is inherently lower in case of dense vapor flows. In fluids made by complex molecules in both the ideal and the nonideal thermodynamic state, the thermodynamic and kinematic fields are decoupled even at freestream conditions for which the flow is highly compressible, and in terms of dissipation mechanisms, the physical behaviour resembles that of an incompressible flow boundary layer [15], [23]. This result is in agreement with those obtained by Pini and de Servi [14] for adiabatic laminar boundary layers of dense vapors at $M_e = 2$.

Figure 3.5 shows a comparison between the $C_f - Re_\theta$ (Fig. 3.5a) and the $C_d - Re_\theta$ (Fig. 3.5b) curves obtained from DNS and those obtained using the correlations by Drela and Giles [5]. Such correlations take into account the effect of flow compressibility by introducing a corrective coefficient that depends on both the shape factor and the free stream Mach number. In Fig. 3.5b, the $C_d - Re_\theta$ trend calculated using the empirical correlation by Schlichting [2], [3] under the assumption of turbulent incompressible flow is also plotted. This correlation reads

$$C_{d,Sc} = 0.0056 Re_\theta^{-\frac{1}{6}}. \tag{3.24}$$

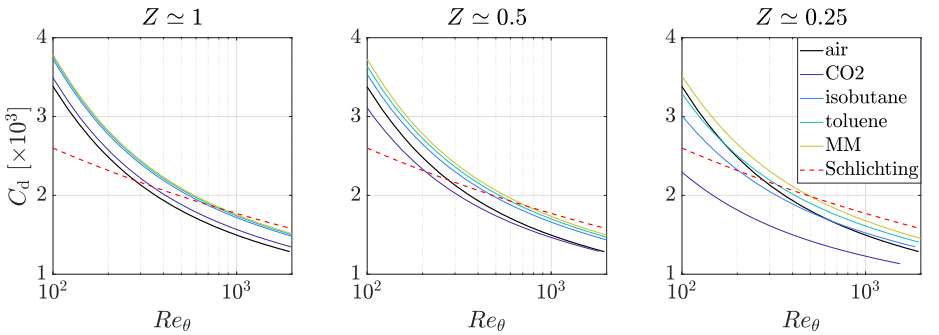

Figure 3.6: Dissipation coefficient *vs* Re_θ for the fluids of Tab. 3.1 at $M_e = 1.4$. For comparison, trends evaluated with the Schclichting correlation are also reported.

Although predicting quite accurately the value of both C_f and C_d for air, Drela and Giles' correlations provide inaccurate results for the *iMM* and *niMM* cases: for the *niMM* case, the predicted C_f and C_d values at fixed Re_θ are up to ~ 30% larger than those obtained from DNS results. In the turbulent regime, the variation of C_d is similar to that predicted by the incompressible Schlichting correlation for the *air* case in the proximity of the plate trailing edge, while an offset (~ 7%) is observed for the other two cases. Such correlations have been validated only for transonic low-Reynolds number flows of air and do not take into account the effect of the fluid molecular complexity and the strong variations in thermophysical properties characterizing dense organic vapors. According to Schlichting, for a zero-pressure gradient boundary layer flow in equilibrium, the relation between the dissipation and the skin friction coefficient is

$$C_d = \frac{C_f}{2}\frac{H^*}{2}, \tag{3.25}$$

where $H^* = \theta^*/\theta$ is the energy shape factor, θ^* and θ being the kinetic energy and momentum thicknesses, respectively. In the turbulent flow region, $H^* \sim 1.774$ for all cases, which is in line with the value computed by Jardine [34]. As a consequence, changes in the dissipation coefficient between the three cases are solely due to changes in the value of the skin friction coefficient.

3.4.2. DISSIPATION ANALYSIS THROUGH ROM

Figure 3.6 shows the variation of the dissipation coefficient C_d with Re_θ for flows of the fluids reported in Tab. 3.1 and the thermodynamic states listed in Tab. 3.4. The results have been calculated with *BLnI* assuming a fully turbulent flow and refer to boundary layer flows with $M_e = 1.4$. The $C_d - Re_\theta$ trend obtained with the correlation by Schlichting (Eq. 3.24) valid for incompressible flows of air has also been plotted. Results for air obtained using the perfect gas equation of state are also displayed.

Regardless of the thermodynamic state, at a fixed Re_θ, C_d values are lower for boundary layer flows of fluids made of simple molecules than for those of complex organic compounds. This is due to their large heat capacity, which results in a quasi-isothermal temperature profile within the boundary layer, as can also be observed in the DNS re-

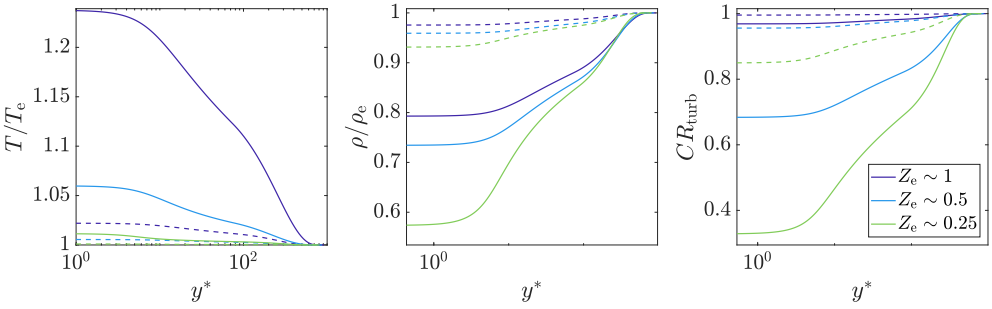

Figure 3.7: Normalized (a) temperature, (b) density, and (c) turbulent Chapman-Rubesin parameter profiles across the boundary layer thickness as a function of y^* for carbon dioxide and siloxane MM and three different free-stream Z_e values. Continuous line denote flows of CO_2, dashed line those of siloxane MM.

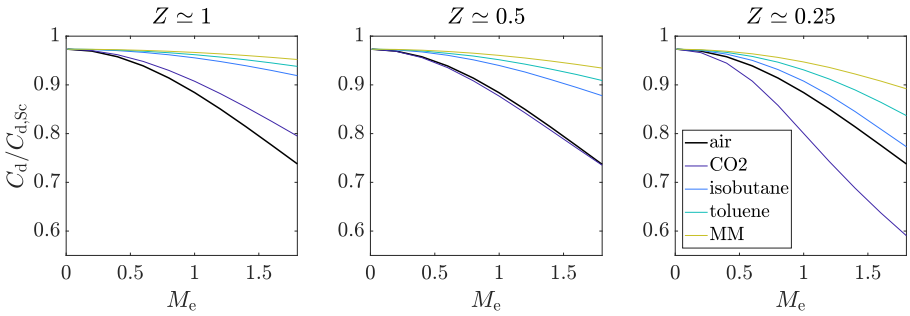

Figure 3.8: Variation of the dissipation coefficient C_d with the free-stream Mach number M_e for several fluids in the turbulent regime. Three different free-stream thermodynamic states are analyzed: (a) $Z_e \sim 1$, (b) $Z_e \sim 0.5$, and (c) $Z_e \sim 0.25$. The dissipation coefficient has been normalized with the C_d value calculated using the Schlichting correlation.

sults. The decrease of the dissipation coefficient with the fluid molecular complexity is more pronounced at $Z_e \sim 0.25$, i.e., at states in the proximity of the critical point one, where thermophysical properties are largely varying. As can be inferred from Eq.3.27, the value of the dissipation coefficient depends on two dimensionless quantities: the temperature ratio T/T_e and the Chapman-Rubesin parameter CR. Figure 3.7a-c shows the trend of these two parameters, together with that of the density ratio ρ/ρ_e (Fig. 3.7b) across the boundary layer thickness, for flows of CO_2 and siloxane MM. In both cases, if $Z_e \to 0$, the boundary layer becomes more isothermal due to the increase of the fluid heat capacity in the dense vapor region. However, larger density gradients across the boundary layer are observed (Fig. 3.7b), with respect to flows of fluids in the dilute gas state. The effect of decreasing density across the boundary layer prevails over the one due to the increase of the dynamic viscosity, whose value scales with the temperature. As a consequence, the value of the Chapman-Rubesin parameter decreases. Consequently, with reference to Eq. 3.27, all fluids exhibit a decrease of the C_d value if the fluid state approaches that of the critical point. In summary, for the investigated fluids, the lower the Z_e is, the larger the density variations across the boundary layer caused by friction heating are, and the lower the associated irreversible entropy generation becomes.

Finally, Figure 3.8 shows the change of the ratio $C_d/C_{d,Sc}$ as a function of the freestream Mach number at fixed $Re_\theta = 10^3$ for all the fluids listed in Tab.3.1. It can be observed that $C_d/C_{d,Sc}$ approaches unity for compounds characterized by high molecular complexity in the dilute gas state and low M_e; conversely, it decreases with decreasing molecular complexity, Z_e values and increasing M_e values. The effect of compressibility, i.e., of the free-stream Mach number, is to enhance friction heating, which can sensibly change the velocity distribution across the boundary layer and reduce the wall skin friction coefficient, especially in fluids made of simple molecules and in the dilute gas state.

3.4.3. FLOW FIELD ANALYSIS

Figure 3.9a shows the velocity profiles in wall units, while Figure 3.9b depicts the compressible van-Driest velocity profile as a function of $y^* = \bar{\rho} y u_\tau^*/\bar{\mu}$, being $u_\tau^* = \sqrt{\tau_w/\bar{\rho}}$ and τ_w the shear stress at the wall. Both profiles are evaluated at a location such that $Re_\theta = 800$. For a compressible boundary layer flow, the van Driest scaling reads

$$u^* = \frac{1}{\sqrt{\tau_w/\bar{\rho}}} \int_0^{u_e} \sqrt{\frac{\bar{\rho}}{\rho_w}} \mathrm{d}u. \tag{3.26}$$

Results obtained with *BLnI* for the same Re_θ are also reported. Regardless of the adopted scaling, no major deviations from the analytical law of the wall are observed for all cases in the viscous sublayer and in the buffer zone, where the peak in turbulence production is observed, see Fig. 3.10a. However, in the logarithmic region, the values obtained with the ROM do not fully overlap those obtained with the DNS. With respect to the velocity profiles obtained with the Van Driest transformation (Fig. 3.9b), a $\sim 1.5\%$ difference between the u^* values evaluated with the DNS and those evaluated with the ROM is observed at $y^* = 40$ for the *iMM* and *niMM* cases. Such a deviation is lower than that observerd in the *air* case ($\sim 6\%$ at $y^* = 40$). For the *air* case, smaller variations are instead

observed if a traditional $u^+(y^+)$ scaling is used, in line with the findings of Sciacovelli *et al* [16].

Figure 3.10a shows the turbulence production across the boundary layer thickness at a location such that $Re_\theta = 800$ for all the cases listed in Tab. 3.2. The turbulence production peaks at $y^+ \sim 10$ in all the cases. The peak is slightly more pronounced in the *air* case, while the *niMM* case exhibits the lowest maximum value of normalized turbulent production. However, the differences are minimal and are arguably due to numerical dispersion.

Figure 3.10b displays the temperature profiles across the boundary layer evaluated at a x location corresponding to $Re_\theta = 800$. Results obtained from both the DNS and *BLnI* are plotted. It can be observed that the temperature increase in the proximity of the wall strongly depends on both the fluid molecular complexity and the thermodynamic fluid state. In particular, the temperature difference between the wall and the free stream is maximum in the case of air, while the boundary layer of siloxane MM is nearly isothermal in both the investigated thermodynamic conditions. This finding is inherently related to the large heat capacity of the organic fluid, or, similarly, to its high number of molecular degrees of freedom, which enables the fluid molecule to store more thermal energy than that stored by a molecule characterized by a lower number of degrees of freedom. Among the three cases, the *niMM* case shows a near-constant temperature profile, due to the larger heat capacity of siloxane MM in the dense vapor state. In agreement with the findings by Sciacovelli *et al* [16], boundary layer flows of organic fluids in the compressible flow regimes typical of turbomachinery ($M_\mathrm{e} \sim 1-2$) can thus be considered isothermal and exhibit features comparable to those characterizing incompressible flows. Furthermore, the temperature profile strongly affects the value of the dissipation coefficient. Using the Falkner-Skan variable transformation, one can write, for a turbulent flow,

$$C_\mathrm{d} = \frac{1}{\sqrt{Re_x}} \int_0^{\eta_\mathrm{e}} CR \frac{T_\mathrm{e}}{T} \tilde{v}^2 \mathrm{d}\eta, \tag{3.27}$$

where CR here takes also into account the contribution due to the eddy viscosity. At a fixed Reynolds number, for an ideal gas, variations of T_e/T prevail over those of CR, thus leading to a reduction of the C_d value for simple fluid molecules in the compressible flow regime.

Figure 3.11 shows the plots of the time-averaged density, viscosity, and Chapman-Rubesin parameter across the boundary layer as a function of the semi-locally scaled wall coordinate y^* for the three cases of Tab. 3.2 at a streamwise location corresponding to $Re_\theta = 800$. Results of the transitional boundary layer flow simulations performed with *BLnI* are also indicated. The averaged density (Fig. 3.11a) monotonically increases from the wall towards the free stream for all the cases. However, density variations are much smaller in the *iMM* and *niMM* cases, the smallest variations being observed in the dilute gas case *iMM*. Moreover, for all the cases, the density profile resembles the velocity profile, see Fig. 3.9. In particular, a linear profile of $\bar{\rho}$ with y^* is observed for $y^* \lesssim 12$ and a logarithmic one for $y^* \lesssim 100$. These results slightly differ from those obtained by Sciacovelli *et al*, who calculated such values only in boundary layer flows of dense organic vapor, whereas density variations in air flows better correlate with temperature variations. This difference is arguably due to the large free stream Mach number values

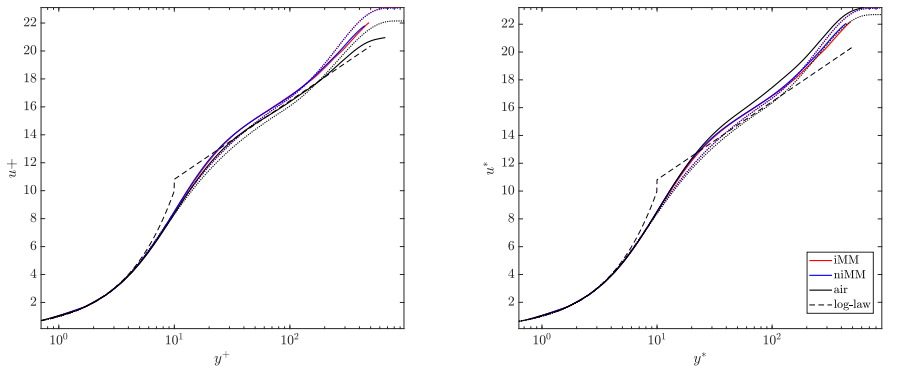

Figure 3.9: Velocity profiles in (a) wall coordinates and (b) van Driest transformed coordinates. Continuous lines denote the values obtained with DNS, whereas dotted ones denote those obtained with the *BLnI* code. Black dashed lines indicate the linear and logarithmic laws, with $k = 0.41$ and $C = 5.2$.

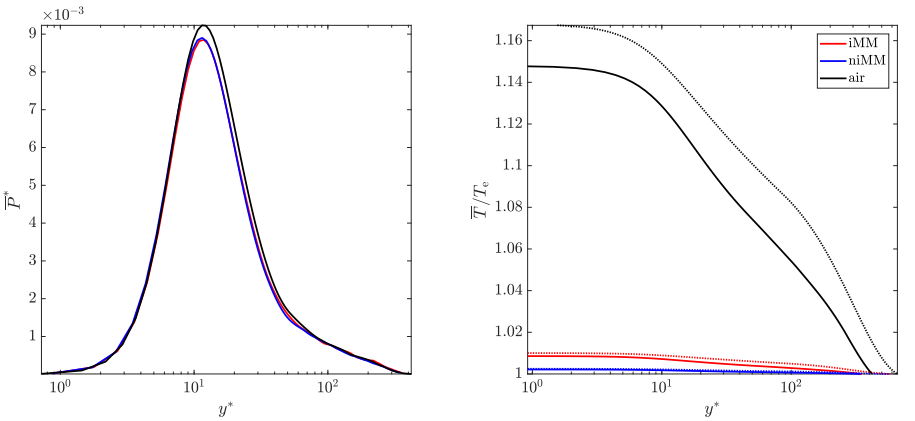

Figure 3.10: (a) Normalized turbulence production $\overline{P}^* = \overline{P} \cdot \delta / (\rho_e V_e^3)$ *vs* y^+, and (b) temperature profiles for all the cases listed in Tab. 3.2. Continuous lines correspond to the values obtained with DNS, whereas dotted ones indicate those obtained with the ROM. The trends have been evaluated at a location where $Re_\theta = 800$.

($M_e = 2.25$ and $M_e = 6$) selected by the authors. The wall friction heating to which supersonic and hypersonic air flows are subjected is larger than the one characterizing the flows investigated in this work, where $M_e = 0.95$: in particular, the wall-to-free-stream temperature ratio at $M_e = 6$ is 6.5 [16], while, at the Mach number ($M_e = 0.95$) chosen for this simulation is 1.16 (Fig. 3.10b): thus, a larger influence of the temperature on the density field can be observed in hypersonic flows. Moreover, the temperature profile is decoupled from the density profile in the *iMM* and *niMM* cases due to the larger number of molecular degrees of freedom and, consequently, the larger heat capacity characterizing these fluids which, in turn, minimizes the friction heating at the wall.

The viscosity profile (Fig. 3.11b) qualitatively follows the profile of the temperature for the *air* and *iMM* cases, with a larger wall-to-free-stream ratio calculated for the *air* case. Conversely, the *niMM* case shows a liquid-like viscosity variation, i.e., the viscosity increases across the boundary layer, with a profile similar to that of the density. This effect has already been discussed in several other works [15], [16], [35]. However, the increase in viscosity across the boundary layer is here smaller than the one estimated by Sciacovelli *et al* due to the use of a different and more accurate model for the transport properties of siloxane MM [17]. The local value of the Chapman-Rubesin parameter CR increases towards the free stream, for all three cases (Fig. 3.11c). Larger wall-to-free stream differences are observed in the *air* case ($CR \sim 0.96$ at the wall) than in the other two. It can also be noted that the CR value in the dilute gas case *iMM* does not sensibly depart from unity, whereas it exhibits a larger departure from unity in the dense vapor case, *niMM*. As opposed to the temperature profile (Fig. 3.10b), larger density variations are observed in the dense vapor case than in the dilute gas case due to the strong gradients of thermo-physical properties characterizing fluid states in the proximity of the critical point. This variation strongly influences that of CR, which, in turn, influences the overall dissipation within the boundary layer, see Eq. 3.27. The influence of both the Chapman-Rubesin parameter and the dense vapor state on the dissipation coefficient is further discussed in Sec.3.4.2. Although a quantitative mismatch is observed, the values obtained with *BLnI* are qualitatively in agreement with those obtained from DNS for both the density, the viscosity, and the Chapman-Rubesin parameter. As a consequence, the reduced-order model is deemed sufficiently accurate for carrying out systematic studies aimed at providing evaluations of integral boundary layer parameters such as the C_d in the laminar and turbulent flow regime.

Figure 3.12 shows the variations of the root-mean-square of the velocity, density, and pressure fluctuations across the boundary layer for the three cases of Tab. 3.2 at a streamwise location corresponding to $Re_\theta = 800$. The turbulence intensity profiles (Fig. 3.12a) feature a similar variation in all three cases. Deviations are mainly observed in the outer region, i.e., $y^* > 300$, where both the *iMM* and *niMM* cases display a plateau at $y^* \sim 700$, whereas the *air* exhibits a plateau at $y^* > 10^3$. The same profile is also observed for the turbulence intensity (not shown), defined as $Tu = \sqrt{2/3k}/V_e^3$, where k is the turbulence kinetic energy, which also takes into account the intensity of the turbulent fluctuations in the y and z directions. The peak in turbulence intensity occurs at $y^* \sim 12$, which corresponds to the location of maximum turbulence production. Conversely, the root-mean-square of the density fluctuations (Fig. 3.12b) reaches a maximum at $y^* \sim 30$ in all the investigated cases. The maximum in the root-mean-square of the pressure fluctua-

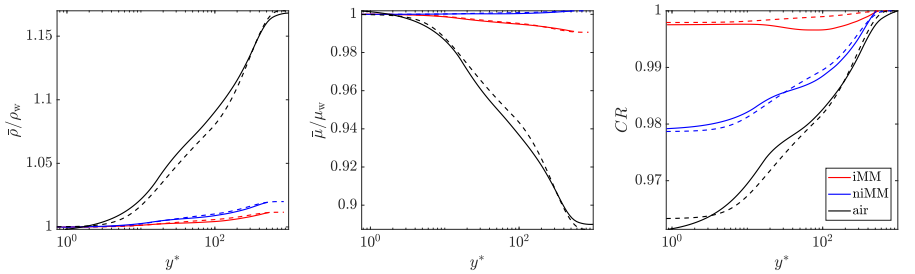

Figure 3.11: Time-averaged (a) density, (b) dynamic viscosity and (c) Chapman-Rubesin *vs* y^* for the cases listed in Tab. 3.2. The statistics are normalized with the value of the corresponding variable evaluated at the wall. Continuous lines denote quantities evaluated by means of DNS; dashed lines, instead, those calculated with the *BLnI* code.

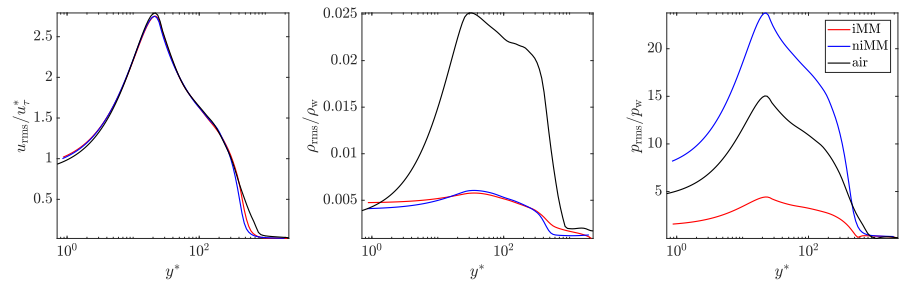

Figure 3.12: Root-mean square (a) streamwise velocity, (b) density and (c) pressure fluctuations *vs* y^* for the cases listed in Tab. 3.2. Velocity fluctuations are normalized with the semi-local friction velocity u_τ^*, see Eq. 3.26. Temperature and pressure fluctuations are normalized with the value of the corresponding variable evaluated at the wall.

tions, instead, is observed at $y^* \sim 20$. However, the peak is less pronounced in the cases in which siloxane MM is the working fluid. In particular, the relative deviation between the value of the density fluctuation at $y^* \sim 12$ and $y^* \sim 1$ is 21% for the *iMM* and 45% for the *niMM* cases, whereas this is much larger for the *air* case (530%). This is in line with what has been discussed about the time-average density, which shows larger variations across the boundary layer in the *air* case. Overall, regardless of the fluid and its thermodynamic state, Morkovin's hypothesis for which density fluctuations are negligible ($\rho_{rms}/\bar{\rho}$) is satisfied, in agreement with the findings by Sciacovelli *et al.*

Finally, Figure 3.13 shows the instantaneous snapshots of the magnitude of the density gradient $|\nabla\rho|$ for each case after 150k time steps. The density gradient is normalized by $\bar{\rho}/L$. Elongated, sheet-like flow structures corresponding to high-density gradients moving towards the boundary layer edge are observed in the *air* case. Conversely, high-density gradient structures are concentrated on the wall in both the *iMM* and *niMM* cases. This distribution is arguably due to the inherently larger density characterizing siloxane MM.

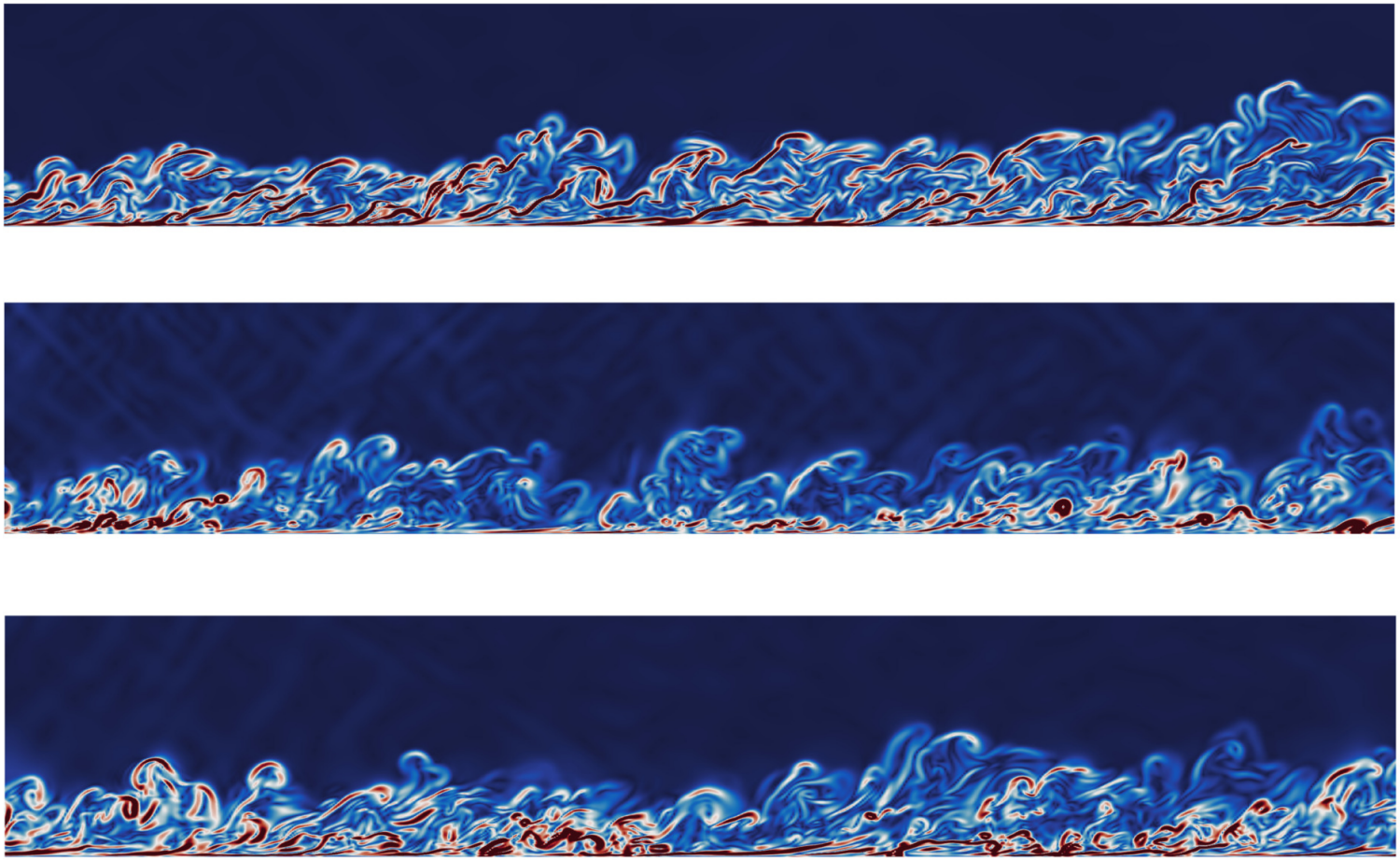

Figure 3.13: Normalized density gradient ($\nabla\rho/(\bar{\rho}/L)$) at for the cases (a) *air*, (b) *iMM*, and (c) *niMM*. The snapshots have been captured after 150k time steps.

3.5. CONCLUSION

Direct numerical simulations of zero-pressure gradient boundary layer flows of air and siloxane MM with the fluid in both dilute gas and dense vapor thermodynamic states have been performed. All dissipation sources have been discerned and analyzed. The trend of both the skin friction and the dissipation coefficients as a function of the Reynolds number, as well as those of the velocity and temperature profiles, have been discussed and compared against those obtained from an in-house reduced-order model solving the two-dimensional turbulent boundary layer equations in transformed coordinates. Results from the reduced-order model have then been used to assess the influence of the fluid molecular complexity, the thermodynamic state, and the flow compressibility on the dissipation coefficient. Based on the results obtained from this work, the following conclusions can be drawn.

1. At fixed Reynolds number, turbulent boundary layer flows of fluids made of complex molecules are characterized by a higher value of both the skin friction and the dissipation coefficient than flows of air. This is due to the decoupling between the thermal and the kinematic fields, as a consequence of the larger value of heat capacity of complex molecular fluids.

2. Regardless of the fluid thermodynamic state, turbulent boundary layer flows of complex molecules fluids can be assumed isothermal.

3. The contribution to the overall loss due to irreversible heat transfer is negligible in boundary layer flows of molecularly complex fluids, regardless of their thermodynamic state.

4. For a given fluid, at a fixed Reynolds number, the overall dissipation expressed in terms of dissipation coefficient decreases if the state approaches that of the critical point. This is due to the large density gradients characterizing the flow across the shear layer, which leads to a decrease in the Chapman-Rubesin parameter value and, thus, of the dissipation coefficient.

5. In general, boundary layer flows of fluids made of simple molecules in the dense vapor state are less dissipative than those of complex organic compounds in the dilute gas state. This is due to the combined effects of the large density gradients characterizing states in the proximity of the critical point and the wall friction heating, which prevails in flows of fluids made of simple molecules.

Future works will investigate more in detail the structure of density and pressure fluctuations in ideal gas and dense vapor boundary layers. Flows of fluids other than air and siloxane MM will also be studied with the reduced-order model, as well as the effect of favourable and adverse pressure gradients. Analyses of the effect of the wall heat transfer in the boundary layer flow of organic fluids are also envisioned. The ultimate research goal is to develop an analytical model for the dissipation coefficient C_d as a function of the Reynolds number, the thermodynamic fluid state, the molecular complexity, the boundary layer shape factor, and the free-stream Mach number. Such a model can then be used to estimate the profile losses in internal flow devices such as turbomachinery or heat exchangers during the conceptual design phase.

3.6. ACKNOWLEDGEMENT

The authors acknowledge the contribution of dr. Carlo de Servi, dr. Adam J. Head, Dominic Dijkshoorn, and Federico Pizzi to the development and verification of *BLnI*. This research has been supported by the Applied and Engineering Sciences Domain (TTW) of the Dutch Organization for Scientific Research (NWO), Technology Program of the Ministry of Economic Affairs, grant # 15837.

3.7. APPENDIX A: COEFFICIENTS FOR THE COMPRESSIBLE FALKNER-SKAN TRANSFORMED EQUATIONS

With reference to Eqs. 3.9-3.10, the coefficients for the compressible Falkner-Skan transformed boundary layer equations read as follows.

$$b = CR\left(1+\nu^+\right), \qquad \nu^+ = \frac{\nu_\mathrm{T}}{\nu}, \tag{3.28}$$

$$c = \frac{\rho_\mathrm{e}}{\rho}, \qquad CR = \frac{\rho\mu}{\rho_\mathrm{e}\mu_\mathrm{e}}, \qquad CR_\mathrm{e} = \frac{\rho_\mathrm{e}\mu_\mathrm{e}}{\rho_0\mu_0}, \tag{3.29}$$

$$d = \frac{CV_\mathrm{e}^2}{h_{0,\mathrm{e}}}\left[1-\frac{1}{\mathrm{Pr}}+\nu^+\left(1-\frac{1}{\mathrm{Pr}_\mathrm{T}}\right)\right], \tag{3.30}$$

$$e = \frac{C}{\mathrm{Pr}}\left(1+\nu^+\frac{\mathrm{Pr}}{\mathrm{Pr}_\mathrm{T}}\right), \tag{3.31}$$

$$\tag{3.32}$$

$$f' = \frac{u}{u_\mathrm{e}}, \tag{3.33}$$

$$g = \frac{h_0}{h_{0,\mathrm{e}}}, \tag{3.34}$$

$$\tag{3.35}$$

$$m_1 = \frac{1}{2}\left[1+m_2+m_3\right] = \frac{1}{2}\left[1+m_3+m_4+m_5\right], \tag{3.36}$$

$$m_2 = \frac{x}{u_\mathrm{e}}\frac{\mathrm{d}u_\mathrm{e}}{\mathrm{d}x} = m_4+m_5 = \frac{m_4}{1+(\Gamma-1)\,M_\mathrm{e}^2}, \tag{3.37}$$

$$m_3 = \frac{x}{C_\mathrm{e}}\frac{\mathrm{d}C_\mathrm{e}}{\mathrm{d}x}, \tag{3.38}$$

$$m_4 = \frac{x}{M_\mathrm{e}}\frac{\mathrm{d}M_\mathrm{e}}{\mathrm{d}x}, \tag{3.39}$$

$$m_5 = \frac{x}{c_\mathrm{e}}\frac{\mathrm{d}c_\mathrm{e}}{\mathrm{d}x}. \tag{3.40}$$

In the equations, ν, ν_T and c denote the kinematic viscosity of the fluid, the turbulent eddy viscosity, and the speed of sound.

3.8. APPENDIX B: THE CEBECI-SMITH TURBULENCE MODEL

The Cebeci-Smith model [21] is an algebraic 0-equations eddy viscosity turbulence model. It models the eddy viscosity as a function of the turbulent velocity field, the density ratio $c = \rho_e/\rho$, the Chapman-Rubesin parameter CR, and the Reynolds-number Re_x. The non-dimensional eddy viscosity $\nu^+ = \nu_T/\nu$ for the inner and outer layers reads

$$\left(\nu^+\right)_{\text{inner}} = \kappa^2 \frac{1}{C}\frac{1}{c^3}\sqrt{\text{Re}_x} I^2 v \left[1-\exp\left(-y/A\right)\right]^2 \gamma_{\text{tr}}\gamma, \qquad 0 \le \eta \le \eta_c, \tag{3.41}$$

$$\left(\nu^+\right)_{\text{outer}} = \alpha \frac{1}{C}\frac{1}{c^2}\sqrt{\text{Re}_x}\left[\int_0^{\eta_e} c\,(1-u)\,\mathrm{d}\eta\right]\gamma_{\text{tr}}\gamma, \qquad \eta_c \le \eta \le \eta_e, \tag{3.42}$$

where η_c is the location of the inner layer edge in transformed coordinates, and

$$y/A = \frac{N}{A^+} c^{-3/2}\frac{\sqrt{C_w}}{C}\text{Re}_x^{1/4} I v_w^{1/2}, \qquad I = \int_0^{\eta} c\,\mathrm{d}\eta, \qquad I_e = \int_0^{\eta_e} c\,\mathrm{d}\eta, \tag{3.43}$$

$$N^2 = 1 - 11.8 C_w c_w^3 p^+, \qquad p^+ = \frac{m_2}{\text{Re}_x^{1/4}}\left(C_w c_w \nu_w\right)^{-3/2}, \tag{3.44}$$

$$\gamma = \left(1 + 5.5\left(I/I_e\right)^6\right)^{-1}. \tag{3.45}$$

The closure coefficients are set to

$$\kappa = 0.40, \qquad A^+ = 26, \qquad \alpha = 0.0168. \tag{3.46}$$

For transitional boundary layers, the intermittency factor γ_{tr} reads

$$\gamma_{\text{tr}} = 1 - e^{\left(-G_{\text{tr}}(x-x_{\text{tr}})\int_{x_{\text{tr}}}^{x}\frac{\mathrm{d}x}{u_e}\right)}, \tag{3.47}$$

with

$$G - \text{tr} = 8.33\cdot 10^4 \frac{V_e^3}{\nu_e} Re_x^{-1.34} \tag{3.48}$$

The turbulent Prandtl number Pr_T model reads

$$Pr_T = \frac{\kappa\left[1-\exp\left(-y/A\right)\right]}{\kappa_h\left[1-\exp\left(-y/B\right)\right]}, \tag{3.49}$$

where

$$y/B = \frac{N}{B^+} c^{-3/2}\frac{\sqrt{C_w}}{C}\text{Re}_x^{1/4} I v_w^{1/2}, \tag{3.50}$$

$$B^+ = \frac{B^{++}}{Pr^{1/2}}, \tag{3.51}$$

$$B^{++} = \sum_{i=1}^{5} C_i \left(\log_{10} Pr\right)^{i-1}, \tag{3.52}$$

being Pr the Prandtl number, and the closure coefficients whose values are set to

$$\kappa_h = 0.44, \quad C_1 = 34.96, \quad C_2 = 28.79, \quad C_3 = 33.95, \quad C_4 = 6.33, \quad C_5 = -1.186. \tag{3.53}$$

BIBLIOGRAPHY

[1] M. Pini and C. De Servi, "Entropy generation in laminar boundary layers of non-ideal fluid flows", *Non-Ideal Compressible Fluid Dynamics for Propulsion and Power: Lecture Notes in Mechanical Engineering*, F. di Mare, A. Spinelli, and M. Pini, Eds., pp. 104–117, 2020. DOI: 10.1007/978-3-030-49626-5_8.

[2] J. D. Denton, "The 1993 IGTI scholar lecture: Loss mechanisms in turbomachines", *Journal of Turbomachinery*, vol. 115, no. 4, pp. 621–656, Oct. 1993, ISSN: 0889-504X. DOI: 10.1115/1.2929299.

[3] H. Schlichting and K. Gersten, *Boundary-layer theory*, en, 9th. New York, NY: Springer Berlin Heidelberg, 2016, ISBN: 978-3-662-52917-1.

[4] F. M. White and J. Majdalani, *Viscous fluid flow*. McGraw-Hill New York, 2006, vol. 3.

[5] M. Drela and M. B. Giles, "Viscous-inviscid analysis of transonic and low Reynolds number airfoils", en, *AIAA Journal*, vol. 25, no. 10, pp. 1347–1355, Oct. 1987, ISSN: 0001-1452, 1533-385X. DOI: 10.2514/3.9789.

[6] P. Colonna, E. Casati, C. Trapp, *et al.*, "Organic Rankine Cycle Power Systems: From the Concept to Current Technology, Applications, and an Outlook to the Future", en, *Journal of Engineering for Gas Turbines and Power*, vol. 137, no. 10, p. 100 801, Oct. 2015, ISSN: 0742-4795. DOI: 10.1115/1.4029884.

[7] K. Brun, P. Friedman, and R. Dennis, *Fundamentals and applications of supercritical carbon dioxide (sCO2) based power cycles*. Woodhead publishing, 2017.

[8] K. Herold, R. Radermacher, and S. Klein, *Absorption Chillers and Heat Pumps*. Taylor & Francis, 1996, ISBN: 9780849394270.

[9] A. Giuffre, P. Colonna, and M. Pini, "The Effect of Size and Working Fluid on the Multi-Objective Design of High-Speed Centrifugal Compressors", en, *International Journal of Refrigeration*, vol. 143, pp. 43–56, Nov. 2022, ISSN: 01407007. DOI: 10.1016/j.ijrefrig.2022.06.023.

[10] J. Schiffmann and D. Favrat, "Design, experimental investigation and multi-objective optimization of a small-scale radial compressor for heat pump applications", *Energy*, vol. 35, no. 1, pp. 436–450, 2010, ISSN: 0360-5442. DOI: https://doi.org/10.1016/j.energy.2009.10.010.

[11] P. A. Thompson, "A Fundamental Derivative in Gasdynamics", en, *Physics of Fluids*, vol. 14, no. 9, p. 1843, 1971, ISSN: 00319171. DOI: 10.1063/1.1693693.

[12] A. Kluwick, "Interacting laminar boundary layers of dense gases", in *Fluid- and Gasdynamics*, G. H. Schnerr, R. Bohning, W. Frank, and K. Bühler, Eds. Vienna: Springer Vienna, 1994, pp. 335–349, ISBN: 978-3-7091-9310-5. DOI: 10.1007/978-3-7091-9310-5{_}37.

[13] M. S. Cramer, S. T. Whitlock, and G. M. Tarkenton, "Transonic and boundary layer similarity laws in dense gases", *Journal of Fluids Engineering, Transactions of the ASME*, vol. 118, no. 3, pp. 481–485, 1996, ISSN: 1528901X. DOI: 10.1115/1.2817783.

[14] M. Pini and C. De Servi, "Entropy generation in laminar boundary layers of non-ideal fluid flows", *Lecture Notes in Mechanical Engineering*, pp. 104–117, 2020. DOI: 10.1007/978-3-030-49626-5_8.

[15] L. Sciacovelli, P. Cinnella, and X. Gloerfelt, "Direct numerical simulations of supersonic turbulent channel flows of dense gases", *J. Fluid Mech.*, vol. 821, pp. 153–199, Jun. 2017, ISSN: 0022-1120, 1469-7645. DOI: 10.1017/jfm.2017.237.

[16] L. Sciacovelli, X. Gloerfelt, D. Passiatore, P. Cinnella, and F. Grasso, "Numerical Investigation of High-Speed Turbulent Boundary Layers of Dense Gases", en, *Flow Turbulence Combust*, vol. 105, no. 2, pp. 555–579, Aug. 2020, ISSN: 1386-6184, 1573-1987. DOI: 10.1007/s10494-020-00133-1.

[17] M. Thol, F. Dubberke, G. Rutkai, *et al.*, "Fundamental equation of state correlation for hexamethyldisiloxane based on experimental and molecular simulation data", en, *Fluid Phase Equilibria*, vol. 418, pp. 133–151, Jun. 2016, ISSN: 03783812. DOI: 10.1016/j.fluid.2015.09.047.

[18] E. W. Lemmon, I. H. Bell, M. L. Huber, and M. O. McLinden, *NIST standard reference database 23: Reference fluid thermodynamic and transport properties-REFPROP, version 10.0, National Institute of Standards and Technology*, 2018. DOI: 10.18434/T4JS3C.

[19] W. F. Hughues and J. A. Brighton, *Fluid Dynamics (Schaum's Outline Series)*, en, 2nd. McGraw-Hill, US, 1983, ISBN: 978-0070311107.

[20] A. P. S. Wheeler, R. D. Sandberg, N. D. Sandham, R. Pichler, V. Michelassi, and G. Laskowski, "Direct Numerical Simulations of a High-Pressure Turbine Vane", en, *Journal of Turbomachinery*, vol. 138, no. 7, Jul. 2016, ISSN: 0889-504X, 1528-8900. DOI: 10.1115/1.4032435.

[21] T. Cebeci, *Convective Heat Transfer* (Convective Heat Transfer v. 2). Horizons Pub., 2002, ISBN: 978-0-9668461-4-0.

[22] T. Cebeci and A. M. O. Smith, *Analysis of turbulent boundary layers* (Applied mathematics and mechanics 15), en. New York: Academic Press, 1974, ISBN: 978-0-12-164650-9.

[23] F. Tosto, C. Lettieri, M. Pini, and P. Colonna, "Dense-vapor effects in compressible internal flows", en, *Physics of Fluids*, vol. 33, no. 8, p. 086 110, Aug. 2021, ISSN: 1070-6631, 1089-7666. DOI: 10.1063/5.0058075.

[24] D. A. Kouremenos and K. A. Antonopoulos, "Isentropic exponents of real gases and application for the air at temperatures from 150 K to 450 K", *Acta Mech.*, vol. 65, no. 1-4, pp. 81–99, Jan. 1987, ISSN: 0001-5970, 1619-6937. DOI: 10.1007/BF01176874.

[25] F. Tosto, A. Giuffré, P. Colonna, and M. Pini, "Non-ideal Effects in Compressible Swirling Flows", en, in *Proceedings of the 3rd International Seminar on Non-Ideal Compressible Fluid Dynamics for Propulsion and Power*, M. Pini, C. De Servi, A. Spinelli, F. di Mare, and A. Guardone, Eds., vol. 28, Series Title: ERCOFTAC Series, Cham: Springer International Publishing, 2021, pp. 36–43, ISBN: 978-3-030-69305-3. DOI: 10.1007/978-3-030-69306-0_5.

[26] C. K. W. Tam and J. C. Webb, "Dispersion-Relation-Preserving Finite Difference Schemes for Computational Acoustics", *Journal of Computational Physics*, vol. 107, no. 2, pp. 262–281, 1993, ISSN: 0021-9991. DOI: https://doi.org/10.1006/jcph.1993.1142.

[27] T. J. Poinsot and S. K. Lele, "Boundary Conditions for Direct Simulations of Compressible Viscous Flows", en, p. 26,

[28] A. P. S. Wheeler and R. D. Sandberg, "Numerical investigation of the flow over a model transonic turbine blade tip", en, *Journal of Fluid Mechanics*, vol. 803, pp. 119–143, Sep. 2016, ISSN: 0022-1120, 1469-7645. DOI: 10.1017/jfm.2016.478.

[29] P. J. Przytarski and A. P. S. Wheeler, "Accurate Prediction of Loss Using High Fidelity Methods", en, *Journal of Turbomachinery*, vol. 143, no. 3, p. 031 008, Mar. 2021, ISSN: 0889-504X, 1528-8900. DOI: 10.1115/1.4050115.

[30] A. P. S. Wheeler, "High Fidelity Simulation of Dense Vapour Flows", in *Proceedings of the 33rd International Conference on Parallel Computational Fluid Dynamics*, Alba, Italy, 2022, p. 4.

[31] J. Poggie, N. J. Bisek, and R. Gosse, "Resolution effects in compressible, turbulent boundary layer simulations", en, *Computers & Fluids*, vol. 120, pp. 57–69, Oct. 2015, ISSN: 00457930. DOI: 10.1016/j.compfluid.2015.07.015.

[32] F. H. Clauser, "The Turbulent Boundary Layer", in ser. Advances in Applied Mechanics, H. L. Dryden and T. v. Kármán, Eds., vol. 4, ISSN: 0065-2156, Elsevier, 1956, pp. 1–51. DOI: https://doi.org/10.1016/S0065-2156(08)70370-3.

[33] SURF, *Dutch National Supercomputer Snellius*, 2023.

[34] L. J. Jardine, "The Effect of Heat Transfer on Turbine Performance", en, p. 185,

[35] T. Chen, B. Yang, M. Robertson, and R. Martinez-Botas, "Direct Numerical Simulation of Real-gas Effects within Turbulent Boundary Layers for Fully-developed Channel Flows", en, *Journal of the Global Power and Propulsion Society*, vol. 5, pp. 216–232, Dec. 2021, ISSN: 2515-3080. DOI: 10.33737/jgpps/133600.

4

Flow Deviation and Critical Choking in Transonic Turbine Cascades Operating with Non-Ideal Compressible Flows

Part of the content of this chapter appeared in:
F. Tosto, A. Giuffré, P. Colonna, and M. Pini, *Flow deviation and critical choking in transonic turbine cascades operating with non-ideal compressible flows*, Journal of the Global Power and Propulsion Society, August 2022, doi: 10.33737/jgpps/151659.

In this work we examine the flow deviation and its relationship to critical choking, i.e., choking of the meridional component of velocity, in transonic turbine cascades operating with non-ideal compressible flows. To this purpose, a generalized expression of the corrected flow per unit area as a function of both the thermodynamic state and the molecular complexity of the working fluid, the Mach number, and the amount of swirl is derived. The trends of the corrected flow with respect to these quantities are used to infer physical insights on the flow deviation and on the operability of transonic turbine cascades in off-design conditions. Moreover, reduced-order models for the estimation of the flow deviation and the preliminary assessment of the losses have been developed and validated against the results of CFD simulations performed on a representative transonic turbine stator. Results suggest that flows of dense organic vapors exhibit larger deviations than those pertaining to compounds made of simple molecules, e.g., air. Furthermore, transonic turbines expanding dense vapors reach critical choking conditions at lower Mach numbers than the ones operating with simple molecules and are affected by larger dissipation due to viscous mixing.

4.1. INTRODUCTION

The defining feature of highly transonic turbine stators is the considerable difference between the blade metal angle and the actual flow angle downstream of the trailing edge, namely, the flow deviation. Accurately predicting the flow deviation is particularly relevant during the preliminary design of axial turbines, as small errors can turn into large variations of specific work, power output, and efficiency [1].

Several models for estimating the magnitude of the flow deviation are available in the literature. Among these, correlations by Traupel [2] and Ainley and Mathieson [3] are still widely used to preliminary estimate the deviation during the turbine meanline design. However, although such correlations have been thoroughly assessed for conventional turbine applications using air or steam as working fluids, no analysis has been performed on turbines operating with fluids in the dense vapor thermodynamic state yet. Such machinery is used, for example, in organic Rankine cycle power systems [4]. In the thermodynamic cycle, a dense organic vapor (e.g., fluorocarbon, hydrocarbon, or siloxane) is expanded in a turbine starting from a thermodynamic inlet state close to that of the critical point. These turbines operate with comparatively higher expansion ratios than those characterizing conventional ones. Moreover, the flow is highly transonic/supersonic, arguably leading to significant flow deviations downstream of the stator vane.

Studying the influence of both the non-ideality associated with the dense vapor state and the molecular complexity of the working fluid on the internal flow field is thus paramount to correctly designing turbine cascades and accurately predicting the flow deviation. The non-ideal fluid dynamics of dense vapor flows is governed by the so-called fundamental derivative of gas dynamics [5], defined as

$$\Gamma \equiv 1 + \frac{\rho}{c}\left(\frac{\partial c}{\partial \rho}\right)_s = \frac{1}{2}\left[\gamma_{pv} + 1 - \frac{v}{\gamma_{pv}}\left(\frac{\partial \gamma_{pv}}{\partial v}\right)_s\right], \tag{4.1}$$

where ρ is the density, c the speed of sound, and s the entropy. Equation 4.1 also introduces the generalized isentropic pressure-volume exponent [6], defined as

$$\gamma_{pv} = -\frac{v}{p}\left(\frac{\partial p}{\partial v}\right)_s = -\frac{v}{p}\frac{c_p}{c_v}\left(\frac{\partial p}{\partial v}\right)_T = \frac{\gamma}{\beta_T p}, \tag{4.2}$$

where γ is the ratio of the specific heats and β_T is the fluid isothermal compressibility. In the dilute gas state, $\gamma_{pv} \to \gamma$ and $\Gamma \to (\gamma+1)/2$, where γ is the ratio of specific heats. Conversely, if the fluid is in the dense vapor state, the γ_{pv} value varies over the expansion. As a consequence, the internal flow pattern substantially departs from the one which can be encountered in machines operating with fluids such as steam or air. For example, expansions in convergent-divergent nozzle cascades from supercritical inlet thermodynamic states can exhibit strong non-ideal effects which determine a different shock and expansion pattern from that characterizing ideal gas processes [7]. Previous works [8], [9] pointed out that the average value of γ_{pv} over an expansion can be used to measure the influence of non-ideal flow effects on the turbine performance and operation. In particular, compressibility effects in turbomachinery blade rows operating in the non-ideal compressible flow regime can be greatly enhanced or mitigated depending on

whether the generalized isentropic exponent γ_{pv} is higher or lower than the heat capacity ratio γ of the fluid in the limit of dilute gas [7], [10]. Furthermore, if evaluated under the limit $v \to \infty$, both Γ and γ_{pv} show a monotonic decreasing trend with the molecular complexity of the fluid [11]. In addition, thermodynamic dense vapor states of organic compounds, such as the ones used in ORC power systems, are characterized by values of Γ and γ_{pv} which are significantly lower than those characterizing the dilute gas state. Therefore, it is expected that non-ideal flow effects significantly affect the flow deviation downstream of the cascade.

Non-ideal effects also influence the turbine loss breakdown which, in turn, affects also the design of the cascade. Indeed, the presence of strong gradients of thermophysical properties, together with flow compressibility, affects the dissipation produced by various loss mechanisms, such as those associated with viscous effects in boundary layers, shocks, and mixing at the blade trailing edge. Eventually, this results in optimal designs that are significantly different from those that would be obtained through the application of existing best practices [9], [12].

An additional problem that may arise in ORC turbines is the onset of critical choking conditions, which is intimately connected to the flow deviation. Critical choking occurs when the meridional Mach number at the cascade outlet reaches unity. This condition differs from the turbine choking conditions, which, in turn, arises when the Mach number in the passage throat reaches unity. When a turbine vane is in critical choking conditions, both its operability and efficiency are severely compromised. Therefore, the design of ORC turbines has to be carried out to avoid critical choking in both design and off-design conditions. Furthermore, in mini-ORC turbines, the expansion ratio is so high that the flow is strongly supersonic and the machine might meet critical choking at partial load [13].

This paper presents a study on the effects of fluid molecular complexity and thermodynamic non-ideality on both flow deviation and critical choking. The analysis is first addressed from a conceptual standpoint by resorting to theoretical models. Then, Reynolds Averaged Navier-Stokes (RANS) simulations are performed to obtain quantitative information on the value of flow deviation in a representative transonic ORC turbine vane. Results are compared against trends obtained by reduced-order physical models (ROM) that can be used for design purposes. Finally, a loss breakdown analysis is performed to gain further insights into the mechanisms of dissipation in the boundary layer and in the mixing region and their relation with flow deviation. The paper is structured as follows. Section 4.2 introduces the concept of corrected mass flow per unit area in swirling flows of dense vapors. Qualitative findings regarding the deviation downstream of a transonic turbine cascade, as well as the role of the isentropic exponent γ_{pv} on the flow expansion, are discussed. Section 4.3 reports the methodology and the results of the numerical assessment conducted on a representative transonic turbine cascade. The trends of both flow deviation (Sec. 4.3.2) and irreversible entropy generation (Sec. 4.3.3) with flow compressibility, fluid molecular complexity, and thermodynamic non-ideality are discussed. Insights on the physical mechanisms explaining such trends are also provided. The accuracy of the reduced order models is then evaluated against the numerical results. Finally, the main outcomes of this work are summarized in section 4.4.

4.2. THEORETICAL BACKGROUND

4.2.1. INFLUENCE COEFFICIENTS FOR COMPRESSIBLE SWIRLING FLOWS

Swirling flows (Fig. 4.1) are characterized by the presence of a meridional V_m and a tangential V_θ component of the velocity vector. Considering an infinitesimal control volume of radius $\mathrm{d}r$, angular sector $\mathrm{d}\theta$, and length $\mathrm{d}x$, the conservation equations for a swirling flow with variable cross-section area A, frictional wall stresses τ_w, variable radius r, and energy transfer as heat to the fluid $\mathrm{d}q$ read [14]

$$\frac{\mathrm{d}\rho}{\rho}+\frac{\mathrm{d}V_m}{V_m}+\frac{\mathrm{d}A}{A}=0, \tag{4.3}$$

$$\frac{\mathrm{d}p}{p}+\gamma_{pv}M_m^2\frac{\mathrm{d}V_m}{V_m}=\gamma_{pv}M_\theta^2\frac{\mathrm{d}r}{r}-\frac{1}{2}\gamma_{pv}\frac{M_m^2}{\cos\alpha}\frac{4C_\mathrm{f}\mathrm{d}m}{d_\mathrm{H}}, \tag{4.4}$$

$$\frac{\mathrm{d}V_\theta}{V_\theta}=-\frac{\mathrm{d}r}{r}-\frac{1}{2\cos\alpha}\frac{4C_\mathrm{f}\mathrm{d}m}{d_\mathrm{H}}, \tag{4.5}$$

$$\frac{\mathrm{d}T}{T}+\frac{G-(\gamma-1)}{\gamma_{pv}}\frac{\mathrm{d}p}{p}+\frac{G^2M^2}{\gamma-1}\frac{\mathrm{d}u}{u}=\frac{\mathrm{d}q}{c_pT}, \tag{4.6}$$

and they govern the conservation of mass, meridional momentum along the m direction, tangential momentum along the θ direction, and energy, respectively. In the equations, V is the absolute flow velocity, ρ the density, A the cross-section area, p the pressure, A_w the wetted surface area around the control volume, α the angle between the velocity vector and the meridional direction, G the Gr uneisen parameter for fluids [11], [15]. The contribution due to wall friction, τ_w, has been rewritten as a function of the non-dimensional friction coefficient C_f and of the so-called hydraulic diameter, defined as $d_\mathrm{H}=4A/p_\mathrm{w}$, where p_w is the wet perimeter of the wall. The relation between meridional and tangential velocity, in differential terms, is given by

$$\frac{\mathrm{d}V}{V}=cos^2\alpha\frac{\mathrm{d}V_m}{V_m}+\sin^2\alpha\frac{\mathrm{d}V_\theta}{V_\theta} \tag{4.7}$$

The arbitrary equation of state in the volumetric form $p=\rho ZRT$ together with the calorimetric equation of state $h=h(T,p)$, forming the thermodynamic model, close the set of equations. These can be combined in the following equation:

$$\frac{\mathrm{d}\rho}{\rho}=\frac{\gamma}{\gamma_{pv}}\frac{\mathrm{d}p}{p}-\frac{\gamma-1}{G}\frac{\mathrm{d}T}{T} \tag{4.8}$$

Similarly to the procedure shown in Chap. 2, the system of equations can be manipulated to obtain analytical relations between the infinitesimal variation of each flow quantity, for instance, pressure or temperature, and the variation of cross-sectional area, the energy transfer as heat, the change in radius, and the friction at the wall. Using this approach, it is possible to define a set of influence coefficients that relate the change of a given flow variable to the change of cross-sectional area, the energy transfer as heat, and

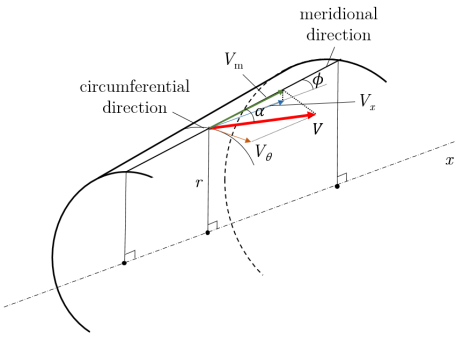

Figure 4.1: Axisymmetric swirling flow in a duct with velocity components.

the wall friction. Table 4.1 lists all the influence coefficients. All the relations can be cast as

$$\left.\begin{aligned} \Phi &= f_1\left(\frac{\mathrm{d}A}{A}\right) + f_2\left(\frac{\mathrm{d}q}{c_p T}\right) + f_3\hat{A} + f_4\hat{B}, \\ f_i &= f_i(\gamma, \gamma_{pv}, \Gamma, G, \Psi, M), \qquad i = 1, \ldots, 4, \end{aligned}\right\} \tag{4.9}$$

where Φ is the normalized differential variation of a thermodynamic or fluid dynamic variable, e.g., temperature or flow velocity, C_f is the Fanning friction factor, and d_H is the hydraulic diameter, and

$$\Psi \equiv \rho\left(\frac{\partial c^2}{\partial p}\right)_\rho = \gamma_{pv} + \left(\frac{\partial \gamma_{pv}}{\partial p}\right)_\rho p. \tag{4.10}$$

The parameters $\hat{A}$ and $\hat{B}$ are defined in Tab. 4.1. In contrast to the influence coefficients for the one-dimensional channel flow (Chap. 2), the coefficients f_i here depend on both the meridional and the tangential Mach numbers, and on the non-dimensional fluid properties γ, γ_{pv}, Γ, G, and Ψ. As a result, each of the flow quantities in the first column listed in Tab. 4.1 is given by the summation of the product between each independent variable in the first row and the corresponding influence coefficient.

4.2.2. CORRECTED MASS FLOW AND CRITICAL CHOKING

The corrected flow per unit area, which is a direct measure of the flow capacity of the stage [14], allows one to conceptually understand the influence of flow deviation on the performance of turbine cascades. This quantity is also particularly useful to examine choking regimes.

The expression of the corrected mass flow per unit area for ideal gas flows can be rearranged to highlight the role of the swirl velocity component. With reference to Fig. 4.1, the corrected flow per unit area reads

$$\dot{m}_\mathrm{corr} = \frac{\dot{m}\sqrt{RT_\mathrm{t}}}{p_\mathrm{t} A\sqrt{\gamma}} = \sqrt{\frac{T}{T_\mathrm{t}}}\frac{\rho}{\rho_\mathrm{t}}\frac{V_m}{\sqrt{\gamma RT_\mathrm{t}}} = M_\mathrm{m} f(M), \tag{4.11}$$

Table 4.1: Influence coefficients for a swirling flow.

	$\frac{\mathrm{d}A}{A}$	$\frac{\mathrm{d}q}{c_p T}$	$\hat{A} = \frac{\mathrm{d}r}{r} + \frac{1}{2\cos\alpha}\frac{4C_\mathrm{f}\mathrm{d}m}{d_\mathrm{H}}$	$\hat{B} = -\gamma_{pv} M_\theta^2 \frac{\mathrm{d}r}{r} + \frac{1}{2}\gamma_{pv}\frac{M_m^2}{\cos\alpha}\frac{4C_\mathrm{f}\mathrm{d}m}{d_\mathrm{H}}$
$\frac{\mathrm{d}p}{p}$	$\gamma_{pv}\frac{M_m^2}{1-M_m^2}$	$-\gamma_{pv}\frac{\gamma-1}{G}\frac{M_m^2}{1-M_m^2}$	$-\gamma_{pv} G \frac{M_m^2 M_\theta^2}{1-M_m^2}$	$-\frac{1+GM_m^2}{1-M_m^2}$
$\frac{\mathrm{d}T}{T}$	$-G\frac{M_m^2}{1-M_m^2}$	$\frac{1-\gamma M_m^2}{1-M_m^2}$	$\frac{G^2 M_\theta^2}{\gamma-1}\frac{1-\gamma M_m^2}{1-M_m^2}$	$\frac{G}{\gamma_{pv}(\gamma-1)}\frac{G(1+\gamma M_m^2)-(\gamma-1)}{1-M_m^2}$
$\frac{\mathrm{d}\rho}{\rho}$	$\frac{M_m^2}{1-M_m^2}$	$-\frac{\gamma-1}{G}\frac{1}{1-M_m^2}$	$-G\frac{M_\theta^2}{1-M_m^2}$	$-\frac{G+1}{\gamma_{pv}(1-M_m^2)}$
$\frac{\mathrm{d}V_m}{V_m}$	$-\frac{1}{1-M_m^2}$	$\frac{\gamma-1}{G}\frac{1}{1-M_m^2}$	$\frac{GM_\theta^2}{1-M_m^2}$	$\frac{G+1}{\gamma_{pv}(1-M_m^2)}$
$\frac{\mathrm{d}V_\theta}{V_\theta}$	0	0	-1	0
$\frac{\mathrm{d}V}{V}$	$-\frac{\cos^2\alpha}{1-M_m^2}$	$\frac{\gamma-1}{G}\frac{\cos^2\alpha}{1-M_m^2}$	$-\frac{1-(G+1)M_m^2}{1-M_m^2}\sin^2\alpha$	$\frac{G+1}{\gamma_{pv}}\frac{\cos^2\alpha}{(1-M_m^2)}$
$\frac{\mathrm{d}s}{c_p}$	0	1	$\frac{G^2 M_\theta^2}{\gamma-1}$	$\frac{G^2}{\gamma_{pv}(\gamma-1)}$
$\frac{\mathrm{d}M_m}{M_m}$	$-\frac{1+(\Gamma-1)M_m^2}{1-M_m^2}$	$\frac{\gamma-1}{G}\left[\frac{\Gamma}{1-M_m^2}-\frac{\Psi}{2}\right]$	$\frac{\gamma-1}{G}\left[\frac{\Gamma}{1-M_m^2}-\frac{\Psi}{2}\right]$	$\frac{G+1}{\gamma_{pv}}\left[\frac{\Gamma}{1-M_m^2}-\frac{G}{G+1}\frac{\Psi}{2}\right]$

where M_m is the meridional Mach number, and

$$f(M) = \left(1 + \frac{\gamma - 1}{2} M^2\right)^{-\frac{\gamma+1}{2(\gamma-1)}}. \tag{4.12}$$

We are here neglecting the swirl component in the radial direction, i.e., $\phi = 0$ in Fig. 4.1.

Using the relations proposed by [16], Eq. 4.11 can be generalized to an arbitrary fluid in whichever state by making use of the isentropic exponent γ_{pv}. If the fluid state is sufficiently far from the critical point, the partial derivative in Eq. 4.1 can be neglected, and an analytical relation between γ_{pv} and Γ holds. Such an approximation has been exploited, for example, in some experimental and numerical works on turbine cascades for ORC power systems [10], [17]. The general definition of the corrected mass flow is thus given by

$$\dot{m}_\mathrm{corr} = \frac{\dot{m}\sqrt{Z_\mathrm{t} R T_\mathrm{t}}}{p_\mathrm{t} A \sqrt{\gamma_{pv}}} = \frac{M_m}{\left(1 + \frac{\gamma_{pv}-1}{2} M^2\right)^{\frac{\gamma_{pv}+1}{2(\gamma_{pv}-1)}}}, \tag{4.13}$$

where $Z_\mathrm{t} = p_\mathrm{t}/(\rho_\mathrm{t} R T_\mathrm{t})$ is the flow compressibility factor defined at total conditions. Further algebraic manipulation leads to

$$\dot{m}_\mathrm{corr} \simeq \frac{\dot{m}}{\rho_\mathrm{t} c_\mathrm{t} A} = \left(1 + \frac{\gamma_{pv} - 1}{2} M^2\right) \sqrt{\frac{M^2}{1 + \frac{\gamma_{pv}-1}{2} M^2} - \left(\frac{V_\theta}{\sqrt{\gamma_{pv,\mathrm{t}} Z_\mathrm{t} R T_\mathrm{t}}}\right)^2}, \tag{4.14}$$

where the second term under the square root is the so-called swirling parameter and denotes the amount of swirl of a given flow. Equation 4.14 shows the relation between the corrected flow per unit area and the swirling parameter. Using the isentropic relation $p_\mathrm{t}/p = f(M, \gamma_{pv})$, which is valid regardless of the thermodynamic state of the fluid [18], Eq. 4.13 can also be rewritten in terms of both pressure ratio and flow (swirl) angle, namely

$$\dot{m}_\mathrm{corr} = \left(\frac{p_\mathrm{t}}{p}\right)^{\frac{\gamma_{pv}+1}{2\gamma_{pv}}} \sqrt{\frac{2}{\gamma_{pv} - 1} \left[\left(\frac{p}{p_\mathrm{t}}\right)^{\frac{1-\gamma_{pv}}{\gamma_{pv}}} - 1\right]} \cos\alpha. \tag{4.15}$$

Note that the accuracy of the results obtained by applying the above equations depends on the actual variation of γ_{pv} along an expansion process and is therefore related to the extent of the flow non-ideality, namely on the relative difference between γ and γ_{pv}, and to the flow Mach number.

Equations 4.14 and 4.15 allow us to investigate the influence of the working fluid and the operating thermodynamic state on the swirling flow developing in turbine cascades. The entity of the deviation of the γ_{pv} value from that of the ratio of the specific heats γ is used to measure the fluid non-ideality. Figure 4.2 shows the contours of γ_{pv} for two fluids at a different level of complexity of their fluid molecules, namely siloxane MM and CO_2. These processes highlight that flow expansions in such machinery exhibit γ_{pv} values that not only non-monotonically vary over the process, but can also be significantly lower than the γ value of the fluid computed in the dilute gas state.

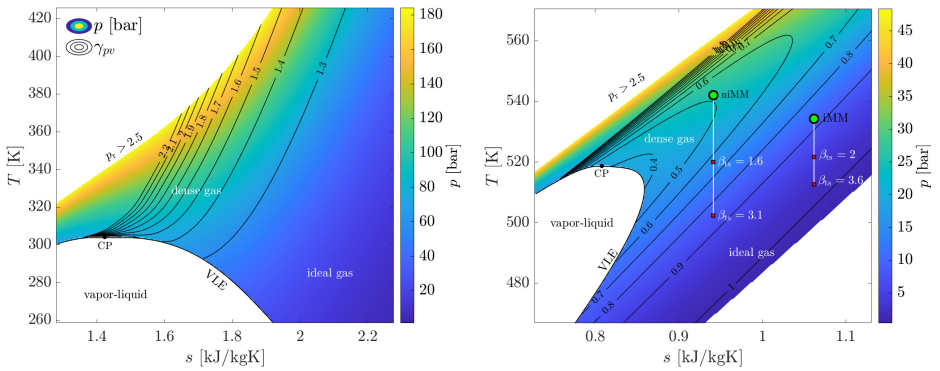

(a) (b)

Figure 4.2: Thermodynamic temperature-entropy diagrams of CO_2 (a) and siloxane MM (b). Pressure and γ_{pv} contours are reported. γ_{pv} values have been calculated using the relation $\gamma_{pv} = \gamma/(\beta_T p)$ (see Eq. 4.1), where β_T has been estimated resorting to a well-known database of fluid properties [19]. CP and VLE denote the critical point and saturation vapor-liquid curve. Figure 4.2b also shows the expansion processes of cases iMM and niMM, which are discussed in Sec. 4.3.

	M_{mol} [kg/kmol]	T_{cr} [K]	p_{cr} [bar]	γ_∞	$\gamma_{pv,\text{min}}$	$\gamma_{pv,\text{max}}$	Γ_∞
air	28.96	132.82	38.50	1.40	1.44	2.85	1.20
CO_2	44.01	304.13	73.77	1.29	0.86	4.33	1.13
cyclo-pentane	70.13	511.72	45.71	1.06	0.57	4.11	1.03
MM	162.3	518.70	19.31	1.03	0.39	4.75	1.01

Table 4.2: Characteristic fluid properties of air, carbon dioxide, and siloxane MM. γ_∞ is the specific heat ratio calculated in the dilute gas state. The lower and upper bound of γ_{pv} are those occurring in the thermodynamic region defined by $s > 1.01 s_{\text{cr}}$ and by the thermal stability limits of each molecule.

Table 4.2 lists the main properties of the fluids investigated in this work, together with the maximum and minimum values of γ_{pv} occurring in the thermodynamic region bounded by $p < 2.5 p_{\text{cr}}$ and $s > s_{\text{cr}}$. Note that the higher the molecular complexity, the lower the γ_{pv} value that the fluid exhibits in the considered thermodynamic region [11].

Figure 4.3 shows the trend of corrected flow per unit area as a function of the meridional Mach number M_{m} for two values of generalized isentropic exponent γ_{pv}. The first γ_{pv} value is representative of a dilute bi-atomic gas such as air, while the second one is representative of a dense organic vapor. In the charts, lines of constant absolute Mach number M, swirl angle α, and swirl parameter $\hat{V}_\theta = V_\theta / \sqrt{\gamma_{pv,\text{t}} Z_\text{t} R T_\text{t}}$ are also displayed. The graphs show that the vertical line corresponding to $M_m = 1$ passes through the maxima of the curves at constant $\hat{u}_\theta$. This means that critical choking in swirling flows is reached when the magnitude of the meridional velocity component equals that of the speed of sound and the flow is already in the supersonic regime, i.e., $M > 1$. The value of the total Mach number at which choking occurs strongly depends on the γ_{pv} value. For instance, by assuming $\hat{V}_\theta = 0.75$, critical choking is achieved at $M \approx 1.2$ for $\gamma_{pv} = 0.8$ and at $M \approx 1.4$ for $\gamma_{pv} = 1.4$. This finding has important consequences on both the

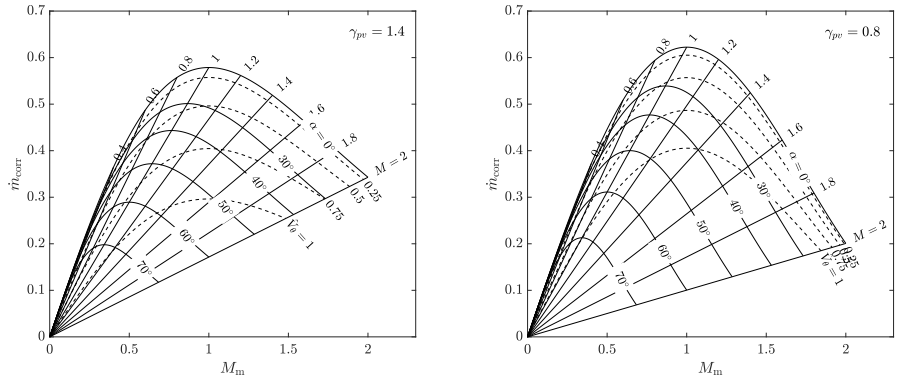

Figure 4.3: Corrected mass flow per unit area *vs* meridional Mach number for different values of total Mach number M, swirl angle α, swirl velocity parameter $\hat{V}_\theta$. Graphs are reported for the cases (a) $\gamma_{pv} = 1.4$ and (b) $\gamma_{pv} = 0.8$.

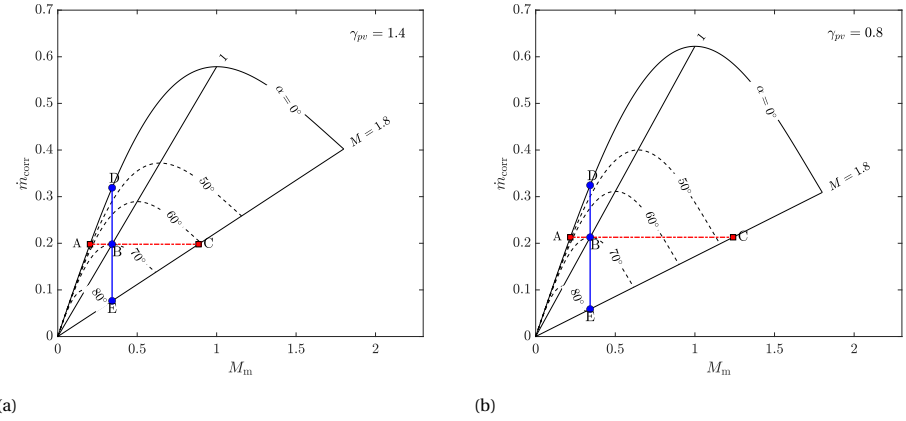

Figure 4.4: Characteristic flow state trajectories on the $\dot{m}_{\mathrm{corr}} - M_{\mathrm{m}}$ diagrams. Line A→C illustrates a process at constant $\dot{m}_{\mathrm{corr}}$; line D→E illustrates a process at constant M_{m}. Graphs are reported for the cases (a) $\gamma_{pv} = 1.4$ and (b) $\gamma_{pv} = 0.8$.

design and operation of a turbine. Given that the line at $M_m = 1$ represents the physical limit of operation of a turbine ($M_m > 1$ would entail the impossibility of the flow to adapt to outlet conditions), it is common practice to design swirling devices in the transonic/supersonic regime with sufficient margin from that limit. If the working fluid is in a condition such that $\gamma_{pv} < \gamma$ over the expansion process, the condition $M_m = 1$ would be reached at a lower value of absolute Mach number, and thus the turbine vane cannot be designed for highly supersonic flows. Conversely, if the working fluid is in a condition such that $\gamma_{pv} > \gamma$, no such problem exists. However, a quantitative estimate of suitable ranges of Mach number for safe operation can only be estimated once the amount of

c [m]	c_x [m]	γ [^{o}]	s [m]	α_1 [^{o}]	$\hat{\alpha}$ [^{o}]	t [mm]	σ_x
0.0205	0.0126	50.72	0.0172	0	68.8	0.054	0.73

Table 4.3: Geometry features of the iMM-Kis3 turbine stator blade. Here, t denotes the trailing edge thickness. See Fig. 5.3 for the nomenclature.

swirl is known.

Figures 4.4a-b provide further useful insights on turbine flows. Here, only a subset of the curves of Figs. 4.3a-b are displayed. The lines A-B-C and D-E identify two different gas-dynamic processes. The horizontal A-B-C line (constant corrected flow) represents the initial (point B) and final states of either a post-expansion (point C) or post-compression (point A) process occurring downstream of a choked turbine vane with $\alpha = 70°$. Over the B-C process, the flow is expanded up to $M = 1.8$ and deflected towards the meridional direction. The deviation from the initial condition at point B is $> 20°$ when $\gamma_{pv} = 0.8$ and $\approx 10°$ when $\gamma_{pv} = 1.4$. In other words, the post-expanding flow downstream of a stator row operating in a thermodynamic state such that $\gamma_{pv} < \gamma$ is subject to deviations that are significantly larger than those occurring in the $\gamma_{pv} > \gamma$ case. Because of that, the assumption of small or negligible flow deviation, underlying most of the mean-line design methods, is arguably incorrect for dense vapors of fluids made of complex molecules. A careful evaluation of the flow deviation downstream of the blade trailing edge becomes thus necessary during the preliminary design of the turbine. These considerations hold for convergent turbine nozzles: turbine nozzles designed to achieve a supersonic exit Mach number will not exhibit large flow deviation if operated at the design Mach number.

The vertical lines D-E in Figs. 4.4a-b exemplify a flow expansion in which the Mach number increases from ≈ 0.5 to ≈ 1.8 at constant $M_\mathrm{m} = 0.3$. This process represents an expansion in a supersonic axial turbine vane designed at a constant flow coefficient in which the post-expansion is negligible. During the expansion, the flow accelerates, the swirl angle increases from 0° to roughly 80°, and the corrected mass flow rate decreases because of the corresponding increase of annulus area. The reduction of $\dot{m}_\mathrm{corr}$ and the associated increase of annulus area is more pronounced with decreasing values of γ_{pv}, as a direct consequence of the increase in volumetric flow ratio ρ_t/ρ. This finding corroborates the previous results: the design of an efficient stator expanding a flow in dense-vapor thermodynamic states is arguably more challenging to accomplish.

4.3. COMPUTATIONAL RESULTS

4.3.1. METHODOLOGY

The qualitative outcomes of the theoretical analysis have been verified by performing RANS simulations of a representative cascade. Figure 5.3 shows the computational domain of the blade vane investigated in this study. The blade corresponds to the mid-span profile of the iMM-Kis3 turbine stator designed by Giuffré and Pini[9]. Table 5.1 lists the main specifications of the baseline axial stator, which consists of 42 blades in total, and is designed to work at total-to-static loading coefficient of $K_\mathrm{is} = 3$, flow coefficient of $\phi = 0.55$ and total-to-static degree of reaction of $\chi^* = 0.3$.

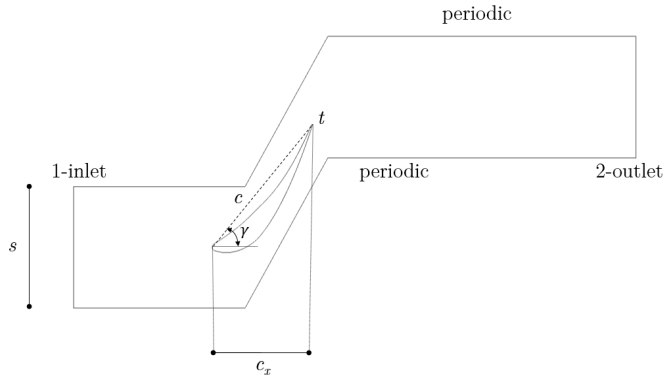

Figure 4.5: Sketch of the iMM-Kis3 turbine blade and relative flow domain.

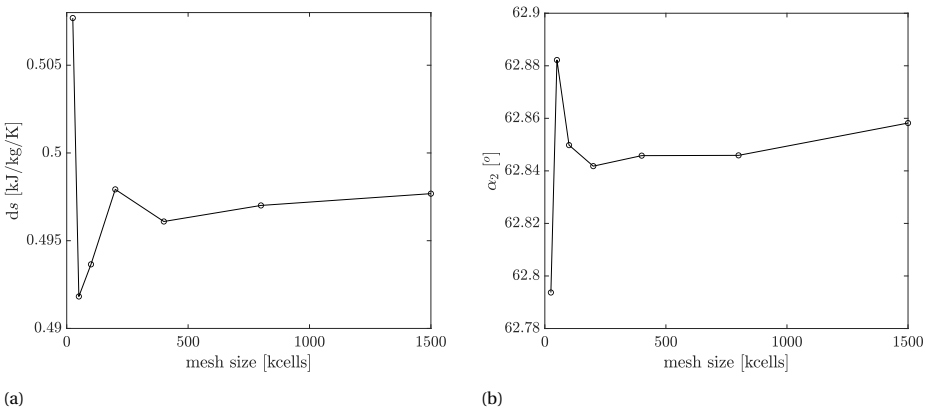

Figure 4.6: Mesh sensitivity analysis. (a) Entropy generation across the vane ($ds = s_2 - s_1$) *vs* mesh size. (b) Outlet flow angle *vs* mesh size.

To avoid upstream effects and enhance mixing downstream of the blade, the inlet and the outlet of the domain have been placed $\sim 1.5c_x$ upstream of the leading edge and $\sim 3.5c_x$ downstream of the trailing edge, respectively. Four different working fluids are considered, namely air (ideal gas), carbon dioxide (CO_2), cyclopentane and siloxane MM. Table 4.4 lists the cases considered in this study. For each test case, i.e., for each fluid, simulations with increasing values of β_{ts} (and thus of α_{ts}) have been carried out. The β_{ts} values have been chosen such that all regimes, from choking onset at the throat ($M_a = 1$) to the proximity of critical choking ($M_{x,2} \simeq 0.9$) are simulated.

The domain has been meshed with quadrilateral elements using the commercial grid generator of a well-known CFD software package [20]. To ensure proper mesh resolution, both local refinement in the proximity of the blade walls and average cell size are kept constant for all the investigated cases. The average cell size in the flow domain is set to $3.75 \cdot 10^{-5}$ m. Cell clustering is introduced near the blade walls to guarantee $y^+ < 1$.

case	fluid	$T_{t,in,r}$	$p_{t,in,r}$	$Z_{t,in}$	β_{ts}	α_{ts}	Re_2 [$\times 10^6$]
air	air ideal gas	3.56	0.39	1.0	2.4 - 4.0	1.9 - 2.7	1.5 - 1.3
iCO_2	carbon dioxide	3.0	1.0	1.0	2.3 - 4.1	2.0 - 3.3	3.8 - 3.1
iCP	cyclopentane	1.0	0.25	1.0	2.1 - 3.7	2.1 - 3.7	2.7 - 2.1
iMM	siloxane MM	1.03	0.5	0.84	2.0 - 3.6	2.2 - 4.0	3.7 - 2.9
niMM		1.045	1.3	0.41	1.6 - 3.2	2.35 - 5.7	11.8 - 8.1

Table 4.4: Test cases considered in this study. Total inlet conditions are normalized with the critical pressure and temperature of each fluid. The Reynolds number Re_2 is computed using the outlet flow conditions and the blade chord as reference length.

To ensure compatibility with the three-dimensional solver, the mesh has been extruded of $5 \cdot 10^{-6}$ m along the spanwise direction. Figures 4.6a-b show the results of the grid independence study conducted for the case niMM at $\beta_{ts} = 1.75$. For this study, results obtained with a mesh of 200k cells are deemed grid independent. The SST $k-\omega$ model is employed to compute the turbulent stresses as commonly done in these cases [21]. To ensure that all the flow processes occur in the dilute gas state ($Z \sim 1$), except for the niMM case), total pressure and temperature are prescribed at the domain inlet according to the values reported in Tab. 4.4. The desired total-to-static pressure ratio is obtained by fixing the value of the static pressure at the outlet. No-slip conditions are established at the blade walls. Translational periodic interfaces are set at the upper and lower bounds of the domain, while symmetry boundary conditions are assumed on the two remaining interfaces. A turbulent intensity value of 5% and a turbulent viscosity ratio $\mu_T/\mu = 10$ were used throughout this study. The turbulent Prandtl number is set to $Pr_t = 0.9$, in accordance with Otero *et al* [22]. The advective fluxes are discretized with total variation diminishing schemes. Turbulent fluxes are discretized with a first-order upwind scheme. A central difference scheme is used to discretize the viscous fluxes. The fluid properties are calculated with a look-up table approach, resorting to a well-known library for the estimation of thermophysical properties [19].

The values of the deviation obtained from CFD simulations are compared against those obtained from a reduced-order model (ROM). Following the analysis proposed by Denton [23], the ROM is based on a control volume approach to estimate the entropy generation due to mixing and the flow deviation downstream of the passage throat. Figure 4.7 shows the control volume used for the calculations. The volume is enclosed between the location of the throat (a) and the outlet section over which the flow is assumed to be fully mixed (mo). The flow at the throat is chocked, i.e., $M_a = 1$. The flow properties at the throat are calculated knowing the values of the inlet total conditions, according to Tab. 4.4, and the entropy s_a evaluated at the throat. s_a is computed as the sum of the entropy generated within the blade boundary layers Δs_{bbl} and the entropy s_{in} at the passage inlet. The Δs_{bbl} value is calculated using the reduced-order model described by Giuffré and Pini [9]. With reference to the nomenclature in Fig. 4.7, the mass conservation, axial momentum balance, tangential momentum balance, and energy conservation equations for the considered control volume read, respectively,

$$\rho_a V_a \left(a - \delta^*\right) = \rho_{mo} V_{mo} \cos\alpha_{mo} s = \dot{m}, \tag{4.16}$$

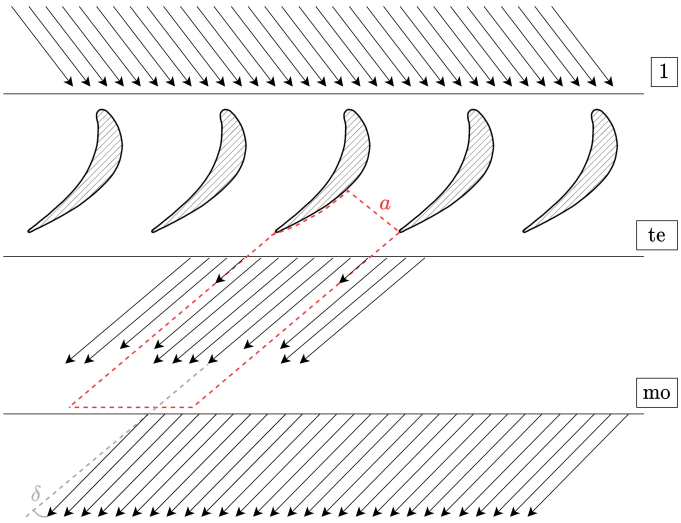

Figure 4.7: Control volume used for the estimation of flow deviation and mixing losses.

$$p_a a + p_b t + p_{ss} l \sin\psi + \dot{m} V_a - \rho_a V_a^2 \theta s = \dot{m} V_{mo} \cos\delta + p_{mo} \cos\alpha_a s, \tag{4.17}$$

$$p_{ss} l \cos\psi = p_{mo} \sin\alpha_a s + \dot{m} V_{mo} \cos\delta, \tag{4.18}$$

and

$$\dot{m}\left(h_a + \frac{V_a^2}{2}\right) - \rho_a \frac{V_a^3}{2}\theta^* = \dot{m}\left(h_{mo} + \frac{V_{mo}^2}{2}\right). \tag{4.19}$$

where $\delta = \alpha_{mo} - \alpha_a$, α_a being the gauge angle, i.e. $\alpha_a \sim \arccos(a/s)$, and α_{mo} the flow angle at the outlet. p_{ss} denotes the pressure acting over the rear length of the blade suction side, while ψ identifies the angle between the camber line at the trailing edge and the segment l connecting the trailing edge to the intersection between the throat and the suction side. For simplicity, we assumed $\psi = 0$ for all the cases investigated in this work. At the trailing edge, the displacement thickness δ^*, the momentum thickness θ, and the kinetic energy thickness θ^* are taken into account. Average values of these quantities have been set according to the results of the numerical simulations conducted in this work, i.e., $\delta^*/\theta = 1.6$, $\theta/t = 0.075$, and $\theta^*/t = 0.085$. The base pressure has been calculated according to correlations by Sieverding and Manna [24]. The system of equations is closed by a multiparameter equation of state (EoS) model [19]. Given the outlet pressure p_{mo} from the fixed β_{ts} values listed in Tab. 4.4, the solution of the system of equations provides the value of both the deviation δ and the mixing losses, which are computed as

$$\zeta_{mix} = \frac{T_{mo}\Delta s_{mix}}{h_{t,mo} - h_{mo}}, \tag{4.20}$$

where $\Delta s_{mix} = s_{mo} - s_a$ denotes the entropy generation between the mixed-out section and the throat.

Shock losses within the mixing region are estimated using the Rankine-Hugoniot relations for a dense vapor fluid [25]. The post-shock entropy s_{shock} is calculated knowing

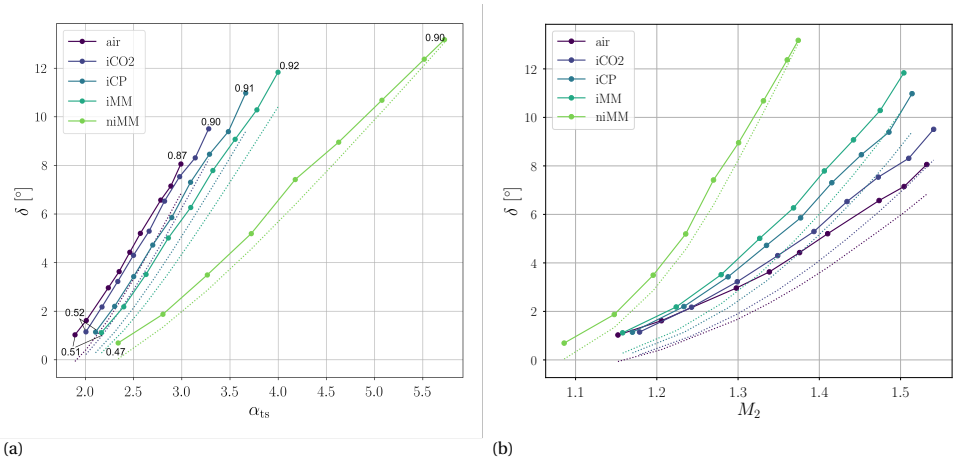

Figure 4.8: Flow deviation at the blade trailing edge *vs* volumetric flow ratio (a) and outlet Mach number (b) for the cases reported in Tab. 4.4. Continuous and dashed lines denote the results of CFD and of the reduced-order model, respectively. Values of the measured axial Mach number are also reported.

the values of both Mach number and pressure upstream of the shock and that of the shock angle. Relations for both the shock angle and the pre-shock state as a function of the fluid and β_{ts} have been developed by correlating the results of the RANS simulations performed in this study. The shock loss coefficient is then calculated as

$$\zeta_{shock} = \frac{T_{mo}\Delta s_{shock}}{h_{t,mo} - h_{mo}}, \tag{4.21}$$

where $\Delta s_{shock} = s_{shock} - s_a$ denotes the entropy generation between the post-shock state and the throat.

4.3.2. FLOW DEVIATION

Figure 4.8a shows the flow deviation downstream of the trailing edge as a function of the total-to-static volumetric flow ratio. For the dilute gas cases, the deviation increases with α_{ts}, with moderate quantitative differences among the various fluids ($\approx$ 14% at $\alpha_{ts} = 3.25$). The trends predicted by the mixing model are in good agreement with those obtained with CFD, with the ROM slightly underestimating the value of δ. The niMM case, instead, is characterized by values of deviation at fixed α_{ts} that are lower by approximately 42% at $\alpha_{ts} = 4$, as compared to those calculated for the iMM case. In summary, for a fixed value of the volumetric flow ratio, the flow deviation decreases with both the fluid molecular complexity and the degree of thermodynamic non-ideality, as measured by the average value of γ_{pv} over the expansion process. The opposite trend occurs if the deviation is plotted as a function of the outlet Mach number M_2 (Fig. 4.8b), i.e., δ increases when the average value of γ_{pv} decreases, for the same value of M_2.

Figure 4.8b also shows that the expansion needed to obtain an axial Mach number of 0.9 and, consequently, the critical choking of the cascade, decreases with the molecular complexity of the fluid and the thermodynamic non-ideality. When the thermodynamic

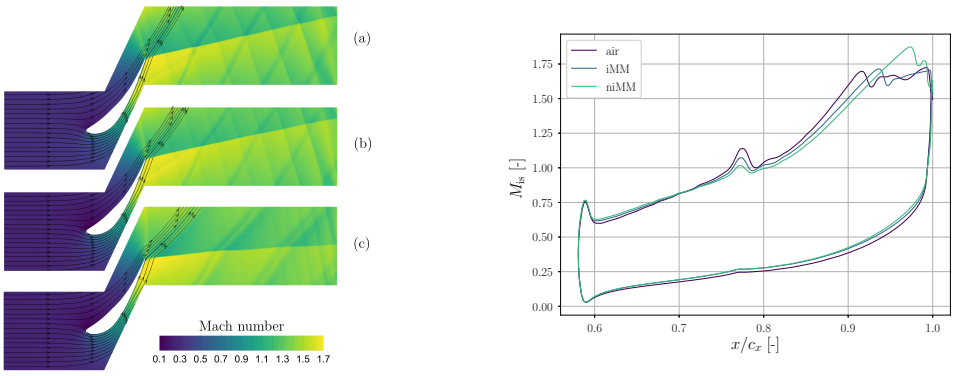

(a) (b)

Figure 4.9: (a) Detail of the flow at the blade trailing edge at $M_2 = 1.36$. Streamlines are traced in the proximity of the blade surface to highlight the flow deviation. (a) air, $\beta_{ts} = 3.2$ (b) iMM, $\beta_{ts} = 2.8$, (c) niMM, $\beta_{ts} = 3$. (b) Isentropic Mach number distribution over the blade for three different cases at fixed $M_2 = 1.36$.

state of siloxane MM approaches that of the critical point, the $M_{ax} = 0.9$ condition is reached at $M \sim 1.38$. Conversely, for the case iMM, such condition is reached at $M \sim 1.5$. Figure 4.9a displays the Mach number contours in both the vane passage and the wake for the three cases: air, iMM, and niMM at constant outlet Mach number. For the same cases, the blade loading is also depicted in Fig. 4.9b. The streamlines highlight that the flow deviation increases with the complexity of the working fluid and while approaching the dense vapor state.

Given the higher average value of γ_{pv} in the iMM expansion, the margin with respect to critical choking is larger if compared to the niMM case, in agreement with the results presented in Sec. 4.2. Conversely, when $\gamma_{pv} << \gamma$ (the niMM case, in this study), the critical choking onset occurs at lower Mach numbers, limiting thus the operability of the cascade. The reason why the flow deviation increases with Mach number, fluid molecular complexity and thermodynamic non-ideality can be inferred from an analogy with one-dimensional nozzle flows. For an arbitrary fluid, the area variation needed to obtain a desired Mach variation reads [5]

$$\frac{\mathrm{d}A}{A} = -\frac{1-M^2}{1+(\Gamma-1)M^2}\frac{\mathrm{d}M}{M} \tag{4.22}$$

where Γ is the fundamental derivative of gas dynamics. Given a supersonic expansion at a fixed inlet Mach number, the nozzle area increase $\mathrm{d}A$ required to obtain a fixed outlet Mach number is inversely proportional to Γ. Similarly to nozzle flows, for fluids operating in states where the Γ value is low, the expansion through a converging turbine cascade requires a larger post-expansion cross-section. The flow rotation due to the expansion fan at the trailing edge determines the entity of the flow deviation during post-expansion in the unguided region. Both fluid molecular complexity and thermodynamic state affect the entity of the rotation, which is described by the Prandtl-Meyer function $\nu(M)$. For a dense vapor fluid, an approximated relation for $\nu(M)$ can be retrieved by

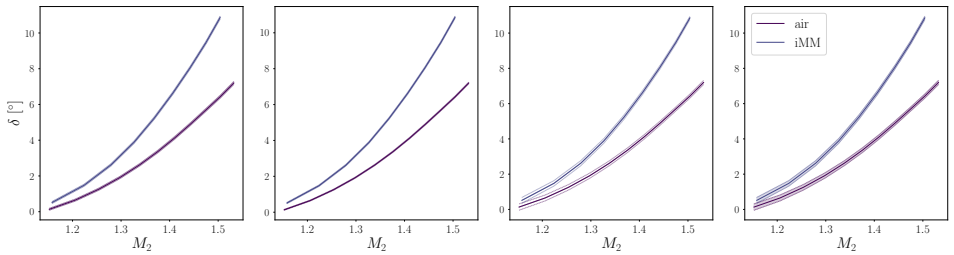

Figure 4.10: Sensitivity of the flow deviation to parameters of the ROM for the air and iMM cases. Sensitivity to (a) δ^*/θ, (b) θ/t, (c) θ^*/t and (d) base pressure coefficient p_b. The continuous red line is the deviation value obtained using the baseline value for each parameter. The shaded areas highlight the influence of each parameter if varied by 50% with respect to its baseline value.

solving the conservation equations and using the thermodynamic relations by Baltadjiev *et al* [18]. This yields

$$\nu(M) = \int \left(\sqrt{M^2-1}\right)\left(1+\frac{\gamma_{pv}-1}{2}M^2\right)^{-1}\frac{\mathrm{d}M}{M}. \tag{4.23}$$

Equation 4.23 holds under the assumption of constant γ_{pv} between static and stagnation quantities; this condition is usually satisfied if the state of the fluid is far from the vapor-liquid critical state, where large gradients of γ_{pv} do not occur. If γ_{pv} is assumed constant and >1, Eq. 4.23 can be integrated to obtain

$$\nu(M) = \sqrt{\frac{\gamma_{pv}+1}{\gamma_{pv}-1}}\arctan\sqrt{\frac{\gamma_{pv}-1}{\gamma_{pv}+1}(M^2-1)} - \arctan\sqrt{M^2-1}. \tag{4.24}$$

which differs from the canonical ideal gas version for the presence of the isentropic exponent γ_{pv} in place of γ. The value of the Prandtl-Meyer function increases with decreasing γ_{pv}, leading thus to increased flow turning at a fixed supersonic outlet Mach number. Experimental and numerical results by Dura Galiana *et al* [26] confirm this trend.

Large flow deviations have relevant implications for turbine design and operation. Larger deviations imply higher axial Mach numbers, thus limiting the maximum allowable stage volumetric flow ratio. Moreover, off-design operation becomes more challenging as critical choking occurs at a lower Mach number. Furthermore, an incorrect prediction of the flow deviation can lead to a sizeable offset in the power output of the turbine at the design point.

For completeness, Figs. 4.10a-c show the sensitivity of the deviation to variations in displacement thickness, momentum thickness, kinetic energy thickness and base pressure coefficient. Results are reported for air and siloxane MM (case iMM). In each graph, each parameter is varied by ±50% with respect to the baseline value, while the other two parameters are kept constant. For a fixed trailing edge thickness to pitch ratio, the influence of δ^*/θ, θ/t, and θ^*/t on the flow deviation is negligible. For the air case,

the maximum calculated variation is ~ 3% for δ^*/θ, ~ 1.5% for θ/t, and ~ 4% for θ^*/t. Larger discrepancies are observed in case of variations of the base pressure coefficient (Fig. 4.10c), with the largest offset being ~ 28% for air at $M_2 = 1.25$.

4.3.3. LOSS BREAKDOWN

The analysis has been complemented by comparing the loss trends computed with the models derived from first principles and the ones extracted from CFD simulations. The two investigated loss mechanisms are dissipation due to viscous stresses in the boundary layer, and viscous mixing occurring downstream of the trailing edge.

The boundary layer loss obtained from CFD simulations is computed according to the methodology described by Duan *et al* [27]. With reference to Fig. 4.11, first, the blade surface is partitioned into segments (Δl_i) and, for each couple of adjacent grid points (i and $i+1$), the normal to the surface is calculated. Then, for each point along the normal direction, the values of the flow quantities ρ, V, T, s are extracted by interpolating the simulation results evaluated at the adjacent grid points. This process is iterated up to the edge of the boundary layer, which is here deemed as the location where $\partial s/\partial y \rightarrow 0$. The entropy production rate per unit area within each control volume defined by two adjacent normals can then be computed using the second law of thermodynamics as

$$\dot{S} = \frac{d}{dx}\int_0^{\delta_{\mathrm{bl}}} \rho V(s - s_{\mathrm{e}})\mathrm{d}y. \tag{4.25}$$

The local value of the dissipation coefficient can be calculated by normalizing the entropy production rate as

$$C_{\mathrm{d}} = \frac{T_{\mathrm{e}}\dot{S}}{\rho_{\mathrm{e}} V_{\mathrm{e}}^3}, \tag{4.26}$$

and the overall specific entropy production due to boundary layer friction can be approximated as

$$\Delta s_{\mathrm{bbl}} = \frac{1}{\dot{m}}\oint_{\mathrm{blade}} \frac{C_{\mathrm{d}}\rho_{\mathrm{e}} V_{\mathrm{e}}^3}{T_{\mathrm{e}}}\, dl \approx \frac{1}{\dot{m}}\sum_i \frac{C_{\mathrm{d,i}}\rho_{\mathrm{e,i}} V_{\mathrm{e,i}}^3}{T_{\mathrm{e,i}}}\Delta l_{\mathrm{i}}. \tag{4.27}$$

The boundary layer dissipation can finally be computed as

$$\zeta_{\mathrm{bbl}} = \frac{T_2 \Delta s_{\mathrm{bbl}}}{h_{\mathrm{t},2} - h_2}. \tag{4.28}$$

Once the dissipation due to blade boundary layer friction is known, the remaining two-dimensional losses are divided into two components, see Mee *et al* [28]: wake-free losses and wake-induced losses. Wake-induced losses are those related to the trailing edge base region and the mixing of boundary layers downstream of the blade row. The wake region is identified by inspecting the pitch-wise trend of the turbulent kinetic energy k extracted from the CFD results at $x = x_{\mathrm{te}} + 0.5 \cdot c_x$, as displayed in Fig. 4.12b. The mass flow averaged entropy $\bar{s}_{\mathrm{w}}$ computed using entropy values at pitch-wise locations where $\kappa > 0.7 \cdot \kappa_{\max}$ is used to calculate the wake-induced loss coefficient, (see Fig. 4.12a), defined as

$$\zeta_{\mathrm{w}} = \frac{T_2 \Delta s_{\mathrm{w}}}{h_{\mathrm{t},2} - h_2}, \tag{4.29}$$

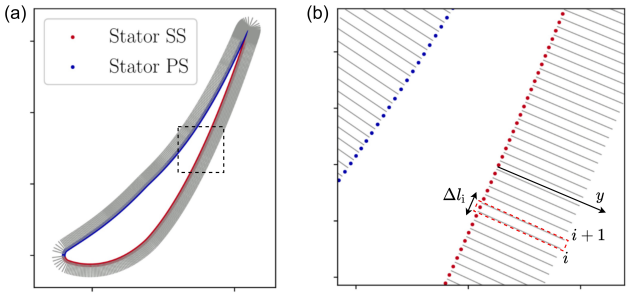

Figure 4.11: Computation of blade boundary layer loss from CFD data. (a) Evaluation of normals to the blade surface. (b) Calculation of entropy generation in each control volume through numerical quadrature.

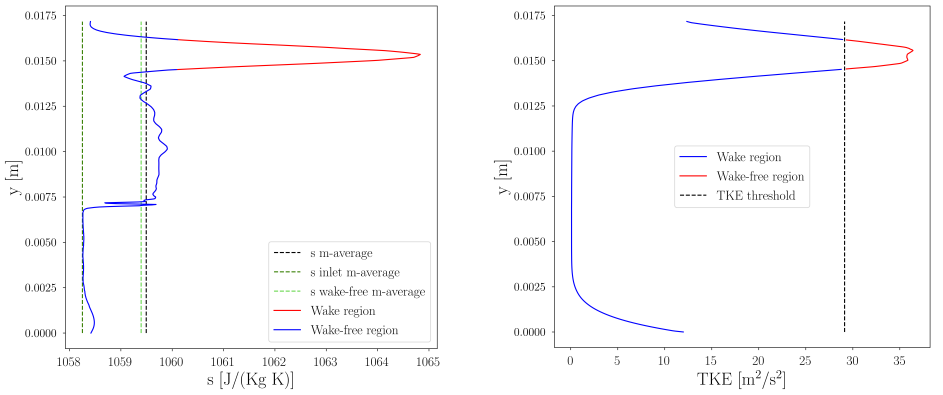

(a) (b)

Figure 4.12: (a) Entropy and (b) turbulence kinetic energy profile evaluated at $x = x_{te} + 0.5 \cdot c_x$ for test case iMM, $\beta_{ts} = 2.4$. The entropy profile is used to compute shocks-induced loss from CFD data.

where $\Delta s_w = \bar{s}_w - s_1 - \Delta s_{bbl}$. On the other hand, the entropy increase corresponding to $\kappa < 0.7 \cdot \kappa_{max}$ is mass flow averaged to obtain the wake-free loss coefficient, defined as

$$\zeta_{wf} = \frac{T_2 \Delta s_{wf}}{h_{t,2} - h_2}, \tag{4.30}$$

where $\Delta s_{wf} = \bar{s}_{wf} - s_1 - \Delta s_{bbl}$ and $\bar{s}_{wf}$ is the mass flow averaged wake-free entropy.

The stacked plots in Fig. 4.13 show the results of the loss breakdown analysis for the iMM (Figs. 4.13a, 4.13b) and the niMM (Figs. 4.13c and 4.13d) test cases. In particular, Figures 4.13a and 4.13c display the contribution of the boundary layer, wake-free and wake losses extracted from the CFD simulations, together with the overall loss computed with the ROM, for comparison purposes. Conversely, Figs. 4.13b and 4.13d display the contribution of boundary layer, shock, and mixing losses estimated with the ROM described in Sec.4.3.1, together with the total passage loss calculated by the RANS simulations. The trend of the total passage loss estimated with CFD is in agreement with that

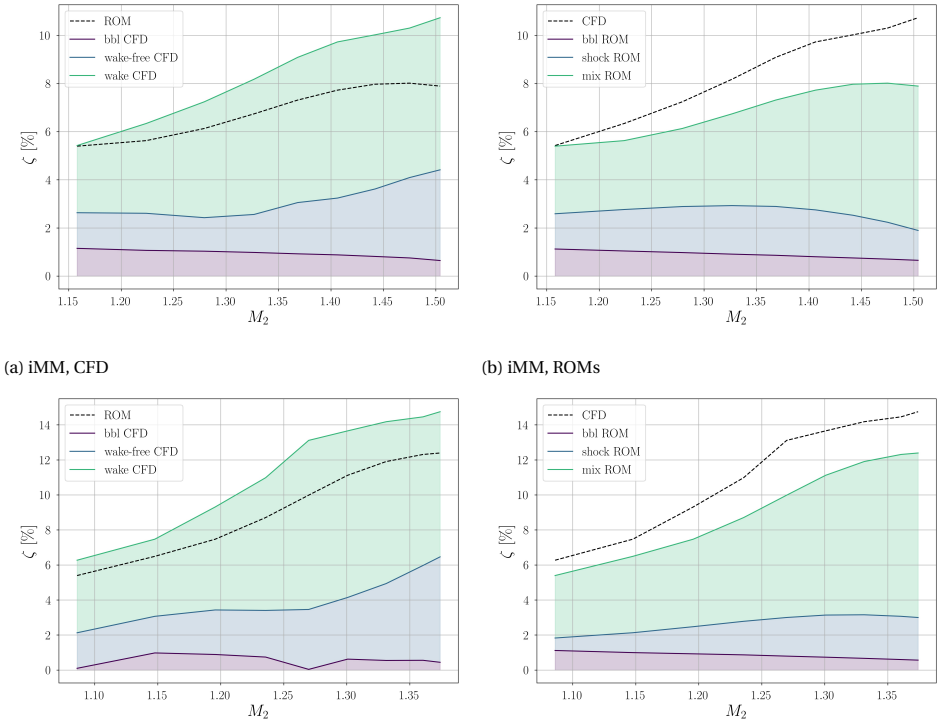

(a) iMM, CFD

(b) iMM, ROMs

(c) niMM, CFD

(d) niMM, ROMs

Figure 4.13: Loss breakdown for the (a-b) iMM and (c-d) niMM cases. Loss estimations from (a-c) CFD results and (b-d) ROMs of Sec. 4.3.1 are reported for both cases. The total passage loss estimated with (a-c)) ROMs and (b-d) CFD results are also reported in dashed lines.

calculated with the ROM. However, the ROM underestimates the total loss and the deviation scales with the outlet Mach number. This offset can be attributed to the shock loss model, which takes into account only the contribution of the main shock downstream of the trailing edge and does not account for the entropy generation due to secondary and reflected shocks, see Fig. 4.9a.

Figure 4.14a displays the variation of the values of specific entropy generation due to viscous effects in boundary layers as a function of the outlet Mach number for the cases of Tab. 4.4. The figure presents a comparison between results obtained with the reduced-order model developed by Giuffré and Pini [9] and those calculated by means of CFD simulations. Both models predict that boundary layer losses decrease with the outlet Mach number. Except for the non-ideal case niMM, in all other cases, the predicted value of dissipation at a fixed M_2 is rather similar. At $M_2 = 1.4$, the maximum variation between the various cases is $< 2\%$. Lower boundary layer losses are predicted in case the flow is non-ideal (niMM). The motivation is twofold. First, the fluid undergoing an expansion from a dense vapor state is affected by a larger density gradient if compared to a similar expansion in the ideal gas state. As a consequence, the specific entropy production rate,

which depends also on the density gradient along the blade surface, is larger in the niMM case, see equation 4.25. In turn, the difference between the two values is due solely to thermodynamics, given that the blade loading is almost constant at fixed outlet Mach number for all the considered cases, see Figure 4.9b. Second, at fixed blade loading, the value of the Reynolds number of the cascade is lower for expansions of fluids made of simple molecules in the dilute gas state and larger for expansions of dense organic vapors, see Tab. 4.4. As a consequence, lower values of dissipation coefficient and, thus, of fluid-dynamic loss, characterize dense vapor expansions.

Figure 4.14b shows the trend of the loss coefficient $\zeta_{\text{no-bbl}}$ due to dissipation occurring in the free-stream and in the wake region as a function of the outlet Mach number, for the cases of Tab. 4.4. In the CFD loss breakdown framework, the dissipation accounts for the wake and wake-free losses, while in the ROM it accounts for mixing and shock losses downstream of the throat. The dissipation increases with the outlet Mach number for all the considered cases. Moreover, flows of fluids made of complex molecules are affected by larger mixing losses. Results from CFD simulations and from the ROM are qualitatively in agreement. However, at fixed M_2, the ROM underestimates the losses compared to CFD simulation results. At $M_2 \sim 1.4$, the loss coefficient estimated by the two models differs by $\sim 2\%$. This discrepancy can be arguably attributed to the fact that the shock loss model does not account for the entropy generation due to shock wave reflection and secondary effects, i.e., boundary layer-shock interactions. Moreover, both methods predict a larger loss coefficient at fixed outlet Mach number for the niMM case compared to the dilute gas cases. At $M_2 = 1.36$, the mixing loss calculated for the niMM case is $\sim 6\%$ larger than the corresponding dilute gas case, i.e., iMM. Free-stream and wake losses are considerably larger than boundary layer losses, which are on the order of 1%. $\zeta_{\text{no-bbl}}$ is also plotted as a function of the volumetric flow ratio α_{ts} in Fig. 4.15a. Remarkably, $\zeta_{\text{no-bbl}}$ becomes only a function of α_{ts}, regardless of the working fluid and the thermodynamic state. This is in line with the findings by Giuffré and Pini [9].

The effect of the fluid molecular complexity and of the thermodynamic state on the mixing loss can be analytically evaluated by using a simplified version of the mixing model introduced in Sec. 4.3.1, see Osnaghi [1]. By neglecting the contributions of both the base pressure and the boundary layer quantities δ^* and θ, and by assuming $M_a = 1$ at the throat and by also assuming that a general equation of state model in the form $pv = ZRT$ holds, one can predict the flow deviation according to

$$\tan\delta = \frac{-\frac{\gamma_{pv}}{\gamma_{pv}-1}\frac{p_{\text{mo}}}{p_a}\tan\alpha_a}{1+\gamma_{pv}-\frac{p_{\text{mo}}}{p_a}} + \frac{\sqrt{\frac{\gamma_{pv}+1}{\gamma_{pv}-1}\left(1-\frac{p_{\text{mo}}}{p_a}\right)^2+\left(\frac{\gamma_{pv}}{\gamma_{pv}-1}\frac{p_{\text{mo}}}{p_a}\tan\alpha_a\right)^2}}{1+\gamma_{pv}-\frac{p_{\text{mo}}}{p_a}}, \tag{4.31}$$

$$\frac{V_{\text{mo}}}{V_a} = \frac{1}{\cos\delta}\left[1+\frac{1}{\gamma_{pv}}\left(1-\frac{p_{\text{mo}}}{p_a}\right)\right], \tag{4.32}$$

and

$$\frac{\rho_a}{\rho_{\text{mo}}} = \frac{p_a}{p_{\text{mo}}}\left[1+\frac{\gamma_{pv}-1}{2}\left(1-\frac{V_{\text{mo}}^2}{V_a^2}\right)\right], \tag{4.33}$$

where p_{mo}/p_a is the independent variable. Also here, relations between stagnation and static variables p, T, and Z have been estimated with the equations proposed by Baltad-

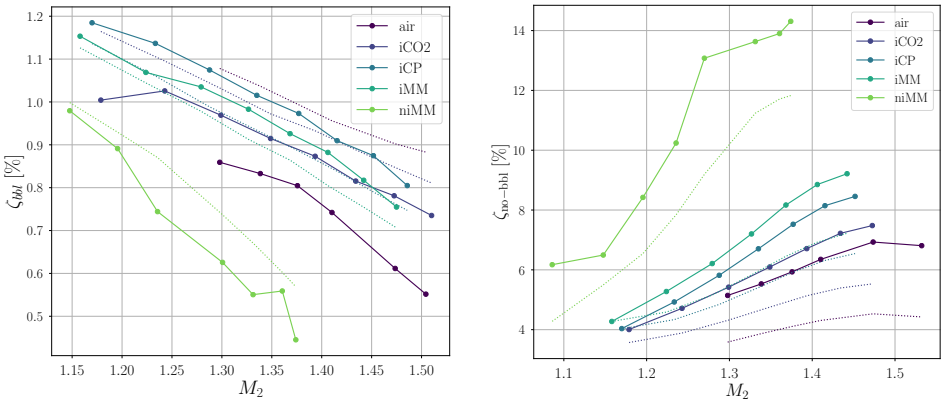

(a) (b)

Figure 4.14: Blade boundary layer loss (a) and trailing edge loss *vs* outlet Mach number M_2 for the cases reported in Tab. 4.4. Continuous and dashed lines denote the results of CFD and ROM, respectively.

jiev *et al* [18]. The approximated mixing loss can then be calculated as

$$\zeta^*_{\text{mix}} = \frac{\left(\frac{\gamma_{pv}+1}{2}\right)^{\frac{\gamma_{pv}}{\gamma_{pv}+1}} - \frac{p_{\text{mo}}}{p_a}\left(1+\frac{\gamma_{pv}-1}{2}M^2_{\text{mo}}\right)^{\frac{\gamma_{pv}}{\gamma_{pv}+1}}}{\left(\frac{\gamma_{pv}+1}{2}\right)^{\frac{\gamma_{pv}}{\gamma_{pv}+1}} - 1}. \tag{4.34}$$

Figure 4.15b shows the variation of the mixing loss with the throat-to-outlet density ratio, according to Eqs. 4.33-4.34. To account for both fluid molecular complexity and thermodynamic non-ideality, results are reported for three different values of the γ_{pv} exponent. The maxima of the curves identify the $M_{\text{mo},x} = 1$ condition, i.e., critical choking. The plots show that, for $\rho_a/\rho_{\text{mo}} < 1.7$, the mixing is unaffected by the value of γ_{pv}. This result is in qualitative agreement with those reported in Fig 4.15a. However, the maximum of the curves increases with decreasing values of γ_{pv}. Values of $\gamma_{pv} \sim 1$ characterize complex organic fluids such as siloxane MM, and these values decrease if the thermodynamic state of the fluid approaches that of the critical point. This is also in line with the trends that can be observed in Figs. 4.14b.

4.4. CONCLUSIONS

This paper documents an investigation of the flow deviation in transonic turbine cascades operating with non-ideal compressible flows. The definition of corrected mass flow per unit area has been extended to the case of swirling flows in the non-ideal compressible flow regime. The onset of critical choking, i.e., sonic meridional flow at the cascade outlet, and its relationship with flow deviation have been discussed. The influence of the working fluid on the corrected mass flow per unit area, the critical choking occurrence in transonic cascades, and the flow deviation at the blade trailing edge have been both theoretically and numerically investigated. Reduced-order models for the estimation of the flow deviation and the preliminary assessment of the two-dimensional

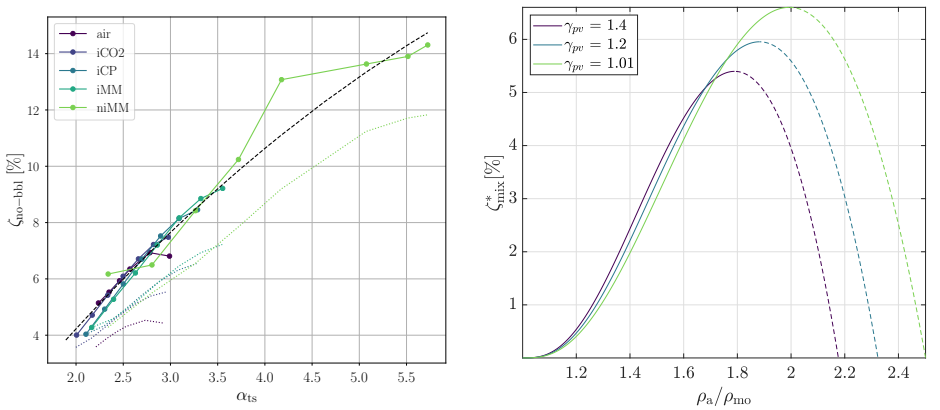

(a) (b)

Figure 4.15: (a) Mixing loss *vs* volumetric flow ratio α_{ts} for the cases reported in Tab. 4.4. Continuous and dashed lines denote the results of CFD and ROM, respectively. The dashed black line depicts a quadratic fit of the data; the fitted equation is reported in the Appendix. (b) Mixing loss *vs* throat-to-outlet density ratio according to the simplified model of equation 4.34.

losses have been derived and validated against the results of CFD simulations. The influence of the working fluid and of the thermodynamic state throughout the expansion has been assessed and quantified with the value of the generalized isentropic exponent γ_{pv}. Based on the outcomes of the work, the following conclusions can be drawn.

1. It is theoretically predicted that lower γ_{pv} values over the expansion entail a lower expansion ratio for the flow to reach critical choking conditions. Furthermore, the flow deviation substantially increases if $\gamma_{pv} < \gamma$.

2. Results from CFD simulations of the flow through a representative ORC turbine cascade corroborate the findings of the theoretical analysis. In particular, it is found that the reason for the increased flow deviation can be explained by means of the Prandtl-Meyer function.

3. The proposed reduced-order model provides accurate trends of flow deviation and mixing loss if compared to the values obtained from CFD simulations. Therefore, the reduced-order model can be used to predict the flow deviation during the preliminary design phase of unconventional axial turbines.

4. The value of the expansion ratio that leads to critical choking decreases with increasing thermodynamic non-ideality and molecular complexity of the fluid. This has consequences on the maximum expansion ratio for which the stage can be designed. For example, for a turbine cascade operating with siloxane MM in thermodynamic conditions similar to those of the niMM test case, the total-to-static expansion ratio cannot exceed ~ 3.

5. The total loss increases with flow compressibility, fluid molecular complexity, and decreasing values of the generalized isentropic exponent γ_{pv}. The largest share of

total loss is due to the mixing of wakes in the trailing edge region and the presence of shock waves.

6. It is found that the volumetric flow ratio is the most suited scaling parameter for cascade loss and flow deviation, regardless of the working fluid and the thermodynamic conditions.

Future work will address the study of the flow deviation in supersonic cascades for axial and radial turbines operating with non-ideal compressible flows. Experimental validation will also be paramount to provide confidence in the findings of this work.

4.5. ACKNOWLEDGMENT

This research has been supported by the Applied and Engineering Sciences Domain (TTW) of the Dutch Organization for Scientific Research (NWO), Technology Program of the Ministry of Economic Affairs, grant # 15837.

4.6. APPENDIX

The CFD results plotted in Fig. 4.15a have been fitted to obtain the following relationship between the loss occurring in the freestream and in the wake region and the volumetric flow ratio α_{ts}:

$$\zeta_{\mathrm{no-bbl}} = -0.220\alpha_{\mathrm{ts}}^2 + 4.527\alpha_{\mathrm{ts}} - 3.946 \tag{4.35}$$

Similarly, the model obtained by fitting the CFD results plotted in Fig. 4.8a resulted in the following relationship between the flow deviation, the volumetric flow ratio α_{ts} and γ_{pv}

$$\delta = -9.328 + 2.009\alpha_{\mathrm{ts}} - 0.104\alpha_{\mathrm{ts}}^2 + 2.112\gamma_{pv} - 4.191\gamma_{pv}^2 + 4.280\alpha_{\mathrm{ts}}\gamma_{pv} \tag{4.36}$$

NOMENCLATURE

SYMBOLS

A Nozzle area
a Throat length
C_{d} Dissipation coefficient
c Sound speed / Blade chord
c_p Specific heat capacity at constant pressure
c_v Specific heat capacity at constant volume
G Grüneisen parameter
h Specific enthalpy
M Mach number
$\dot{m}$ Mass flow rate
Pr_{t} Turbulent Prandtl number
p Pressure
r Radial coordinate
Re Reynolds number
s Specific entropy / Blade pitch

T Temperature
t Trailing edge thickness
V Absolute velocity
$\hat{V}_\theta$ Swirl parameter
v Specific volume
Z Compressibility factor
α Absolute flow angle
$\hat{\alpha}$ Blade metal angle at trailing edge
β Expansion ratio
β_T Isothermal compressibility
Γ Fundamental derivative of gas dynamics
γ Ratio of specific heats / Stagger angle
γ_{pv} Generalized isentropic pressure-volume exponent
δ Flow deviation
δ^* Boundary layer displacement thickness
θ Circumferential coordinate / Momentum thickness
θ^* Kinetic energy thickness
κ Turbulence kinetic energy
μ Dynamic viscosity
ρ Density
σ Blade solidity
ϕ Flow coefficient
χ Degree of reaction
Ψ Normalized thermodynamic derivative $\rho(\partial c^2)/(\partial \rho)_\rho$
ψ Isentropic loading coefficient / Trailing edge-to-throat angle

Subscripts

a Throat section
b Base
bbl Blade boundary layer
cr Critical
e Boundary layer edge
i i-th location
m Meridional component
mix Mixing
mo Mixed-out
r Reduced
ss Suction side
t Stagnation quantity
te Trailing edge
ts Total-to-static
x Axial component
θ Tangential component
∞ Dilute gas state ($v \to \infty$)

1 inlet
2 outlet

ABBREVIATIONS

CFD Computational fluid dynamics
CO_2 Carbon dioxide
MM Hexamethyldisiloxane
RANS Reynolds averaged Navier-Stokes
ROM Reduced-order model

BIBLIOGRAPHY

[1] C. Osnaghi, *Teoria delle turbomacchine*, 1st ed. Esculapio Editrice, 2002, ISBN: 88-86524-95-1.

[2] W. Traupel, *Thermische Turbomaschinen: Band 1: Thermodynamisch-strömungstechnische Berechnung*. Springer Berlin Heidelberg, 2019, ISBN: 978-3-662-13209-8.

[3] D. G. Ainley and G. C. R. Mathieson, "A method of performance estimation for axial flow turbines", Tech. Rep. 2974, 1951.

[4] P. Colonna, E. Casati, C. Trapp, *et al.*, "Organic Rankine Cycle Power Systems: From the Concept to Current Technology, Applications, and an Outlook to the Future", en, *Journal of Engineering for Gas Turbines and Power*, vol. 137, no. 10, p. 100 801, Oct. 2015, ISSN: 0742-4795. DOI: 10.1115/1.4029884.

[5] P. A. Thompson, "A Fundamental Derivative in Gasdynamics", en, *Physics of Fluids*, vol. 14, no. 9, p. 1843, 1971, ISSN: 00319171. DOI: 10.1063/1.1693693.

[6] D. A. Kouremenos and K. A. Antonopoulos, "Isentropic exponents of real gases and application for the air at temperatures from 150 K to 450 K", *Acta Mech.*, vol. 65, no. 1-4, pp. 81–99, Jan. 1987, ISSN: 0001-5970, 1619-6937. DOI: 10.1007/BF01176874.

[7] A. Romei, D. Vimercati, G. Persico, and A. Guardone, "Non-ideal compressible flows in supersonic turbine cascades", en, *Journal of Fluid Mechanics*, vol. 882, Jan. 2020, ISSN: 0022-1120, 1469-7645. DOI: 10.1017/jfm.2019.796.

[8] F. Tosto, A. Giuffré, P. Colonna, and M. Pini, "Non-ideal Effects in Compressible Swirling Flows", en, in *Proceedings of the 3rd International Seminar on Non-Ideal Compressible Fluid Dynamics for Propulsion and Power*, M. Pini, C. De Servi, A. Spinelli, F. di Mare, and A. Guardone, Eds., vol. 28, Series Title: ERCOFTAC Series, Cham: Springer International Publishing, 2021, pp. 36–43, ISBN: 978-3-030-69305-3. DOI: 10.1007/978-3-030-69306-0_5.

[9] A. Giuffre' and M. Pini, "Design Guidelines for Axial Turbines Operating With Non-Ideal Compressible Flows", en, *Journal of Engineering for Gas Turbines and Power*, vol. 143, no. 1, p. 011 004, Jan. 2021, ISSN: 0742-4795, 1528-8919. DOI: 10.1115/1.4049137.

[10] D. Baumgärtner, J. J. Otter, and A. P. S. Wheeler, "The Effect of Isentropic Exponent on Transonic Turbine Performance", en, *Journal of Turbomachinery*, vol. 142, no. 8, p. 081 007, Aug. 2020, ISSN: 0889-504X, 1528-8900. DOI: 10.1115/1.4046528.

[11] F. Tosto, C. Lettieri, M. Pini, and P. Colonna, "Dense-vapor effects in compressible internal flows", en, *Physics of Fluids*, vol. 33, no. 8, p. 086 110, Aug. 2021, ISSN: 1070-6631, 1089-7666. DOI: 10.1063/5.0058075.

[12] D. G. Wilson, "New Guidelines for the Preliminary Design and Performance Prediction of Axial-Flow Turbines", en, *Proceedings of the Institution of Mechanical Engineers, Part A: Power and Process Engineering*, vol. 201, no. 4, pp. 279–290, Nov. 1987, ISSN: 0263-7138. DOI: 10.1243/PIME_PROC_1987_201_035_02.

[13] C. M. De Servi, M. Burigana, M. Pini, and P. Colonna, "Design Method and Performance Prediction for Radial-Inflow Turbines of High-Temperature Mini-Organic Rankine Cycle Power Systems", en, *Journal of Engineering for Gas Turbines and Power*, vol. 141, no. 9, p. 091 021, Sep. 2019, ISSN: 0742-4795, 1528-8919. DOI: 10.1115/1.4043973.

[14] E. M. Greitzer, C. S. Tan, and M. B. Graf, *Internal Flow: Concepts and Applications*. Cambridge University Press, 2004, ISBN: 978-0-511-61670-9. DOI: 10.1017/CBO9780511616709.

[15] V. Arp, J. M. Persichetti, and G.-B. Chen, "The Grüneisen parameter in fluids", *J. Fluids Eng.*, vol. 106, no. 2, pp. 193–200, 1984, ISSN: 00982202. DOI: 10.1115/1.3243100.

[16] N. Baltadjiev, "An investigation of real gas effects in supercritical CO2 compressors", Ph.D. dissertation, Massachussets Institute of Technology, Sep. 2012.

[17] A. P. S. Wheeler and J. Ong, "The Role of Dense Gas Dynamics on Organic Rankine Cycle Turbine Performance", en, *Journal of Engineering for Gas Turbines and Power*, vol. 135, no. 10, p. 102 603, Oct. 2013, ISSN: 0742-4795, 1528-8919. DOI: 10.1115/1.4024963.

[18] N. D. Baltadjiev, C. Lettieri, and Z. S. Spakovszky, "An investigation of real gas effects in supercritical CO2 centrifugal compressors", *Journal of Turbomachinery*, vol. 137, no. 9, Sep. 2015, 091003/1–091003/13, ISSN: 0889-504X. DOI: 10.1115/1.4029616.

[19] E. W. Lemmon, I. H. Bell, M. L. Huber, and M. O. McLinden, *NIST standard reference database 23: Reference fluid thermodynamic and transport properties-REFPROP, version 10.0, National Institute of Standards and Technology*, 2018. DOI: 10.18434/T4JS3C.

[20] ANSYS, *Ansys workbench, release 19.3, ANSYS, canonsburg, pa*, 2019.

[21] N. Anand, S. Vitale, M. Pini, G. J. Otero, and R. Pecnik, "Design Methodology for Supersonic Radial Vanes Operating in Nonideal Flow Conditions", en, *Journal of Engineering for Gas Turbines and Power*, vol. 141, no. 2, p. 022 601, Nov. 2018, ISSN: 0742-4795. DOI: 10.1115/1.4040182.

[22] G. J. Otero R., A. Patel, R. Diez S., and R. Pecnik, "Turbulence modelling for flows with strong variations in thermo-physical properties", *Int. J. Heat Fluid Flow*, vol. 73, pp. 114–123, Oct. 2018, ISSN: 0142727X. DOI: 10.1016/j.ijheatfluidflow.2018.07.005.

[23] J. D. Denton, "The 1993 IGTI scholar lecture: Loss mechanisms in turbomachines", *Journal of Turbomachinery*, vol. 115, no. 4, pp. 621–656, Oct. 1993, ISSN: 0889-504X. DOI: 10.1115/1.2929299.

[24] C. Sieverding and M. Manna, "A Review on Turbine Trailing Edge Flow", en, *IJTPP*, vol. 5, no. 2, p. 10, May 2020, ISSN: 2504-186X. DOI: 10.3390/ijtpp5020010.

[25] D. Vimercati, G. Gori, and A. Guardone, "Non-ideal oblique shock waves", en, *Journal of Fluid Mechanics*, vol. 847, pp. 266–285, Jul. 2018, ISSN: 0022-1120, 1469-7645. DOI: 10.1017/jfm.2018.328.

[26] F. J. Durá Galiana, A. P. Wheeler, and J. Ong, "A Study of Trailing-Edge Losses in Organic Rankine Cycle Turbines", en, *Journal of Turbomachinery*, vol. 138, no. 12, p. 121 003, Jun. 2016, ISSN: 0889-504X. DOI: 10.1115/1.4033473.

[27] P. Duan, C. S. Tan, A. Scribner, and A. Malandra, "Loss Generation in Transonic Turbine Blading", en, *Journal of Turbomachinery*, vol. 140, no. 4, p. 041 006, Feb. 2018, ISSN: 0889-504X. DOI: 10.1115/1.4038689.

[28] D. J. Mee, N. C. Baines, M. L. G. Oldfield, and T. E. Dickens, "An Examination of the Contributions to Loss on a Transonic Turbine Blade in Cascade", en, *Journal of Turbomachinery*, vol. 114, pp. 155–162, 1992. DOI: https://doi.org/10.1115/1.2927979.

5

THE EFFECT OF WORKING FLUID AND COMPRESSIBILITY ON THE OPTIMAL SOLIDITY OF AXIAL TURBINE CASCADES

Part of the content of this chapter appeared in:
F. Tosto, M. Pini and P. Colonna, *The effect of working fluid and compressibility on the optimal solidity of axial turbine cascades*, Journal of the Global Power and Propulsion Society, 2023 (UNDER REVIEW).

The blade solidity, namely the blade chord-to-pitch ratio, largely affects the fluid-dynamic performance of turbomachinery and its cost. For turbo-machines operating with air or steam, the optimal value of the solidity which maximizes the efficiency is estimated with empirical correlations such as the ones proposed by Zweifel [1] and Traupel [2]. However, if the turbomachine operates with unconventional fluids, the accuracy of these correlations is questionable. Examples of such fluids are the organic compounds (e.g., hydrocarbons, siloxanes) used in organic Rankine cycle (ORC) power systems. This study concerns an investigation on how the working fluid, its thermodynamic state, and flow compressibility influence the optimum pitch-to-chord ratio of turbine stages. A first principle reduced-order model (ROM) for the computation of profile losses was developed for this purpose. The ROM results are compared with those obtained from numerical simulations of the flow over two axial turbine cascade geometries. The influence of both the working fluid, the flow compressibility, and the solidity value on both the boundary layer state at the blade trailing edge and the base pressure are evaluated. Models to compute mixing and passage losses in the compressible regime as a function of the axial solidity are proposed and discussed. Results show that the value of the optimal solidity of turbine cascades significantly increases with the flow compressibility, and mildly increases if the fluid is in the

dense vapor state. Moreover, the optimal solidity value is strongly affected by the mixing process occurring downstream of the blade trailing edge. Therefore, currently available models for its estimation, which are solely based on the minimization of the profile losses, are inaccurate.

5.1. INTRODUCTION

The value of the blade solidity, i.e., the ratio c/s between the chord and the pitch, strongly affects the cost and the performance of axial turbines. To reduce the weight and the cost of the machine, high blade spacing, and low solidity values are desired. However, efficient flow turning requires a sufficient number of blades. For low solidity values, the blade loading is high, causing poor fluid guidance and, therefore, flow separation over the rear suction side. Conversely, for high solidity values, the large cascade wetted area leads to considerable viscous dissipation. In summary, there is an optimum value of the axial solidity that minimizes the passage losses. In axial turbines operating with air or steam, this value can be estimated using the empirical correlations proposed by Zweifel [1] and Traupel [2]. The use of Zweifel's criterion is well documented also in recent literature [3]. Although the Zweifel correlation is still largely used to estimate the solidity of air, gas, or steam turbines, its accuracy has not been thoroughly assessed in the case of turbines operating with more molecularly complex working fluids. Examples of such fluids are organic compounds, e.g., fluorocarbons, hydrocarbons, or siloxanes, used as working fluids in organic Rankine cycle (ORC) power systems [4], [5]. These fluids are characterized by large molecular complexity and relatively high critical temperature. Turbines of ORC systems operate with comparatively higher stage expansion ratios than those of more conventional turbines. Moreover, part of the expansion typically occurs in thermodynamic states close to that of the critical point, therefore the flow is affected by non-ideal effects. The magnitude of non-ideal effects in dense vapor flows can be assessed by evaluating the variation of the generalized isentropic pressure-volume exponent [6], defined as

$$\gamma_{pv} = -\frac{v}{p}\left(\frac{\partial p}{\partial v}\right)_s = -\frac{v}{p}\frac{c_p}{c_v}\left(\frac{\partial p}{\partial v}\right)_T, \tag{5.1}$$

where γ is the ratio of the specific heats. If the fluid is in the dense vapor state, the γ_{pv} value changes over the expansion process and the internal flow field substantially depart from that characterizing turbo-machines operating with steam or air. For example, if the fluid is in the dense vapor state, the intensity of shock waves and expansion fans is quantitatively different from that characterizing ideal gas expansions [7]. Moreover, previous research works [3], [8] showed that compressibility effects in turbines operating with the fluid at least partially in the dense vapor state can be enhanced or mitigated depending on whether the γ_{pv} value exceeds that of γ evaluated for ideal gas states [7], [9].

Moreover, the non-ideality of the flow largely affects the loss breakdown, and, consequently, the blade design. All loss sources, i.e., those associated with viscous effects in boundary layers, with shocks, and with mixing at the blade trailing edge, depend on the thermodynamic state of the fluid and the level of flow compressibility [3]. Design parameters, such as the optimal solidity, thus arguably differ from those that would be obtained by applying existing guidelines [3], [10]. To the authors' knowledge, no design

guideline for the selection of the optimal solidity of turbomachinery operating with non-ideal compressible flows is documented in the literature. The only study on the accuracy of the Zweifel's correlation in the case of gas turbines is that of Doughty *et al* [11], who performed an experimental campaign on transonic stator cascades. They found that the Zweifel loading coefficient estimated from their experimental data was significantly higher than the value commonly used to design high-pressure turbine nozzles.

Furthermore, both the Traupel and the Zweifel correlations take into account only the passage loss, while the effects of either wake mixing or shock losses are not considered. As a consequence, the value of the optimal solidity prescribed by these correlations for axial turbines might lead to a sub-optimal design even in the case of steam, air, or gas turbines.

The focus of this study is an investigation of the influence of compressibility, fluid molecular complexity, and thermodynamic non-ideality on the optimal solidity of axial turbine cascades. The research documented in this chapter is a first step towards establishing guidelines for the selection of the optimal solidity for the preliminary design of turbomachines operating with non-ideal compressible flows. Based on Denton's approach [12] and on Coull and Hodson's method [13], a first-principle reduced-order model (ROM) not requiring the use of empirical coefficients was developed to estimate passage losses as a function of axial solidity. The resulting charts provide the value of optimal solidity as a function of cascade flow angles. Numerical simulations of the flow through two exemplary turbine blades were performed to assess the influence of both flow compressibility and axial solidity on losses and to verify the accuracy of the ROM. Optimal solidity values calculated by taking into account either passage losses alone or the overall loss within the domain are compared with the ones resulting from both the ROM and Zweifel's correlation. The influence of the working fluid and its thermodynamic state, flow compressibility, and solidity value on both the boundary layer state at the blade trailing edge and the base pressure is evaluated. Models to evaluate the mixing and the passage losses in the compressible flow regime as a function of the axial solidity are developed and discussed.

The chapter is structured as follows. Section 5.2 describes the approach used to study the effect of solidity on the performance of a turbine cascade. The setup of the computational fluid dynamics (CFD) simulations performed on two representative turbine cascade geometries is also presented. In Section 5.3, two physics-based reduced-order models (ROMs) for the estimation of the optimal solidity in turbine cascades operating with non-ideal flows, based on the incompressible and compressible flow assumption, respectively, are introduced and described. Section 5.4 offers a comparison between the results obtained from the CFD and those obtained from the ROMs. An overview of the limitations of each model is provided, concluding that the models are unsuitable for design purposes. Based on the CFD results, the influence of the flow field in the proximity of the blade trailing edge and in the mixing region on the optimal solidity is also discussed. Finally, Section 5.5 lists the main conclusions drawn from this study and outlines possible next steps.

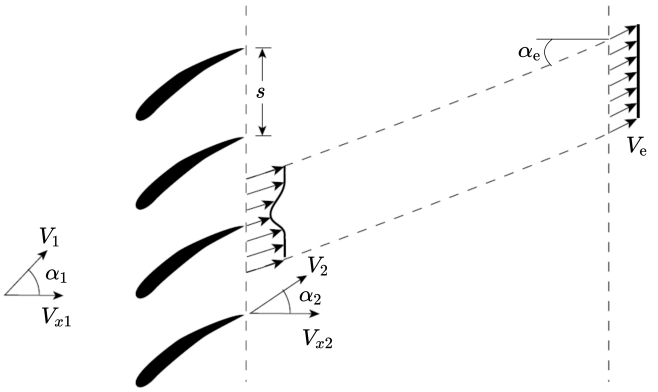

Figure 5.1: Control volume for the estimation of the mixing losses downstream of the blade trailing edge. Adapted from Greitzer *et al* [14]

5.2. EFFECT OF SOLIDITY ON CASCADE PERFORMANCE

The effect of solidity on the fluid dynamic performance of turbine cascades can be investigated, either numerically or experimentally, with three different methods: 1) by changing the blade solidity and optimizing its shape for minimum loss at each operating condition; 2) by changing the solidity for a fixed blade shape, but keeping constant the throat-to-spacing ratio for given operating conditions, thus varying the stagger angle of the cascade; 3) by solely changing the solidity, while keeping the blade shape fixed, and varying the operating conditions. This study is numerical and based on the second method. Following the same approach proposed by Doughty *et al* [11], the blade is rotated about the trailing edge to keep the gauge angle constant, regardless of the solidity value, see Fig. 5.2. The gauge angle χ is defined as

$$\chi = \arccos\left(\frac{o}{s}\right), \tag{5.2}$$

where o denotes the throat length.

In turbine cascades, passage losses are not the only contribution to the overall loss. The solidity can arguably have an effect also on the mixing process occurring downstream of the blade trailing edge which, in turn, contributes to the overall irreversible entropy generation across the cascade. As pointed out by Denton [12], mixing losses depend on the base pressure coefficient, as well as on the displacement and momentum thickness at the trailing edge of the boundary layers developing on the pressure and suction sides. For a compressible flow, mixing losses are also a function of the kinetic energy thickness of the boundary layer. With reference to the control volume shown in Fig. 5.1, where the subscript e denotes the station at which the flow is completely mixed-out, the mass, axial momentum, tangential momentum, and energy conservation equations for the mixing process occurring downstream of a turbine cascade read

Table 5.1: Geometry features of the *iMM-Kis3* and of the *Aachen* turbine blades. γ, α_{m}, and t denote the blade stagger angle, the blade metal angle at the trailing edge, and the trailing edge thickness, respectively.

	c [m]	c_x [m]	γ [^{o}]	s [m]	α_1	α_{m} [^{o}]	t [mm]
iMM-Kis3	0.0205	0.0126	50.72	0.0172	0	68.84	0.054
Aachen	0.0634	0.0543	31.04	0.0418	28.8	71.41	1.405

$$\rho_2 V_2 \left(1 - \frac{\delta^* + t}{s}\right) = \rho_{\mathrm{e}} V_{\mathrm{e}} \cos\alpha_{\mathrm{e}} = \dot{m}, \tag{5.3}$$

$$p_{\mathrm{e}} - p_2 = C_{\mathrm{pb}} \frac{t}{s}(p_{\mathrm{t2}} - p_2) + \rho_2 V_2^2 \left(1 - \frac{\theta}{s} - \frac{\delta^* + t}{s}\right)\cos^2\alpha_2 - \rho_{\mathrm{e}} V_{\mathrm{e}}^2 \cos^2\alpha_{\mathrm{e}}, \tag{5.4}$$

$$\rho_2 V_2^2 \left(1 - \frac{\theta}{s} - \frac{\delta^* + t}{s}\right)\cos\alpha_2 \sin\alpha_2 = \rho_{\mathrm{e}} V_{\mathrm{e}}^2 \cos\alpha_{\mathrm{e}} \sin\alpha_{\mathrm{e}}, \tag{5.5}$$

and

$$\dot{m}\left(h_2 + \frac{V_2^2}{2}\right) - \rho_2 \frac{V_2^3}{2}\theta^* = \dot{m}\left(h_{\mathrm{e}} + \frac{V_{\mathrm{e}}^2}{2}\right). \tag{5.6}$$

In the equations, δ^*, θ, and θ^* denote the displacement, momentum, and kinetic energy thickness, respectively, and p_{b} the base pressure. The base pressure is expressed in terms of the so-called *base pressure coefficient*, defined as

$$C_{\mathrm{pb}} = \frac{p_{\mathrm{b}} - p_2}{p_{\mathrm{t2}} - p_2}, \tag{5.7}$$

where p_{t2} is the stagnation pressure at the exit of the vane. For an incompressible flow, an analytical equation for the loss within the domain can be obtained by simplifying Eqs. 5.3-5.5. The total pressure-based loss coefficient is

$$\zeta_{\mathrm{inc}} = \frac{p_{\mathrm{t1}} - p_{\mathrm{t2}}}{\frac{1}{2}\rho V_1^2}, \tag{5.8}$$

which, for staggered flat plates with no incidence and constant thickness can be simplified as [12]

$$\zeta_{\mathrm{inc}} = -C_{\mathrm{pb}} \frac{t}{s} + 2\frac{\theta}{s} + \left(\frac{\delta^* + t}{s}\right)^2. \tag{5.9}$$

From these equations, it emerges that the base pressure coefficient and the boundary layer integral quantities strongly influence the mixing process and associated losses, ultimately affecting the optimal solidity value.

5.2.1. SETUP OF THE CFD SIMULATIONS

To assess the influence of the axial solidity σ_x on the fluid-dynamic losses, we performed a set of steady-state Reynolds Averaged Navier-Stokes (RANS) simulations of the flow around two blades characterized by different geometrical features. In agreement with the established practice of evaluating the profile losses, to whom the solidity strongly

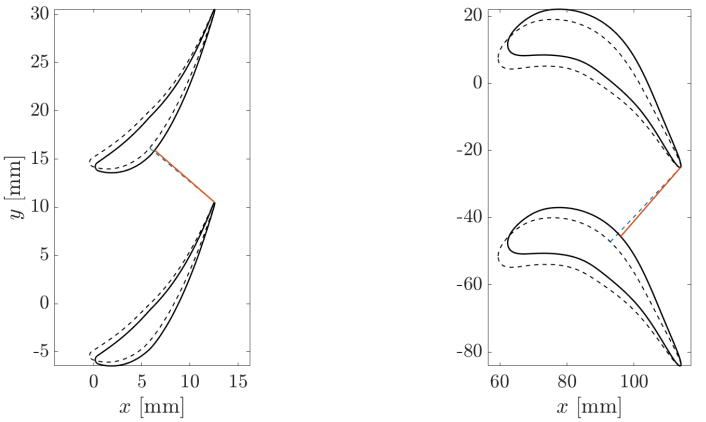

Figure 5.2: Geometric rotation of the blades about the trailing edge used to obtain the value of optimal solidity for (see nomenclature of Table 5.1) the (a) iMM-Kis3 and (b) Aachen turbine blades. Solid lines denote the original geometries, dashed lines are the rotated geometries. The throat length (orange: original geometry, dashed blue: rotated geometry) is varied accordingly to the solidity value to keep the gauge angle constant.

depends, at the blade midspan, two-dimensional computations are deemed sufficient for the scope of this research. Figure 5.3 shows the computational domain of the two blade geometries. The first blade geometry, hereafter referred to as *iMM-Kis3*, is the mid-span section of the turbine stator also considered in the study documented in Ref. [3]. This turbine stage has been designed to operate with siloxane MM, at inlet total temperature and pressure ensuring a compressibility factor of $Z \sim 1$, i.e., in dilute gas conditions. In this analysis, only the fluid-dynamic performance parameters calculated at the mid-span section have been considered. The baseline design of the stator consists of 42 blades featuring an axial solidity value of $\sigma_{x,\text{ref}} = 0.73$. This value has been calculated using the Zweifel criterion in the preliminary design phase, see Ref. [3]. The second blade geometry is the mid-span section of the rotor of the so-called *Aachen* turbine [15], which is representative of highly-loaded cascades. This is the case of, e.g., axial turbines of organic Rankine cycle power plants. The rotor of the *Aachen* turbine was designed to operate with air at a rotational speed of 3500 rpm and a mass flow rate of $\dot{m} = 6.8$ kg/s, with a corresponding outlet relative Mach number of $M_{\text{out,rel}} = 0.3$. The baseline design consists of 41 blades featuring an axial solidity value of $\sigma_{x,\text{ref}} = 1.3$. Table 5.1 lists the main geometrical specifications of both blades. Compared to the *iMM-Kis3* blade, the *Aachen* blade is front-loaded, i.e., characterized by a larger thickness in the proximity of the leading edge, whereas the *iMM-Kis3* is aft-loaded. Moreover, in the *Aachen* blade, the extension of the straight part of the rear suction side is longer, the trailing edge is thicker, and the leading edge is more rounded than in the *iMM-Kis3* blade.

To achieve constant χ for all axial solidity values, both blades are rotated around the trailing edge. Figure 5.2 illustrates the geometrical rotation of both blades. The inlet and the outlet of both domains have been placed $\sim 1.5c_x$ upstream of the leading edge and $\sim 3.5c_x$ downstream of the trailing edge, respectively to avoid upstream effects and to let the flow mix for several chord lengths downstream of the blade. Three sets of simulations

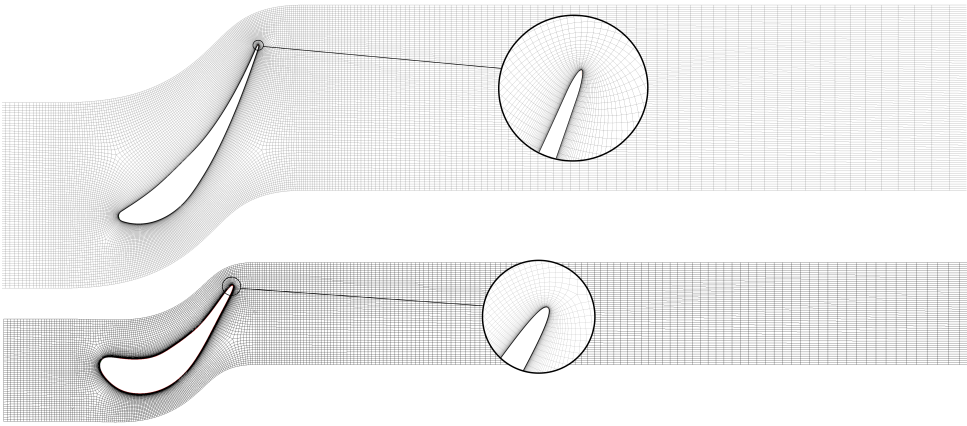

Figure 5.3: Computational grid for (a) the *iMM-Kis3*, an ORC vane expanding MM in the ideal gas state, and (b) the *Aachen* turbine blades. The axial solidity is the value at design conditions, i.e., $\sigma_{x,\text{ref}}$. Only one of every four grid lines is shown.

per blade are considered, each characterized by a different working fluid: for the simulations denoted with iN_2, the working fluid is nitrogen, a compound formed by simple molecules, while for those denoted with *iMM* and *niMM*, the working fluid is siloxane MM, an organic compound used as the working fluid in several ORC turbogenerators. The inlet total temperature and pressure of the iN_2 and *iMM* test cases are prescribed to ensure that the compressibility factor at the inlet is equal to one (ideal gas), while the inlet thermodynamic state of the *niMM* test case is that of a dense vapor. Table 5.2 lists the boundary conditions for each set of simulations.

To investigate the influence of compressibility on the optimal solidity value, three different values of the total-to-static expansion ratio β_{ts} are considered for each case. The first β_{ts} value leads to subsonic downstream Mach numbers ($M_{\text{out}} \sim 0.5$, M_{out} being the Mach number at the outlet of the domain), the second one leads to transonic flow ($M_{\text{out}} \sim 1$), while the third one is set to achieve supersonic flow ($M_{\text{out}} \sim 1.2$). For each value of β_{ts}, 16 different values of the axial solidity, ranging from $\sigma_x = 0.5$ to $\sigma_x = 1.6$ and from $\sigma_x = 0.6$ to $\sigma_x = 1.6$ for the *iMM-Kis3* and the *Aachen* blades, respectively, are considered.

The domain is meshed with quadrilateral elements using a commercial program for turbomachinery blade meshing [16]. A grid is generated for each value of the axial solidity σ_x, resulting in 8 different meshes for each of the two blades. Cell clustering is introduced near the blade walls to guarantee $y^+ < 1$. Figure 5.4 shows the results of the mesh sensitivity analysis for the baseline *iMM-Kis3* blade ($\sigma_{x,\text{ref}} = 0.73$). The graph shows that the deviation in the value of the overall dissipation coefficient ζ_s, defined as

$$\zeta_s = \frac{T_2 (s_2 - s_1)}{h_{\text{t},2} - h_2}. \tag{5.10}$$

between the 320k and the 640k cells meshes is 0.1%. For this study, the 320k cells mesh ensures the best compromise between accuracy of the results and computational cost.

Table 5.2: Setup of the numerical test cases. γ_∞ denotes the ratio of specific heats for $v \to \infty$. The Reynolds number is computed using the blade chord and the isentropic outlet conditions as reference. The last three columns list the values of three total-to-static expansion ratios investigated in each case.

iMM-Kis3	M_{mol} [kg/kmol]	γ_∞	p_{t1} [bar]	T_{t1} [K]
iN2	28	1.4	15	473.15
iMM	162.38	1.025	9.66	534.26
niMM	162.38	1.025	25.1	542.04
Aachen	M_{mol} [kg/kmol]	γ_∞	p_{t1} [bar]	T_{t1} [K]
iN2	28	1.4	15	473.15
iMM	162.38	1.025	9.66	534.26
niMM	162.38	1.025	25.1	542.04
iMM-Kis3	$Re_{2,\text{is}} \cdot 10^6$	$\beta_{\text{ts},1}$	$\beta_{\text{ts},2}$	$\beta_{\text{ts},3}$
iN2	1.75 – 2.50	1.2	2	2.6
iMM	4.47 – 6.29	1.2	1.7	2.2
niMM	12.1 – 17.63	1.075	1.5	2.2
Aachen	$Re_{2,\text{is}} \cdot 10^6$	$\beta_{\text{ts},1}$	$\beta_{\text{ts},2}$	$\beta_{\text{ts},3}$
iN2	5.38 – 7.63	1.2	2	2.6
iMM	15.89 – 18.85	1.15	1.7	2.2
niMM	37.26 – 50.91	1.075	1.5	2.2

All the mesh parameters, e.g., the growth rate of the cells in the proximity of the walls or the average cell size, are fixed and equal to those used for the baseline mesh also for the remaining 7 computational domains of the *iMM-Kis3* blade, which differ only in the value of the solidity and the related geometry rotation. The same mesh parameters have also been fixed for the *Aachen* blade mesh: at $\sigma_{x,\text{ref}} = 1.3$, the resulting mesh size consists of 440k cells.

A commercial CFD software [16] has been used to simulate the flow through the turbine cascades. The SST $k-\omega$ model [17] has been employed to compute the turbulence stresses. Stagnation pressure, stagnation temperature, and turbulent intensity are prescribed at the inlet, according to the values reported in Tab. 5.2. A turbulent intensity value of 5% and a turbulent viscosity ratio μ_T/μ equal to 10 were specified for all simulations. The turbulent Prandtl number was set to $Pr_\text{t} = 0.9$, in accordance with the indications listed in Ref. [18]. The advective fluxes were discretized with a second-order accurate scheme. First-order upwind schemes were instead used to discretize turbulent fluxes. Fluid properties are calculated with a look-up table method and tabulated values were computed with a well-known program [19].

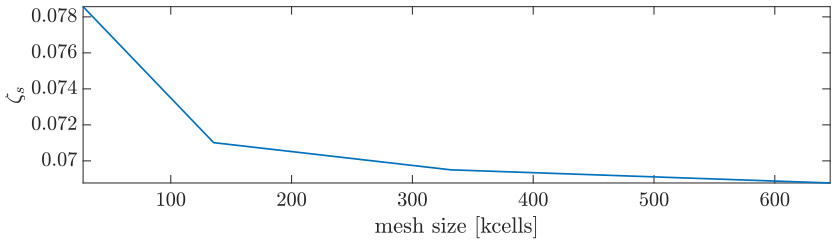

Figure 5.4: Variation of the overall dissipation coefficient ζ_s (Eq. 5.10) as a function of the number of grid cells for the *iMM-Kis3* test case.

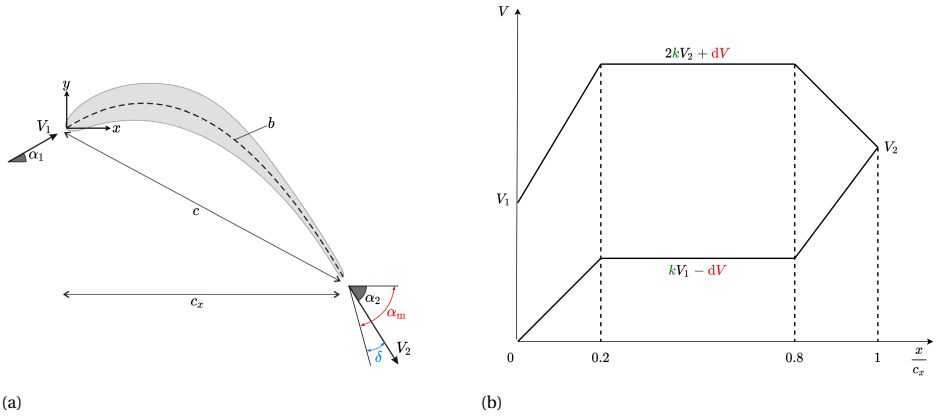

Figure 5.5: (a) Reference blade geometry for the reduced-order model. Blade thickness is neglected in this study. Adapted from Coull and Hodson [13]. (b) Simplified velocity distribution along the blade axial direction.

5.3. REDUCED-ORDER MODELS FOR THE ESTIMATION OF THE OPTIMAL SOLIDITY

Based on the approach proposed by Denton [12], two physics-based reduced-order models for the estimation of the optimal solidity in axial turbines have been developed. Both models are based on a simplified blade loading distribution and provide an estimation of the chord-to-pitch ratio value at which the passage loss is minimized. The first model (*iSol*) is applicable to incompressible flows, whereas the second (*cSol*), is its extension to compressible flows. Results obtained from these models are then compared against those obtained from the Zwifel criterion and from the CFD simulations.

5.3.1. ZWEIFEL CRITERION

The Zweifel criterion is based on the results of experimental campaigns conducted on subsonic turbine linear cascades. The model, in its most general form, reads

$$Z_{\mathrm{Zw}} = \frac{\text{actual blade loading}}{\text{ideal blade loading}} = \frac{\rho V_x (V_{y2} - V_{y1})}{(p_{t1} - p_2)\sigma_x}, \tag{5.11}$$

where ρ is the fluid density, p_{t1} the inlet total pressure, p_2 the outlet static pressure, V_{y1} and V_{y2} the tangential velocities at inlet and outlet, respectively, and V_x the average axial velocity. Z_{Zw} is a coefficient whose value ranges between 0.8 and 1.1 depending on the type of turbine and its application. For example, the Zweifel coefficient of low-pressure turbine stages of modern aircraft engines is approximately 1.1. For an incompressible flow, the correlation reads

$$\sigma_x = \frac{2\cos^2\alpha_2}{Z_{Zw}}\left(\tan\alpha_2 - \tan\alpha_1\right), \tag{5.12}$$

where α_1 and α_2 are the inlet and outlet flow angles.

5.3.2. PHYSICS-BASED MODEL FOR INCOMPRESSIBLE FLOWS (*iSol*)

The incompressible physics-based model has been developed by assuming an exemplary turbine blade geometry (Fig. 5.5a) whose loading is described by the simplified velocity distribution shown in Fig. 5.5b. The flow angles at the inlet and the outlet of the vane are α_1 and α_2, respectively, while δ is the deviation from the outlet metal angle α_m. The blade features a parabolic camber line with a slope at both the leading and the trailing edge equal to the tangent of the flow angles. These assumptions result in the geometric relation

$$\frac{y}{c_x} = -\frac{x}{c_x}\left(A\frac{x}{c_x} + B\right), \tag{5.13}$$

with $A = (\tan\alpha_2 - \tan\alpha_1)/2$ and $B = \tan\alpha_1$. The blade thickness is assumed negligible. Even if, in an actual turbine, the thickness distribution determines the blade loading, this assumption is deemed satisfactory for the given purposes. The velocity distribution, and, consequently, the blade loading, depend on the flow velocities V_1 and V_2 at the inlet and the outlet of the cascade. For an incompressible flow, V_1 and V_2 can be calculated knowing the axial velocity V_x, which is constant along the vane, and the flow angles α_1 and α_2. For a given set of flow angles and a given V_x, the blade loading solely depends on the values of the parameters k and $\mathrm{d}V$, which are independent of V_1 and V_2.

The circulation around the blade suction and pressure sides is equal to that around a control volume encompassing the inlet, outlet and the periodic mid-line of the vane, i.e.,

$$\int_0^1 \left(V_{ss} - V_{ps}\right)\sqrt{1+\left(2A\frac{x}{c_x}+B\right)^2}\,\mathrm{d}\left(\frac{x}{c_x}\right) = \frac{(V_2\sin\alpha_2 - V_1\sin\alpha_1)}{\sigma_x}, \tag{5.14}$$

where V_{ss} and V_{ps} are the values of the absolute velocity along the suction and pressure sides, respectively, and are defined by the distribution shown in Fig. 5.5b. The equation for the balance of the tangential momentum reads

$$\int_0^1 \left(V_{ss}^2 - V_{ps}^2\right)\mathrm{d}\left(\frac{x}{c_x}\right) = \frac{2V_x}{\sigma_x}\left(V_2\sin\alpha_2 - V_1\sin\alpha_1\right) = \frac{2V_x^2}{\sigma_x}\left(\tan\alpha_2 - \tan\alpha_1\right). \tag{5.15}$$

The pairs of k and $\mathrm{d}V$ values satisfying Eqs. 5.14-5.15 can be calculated by eliminating σ_x from the system of equations. For given values of the inlet and outlet flow angles, the

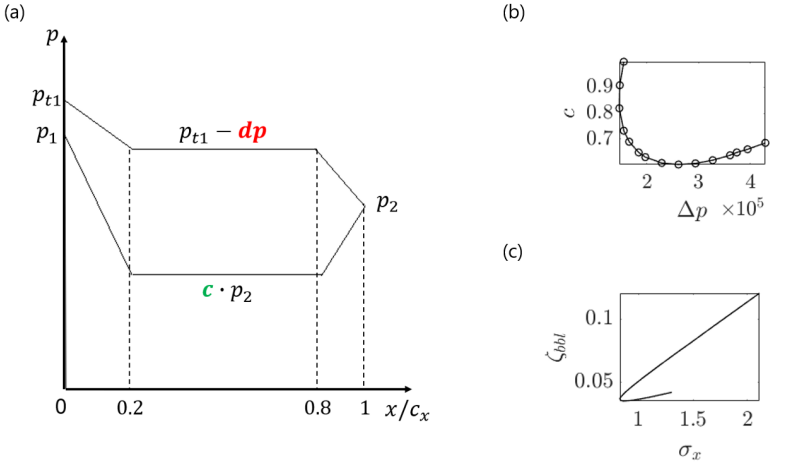

Figure 5.6: (a) Simplified pressure distribution along the blade axial direction. (b) Locus of c and Δp values satisfying Eqs. 5.14, 5.17 and 5.18 (c) Dissipation due to losses in the passage $vs\,\sigma_x$ computed for the c and Δp values shown in graph (b). For graphs (b) and (c), $\alpha_1 = 0^o$, $\alpha_2 = 68.84^o$, $\beta_{ts} = 1.4$. The thermodynamic inlet conditions match those of the *iMM* case.

optimal solidity value can finally be calculated by minimizing the normalized dissipation due to passage losses, defined as

$$\zeta_P = \frac{T\dot{S}_P}{1/2\dot{m}V_x^2} = \frac{2C_d\sigma_x}{V_x^3}\int_0^1 \left(V_{ss}^3 - V_{ps}^3\right)\sqrt{1+\left(2A\frac{x}{c_x}+B\right)^2}\,\mathrm{d}\left(\frac{x}{c_x}\right), \tag{5.16}$$

where C_d is the average boundary layer dissipation coefficient over the blade. Following Denton [12], C_d was assumed constant and equal to 0.002. Unlike Zweifel's correlation, the *iSol* model does not require any empirical closure coefficient, but only the values of the inlet and outlet flow angles, arguably ensuring improved accuracy.

5.3.3. PHYSICS-BASED MODEL FOR COMPRESSIBLE FLOWS (*cSol*)

To provide better estimations in the transonic and supersonic regimes, the incompressible model *iSol* has been modified to treat also compressible flow cases. In contrast to the incompressible case, the axial velocity is not constant but changes with the fluid density according to the mass conservation equation. Moreover, the thermodynamic and kinematic fields are now coupled, and the energy conservation equation is necessary to close the problem. Besides the flow angles α_1 and α_2, the model thus also requires as input the values of the inlet stagnation temperature T_{t1} and pressure p_{t1}, which fix the thermodynamic state of the fluid, and the total-to-static expansion ratio β_{ts}.

The *cSol* model is developed starting from the same simplified blade geometry described in Sec. 5.2 and shown in Fig. 5.5. The blade loading is calculated by integrating the simplified pressure distribution over the pressure and suction sides depicted in Fig. 5.6a, which varies according to the values of the two parameters c and $\mathrm{d}p$. The total pressure p_{t1} and the static pressures p_1 and p_2 define the values of the pressure distri-

bution at the leading and trailing edge: the outlet pressure p_2 is retrieved from the expansion ratio $\beta_{ts} = p_{t1}/p_2$. The inlet density ρ_1 value is set to $0.97\rho_{t1}$, while the entropy at the outlet is set to $s_2 = 1.0001 s_1$. These values have been chosen by averaging those obtained from the results of the CFD simulations performed on the *iMM-Kis3* blade and described in Sec. 5.2. The compressible form of the tangential momentum balance can be expressed as

$$\int_{(l_{ss}+l_{ps})} p\mathbf{n}\cdot\frac{\mathrm{d}\mathbf{l}}{c_{ax}} = \frac{\dot{m}}{s}\frac{V_2\sin\alpha_2 - V_1\sin\alpha_1}{\sigma_x}, \tag{5.17}$$

where p is the pressure over the blade. The energy conservation equation for streamlines following the blade pressure and suction side is given by

$$h_{t1} = h_{ps} + \frac{V_{ps}^2}{2} = h_{ss} + \frac{V_{ss}^2}{2}. \tag{5.18}$$

The combination of Eq. 5.18 with the fluid thermodynamic model allows the velocity distribution over the blade to be retrieved from the pressure distribution. In this study, the thermodynamic properties of the fluid are calculated using a well-known program [19]. The blade circulation equation (Eq. 5.14), which also holds in the compressible flow case, closes the system of equations. For a given set of flow angles and boundary conditions, there are infinite combinations of c and $\mathrm{d}p$ values satisfying Eqs. 5.14, 5.17 and 5.18. The locus of such c and $\mathrm{d}p$ combinations is shown in Fig. 5.6b. The dissipation due to passage losses, which reads

$$\zeta_P = \frac{T_2\dot{S}_P}{\frac{1}{2}\dot{m}V_2^2}, \tag{5.19}$$

where

$$\dot{S}_P = \int_{l_{ps}} \frac{C_d\rho_{ps}V_{ps}^3}{T_{ps}}\mathrm{d}l + \int_{l_{ss}} \frac{C_d\rho_{ss}V_{ss}^3}{T_{ss}}\mathrm{d}l, \tag{5.20}$$

is calculated for each combination of c and $\mathrm{d}p$ satisfying the Pareto front condition. The optimal solidity value corresponding to the minimum loss (Fig. 5.6c) is then evaluated.

5.4. COMPARISON OF MODEL RESULTS

Figures 5.7a-c show the loss breakdown for the *iMM-Kis3* blade obtained from the results of the CFD simulations, see Sec. 5.2. Each loss source is plotted as a function of the axial solidity for the *iN*$_2$, *iMM* and *niMM* cases, respectively, and for each value of the outlet Mach number corresponding to the β_{ts} reported in Tab. 5.2. The loss coefficient $\zeta_s = T_2\Delta s/u_2^2/2$, where the reference temperature and the flow velocity are computed at the outlet boundary, is used to quantify the dissipation produced by each loss source. For all cases, the curves labelled as MF and MO provide the overall entropy increase between the inlet and the outlet of the computational domain, calculated using both mass-flow (MF) and mixed-out (MO) averaging techniques, respectively. The contribution due to the passage losses (P) is calculated as the difference in mass-flow averaged entropy between the inlet section of the computational domain and a section placed in proximity of the trailing edge at $x = 0.98c_x$. The loss due to mixing (MIX) downstream

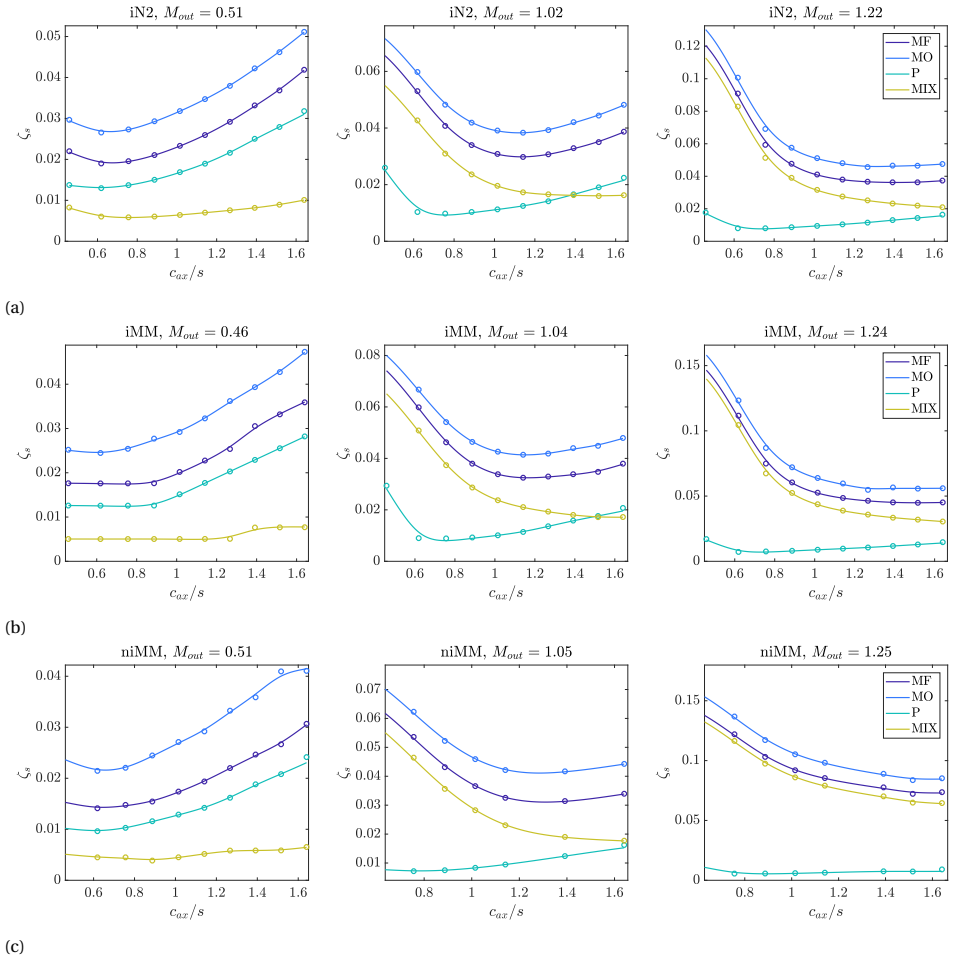

Figure 5.7: Normalized entropy generation *vs* blade axial solidity for the *iMM-Kis3* blade. (a) iN_2, (b) *iMM*, and (c) *niMM*. Left graphs - subsonic, centre graphs - transonic, right graphs - supersonic outlet Mach number. MF: overall mass-flow averaged loss; MO: overall mixed-out averaged loss; P: passage loss; MIX: mixing loss downstream of the blade trailing edge.

of the blade trailing edge, instead, is obtained by subtracting the passage loss from the overall mass-flow averaged one.

Results show that the optimal solidity value increases with the flow compressibility, i.e., with the cascade Mach number, regardless of the working fluid and the thermodynamic conditions. At subsonic operating conditions ($M_{\text{out}} \sim 0.5$, left graphs on Fig.5.7a-c), passage losses prevail over the mixing ones and determine the value of the solidity at which the overall losses are minimized. For all the investigated cases, both the passage and the overall MF and MO averaged losses exhibit a minimum at $\sigma_{x,\text{opt}} \sim 0.65$, and no influence of the fluid and its thermodynamic state is observed. At transonic and supersonic M_{out} values (centre and right graphs in Fig. 5.7a-c, respectively), mixing losses

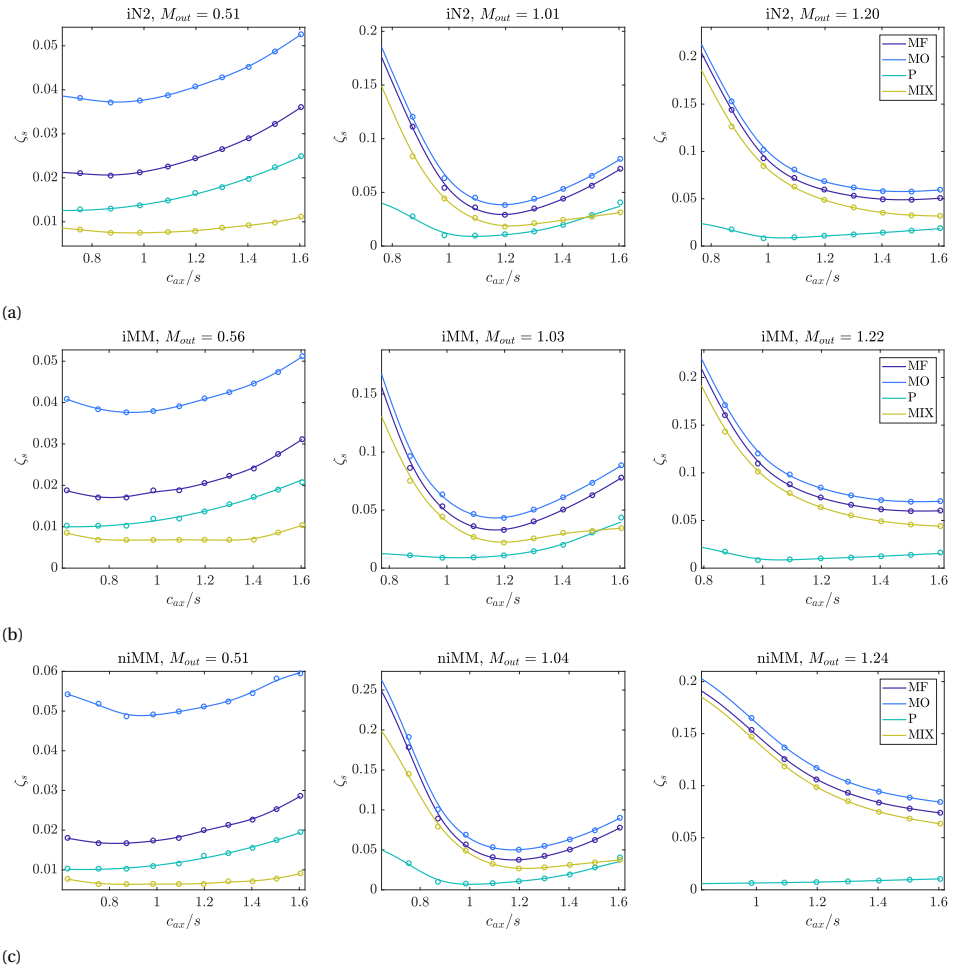

Figure 5.8: Normalized entropy generation *vs* blade axial solidity for the *Aachen* blade. (a) iN_2, (b) *iMM*, and (c) *niMM*. Left graphs - subsonic, centre graphs - transonic, right graphs - supersonic outlet Mach number. MF: overall mass-flow averaged loss; MO: overall mixed-out averaged loss; P: passage loss; MIX: mixing loss downstream of the blade trailing edge.

increase and prevail over the passage ones. Therefore, the optimal solidity value now strongly depends on the trend of the mixing losses. In the supersonic regime, in particular, a monotonically decreasing trend of the mixing losses with σ_x is observed for all the investigated cases. Conversely, little deviations are observed in the value of σ_x minimizing the passage losses ($0.65-0.75$ for all the investigated cases). At fixed solidity and operating conditions, larger mixing losses are observed if the expansion occurs in a complex organic compound (*iMM* and *niMM* cases) rather than in a fluid made of simple molecules (iN_2 case), and the overall loss is minimized at larger $\sigma_{x,\text{opt}}$ values. The increase in mixing losses is even larger if the organic fluid is operated in the dense va-

por state (*niMM* cases). In the transonic regime (central graphs in Fig. 5.7a-c), the $\sigma_{x,\mathrm{opt}}$ value at which the overall MF and MO losses are minimized is ~ 1.15 for the iN_2 and the *iMM* cases, and 1.25 for the *niMM* case. In the supersonic regime (graphs on the right in Fig. 5.7a-c), instead, the $\sigma_{x,\mathrm{opt}}$ value is found within the range 1.2 – 1.3 for the iN_2 case, 1.3 – 1.5 for the *iMM* case, and 1.5 – 1.6 for the *niMM* case.

Figure 5.8 shows the loss breakdown for the *Aachen* blade. Despite the blade being characterized by a larger flow turning and, consequently, a higher loading, the observed trends match those obtained for the *iMM-Kis3* blade: the $\sigma_{x,\mathrm{opt}}$ value minimizing the overall MF and MO losses increases with M_{out}, and the share of the mixing losses on the overall loss increases with M_{out}, exhibiting a decreasing monotonic trend with σ_x at supersonic regimes (right graphs in Fig. 5.8a-c). Depending on the flow regime, the passage losses are minimized at different values of σ_x: if $M_{\mathrm{out}} < 1$ (left graphs in Fig. 5.8a-c), the minimum is observed at $\sigma_x \sim 0.6$, while in the transonic and supersonic cases, the same minimum occurs at $\sigma_x \sim 1$ (centre and right graphs in Fig. 5.8a-c). Note that an optimal solidity value for the *niMM* case in the highly transonic regime (rightmost graph in Fig. 5.8c) has not been found: mixing losses are arguably minimized at larger σ_x values than those investigated in this study.

The physical reason that allows explaining the trends of the losses as a function of the solidity value can be obtained by inspecting the entropy contours of the *iMM-Kis3* blade displayed in Figs. 5.9a-c. The contour plots refer to the *iMM* case at $\beta_{\mathrm{ts}} = 1.7$ or, equivalently, $M_{\mathrm{out}} \sim 1$. At $\sigma_x \sim 0.65$ (Fig. 5.9a), the passage loss is minimized because of the low overall wetted area. However, the poor flow guidance provided by the blades causes flow diffusion on the rear part of the suction side, which entails a considerable boundary layer growth in the vicinity of the trailing edge. As a result, losses are significantly high due to the mixing of a higher portion of low momentum flow with the core flow. At $\sigma_x \sim 1.05$ (Fig. 5.9b), the wetted area increases, leading to an increase of the passage loss. However, mixing losses are lower than in the $\sigma_x \sim 0.65$ case due to the reduction of the flow diffusion in the rear suction side, thanks to the improved flow guidance. At $\sigma_x \sim 1.4$ (Fig. 5.9c), the magnitude of the passage losses equals that of the mixing one, leading to an overall increase of the loss coefficient. The same physical explanation, albeit with a different share of the losses, also applies to supersonic cases. The effect of the solidity on the wake at the blade trailing edge is also visible in the Mach number contours, see Fig. 5.10. The Mach number contour plots also highlight the presence of a shock wave in the proximity of the trailing edge. Similar considerations hold for the *Aachen* blade (not shown).

Figures 5.11a-b depict the trends of the optimal solidity value as a function of the M_{out} for the *iMM-Kis3* and the *Aachen* blades, respectively. Values of $\sigma_{x,opt}$ calculated considering the overall MF and MO loss, and the passage losses only are reported in the chart. The optimal solidity values calculated with Zweifel's criterion assuming $Z_{\mathrm{Zw}} = 0.85$, $Z_{\mathrm{Zw}} = 0.95$ and $Z_{\mathrm{Zw}} = 1.1$, and that estimated by the *iSol* model are also depicted. For both models, $\alpha_2 = \alpha_{\mathrm{m}}$, α_{m} being the outlet blade metal angle. For transonic and supersonic flows, both the *iSol* model and the Zweifel correlations do not provide the same optimal solidity value minimizing the overall loss that has been computed using CFD simulations. This is due to the inherent limitations of both models, which account for the passage loss only and rely on the incompressible flow assumption. For

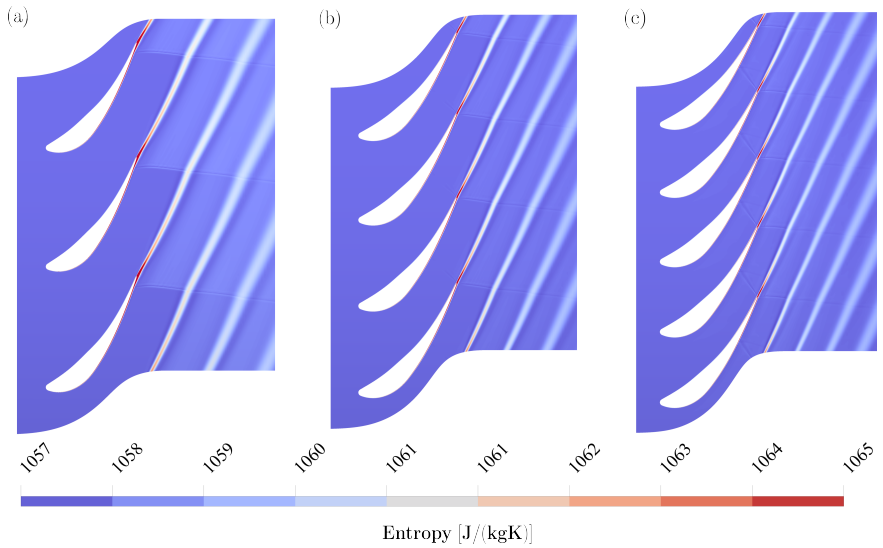

Figure 5.9: Entropy field in the proximity of the blade trailing edge for the *iMM-Kis3* blade, case iMM, $\beta_{ts} = 1.7$. (a) $\sigma_x \simeq 0.65$, (b) $\sigma_x \simeq 1.05$, (c) $\sigma_x \simeq 1.4$.

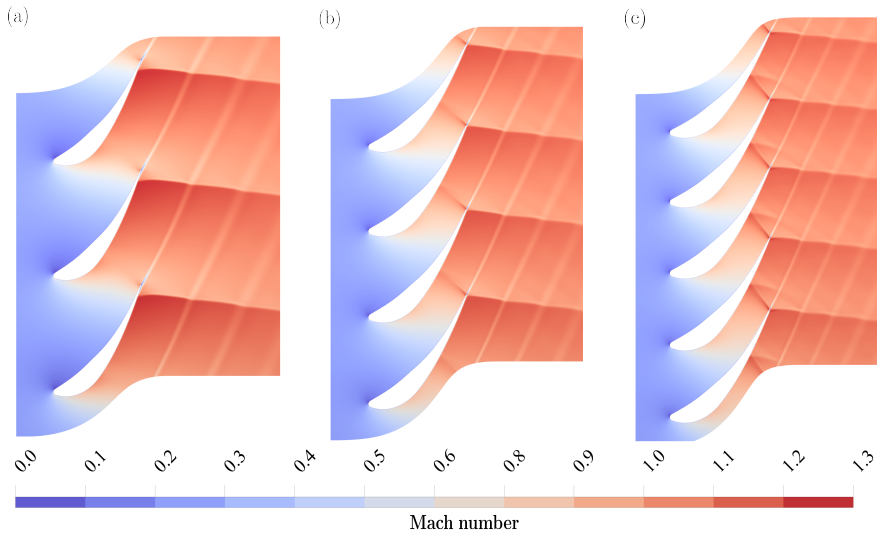

Figure 5.10: Mach number field in the proximity of the blade trailing edge for the *iMM-Kis3* blade, case iMM, $\beta_{ts} = 1.7$. (a) $\sigma_x \simeq 0.65$, (b) $\sigma_x \simeq 1.05$, (c) $\sigma_x \simeq 1.4$.

the *Aachen* blade, the transonic and supersonic cases also exhibit a higher value of the optimal solidity obtained by minimizing only the passage losses. In this blade, passage losses are affected by the presence of a reflected shock on the rear side of the suction side, which largely influences the value of the optimal solidity.

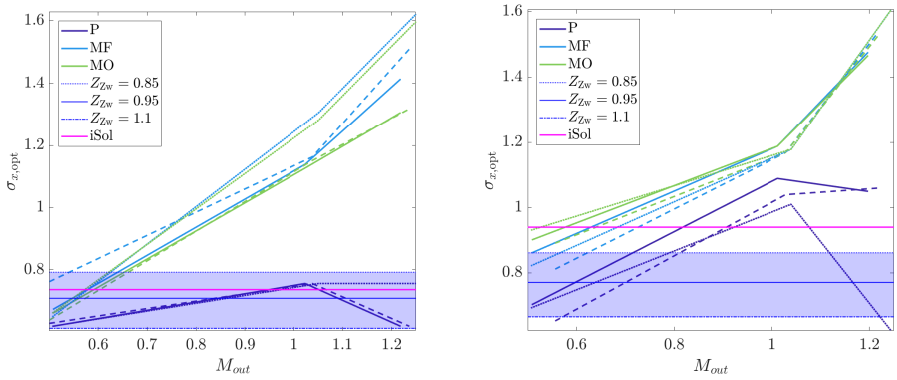

(a) *iMM-Kis3* (b) *Aachen*

Figure 5.11: Optimal solidity *vs* outlet Mach number for (a) the *iMM-Kis3* and (b) the *Aachen* blades. The values predicted by the reduced-order model (ROM) and the Zweifel correlation for three different values of the Z_{ZW} are also displayed. The region of validity of the Zweifel correlation for $Z_{ZW} = 0.8 - 1.1$ is also highlighted in blue. In both graphs, solid lines: *iN2*, dashed lines: *iMM*, dotted lines: *niMM*.

5

Figures 5.12a and 5.13a show the trends of $C_{pb}\, t/s$ as a function of the axial solidity obtained from the CFD simulations for all the cases listed in Tab. 5.2, and for the *iMM-Kis3* and the *Aachen* blades, respectively. Figures 5.12b-d and 5.13b-d, instead, show the trends of θ/s, $(\delta^* + t)^2/s^2$, and θ^*/s as a function of the axial solidity for the *iMM-Kis3* and the *Aachen* blades, respectively. The trends of the mixing losses observed in Figs. 5.7-5.8 are aligned with those of the three boundary layer parameters. No correlation is instead observed with the trends of the base pressure coefficient. It can then be argued that mixing losses are mainly a function of the state of the boundary layer at the trailing edge, which, in turn, is affected by the fluid molecular complexity and the thermodynamic state. Among the four parameters, the momentum and kinetic energy thickness trends exhibit a strong correlation with those observed for both the mixing and the overall loss: for both parameters, the minimum of the curves shifts towards larger solidity values at higher cascade Mach numbers, and the corresponding σ_x values are in line with the $\sigma_{x,\text{opt}}$ ones obtained from the CFD results (Figs. 5.7-5.8). Moreover, similarly to what has been observed for the loss breakdown, the fluid molecular complexity and the thermodynamic state move the minimum of both θ/t and θ^*/t towards larger σ_x values in the transonic and supersonic regimes. Regarding the displacement thickness, the subsonic and transonic cases follow the same trend as that of the overall loss and those of the other boundary layer integral quantities; conversely, the supersonic cases exhibit a minimum at $c_{ax}/s \sim 0.8$ for the *iMM-Kis3* blade, while no minimum is observed in the *Aachen* blade case. However, the contribution of the displacement thickness is smaller in magnitude compared to that of the momentum and kinetic energy thickness.

Figure 5.14a shows the contour plot of the computed optimal solidity values as a function of the flow angles calculated with the *iSol* model. These variations of optimal solidity are compared with those computed with the Zweifel correlation using two different values of the Zweifel coefficient (Fig. 5.14b-c). It can be observed that the optimal σ_x

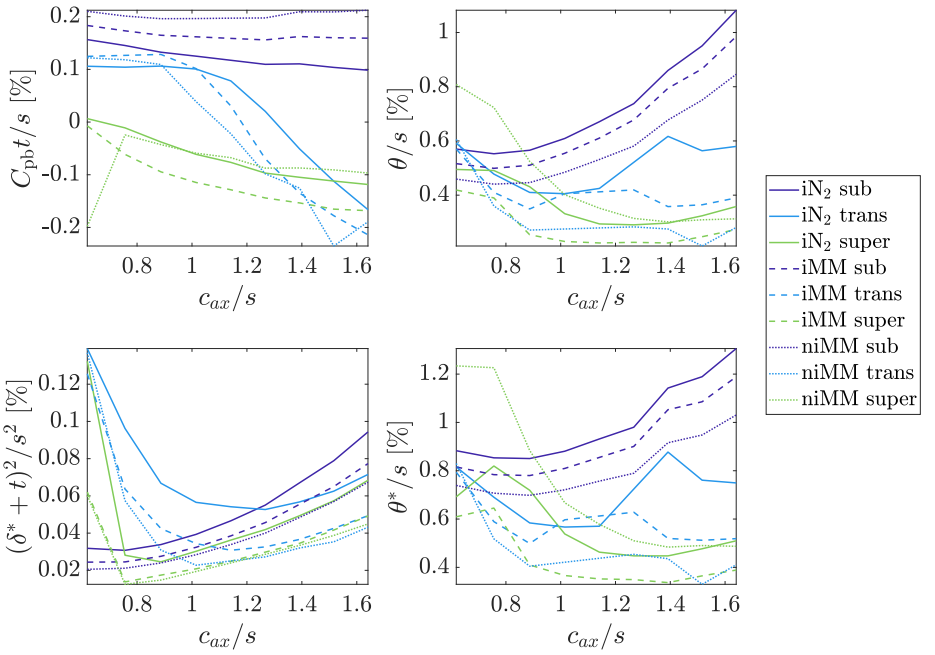

Figure 5.12: Normalized trends of (a) base pressure coefficient, (b) momentum thickness, (c) displacement thickness, and (d) kinetic energy thickness in the proximity of the trailing edge *vs* axial solidity for the *iMM-Kis3* blade. The boundary layer integral parameters are estimated by summing the contributions of both the pressure and the suction side.

trends are very similar, regardless of the model with which they are computed. At fixed α_1 and α_2, the optimal solidity value obtained with *iSol* is within the bounds defined by the values obtained with the Zweifel correlation for $Z_{Zw} = 0.8$ and $Z_{Zw} = 1.1$.

Figure 5.15 shows the results obtained with the *cSol* model for both the *iMM-Kis3* and the *Aachen* blades for the test cases listed in Tab. 5.2. The optimal solidity values obtained with the model are compared against those obtained from CFD considering only the passage loss calculated up to the trailing edge. For the *iN*$_2$ case and the *iMM* one (*iMM-Kis3* blade only), the trend with the Mach number is somewhat in agreement with that obtained with the CFD: both curves exhibit a maximum at transonic conditions, i.e., $M_{out} \sim 1$. However, the absolute values are incorrectly estimated. Predictions and values are instead inaccurate for all the remaining cases: the model fails to match the trends obtained from CFD. In particular, for both the investigated blades, the model does not provide reliable results for the *niMM* case beyond $M_{out} > 0.6$, and, for the *Aachen* blade, *iN*$_2$ and *iMM* cases, the model fails if $M_{out} > 1$. The outcome of this analysis points out that the physics of the problem is not correctly modelled: the possible causes of error can be attributed to i) excessively simplified blade loading distribution; ii) inaccurate C_d value, especially in the presence of strong stream-wise pressure gradients; iii) inability to

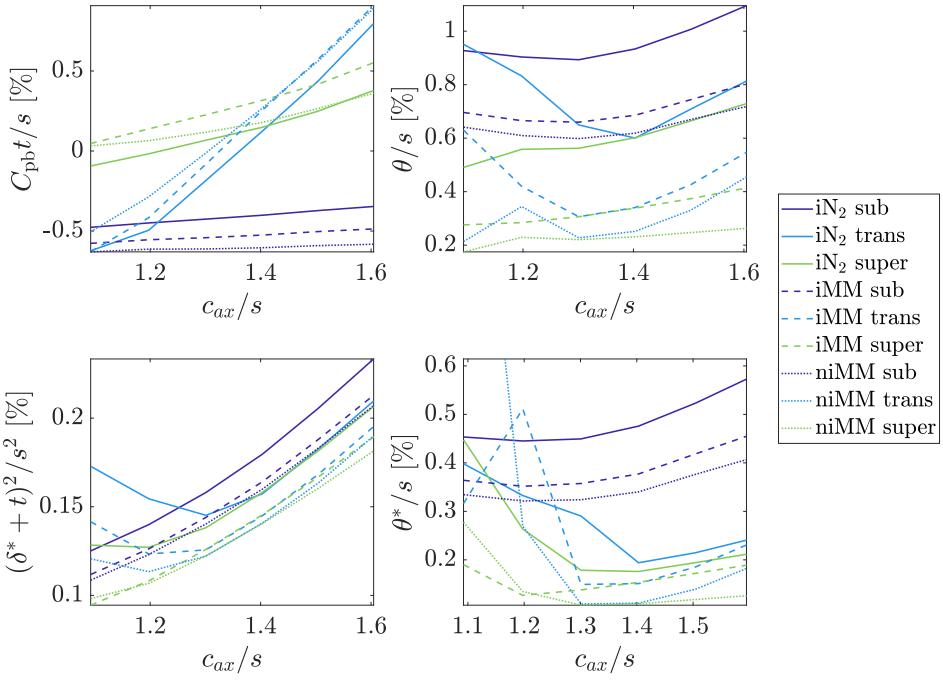

Figure 5.13: Normalized trends of (a) base pressure coefficient, (b) momentum thickness, (c) displacement thickness, and (d) kinetic energy thickness in the proximity of the trailing edge *vs* axial solidity for the *Aachen* blade. The boundary layer integral parameters are estimated by summing the contributions of both the pressure and the suction side.

capture the effect of boundary layer-shock interaction in the compressible flow regime, which results in additional passage loss.

Finally, Figure 5.16a-c shows the mixing loss as a function of the solidity for the *iN*$_2$, *iMM*, and *niMM* cases, respectively. Calculations have been performed for the *iMM-Kis3* blade only. The mixing loss has been estimated using the control volume-based approach described in Sec. 5.2 using as input the base pressure coefficient and the boundary layer integral parameters obtained from CFD and shown in Fig. 5.12. For all three cases, the control volume-based model provides a trend of mixing losses with the solidity which is aligned with that obtained from the RANS calculations up to the transonic regime: the minimum of the mixing losses shifts towards higher σ_x as the outlet Mach number increases. This further corroborates the finding that the mixing losses, and, thus, the optimal solidity value, are strongly affected by the state of the boundary layer at the trailing edge. However, the results for the supersonic regime are not consistent with those obtained from CFD simulations: in particular, the minimum of the mixing losses is located at lower solidity values than those obtained for the transonic case. The model does not account for the loss induced by the fish-tail shock waves forming downstream

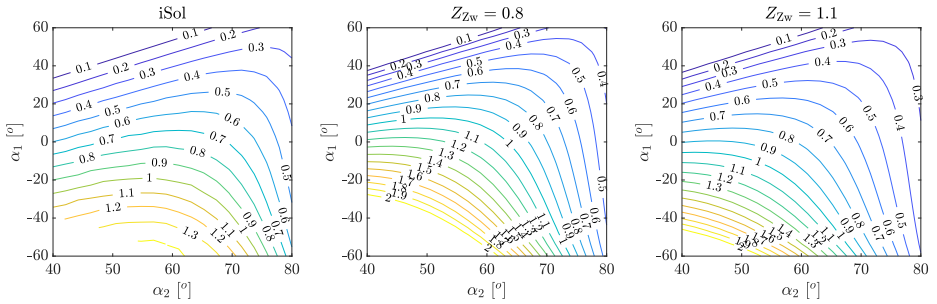

Figure 5.14: Optimal solidity σ_x *vs* flow angles resulting from (a) the *iSol* model, and the Zweifel correlation assuming (b) $Z_{Zw} = 0.8$ and (c) $Z_{Zw} = 1.1$.

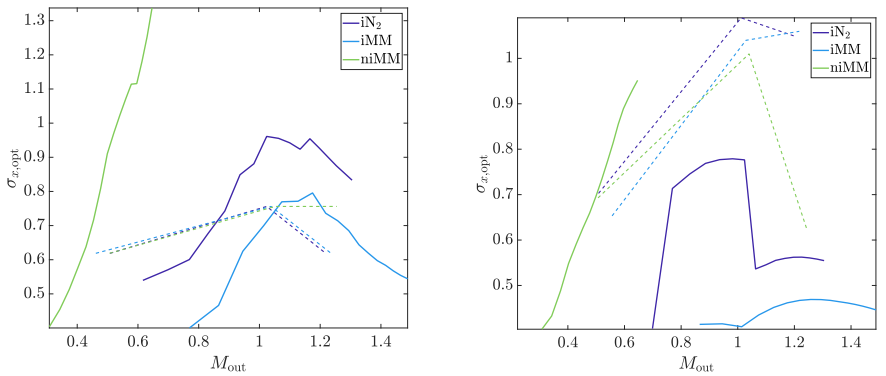

Figure 5.15: Optimal solidity value estimations *vs* outlet Mach number for (a) the *iMM-Kis3* and (b) the *Aachen* blades, respectively. Results obtained with the compressible reduced-order model and the numerical simulations are depicted in solid and dashed lines, respectively.

of the blade trailing edge. In conclusion, the proposed control volume approach for the prediction of the optimal solidity value is incapable of modelling physical phenomena with a sufficient degree of detail, and the optimal solidity value can only be predicted by numerical simulations or experiments.

5.5. CONCLUSIONS AND OUTLOOK

The optimal solidity value is used to determine the number of blades of an axial turbine stage. The work here presented aimed at investigating the influence of the molecular complexity of the working fluid, its thermodynamic state, and flow compressibility on the optimal solidity, as well as developing reduced-order models which can be used to estimate its value during the preliminary design. The optimal solidity values provided by the Zweifel criterion have been compared against those obtained with two-dimensional CFD simulations of the flow around two representative turbine stator blade geometries.

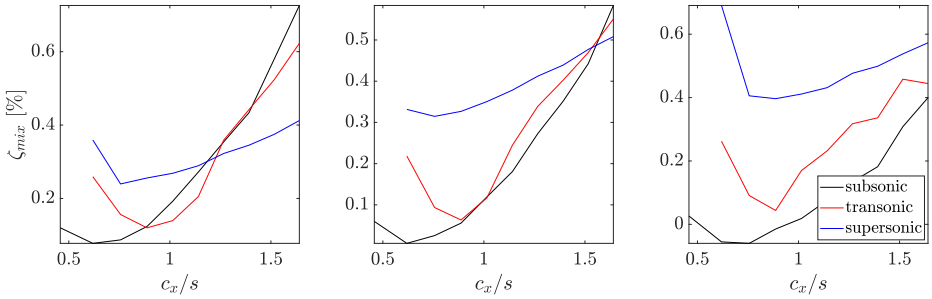

Figure 5.16: Mixing losses computed using the control volume-based model described in Sec. 5.2 *vs* axial solidity for the *iMM-Kis3* blade. Each graph refers to the (a) *air*, (b) *iMM*, and (c) *niMM* cases, respectively.

A loss breakdown analysis based on data obtained from the CFD simulations has also been carried out. Reduced-order models for the estimation of the optimal solidity value based on the minimization of the passage losses in the incompressible (**iSol**) and compressible (**cSol**) regimes have been developed and applied to selected test cases.

Based on the results of the study, the following conclusions can be summarized.

- Both the Zweifel correlation and the reduced-order incompressible flow model (**iSol**) predict inaccurate values of the optimal solidity because they do not account for the mixing loss, which is the primary loss if the flow is transonic or supersonic.
- The higher the cascade outlet Mach number, the higher the optimal solidity value, regardless of the working fluid.
- In the case of transonic and supersonic cascades, the optimal solidity value increases with the molecular complexity of the working fluid. However, this effect is negligible compared to that of the flow compressibility.
- If the working fluid is in a dense vapor state (with a non-negligible departure from ideal gas states), the mixing loss largely prevails over the passage loss, and the optimal solidity value further increases compared to that estimated under the assumption of a dilute gas.
- The compressible flow model (**cSol**), which has been developed for the compressible turbine flow case and is based on the minimization of the passage losses, fails to predict the correct trends and accurate values of optimal solidity.
- The accurate estimation of optimal solidity values requires the development of models and correlations for the estimation of the integral parameters of the boundary layer at the blade trailing edge.
- For a turbine stage operating in the transonic regime $M_{\text{out}} \sim 1$, the results of the numerical investigation show that the minimum of the overall loss is found for $1 < \sigma_{x,\text{opt}} < 1.2$. If the Zweifel correlation is used in the preliminary design, values of the Z_{Zw} coefficient larger than those conventionally recommended in literature have to be employed ($Z_{\text{Zw}} > 1.5$). This would result in turbine stages with

a larger number of blades, entailing an increase in efficiency at the expense of a larger amount of needed material to manufacture the stage.

The research documented in this chapter is the first step toward the development of novel design guidelines for the selection of the optimal solidity of axial and radial Organic Rankine Cycle (ORC) turbines. Future efforts will involve the development of a model for the estimation of the integral parameters of the boundary layer at the blade trailing edge and the implementation of the model described in Ref. [20] for the calculation of the dissipation coefficient C_d.

5.6. ACKNOWLEDGMENT

This research has been supported by the Applied and Engineering Sciences Domain (TTW) of the Dutch Organization for Scientific Research (NWO), Technology Program of the Ministry of Economic Affairs, grant # 15837.

NOMENCLATURE

SYMBOLS

b Blade camber
c Blade chord / 1st scaling parameter for pressure distribution
C_{pb} Base pressure coefficient
C_{d} Dissipation coefficient
$\mathrm{d}V$ 2nd scaling parameter for velocity distribution
$\mathrm{d}p$ 2nd scaling parameter for pressure distribution
h Specific enthalpy
k 1st scaling parameter for velocity distribution
M Mach number
$\dot{m}$ Mass flow rate
o Throat length
p Pressure
Re Reynolds number
s Specific entropy / Blade pitch
T Temperature
t Trailing edge thickness
V Absolute velocity
v Specific volume
Z Compressibility factor
Z_{Zw} Zweifel coefficient
α Absolute flow angle
α_{m} Blade metal angle at trailing edge
β_{ts} Total-to-static expansion ratio
γ Ratio of specific heats
γ_{pv} Generalized isentropic pressure-volume exponent
δ^* Displacement thickness
ζ Loss coefficient

θ Momentum thickness
θ^* Kinetic energy thickness
ρ Density
σ_x Blade axial solidity
χ Gauge angle

SUBSCRIPTS

e Mixed-out state
out Outlet (CFD)
opt Optimal
P Passage
ps Pressure side
s Entropy-related
ss Suction side
t Stagnation quantity
te Trailing edge
ts Total-to-static
x Axial component
y Tangential component
∞ Dilute gas state ($v \to \infty$)
1 Inlet
2 Outlet

ABBREVIATIONS

CFD Computational fluid dynamics
CO_2 Carbon dioxide
MF Mass-flow average
MIX Mixing
MM Hexamethyldisiloxane
MO Mixed-out averaged
P Passage
RANS Reynolds averaged Navier-Stokes
ROM Reduced-order model

BIBLIOGRAPHY

[1] O. Zweifel, *The Spacing of Turbo-Machine Blading Especially with Large Angular Deflection*. Brown Boveri Review, 1945.

[2] W. Traupel, *Thermische Turbomaschinen*. Springer Berlin Heidelberg, 1966, ISBN: 978-3-662-13209-8.

[3] A. Giuffre' and M. Pini, "Design Guidelines for Axial Turbines Operating With Non-Ideal Compressible Flows", en, *Journal of Engineering for Gas Turbines and Power*, vol. 143, no. 1, p. 011 004, Jan. 2021, ISSN: 0742-4795, 1528-8919. DOI: 10.1115/1.4049137.

[4] P. Colonna, E. Casati, C. Trapp, *et al.*, "Organic Rankine Cycle Power Systems: From the Concept to Current Technology, Applications, and an Outlook to the Future", en, *Journal of Engineering for Gas Turbines and Power*, vol. 137, no. 10, p. 100 801, Oct. 2015, ISSN: 0742-4795. DOI: 10.1115/1.4029884.

[5] Knowledge Center on Organic Rankine Cycle (KCORC), "Thermal Energy Harvesting - the Path to Tapping into a Large CO2-free European Power Source", en, Thermal Energy Harvesting Advocacy Group White Paper, 2022, p. 57.

[6] D. A. Kouremenos and K. A. Antonopoulos, "Isentropic exponents of real gases and application for the air at temperatures from 150 K to 450 K", *Acta Mech.*, vol. 65, no. 1-4, pp. 81–99, Jan. 1987, ISSN: 0001-5970, 1619-6937. DOI: 10.1007/BF01176874.

[7] A. Romei, D. Vimercati, G. Persico, and A. Guardone, "Non-ideal compressible flows in supersonic turbine cascades", en, *Journal of Fluid Mechanics*, vol. 882, Jan. 2020, ISSN: 0022-1120, 1469-7645. DOI: 10.1017/jfm.2019.796.

[8] F. Tosto, A. Giuffré, P. Colonna, and M. Pini, "Non-ideal Effects in Compressible Swirling Flows", en, in *Proceedings of the 3rd International Seminar on Non-Ideal Compressible Fluid Dynamics for Propulsion and Power*, M. Pini, C. De Servi, A. Spinelli, F. di Mare, and A. Guardone, Eds., vol. 28, Series Title: ERCOFTAC Series, Cham: Springer International Publishing, 2021, pp. 36–43, ISBN: 978-3-030-69305-3. DOI: 10.1007/978-3-030-69306-0_5.

[9] D. Baumgärtner, J. J. Otter, and A. P. S. Wheeler, "The Effect of Isentropic Exponent on Transonic Turbine Performance", en, *Journal of Turbomachinery*, vol. 142, no. 8, p. 081 007, Aug. 2020, ISSN: 0889-504X, 1528-8900. DOI: 10.1115/1.4046528.

[10] D. G. Wilson, "New Guidelines for the Preliminary Design and Performance Prediction of Axial-Flow Turbines", en, *Proceedings of the Institution of Mechanical Engineers, Part A: Power and Process Engineering*, vol. 201, no. 4, pp. 279–290, Nov. 1987, ISSN: 0263-7138. DOI: 10.1243/PIME_PROC_1987_201_035_02.

[11] R. Doughty, H. Moses, and B. Gregory, "The effect of blade solidity on the aerodynamic loss of a transonic turbine cascade", en, in *30th Aerospace Sciences Meeting and Exhibit*, Reno,NV,U.S.A.: American Institute of Aeronautics and Astronautics, Jan. 1992. DOI: 10.2514/6.1992-393.

[12] J. D. Denton, "The 1993 IGTI scholar lecture: Loss mechanisms in turbomachines", *Journal of Turbomachinery*, vol. 115, no. 4, pp. 621–656, Oct. 1993, ISSN: 0889-504X. DOI: 10.1115/1.2929299.

[13] J. D. Coull and H. P. Hodson, "Blade Loading and Its Application in the Mean-Line Design of Low Pressure Turbines", en, *Journal of Turbomachinery*, vol. 135, no. 2, p. 021 032, Mar. 2013, ISSN: 0889-504X, 1528-8900. DOI: 10.1115/1.4006588.

[14] E. M. Greitzer, C. S. Tan, and M. B. Graf, *Internal Flow: Concepts and Applications*. Cambridge University Press, 2004, ISBN: 978-0-511-61670-9. DOI: 10.1017/CBO9780511616709.

[15] B. Stephan, H. E. Gallus, and R. Niehuis, "Experimental Investigations of Tip Clearance Flow and its Influence on Secondary Flows in a 1-1/2 Stage Axial Turbine", en, in *Volume 1: Aircraft Engine; Marine; Turbomachinery; Microturbines and Small Turbomachinery*, Munich, Germany: American Society of Mechanical Engineers, May 2000, ISBN: 978-0-7918-7854-5. DOI: 10.1115/2000-GT-0613.

[16] ANSYS, *Ansys workbench, release 19.3, ANSYS, canonsburg, pa*, 2019.

[17] F. R. Menter, "Two-equation eddy-viscosity turbulence models for engineering applications", *AIAA Journal*, vol. 32, no. 8, pp. 1598–1605, 1994. DOI: 10.2514/3.12149. eprint: https://doi.org/10.2514/3.12149.

[18] G. J. Otero R., A. Patel, R. Diez S., and R. Pecnik, "Turbulence modelling for flows with strong variations in thermo-physical properties", *Int. J. Heat Fluid Flow*, vol. 73, pp. 114–123, Oct. 2018, ISSN: 0142727X. DOI: 10.1016/j.ijheatfluidflow.2018.07.005.

[19] E. W. Lemmon, I. H. Bell, M. L. Huber, and M. O. McLinden, *NIST standard reference database 23: Reference fluid thermodynamic and transport properties-REFPROP, version 10.0, National Institute of Standards and Technology*, 2018. DOI: 10.18434/T4JS3C.

[20] M. Pini and C. De Servi, "Entropy generation in laminar boundary layers of non-ideal fluid flows", *Non-Ideal Compressible Fluid Dynamics for Propulsion and Power: Lecture Notes in Mechanical Engineering*, F. di Mare, A. Spinelli, and M. Pini, Eds., pp. 104–117, 2020. DOI: 10.1007/978-3-030-49626-5_8.

6

CONCLUSIONS AND PERSPECTIVES

This dissertation reports an investigation of the combined effects of both the thermodynamic state of the working fluid and the complexity of its molecular structure on several paradigmatic one-and-two dimensional compressible flow configurations. The influence of the working fluid on key design parameters of axial turbines operating with organic substances, namely the flow deviation, the critical choking, and the optimal solidity, is treated in detail. The main results have been obtained through Reynolds-Averaged Navier-Stokes (RANS) and Direct Numerical simulations (DNS) of pipe flows, zero-pressure gradient boundary layer flows, and turbine cascade flows. Reduced-order models (ROM) have been developed to estimate the dissipation in boundary layers, the loss breakdown in axial turbines, and the flow deviation downstream of the blade trailing edge, and to investigate the optimal solidity in axial turbines.

6.1. CONCLUSIONS

Concluding remarks are listed at the end of each chapter. In the following, the key takeaways of the entire investigation documented in this dissertation and arising from the research questions from which it stemmed are summarized and further discussed.

1. **What is the influence of the working fluid and its thermodynamic state on the loss mechanisms in internal non-ideal flows?**
   Both the complexity of the molecular structure of the fluid and its thermodynamic state affect the flow field of an internal flow machine. On the one hand, fluid molecular complexity influences the breakdown of thermal and kinetic energy, the latter being lower in complex organic compounds than fluids made of simple molecules due to the larger number of molecular degrees of freedom. A larger viscous dissipation is observed in wall-bounded flows of complex organic compounds compared to those of simpler fluid molecules, e.g., nitrogen or oxygen, due to the lower amount of friction heating characterizing such flows. For example, results obtained from DNS have shown that for a boundary layer flow of

siloxane MM, the overall dissipation at $Re_\theta = 850$ is ~ 5% larger than that of a similar air flow. Moreover, analytical models demonstrate that fluid mixing processes are more dissipative if the substance is characterized by a high complexity of the molecular structure (~ 2.5% larger at $M_{\text{exit}} = 1.4$ for a mixing process occurring in siloxane MM if compared to a baseline air case). On the other hand, if the thermodynamic state of the fluid approaches that of the vapor-liquid critical point, two effects can be observed: mixing losses increase and the viscous dissipation decreases, the latter due to the large density gradients that the flow exhibits across the boundary layer thickness. In the case of an expansion process in siloxane MM occurring in the non-ideal flow regime ($Z \sim 0.5$), the increase in mixing loss compared to an ideal gas expansion is of the order of 5% at $M_{\text{exit}} = 1.4$. As discussed in Chap. 2, an explanation of this finding based on physics is currently lacking.

In summary, turbines operating in kinematic and dynamic similarity, characterized by a similar blade loading, are affected by larger viscous dissipation and mixing losses if the working fluid is an organic compound, the overall loss increasing if the thermodynamic state of the fluid is close to that of the vapor-liquid critical point. Conversely, turbines operating with air or fluids made of simple molecules are characterized by lower viscous dissipation and mixing losses. Overall, given that the mixing accounts for up to one-third of the total loss in axial turbines, one can argue that, if operated in thermodynamic and fluid-dynamic similarity, machines using complex organic compounds as working fluids feature lower efficiency than those using air or steam. For example, the overall increase of fluid dynamic loss for a cascade operating with siloxane MM and with $M_{\text{exit}} = 1.4$ is ~ 3% if compared to a similar cascade operating with air. Given that openly available loss models to estimate the viscous dissipation and the mixing losses in turbine flows do not take into account the effect of either the fluid or its thermodynamic state, the findings here summarized elucidate the physical mechanisms underlying the profile losses in the turbine and the derived knowledge is instrumental in developing new physics-based loss models which can then be used during the preliminary design phase.

As prescribed by non-ideal compressible fluid dynamic (NICFD) theory, analytical studies demonstrate that non-classical effects such as the non-monotonic variation of the Mach number with entropy in Rayleigh and Fanno flow (Chap. 2) can be expected only in case the fluid is a heavy organic compound, such as siloxane D_6, and for thermodynamic conditions in the close proximity of the critical point. Therefore, such effects are not of interest in turbomachinery, as power generation cycles like the ORC one are typically designed and operated away from the critical point.

2. **What is the influence of the working fluid and the thermodynamic fluid state on the flow deviation and the operating range of axial turbines?**
The working fluid has a major influence on the operational range of axial turbines. The work documented in this thesis shows that the choking of the meridional component of the Mach number, i.e., the critical choking, occurs at lower expansion ratios in turbo-machines operating with complex molecule fluids. Moreover, the

closer the thermodynamic state is to that of the critical point, the lower the Mach number at which the critical choking occurs. For the case of cascades operating with an organic compound, e.g., siloxane MM, in the dense vapor state, the total-to-static expansion ratio cannot exceed 3, whereas cascades operating with air can accommodate larger values (~ 4). This finding can be used during the preliminary design phase to determine, for instance, the minimum number of stages of a turbine: knowing the maximum volumetric flow ratio that a stage can accommodate, and that of the turbine, the minimum number of stages can easily be estimated as the ratio between the two. Furthermore, it has been found that the flow deviation angle is primarily a function of the volumetric flow ratio, regardless of the working fluid and its thermodynamic state. Such finding has been exploited to develop an analytical model providing the deviation angle as a function of the volumetric flow ratio, that can be used during preliminary design.

3. **What is the influence of the fluid and its thermodynamic state on guidelines for the selection of the optimal solidity in axial turbines?**
The findings on the loss mechanisms discussed in this dissertation prove that significant differences in the values of key turbine design parameters, such as the optimal cascade solidity, are to be expected depending on the fluid, its thermodynamic state, and the flow compressibility. The work presented in Chap. 5 proves that the value of optimal solidity in cascades operating with non-ideal compressible flows is primarily a function of the mixing losses downstream of the blade trailing edge, which are strongly affected by the flow regime and the thermodynamic state of the fluid. Therefore, existing empirical or semi-empirical correlations for the selection of the optimal solidity that do not consider the effect of mixing losses, like the Zweifel correlation, are not accurate. Attempts at developing models for the estimation of the optimal solidity with an approach based on physics have failed since none of the obtained trends matches those observed from the results of the numerical simulations. It can be concluded that the inherent complexity of the internal flow makes the development of physics-based models for the prediction of mixing losses in axial turbines very challenging: such losses strongly depend on the state of the boundary layer at the blade trailing edge, on the flow in the wake region, and on the shock-wave pattern. These flow phenomena are strongly correlated to the blade geometry, the blade loading, and the upstream flow conditions, and their modelling through rigorous analytical models is arguably not feasible.

6.2. PERSPECTIVES

The research presented in this dissertation is a stepping stone toward the understanding of non-ideal effects in dense vapor flows and the development of generalized guidelines for the design of unconventional turbomachinery. Based on the previously outlined conclusions, suggestions for future work are gathered in the following.

- Literature shows that mixtures as working fluids can be advantageous in improving the energy conversion efficiency of ORC turbogenerators. The usage of mixtures

introduces additional variables, i.e., the molar fraction of each fluid component, whose effect on the flow field must be analyzed. Extending the theoretical framework presented in Chap. 2 to flows of mixtures is thus paramount to characterize both non-ideal effects and the influence of mixture composition.

- In Chapter 2, the results obtained from the high-fidelity numerical simulations have been compared against those provided by a reduced-order model implementing the Cebeci-Smith algebraic model to estimate the eddy viscosity. However, more accurate turbulence models commonly used in engineering, such as the Spalart-Allmaras or the Menter k-omega SST ones, have not been implemented in the reduced-order model yet: therefore, their accuracy in the case of dense vapor flows has not been assessed. Future efforts should then be focused on assessing the accuracy of eddy viscosity models on simulations of dense vapor flows, and on properly tuning the coefficients for these challenging cases.

- The influence of wall-to-flow heat transfer on flow characteristics within the boundary layers has not been investigated yet in the case of dense vapor flows. Research devoted to studying wall-bounded flows of dense vapors in the presence of energy transfer from the wall with the aid of direct numerical simulations can elucidate the effect of fluid molecular complexity and of non-ideal thermodynamic properties on viscous dissipation and on the heat transfer coefficient.

- The results presented in Chap. 5 show that the choice of the optimal number of blades in axial turbines depends on the fluid, its thermodynamic states, and the flow compressibility. However, the developed physics-based models could not predict the optimal solidity value, due to the strong complexity of the flow field. In the author's opinion, improved reduced-order design models must resort to data-driven techniques, e.g., artificial neural networks (ANN), aiming at deriving relations for all the key design parameters (e.g., solidity, trailing edge thickness, blade thickness distribution, etc). To train, validate and test such data-driven models, a large database of numerical simulations spanning over different blade geometries and operating conditions should thus be generated. The development of such a model would require the creation of a numerical infrastructure able to: i) design a set of turbine blades characterized by different blade thicknesses and trailing edge thicknesses; ii) perform steady-state Reynolds-Averaged Navier-Stokes simulations of each blade flow passage for different values of the outlet Mach number, the inlet thermodynamic conditions, and the solidity value; iii) compute the loss breakdown, the blade loading, the dissipation coefficient associated with both the pressure and the suction surfaces, the base pressure coefficient, and the boundary layer integral parameters at the trailing edge; iv) feed an AI algorithm to develop correlations for the boundary layer integral parameters, and, moreover, the optimal solidity as a function of the blade shape parameters and the operating conditions.

APPENDIX

SOFTWARE

The research discussed in this dissertation has been carried out using several software packages and codes. In the following, the main ones are listed.

ANALYSIS OF NON-IDEAL RAYLEIGH AND FANNO FLOWS (QUASI1DANALYSIS)

Quasi1DAnalysis solves the compressible one-dimensional equations for Rayleigh and Fanno flows. The solver is coupled with FluidProp for the estimation of the fluid properties. The code is accessible via the QR code below.

BOUNDARY LAYER NON-IDEAL (BLNI) SOLVER

BLnI solves the two-dimensional boundary layer equations. Real gas thermophysical properties are estimated using the FluidProp package. Main developers: dr. Carlo de Servi, Francesco Tosto. The code is accessible via the QR code below.

TURBOLOSS

TurboLoss is a Python script performing loss breakdown analysis for axial turbine stages from CFD simulations. Main developer: Andrea Giuffré, TU Delft. The code is accessible via the QR code below.

3DNS

3DNS is a Fortran-based high-fidelity flow solver written by Prof. Andrew Wheeler, Whittle Laboratory, University of Cambridge. The Desktop open toolkit is available at `https://www.3dns.org/`. The code is accessible via the QR code below.

ACKNOWLEDGEMENTS

It's a tough world, and intense life,
moments of happiness, and uncertain future.

Antonio De La Cuesta

This dissertation is the result of more than four years of work. I reserve these few lines to acknowledge the contributions of all the people that have made this long journey possible.

I want to express my sincere gratitude to my supervisor, dr. Matteo Pini, for his invaluable guidance, ideas, and continuous feedback during our research journey. Without his support, achieving our research goals would not have been possible. I also extend my heartfelt thanks to my promotor, prof. dr. Piero Colonna, for his boundless enthusiasm and constructive critique, which has motivated my growth as a researcher and an individual.

I want to thank dr. Claudio Lettieri, whose initial contributions laid the foundation for this research. I'm also grateful to prof. dr. Andrew Wheeler for his assistance with configuring 3DNS, setting up high-fidelity simulations, and granting me the opportunity to visit the Whittle Laboratory in Cambridge.

I would also like to extend my sincere appreciation to dr. Carlo de Servi, dr. Adam J. Head, and the soon-to-be doctors Andrea Giuffré and Nitish B. Chandrasekaran, whose precious technical contributions and suggestions have helped me to shape different parts of this research. Thanks to Evert Bunschoten for translating the summary and the propositions into Dutch.

I am deeply grateful to all my colleagues and friends for their unwavering support throughout these years. Though the list is long, please accept this heartfelt appreciation as my way of expressing gratitude to each and every one of you.

And last but not least, the biggest thanks go to my family, namely my sister Erica and her partner Tobias, my aunt Pina, and my parents Carmela and Antonino, to whom this dissertation is dedicated. In tutti questi anni via dall'Italia, siete sempre stati il principale punto di riferimento. Il vostro amore e supporto incondizionato mi ha permesso di andare avanti anche nei momenti piú difficili. Grazie.

Delft, 25th September 2023

Francesco Costa

CURRICULUM VITÆ

Francesco Tosto was born in Torino, Italy, on the 15th of April 1993. He obtained his Bachelor's degree in Aerospace Engineering from Politecnico di Torino in 2015. The same year, he started his Master's degree in Aerospace Engineering at the same institute. Thanks to his academic results, Francesco was rewarded with an Erasmus+ scholarship and the opportunity to take part in a Double Degree exchange program with the KTH Royal Institute of Technology in Stockholm, Sweden. There, he enriched his knowledge in aerodynamics and fluid dynamics, specializing in Computational Fluid Dynamics (CFD). He carried out his Master's Thesis internship in Scania CV AB, Södertälje, Sweden. There, he investigated the performance and the internal flow of centrifugal compressors for automotive turbochargers. In February 2018, Francesco was appointed as a Ph.D. candidate at the Faculty of Aerospace of TU Delft under the supervision of dr. Matteo Pini and prof. dr. Piero Colonna. Currently, he is working as a Postdoc researcher in the Propulsion and Power group at the Faculty of Aerospace of TU Delft.

Francesco's research focuses on the study of the influence of the working fluid on the design and the performance of turbomachinery for applications such as organic Rankine cycle (ORC) power systems. His research entails the investigation of non-ideal effects on boundary layer flows of dense vapors and the development of improved design guidelines for unconventional turbomachinery. He is specialized in computational fluid dynamics, in particular in Reynolds Averaged Navier-Stokes (RANS) and direct numerical (DNS) simulations.

LIST OF PUBLICATIONS

JOURNAL ARTICLES

4. **F. Tosto**, M. Pini and P. Colonna, *The effect of working fluid and compressibility on the optimal solidity of axial turbine cascades*, Journal of the Global Power and Propulsion Society, 2023 (UNDER REVIEW)

3. **F. Tosto**, A. Wheeler and M. Pini, *Investigation of Non-Ideal Effects in Compressible Boundary Layers of Dense Vapors*, Physics of Fluids, 2023 (TO BE SUBMITTED)

2. **F. Tosto**, A. Giuffré, P. Colonna, and M. Pini, *Flow deviation and critical choking in transonic turbine cascades operating with non-ideal compressible flows*, Journal of the Global Power and Propulsion Society, August 2022, doi: 10.33737/jgpps/151659.

1. **F. Tosto**, C. Lettieri, M. Pini, and P. Colonna, *Dense-vapor effects in compressible internal flows*, Physics of Fluids, vol. 33, no. 8, p. 086110, Aug. 2021, doi: 10.1063/5.0058075.

CONFERENCE PROCEEDINGS

4. **F. Tosto**, A. Wheeler, and M. Pini, *High Fidelity Simulations and Modelling of Dissipation in Boundary Layers of Non-Ideal Fluid Flows*, 4th International Seminar on Non-Ideal Compressible Fluid Dynamics for Propulsion & Power, October 3-4, 2022, London, UK.

3. **F. Tosto**, D. Pasquale, P. Colonna, and M. Pini, *The effect of working fluid and compressibility on the optimal solidity in ORC turbine cascades*, 6th International Seminar on ORC Power Systems, October 11-13, 2021, Munich, Germany.

2. **F. Tosto**, A. Giuffré, P. Colonna, and M. Pini, *Non-ideal Effects in Compressible Swirling Flows*, Proceedings of the 3rd International Seminar on Non-Ideal Compressible Fluid Dynamics for Propulsion & Power, Springer International Publishing, 2021, pp. 36–43. doi: 10.1007/978-3-030-69306-0-5.

1. **F. Tosto**, C. Lettieri, M. Pini, P. Colonna, *1D Modelling of some paradigmatic non-ideal compressible flows*, 5th International Seminar on ORC Power Systems, September 9-11, 2019, Athens, Greece.